



D  
A  
S  
H

# DIGITAL ACCESS TO SCHOLARSHIP AT HARVARD

## A Search for the Higgs Boson Produced in Association With a Vector Boson Using the ATLAS Detector at the LHC

The Harvard community has made this article openly available.  
Please share how this access benefits you. Your story matters.

Citation	Mercurio, Kevin. 2015. A Search for the Higgs Boson Produced in Association With a Vector Boson Using the ATLAS Detector at the LHC. Doctoral dissertation, Harvard University, Graduate School of Arts & Sciences.
Accessed	December 4, 2015 1:49:16 PM EST
Citable Link	<a href="http://nrs.harvard.edu/urn-3:HUL.InstRepos:14226092">http://nrs.harvard.edu/urn-3:HUL.InstRepos:14226092</a>
Terms of Use	This article was downloaded from Harvard University's DASH repository, and is made available under the terms and conditions applicable to Other Posted Material, as set forth at <a href="http://nrs.harvard.edu/urn-3:HUL.InstRepos:dash.current.terms-of-use#LAA">http://nrs.harvard.edu/urn-3:HUL.InstRepos:dash.current.terms-of-use#LAA</a>

*(Article begins on next page)*

©2014 - Kevin Michael Mercurio

All rights reserved.

Dissertation Advisor

Author

**John Huth**

**Kevin Michael Mercurio**

## A Search for the Higgs Boson Produced in Association with a Vector Boson Using the ATLAS Detector at the LHC

### Abstract

This dissertation presents two searches for the Standard Model Higgs boson produced in association with a vector boson and decaying via  $H \rightarrow b\bar{b}$ . Specifically, the processes are:  $ZH \rightarrow \ell^+\ell^-b\bar{b}$  alone, and again in combination with the  $ZH \rightarrow \nu\bar{\nu}b\bar{b}$  and  $WH \rightarrow \ell\nu b\bar{b}$  processes. The dataset used for the analysis consists of  $4.7 \text{ fb}^{-1}$  at  $\sqrt{s} = 7 \text{ TeV}$  and  $20.3 \text{ fb}^{-1}$  at  $\sqrt{s} = 8 \text{ TeV}$  from LHC collisions. The search was optimized without bias to a particular mass of the Standard Model Higgs boson. Background processes contributing to the total number of observed events are estimated using a combination of Monte Carlo simulation and data-driven techniques. Utilizing a maximum-likelihood analysis, an observed upper limit on the cross section at the 95% confidence interval for the  $ZH \rightarrow \ell^+\ell^-b\bar{b}$  channel is set at 2.76 times the Standard Model cross section with an expected limit of 2.54, and the observed upper limit for the combined search is 2.3 times the Standard Model cross section, with an expected limit of 1.01. Furthermore, compatibility with the Standard Model expectation is evaluated through the parameter  $\mu = \frac{\sigma_{observed}}{\sigma_{StandardModel}}$  and found to be  $0.17 \pm 1.4$  for the  $ZH \rightarrow \ell^+\ell^-b\bar{b}$  analysis, and  $1.09 \pm 0.61$  for the combined analysis, both consistent with the Standard Model expectation of 1.

# Contents

Title Page . . . . .	i
Abstract . . . . .	iii
Table of Contents . . . . .	iv
List of Figures . . . . .	ix
List of Tables . . . . .	xvii
Acknowledgments . . . . .	xx
<b>1 Introduction</b>	<b>1</b>
<b>2 The Standard Model of Particle Physics</b>	<b>3</b>
2.1 The Standard Model and the Higgs Mechanism . . . . .	4
2.1.1 The Electroweak Sector . . . . .	5
2.1.2 The Higgs Sector . . . . .	7
2.2 Higgs Boson Production and Decay at the LHC . . . . .	10
2.3 Discovery of the Higgs boson at the LHC . . . . .	13
<b>3 The Large Hadron Collider</b>	<b>19</b>
3.1 The Injection Chain for the LHC . . . . .	22
3.2 The Design of the Large Hadron Collider . . . . .	23
3.3 The Luminosity Measurement . . . . .	26
3.3.1 Methodology . . . . .	27
3.3.2 Calibration of $\sigma_{vis}$ for Luminosity Determination . . . . .	29
3.3.3 Performance During Run I . . . . .	30
<b>4 The ATLAS Detector</b>	<b>35</b>
4.1 The ATLAS Coordinate System . . . . .	38
4.2 The Magnetic Field of the ATLAS Detector . . . . .	39
4.3 The Inner Detector . . . . .	40
4.3.1 The Pixel Detector . . . . .	44
4.3.2 The Semiconductor Tracker . . . . .	45
4.3.3 The Transition Radiation Tracker . . . . .	46

4.4	The ATLAS Calorimeter System . . . . .	47
4.4.1	The Electromagnetic Calorimeter . . . . .	49
4.4.2	The Hadronic Calorimeter . . . . .	53
4.4.3	The Forward Calorimeter . . . . .	55
4.5	The Muon Spectrometer . . . . .	55
4.5.1	The Monitored Drift Tubes . . . . .	58
4.5.2	The Cathode Strip Chambers . . . . .	61
4.5.3	The Resistive Plate Chambers . . . . .	62
4.5.4	The Thin Gap Chambers . . . . .	63
4.6	Forward Detectors for Luminosity Measurement . . . . .	65
4.7	Trigger and Data Acquisition . . . . .	66
4.7.1	L1 Muon Trigger . . . . .	67
4.7.2	L1 Calo Trigger . . . . .	68
5	<b>Physics Object and Event Reconstruction in ATLAS</b>	71
5.1	Inner Detector Track Reconstruction . . . . .	72
5.2	Primary Vertex Reconstruction . . . . .	74
5.3	Electron Reconstruction . . . . .	75
5.4	Muon Reconstruction . . . . .	78
5.5	Jet Reconstruction . . . . .	80
5.5.1	Global Sequential Calibration . . . . .	82
5.6	Identification and Calibration of $b$ -jets . . . . .	83
5.6.1	MV1 and MV1c $b$ -tagging Algorithms . . . . .	88
5.7	Missing Transverse Energy Reconstruction . . . . .	90
6	<b>Data Samples and Monte Carlo Simulation</b>	94
6.1	Data Samples . . . . .	94
6.2	Monte Carlo Simulation . . . . .	95
6.2.1	Signal Modeling . . . . .	96
6.2.2	Background Modeling . . . . .	96
6.2.3	Corrections for Reconstructed Objects . . . . .	99
	Vertex-Z Correction . . . . .	99
	Trigger Efficiency Correction . . . . .	99
	Muon Corrections . . . . .	100
	Electron Corrections . . . . .	105
	Jet Corrections . . . . .	111
	$b$ -tagging Corrections . . . . .	111
7	<b>Analysis Strategy and Event Selection</b>	115
7.1	Analysis Strategy . . . . .	115
7.2	Physics Object Selection . . . . .	118
7.2.1	Lepton Definition . . . . .	118

7.2.2	Additional Lepton Selection Information . . . . .	119
7.2.3	Jet Selection Criteria . . . . .	121
7.2.4	Removal of Overlapping Objects . . . . .	122
7.2.5	$b$ -jet Tagging Requirements . . . . .	123
Truth-Tagging . . . . .	124	
Biases from Truth Tagging . . . . .	125	
Biases from Generators . . . . .	126	
7.2.6	Missing Energy Selection . . . . .	127
7.3	Improvements to the $m_{b\bar{b}}$ Resolution . . . . .	127
7.3.1	Kinematic Likelihood Fit . . . . .	128
7.4	Event Selection . . . . .	131
7.4.1	Event Cleaning . . . . .	132
7.4.2	Trigger Selection . . . . .	133
7.4.3	Lepton Selection . . . . .	134
7.4.4	Jet Selection . . . . .	134
7.4.5	Kinematic Requirements to Define Analysis Regions . . . . .	135
<b>8</b>	<b>Characterization of Signal and Background Processes</b>	<b>138</b>
8.1	Signal Modeling and Theoretical Uncertainties . . . . .	139
8.1.1	$p_T^V$ -dependent NLO Electroweak Correction . . . . .	141
8.1.2	Uncertainties on the Inclusive Cross Section . . . . .	141
8.1.3	Uncertainties on the Signal Acceptance . . . . .	143
8.1.4	QCD Uncertainties on the Signal $p_T^V$ . . . . .	146
8.2	Modeling of the Background Processes . . . . .	150
8.2.1	Modeling of the $Z+jets$ Background . . . . .	150
2-jet to 3-jet Ratio, Flavor Fractions . . . . .	152	
$\Delta\phi$ Correction . . . . .	153	
$p_T^Z$ Correction . . . . .	155	
Systematic Uncertainty on the $m_{b\bar{b}}$ Shape . . . . .	158	
8.2.2	Modeling of the $t\bar{t}$ Background . . . . .	162
Top $p_T$ Correction . . . . .	162	
Uncertainty on the 2-jet to 3-jet Ratio . . . . .	164	
Residual $p_T^Z$ Uncertainty . . . . .	165	
Systematic Uncertainty on the $m_{b\bar{b}}$ Shape . . . . .	168	
8.2.3	Modeling of the Diboson Background . . . . .	170
Uncertainties on the 2-jet to 3-jet Ratio . . . . .	171	
Cross Section Uncertainties from PDF and $\alpha_S$ . . . . .	172	
Systematic Uncertainty on the $m_{b\bar{b}}$ Shape . . . . .	174	
8.2.4	Modeling of the Single-Top Background . . . . .	176
8.2.5	QCD multijet and Non-collision Background . . . . .	177
8.2.6	Modeling of the $W+jets$ Background . . . . .	180

<b>9 Statistical Analysis Model</b>	<b>181</b>
9.1 Introduction to the Profile Likelihood Method . . . . .	182
Template Morphing . . . . .	185
9.1.1 Variables and Analysis Regions in the Likelihood . . . . .	188
9.2 Systematic Uncertainties . . . . .	189
9.2.1 Experimental Systematic Uncertainties . . . . .	192
Luminosity and Pile-up Uncertainty . . . . .	192
Electron-specific Uncertainties . . . . .	193
Muon-specific Uncertainties . . . . .	193
Jet-specific Uncertainties . . . . .	194
Missing Transverse Energy . . . . .	197
Flavor Tagging . . . . .	197
Smoothing . . . . .	198
List of Experimental Nuisance Parameters . . . . .	200
9.2.2 Systematic Uncertainties for Signal Modeling . . . . .	202
9.2.3 Systematic Uncertainties for Background Modeling . . . . .	202
$Z + \text{jet}$ Modeling Uncertainties . . . . .	202
$t\bar{t}$ Modeling Uncertainties . . . . .	203
Diboson Modeling Uncertainties . . . . .	204
9.2.4 Pruning of the Systematic Uncertainties . . . . .	209
9.3 Input Distributions to the Fit . . . . .	211
9.4 Binning Transformation . . . . .	217
9.4.1 General description . . . . .	217
9.5 Interpreting the Profile Likelihood Fit . . . . .	220
9.6 Post-fit Distributions . . . . .	225
<b>10 Results</b>	<b>231</b>
10.1 Validation through Diboson Process . . . . .	231
10.2 Higgs Search Results . . . . .	235
10.2.1 Higgs Signal Strength . . . . .	236
10.2.2 Limits on the Cross Section for the $ZH \rightarrow \ell^+ \ell^- b\bar{b}$ Process . . .	236
10.3 Discussion of Results . . . . .	237
<b>11 Combined Search</b>	<b>239</b>
11.1 Motivation for the Combination . . . . .	239
11.2 Object and Event Selection . . . . .	240
11.2.1 Event Selection . . . . .	240
11.2.2 Lepton Selection for Event Categorization . . . . .	241
11.2.3 Jet Selection for Event Categorization . . . . .	242
11.2.4 Event Kinematic Selection . . . . .	242
11.3 Background Modeling . . . . .	243
11.3.1 $W + \text{jets}$ Modeling . . . . .	245

11.3.2 Single-top Modeling . . . . .	249
11.3.3 Multijet Background Estimate from Data . . . . .	251
0-lepton Multijet Estimate . . . . .	251
1-lepton Multijet Estimate . . . . .	253
11.4 Extension of the Profile Likelihood Fit . . . . .	255
11.5 Inclusion of the $\sqrt{s} = 7$ TeV Analysis . . . . .	261
11.6 Results of the Combined Analysis . . . . .	262
11.6.1 Validation through Diboson Processes . . . . .	262
11.6.2 Higgs Analysis Results . . . . .	263
Higgs Signal Strength . . . . .	267
Excess Relative to Background Expectation . . . . .	269
Upper Limit on the Cross Section . . . . .	269
<b>12 Conclusion and Future Prospects</b>	<b>271</b>
<b>Bibliography</b>	<b>274</b>
<b>A Prefit distributions for the 3-jet region</b>	<b>284</b>
<b>B Postfit distributions for the 3-jet region</b>	<b>291</b>

# List of Figures

2.1	The particle content of the Standard Model [117]. . . . .	5
2.2	The four leading-order processes with the highest production cross sections for the Higgs boson in a pp collider such as the LHC. (a) The gluon-gluon fusion process, (b) Associated production with a vector boson, (c) The vector boson fusion process, and (d) Associated production with a pair of top quarks. . . . .	11
2.3	The production cross sections as a function of Higgs boson mass for a variety of production mechanisms for the LHC operating at $\sqrt{s} = 8$ TeV [88]. . . . .	12
2.4	The branching ratio as a function of Higgs boson mass for a variety of decay modes [88]. . . . .	14
2.5	The four-lepton invariant mass from the ATLAS $H \rightarrow ZZ$ analysis. The Higgs signal contribution is shown for $m_H = 125$ GeV as the blue histogram. The expected background contributions, $ZZ^*$ (red histogram) and $Z + \text{jets}$ plus $t\bar{t}$ (violet histogram), are shown for the combination of the 7 TeV and 8 TeV results [44]. . . . .	16
2.6	The di-photon invariant mass from the ATLAS $H \rightarrow \gamma\gamma$ analysis. The Higgs signal contribution and background expectation are shown. The bottom panel shows the background-subtracted data and the expected Higgs signal contribution. The result corresponds to the combination of the 7 TeV and 8 TeV data [43]. . . . .	17
2.7	Higgs results from combinations of the 7 TeV and 8 TeV data with the ATLAS detector [111]. . . . .	18
3.1	The layout of the major experiments on the LHC [73]. . . . .	21
3.2	The LHC Injector Chain, showing the layout of the accelerator complex and the energy achieved for protons at the exit of each system [73]. . .	22
3.3	A cross-sectional view of an LHC dipole magnet [45]. . . . .	24

3.4	A measurement of the specific interaction rate as a function of the horizontal separation of the beams for a specific BCID. The residual deviation of the data from the Gaussian plus constant term fit, normalized at each point to the statistical uncertainty ( $\sigma_{data}$ ), is shown in the bottom panel. A value for $\mu_{vis}$ is obtained from such data by combining the measurement with independent measurements of $n_1$ and $n_2$ [22]. . . . .	31
3.5	Integrated luminosity collected by the ATLAS experiment as a function of calendar day in 2011 (left) and 2012 (right). The green area represents the total integrated luminosity delivered by the LHC, and the yellow area represents the integrated luminosity recorded by the ATLAS detector. The difference is due to the safety precaution of keeping sensitive electronics in low-voltage mode before the beam is ensured to be stable [16]. . . . .	33
3.6	The peak value of the average number of interactions per bunch crossing as a function of calendar day, as recorded by ATLAS [16]. . . . .	34
3.7	The integrated luminosity collected during Run I of the LHC as a function of the maximum average number of interactions per bunch crossing [16]. . . . .	34
4.1	A schematic of the ATLAS detector [32]. . . . .	37
4.2	(Left) The layout of the ATLAS Magnet System. The orange, oval rings forming the outer layer of the cylinder represent the toroidal magnets of the Muon Spectrometer. The interior cylinder represents the four layers used to model the Tile calorimeter, which contains the solenoid windings. (Right) A cross-sectional view of the ATLAS magnetic field strength. The inner red circle with radius 1 m is the strength of the solenoid, while the outer, less homogeneous region with 8-fold symmetry is the strength of the toroid system. Return fluxes appear as the thin rings at $R \sim 2.5$ m and $R \sim 4$ m [32]. . . . .	41
4.3	The material budget of the ATLAS Inner Detector traversed by a straight track, as measured at the exit of the Inner Detector envelope in terms of (left) radiation lengths $X_0$ , and (right) interaction lengths $\lambda_0$ [32]. . . . .	42
4.4	A schematic of the envelopes of the sub-detectors in a quarter-section of the ATLAS Inner Detector [32]. . . . .	43
4.5	A schematic of the ATLAS calorimeter [32]. . . . .	49

4.6	Cumulative amount of material in the calorimeter systems [32]. The amount of material in terms of radiation lengths $X_0$ for the EM barrel (top right) and EM barrel (top left). The amount of material in terms of nuclear interaction lengths for the different hadronic calorimeter layers, as well as the total EM calorimeter and the material before the calorimeter (bottom center) . . . . .	51
4.7	A sketch of the EM calorimeter geometry and readout granularity (left) and a photo of a partially stacked barrel module showing the accordion design [32]. . . . .	53
4.8	The layout of the ATLAS Muon Spectrometer [32]. . . . .	57
4.9	The layout of the muon spectrometer [31]. A cross-sectional view is shown on top, and a cut-away side view is shown on bottom. . . . .	59
4.10	Primary contributions to muon stand-alone tracking resolution [21]. . . . .	60
4.11	Layout of an MDT chamber [31]. Two multilayers, each with three layers of tubes are shown, along with the support structure and the optical alignment system. . . . .	61
4.12	A schematic of an MDT tube while a traversing muon has ionized the gas. The first electrons to reach the wire are from the point of closest approach, or $R_{min}$ , and form the leading edge of the hit signal [31]. . . . .	62
4.13	A schematic of a CSC chamber. [31]. . . . .	62
4.14	A schematic of an RPC chamber (left) and the material layers of an RPC gas gap (right). The right figure is a zoom-in version of the left figure. [31]. . . . .	63
4.15	A schematic of TGC chambers, a TGC triplet (left) and doublet (right) [31]. . . . .	64
4.16	A diagram of the trigger logic for the L1 Muon Trigger [32]. . . . .	69
4.17	A diagram of the trigger logic for the L1 Calo Trigger Cluster Processor algorithm [32]. . . . .	70
5.1	A drawing of several calorimeter cells demonstrating the creation of topoclusters from neighboring cells given the cell energy as a function of the noise threshold [73]. . . . .	81
5.2	The relative resolution of jets as a function of $p_T$ for several calibration methods. [23]. . . . .	84
5.3	Histograms of the two input variables to the likelihood ratio analysis for the IP3D $b$ -tagging alrogithm. The negative impact parameters correspond to those tracks which are determined to cross the jet axis behind, rather in front of, the primary vertex. [18]. . . . .	87
5.4	The output weight of the JetFitter $b$ -tagging algorithm. Higher weights correspond to a greater likelihood of the candidate jet being a $b$ -jet [18]. . . . .	89
5.5	The rejection of light jets and charm jets as a function of $b$ -tagging efficiency for a variety of tagging algorithms [26]. . . . .	92

6.1	Scale factors for electron triggers as a function of $\eta$ . The ratio of data/MC is applied to reweight the efficiency in Monte Carlo events to match the efficiency measured in data. [19]. . . . .	100
6.2	The reconstruction efficiency for Combined, Segment-Tagged, and Calo Muons. The bottom panel shows the ratio between measured and simulated efficiencies, which is used to weight events as a correction [28].	102
6.3	Di-muon invariant mass before and after the application of the correction for mis-modeling of the muon reconstruction efficiency [28]. . . . .	103
6.4	Corrections to the muon momentum resolution: $\Delta a^{MS}$ [28]. . . . .	104
6.5	Corrections to the muon momentum scale for Muon Spectrometer track measurements [28]. . . . .	104
6.6	Reconstruction efficiency for electrons as a function of $\eta$ in four $p_T$ ranges. The bottom panel of each figure is the ratio of the efficiency in data to that in Monte Carlo simulation [20]. . . . .	108
6.7	Identification efficiency for electrons as a function of $\eta$ in four $p_T$ ranges. The bottom panel of each figure is the ratio of the efficiency in data to that in Monte Carlo simulation [20]. . . . .	109
6.8	The di-electron invariant mass from events consistent with a $Z$ -boson decay. Data and Monte Carlo simulation are shown, and the fit of a Breit-Wigner convoluted with a Crystal Ball function is shown in red [36].	110
6.9	Corrections to the $b$ -tagging efficiency. . . . .	114
7.1	Truth tagging $\Delta R$ correction. . . . .	125
7.2	Generator dependence of flavor tagging for exclusive MV1c 70% OP. .	126
7.3	The $p_T$ -reco correction as a function of the jet's $p_T$ -reco. . . . .	128
7.4	Dijet invariant mass before and after applying a kinematic likelihood fit in $ZH(125)$ simulation. . . . .	131
7.5	$b$ -tagging categories . . . . .	135
8.1	Leading order Feynman diagrams for quark-initiated $VH$ production. .	140
8.2	Leading order Feynman diagrams for gluon-initiated $ZH$ production. .	140
8.3	Differential NLO Electroweak $VH$ production cross section correction.	142
8.4	Normalized $p_T^V$ distribution for signal QCD scale uncertainty studies. .	147
8.5	Normalized $p_T^V$ distribution for the study of the PDF uncertainty . .	149
8.6	$\Delta\phi$ distribution for $Z+jets$ events . . . . .	156
8.7	$\Delta\phi$ correction for the $Z+jets$ background. The data points represent the ratio of data/MC in the 0-tag analysis region for the 2-lepton analysis, where the contribution from the non- $Z+jets$ backgrounds have been subtracted from both data and the MC before taking the ratio. The black line is a linear fit to this ratio, which defines the correction. Systematic variations of 150% and 50% of the correction value are shown as red and blue lines, respectively. . . . .	157

8.8	$p_T^Z$ for $Z+jets$ events before corrections have been applied. . . . .	159
8.9	$m_{b\bar{b}}$ systematic uncertainty for $Z+jets$ events . . . . .	161
8.10	The top $p_T$ differential cross section with the 7 TeV dataset is shown for several Monte Carlo Simulations. Disagreement between data and Monte Carlo motivates correcting the $p_T$ of the top quarks to improve the modeling of the top background for the analysis presented in this thesis. . . . .	163
8.11	All generator comparisons for $t\bar{t}$ $m_{b\bar{b}}$ systematics. . . . .	169
8.12	POWHEG+Pythia8 and Herwig comparison for the ZZ diboson process. The systematic uncertainties from the parton shower and hadronization model are estimated by taking fitting the ratio of the different predictions with Equation 8.2. The POWEHEG+Pythia8 simulation is shown in blue, and Herwig shown in red. . . . .	175
8.13	Example of the multijet template fit to the $m_{ee}$ distribution in the 1-tag region for the estimation of the multijet background. The data are shown as black points, and the multijet template is shown in blue after being fit to the data. $Z+jets$ is represented with the purple histogram and all other backgrounds ( $t\bar{t}$ , single-top, diboson) are in green. . . . .	178
8.14	Plot of the di-lepton invariant mass for the muon channel in the 0-tag control region. For the muon channel, the contributions from both multijet and $W+jets$ background are negligible compared to the top, diboson, and $Z+jets$ backgrounds [109]. . . . .	179
9.1	Example of a morphing template. . . . .	186
9.2	Pre-fit MV1c distributions of the tagged jet for the 2-lepton 2-jets 1-tag regions . . . . .	211
9.3	Pre-fit $m_{b\bar{b}}$ distributions for the 2-lepton 2-jet analysis regions with $0 < p_T^Z < 90 \text{ GeV}$ . . . . .	212
9.4	Pre-fit $m_{b\bar{b}}$ distributions for the 2-lepton 2-jet analysis regions with $90 < p_T^Z < 120 \text{ GeV}$ . . . . .	213
9.5	Pre-fit $m_{b\bar{b}}$ distributions for the 2-lepton 2-jet analysis regions with $120 < p_T^Z < 160 \text{ GeV}$ . . . . .	214
9.6	Pre-fit $m_{b\bar{b}}$ distributions for the 2-lepton 2-jet analysis regions with $160 < p_T^Z < 200 \text{ GeV}$ . . . . .	215
9.7	Pre-fit $m_{b\bar{b}}$ distributions for the 2-lepton 2-jet analysis regions with $p_T^Z > 200 \text{ GeV}$ . . . . .	216
9.8	$m_{b\bar{b}}$ binning transformation . . . . .	219
9.9	2-lepton fit pulls for $b$ -jet tagging. . . . .	222
9.10	2-lepton fit pulls for $Z+jets$ modeling parameters. . . . .	222
9.11	2-lepton fit pulls for normalization parameters. . . . .	223
9.12	Ranking of the importance of the systematic uncertainties. . . . .	224

9.13 Post-fit MV1c distribution of the tagged jet for the 2-lepton 2-jets 1-tag regions . . . . .	225
9.14 Post-fit $m_{b\bar{b}}$ distributions for the 2-lepton 2-jet regions with $0 < p_T^V < 90 \text{ GeV}$ . . . . .	226
9.15 Post-fit $m_{b\bar{b}}$ distributions for the 2-lepton 2-jet regions with $90 < p_T^V < 120 \text{ GeV}$ . . . . .	227
9.16 Post-fit $m_{b\bar{b}}$ distributions for the 2-lepton 2-jet regions with $90 < p_T^V < 120 \text{ GeV}$ in the 2-lepton fit. . . . .	228
9.17 Post-fit $m_{b\bar{b}}$ distributions for the 2-lepton 2-jet regions with $160 < p_T^V < 200 \text{ GeV}$ . . . . .	229
9.18 Post-fit $m_{b\bar{b}}$ distributions for the 2-lepton 2-jet regions with $p_T^V > 200 \text{ GeV}$ in the 2-lepton fit. . . . .	230
10.1 2-lepton fit pulls for $Z+\text{jets}$ modeling parameters. . . . .	233
10.2 The distribution of $m_{b\bar{b}}$ in data after subtraction of all backgrounds except for the diboson processes, as obtained with the dijet mass analysis for the $\sqrt{s} = 8 \text{ TeV}$ data. The contributions from all $p_T^V$ intervals, number-of-jets and 2-tag $b$ -tagging categories are summed and weighted by their respective values of the ratio of expected diboson boson signal to fitted background. The contribution of the associated $ZH$ production of a Standard Model Higgs boson with $m_h = 125 \text{ GeV}$ is shown as expected for the Standard Model cross section (indicated as $\mu = 1.0$ ). The size of the combined statistical and systematic uncertainty on the fitted background is indicated by the hatched band. . . . .	234
10.3 Expected 95% confidence level upper limits on the normalized signal strength parameter $\mu$ as a function of Higgs boson mass for the $ZH \rightarrow \ell^+ \ell^- b\bar{b}$ analysis. The expected upper limit is given for the background-only hypothesis. The green and yellow bands represent the $1\sigma$ and $2\sigma$ ranges of the expectation for the upper limit in the absence of a signal. The dashed line represents the observed upper limit. . . . .	237
10.4 The observed local $p_0$ as a function of the Higgs boson mass for the $ZH \rightarrow \ell^+ \ell^- b\bar{b}$ analysis. The dashed curves shows the expected local $p_0$ under the hypothesis of a Standard Model Higgs boson signal at that mass point. . . . .	238

11.1 The $\Delta\phi$ distribution observed in data (points with error bars) and expected (histograms) for the 2-jet 0-tag control region of the 1-muon sub-channel, (a) before and (b) after reweighting. All $p_T^W$ intervals are combined. The multijet and simulated-background normalizations are provided by the multijet fits. The size of the statistical uncertainty is indicated by the shaded band. The data-to-background ratio is shown in the lower panel [29]. . . . .	246
11.2 The $p_T^W$ distribution observed in data (points with error bars) and expected (histograms) for the 2-jet 0-tag control region of the 1-muon sub-channel, (a) before and (b) after $\Delta\phi$ reweighting. The multijet and simulated-background normalizations are provided by the multijet fits. The size of the statistical uncertainty is indicated by the shaded band. The data-to-background ratio is shown in the lower panel [29]. . . . .	247
11.3 The distribution of $m_{b\bar{b}}$ in data after subtraction of all backgrounds except for the diboson processes, as obtained with the dijet mass analysis for the $\sqrt{s} = 8$ TeV data. The contributions from all lepton channels, $p_T^V$ intervals, number-of-jets and 2-tag $b$ -tagging categories are summed and weighted by their respective values of the ratio of expected Higgs boson signal to fitted background. The contribution of the associated $WH$ and $ZH$ production of a Standard Model Higgs boson with $m_h = 125$ GeV is shown as expected for the Standard Model cross section (indicated as $\mu = 1.0$ ). The size of the combined statistical and systematic uncertainty on the fitted background is indicated by the hatched band. . . . .	263
11.4 Impact of systematic uncertainties on the fitted signal-strength parameter $\hat{\mu}$ for the $\sqrt{s} = 8$ TeV data. The systematic uncertainties are listed in decreasing order of their impact on $\hat{\mu}$ on the $y$ -axis. The boxes show the variations of $\hat{\mu}$ , referring to the top $x$ -axis, when fixing the corresponding individual nuisance parameter $\theta$ to its post-fit value $\hat{\theta}$ modified upwards or downwards by its post-fit uncertainty, and repeating the fit as explained in the text. The hatched and open areas correspond to the upwards and downwards variations, respectively. The filled circles, referring to the bottom $x$ -axis, show the deviations of the fitted nuisance parameters $\hat{\theta}$ from their nominal values $\theta_0$ , in terms of standard deviations with respect to their nominal uncertainties $\Delta\theta$ . The associated error bars show the post-fit uncertainties of the nuisance parameters, relative to their nominal uncertainties. The red circles with their error bars show the fitted values and uncertainties of the normalization parameters that are floating in the fit and have a pre-fit value of one. . . . .	266
11.5 Fitted Higgs signal strength for combinations of the $\sqrt{s} = 7$ TeV and $\sqrt{s} = 8$ TeV analyses. . . . .	268

11.6 Expected 95% C.L. upper limits on the normalised signal strength as a function of Higgs boson mass for all channels after the combination of the $\sqrt{s} = 7$ TeV and $\sqrt{s} = 8$ TeV analyses. The expected upper limit is given for the background-only hypothesis in blue, and the black dashed line corresponds to the expected upper limit after the injection of the Higgs signal process at $m_H = 125$ GeV. . . . .	270
A.1 Pre-fit MV1c distributions for the 2-lepton 3-jet 1-tag regions . . . . .	285
A.2 Pre-fit $m_{b\bar{b}}$ distributions for the 2-lepton 3-jet analysis regions with $0 < p_T^Z < 90$ GeV. . . . .	286
A.3 Pre-fit $m_{b\bar{b}}$ distributions for the 2-lepton 3-jet analysis regions with $90 < p_T^Z < 120$ GeV. . . . .	287
A.4 Pre-fit $m_{b\bar{b}}$ distributions for the 2-lepton 3-jet analysis regions with $120 < p_T^Z < 160$ GeV. . . . .	288
A.5 Pre-fit $m_{b\bar{b}}$ distributions for the 2-lepton 3-jet analysis regions with $160 < p_T^Z < 200$ GeV. . . . .	289
A.6 Pre-fit $m_{b\bar{b}}$ distributions for the 2-lepton 3-jet analysis regions with $p_T^Z > 200$ GeV. . . . .	290
B.1 Post-fit MV1c distribution for the 2-lepton 3-jets 1-tag regions . . . . .	291
B.2 Post-fit dijet mass analysis plots for the 2-lepton 3-jets regions with $0 < p_T^V < 90$ GeV in the 2-lepton fit. . . . .	292
B.3 Post-fit dijet mass analysis plots for the 2-lepton 3-jets regions with $90 < p_T^V < 120$ GeV in the 2-lepton fit. . . . .	293
B.4 Post-fit dijet mass analysis plots for the 2-lepton 3-jets regions with $120 < p_T^V < 160$ GeV in the 2-lepton fit. . . . .	294
B.5 Post-fit dijet mass analysis plots for the 2-lepton 3-jets regions with $160 < p_T^V < 200$ GeV in the 2-lepton fit. . . . .	295
B.6 Post-fit dijet mass analysis plots for the 2-lepton 3-jets regions with $p_T^V > 200$ GeV in the 2-lepton fit. . . . .	296

# List of Tables

3.1	Differences between the design LHC parameters and those achieved during data taking in 2011 and 2012 [73, 94]. . . . .	32
4.1	The performance goals of ATLAS detector's components [32]. Energy and momentum are listed in GeV and $\oplus$ indicates summation in quadrature. . . . .	38
4.2	Calorimeter parameters. . . . .	50
4.3	The parameters of the Muon Spectrometer [32]. . . . .	56
5.1	Signal and background efficiencies for likelihood (LH) electron identification menus. The efficiencies shown are an average over all $\eta$ and over electron $20 < E_T < 50$ GeV [83]. . . . .	77
5.2	Ordered list of jet properties used in the GSC calibration. . . . .	85
5.3	MV1c versus MV1 operating points. . . . .	91
6.1	Monte Carlo programs used. . . . .	98
7.1	Inclusive Loose, Medium and Tight lepton definitions. . . . .	120
7.2	Requirements for Signal and Veto Jets . . . . .	122
7.3	Trigger table used in the 2012 data analysis. . . . .	133
7.4	Signal lepton analysis selection. . . . .	134
7.5	Event kinematic selection. . . . .	136
8.1	For all three 8 TeV processes $WH \rightarrow \ell\nu b\bar{b}$ , $ZH \rightarrow \ell\ell b\bar{b}$ , and $ZH \rightarrow \nu\nu b\bar{b}$ , the full NLO EW correction is quoted first ( $\Delta_{EW}$ ) and then the only difference from the inclusive to the differential cross section ( $\delta_{EW}$ ). The latter is the one which needs to be applied on top of the inclusive NNLO QCD+NLO EW cross section. The results are quoted in intervals of $p_T^W$ (for $WH$ ) or $p_T^Z$ (for $ZH$ ), using the $p_T$ intervals defined for the analyses. . . . .	142
8.2	Inclusive cross sections and related uncertainties for $WH$ production. .	143
8.3	Inclusive cross sections and related uncertainties for $ZH$ production. .	143

8.4	Inclusive cross sections and related uncertainties for $qq$ and $gg$ initiated $ZH$ production. . . . .	144
8.5	Inclusive acceptance uncertainties derived from scale and PDF variations.	145
8.6	Parameters for linear $p_T^V$ signal shape uncertainty. . . . .	146
8.7	Sample composition for $Z+jets$ modeling studies. . . . .	151
8.8	0tag yield comparison for 2-lepton events. . . . .	152
8.9	ALPGEN/ and SHERPA heavy-flavor jet multiplicity yield comparison in 2-lepton 2tag events. . . . .	154
8.10	ALPGEN/ and SHERPA jet heavy-flavor fraction comparison in 2-lepton 2tag events. . . . .	154
8.11	The event weight for the top $p_T$ correction from the unfolding measurement. The values are corrections to the differential cross section in bins of the transverse momentum of the top quark. . . . .	164
8.12	$t\bar{t}$ 3-to-2-jet ratio and relative difference with the nominal Monte Carlo	166
8.13	$t\bar{t} p_T^V$ uncertainty . . . . .	167
8.14	Parameter values for the $m_{jj}$ shape systematic uncertainties for the $t\bar{t}$ process in four analysis regions. These parameters are for a linear fit of the form $\Delta(m_{jj}) = \text{constant term} + \text{slope} \times m_{jj}$ . . . . .	168
8.15	Monte Carlo generator used for the modeling of the diboson processes and correspondent cross sections. . . . .	171
8.16	Perturbative systematics on $\sigma_2$ from the $C_1$ term of the covariance matrix across the different $p_T^V$ bins. . . . .	172
8.17	Perturbative systematics on $\sigma_2$ from the $C_2$ term of the covariance matrix across the different $p_T^V$ bins. . . . .	173
8.18	Perturbative systematics on $\sigma_{\geq 3}$ from the $C_2$ term of the covariance matrix across the different $p_T^V$ bins. . . . .	173
8.19	PDF+ $\alpha_S$ systematic uncertainties for the $ZZ$ , $WZ$ and $WW$ processes, in the 2-jet and 3-jet analysis regions. . . . .	173
8.20	Parameter values for the $m_{jj}$ shape systematic uncertainties for the $ZZ$ , $WZ$ and $WW$ processes. These parameters correspond to Equation 8.2 and Equation 8.3 . . . . .	175
9.1	Analysis regions used in the profile likelihood . . . . .	189
9.2	Summary of experimental systematic uncertainties. . . . .	201
9.3	Summary of signal-specific nuisance parameters. . . . .	205
9.4	Summary of $Z+jet$ specific nuisance parameters. . . . .	206
9.5	Summary of $t\bar{t}$ specific nuisance parameters. . . . .	207

9.6	The nuisance parameters used in the fit to parametrize the systematics on the diboson backgrounds. For <code>VVJetPDFAlphaPt</code> , the two values represent the normalization change in 2/3Jet region respectively. S=“Shape”, and SO=“Shape Only” meaning explicitly the normalization of each N-jet/M-b-tag/ $p_T^Z$ region is preserved while the shape is varied.	208
9.7	Binning optimization for $m_{b\bar{b}}$ .	219
10.1	Floating normalizations for the Diboson fit.	233
10.2	Floating normalizations for the Higgs fit at $\sqrt{s} = 8$ TeV.	235
10.3	Floating normalizations for the Higgs fit $\sqrt{s} = 7$ TeV.	235
10.4	Best fit value of $\mu$ and the corresponding statistical and systematic uncertainties.	236
11.1	2012 Trigger Table for Combined Analysis.	241
11.2	Signal lepton analysis selection.	241
11.3	Analysis jet multiplicity requirements.	242
11.4	Event kinematic selection.	244
11.5	Regions used in profile likelihood fit for the combined analysis	256
11.6	Summary of $W$ +jet specific nuisance parameters.	258
11.7	Summary of single top specific nuisance parameters.	259
11.8	Normalization nuisance parameters for multijet entering the fit. The 0-lepton uncertainties are correlated between regions. <sup>†</sup> Regions separated by a “ indicate a decorrelation of the parameter between those regions. For example for <code>SysMJE1CaloIso</code> , the parameter is decorrelated among the 2-jet 1-tag and 2-jet 2-tag regions, resulting in 2 total nuisance parameters. All 2-lepton uncertainties are correlated except for when the top $e - \mu$ control region is included in the 2-lepton standalone fit [109].	260
11.9	Rescaling factors obtained from the global fit to the $\sqrt{s} = 8$ TeV data for the normalization of the $t\bar{t}$ , $Wbb$ , $Wcl$ , $Zbb$ , and $Zcl$ backgrounds for the 2-jet events. The errors include the statistical and systematic uncertainties. The $t\bar{t}$ factors are decorrelated across each lepton channel, and $L0$ , $L1$ , and $L2$ represent the 0, 1, and 2-lepton channels, respectively.	265

# Acknowledgments

I would like to take this opportunity to thank John Huth for sharing his expertise across so many fields with me - from particle physics to primitive navigation - and for giving me the freedom to follow my own interests both inside and outside of physics.

Masahiro and Melissa: Thank you for always encouraging me to push further and to learn more. I learned much from you by example.

Joao: Thank you for all the dinner conversations in R1, and for teaming up for such excellent Q-scores in Physics 145, even if we were soon surpassed by Tomo.

David Lopez Mateos: Without you, this dissertation would not have happened. Thank you for all of your guidance, teaching, and support, and for always getting me to set my expectations higher for my own work. And for your Keynote template.

Gabriel: Thank you for making my last year at CERN a fun one and for teaching me a lot along the way. Also, thanks for the gimlets.

Pierluigi, Alberto, corrinne, Geraldine, Hugh, and Bart: Thank you for always taking time to teach me about your different projects and for our many chats over pizza, coffee, and dessert.

Michael, Laura, and Gio: Thank you for teaching me almost everything I know about particle physics. The time you spent giving me guidance and your willingness to answer my questions will always be remembered.

To all of the Harvard students and postdocs: Thank you all for making both Harvard and CERN enjoyable places to live and work over the years.

I would also like to thank Lee Sobotka and Robert Charity from Washington University in St. Louis for taking a chance on a freshman researcher. You got me up to speed quickly and made me excited about physics. Your patience and teaching

## *Acknowledgments*

---

helped me immensely.

Nick, Doug, and Clinton: Thank you for sharing so many adventures with me over the last 6 years. We've been through it all together, and I can't imagine graduate school without you. Never forget to throw an S.

David Jimenez Torres: Thank you for years of being a best friend and an exemplary academic. I'm grateful that you've been an endless source of advice and great memories over the last many, many years. I'm proud to have you as a friend.

Tamra: You've been so wonderful, supportive, and encouraging throughout every page of the dissertation and every day beyond it. Thank you for making me happy, and for not making me share my milkshakes.

To my family: Thank you. I can't express how much it means to me that you've been endlessly supportive in so many ways as I dived deeply into physics and into new endeavors.

# Chapter 1

## Introduction

This thesis describes a search for the Standard Model Higgs Boson produced through the associated-production mechanism of  $\text{pp} \rightarrow VH$ , with the Higgs decaying via  $H \rightarrow b\bar{b}$ , at  $\sqrt{s} = 8$  TeV with the ATLAS detector at CERN. The goal is to extract a measurement of the ratio of the measured cross section times branching ratio for the  $ZH \rightarrow \ell^+ \ell^- b\bar{b}$  process to the theoretical expectation given by the Standard Model. Chapter 2 discusses the theoretical background of the Standard Model Higgs boson, highlighting the role of the Higgs mechanism for electroweak symmetry breaking. This chapter also discusses the recent discovery of a new boson consistent with the Standard Model expectation for the Higgs Boson, to put this search into the context of a program of precision Higgs measurements. The following chapter, Chapter 3, discusses the accelerator complex at the CERN laboratory. Chapter 4 provides a detailed survey of the components and capabilities of the ATLAS detector. Next, Chapter 5 is an in-depth description of the methods used to identify and reconstruct physical objects within the ATLAS detector.

Turning to the  $ZH \rightarrow \ell^+\ell^- b\bar{b}$  measurement, Chapter 6 describes the dataset and Monte Carlo simulation used, as well as necessary corrections to the Monte Carlo simulation, motivated by ancillary measurements with ATLAS data. Following in Chapter 7 is a discussion of the selection of events for analysis, including kinematic requirements on all physics objects in the final state. These objects are analyzed further in Chapter 8, which discusses the modeling of the signal process and the major background processes, namely  $Z$ +jets production,  $t\bar{t}$  pair production, and diboson production. Chapter 8 also enumerates the sources of systematic uncertainty associated with the modeling of each signal and background process.

The statistical technique used to extract the measurement is presented in detail in Chapter 9. This chapter also contains all input distributions to the fitting procedure, as well as the corresponding post-fit distributions.

The results of the  $ZH \rightarrow \ell^+\ell^- b\bar{b}$  search are presented in Chapter 10, including the limit on the cross section times branching ratio for this process as well its compatibility with the Standard Model expectation. Finally, results from a similar approach that combines this channel with the  $ZH \rightarrow \nu\bar{\nu} b\bar{b}$  and  $WH \rightarrow \ell\nu b\bar{b}$  channels follows in Chapter 11.

# Chapter 2

## The Standard Model of Particle Physics

All observed matter in the universe and the fundamental interactions between particles of this matter, save for gravity, are described by the Standard Model of particle physics. This chapter provides an overview of the Standard Model as it pertains to the measurement discussed in this thesis, while leaving the rich history and beauty of the theoretical details to the proper references. Section 2.1 discusses the phenomenology of the Standard Model as well as the Lagrangian for the Electroweak sector. Additionally, the Higgs mechanism is discussed in the context of mass generation for the other fundamental particles. In Section 2.2, the production of Higgs bosons at a proton-proton collider such as the Large Hadron Collider is discussed, as well as the decay modes of the boson. Finally, Section 2.3 covers the discovery of a new boson at the Large Hadron Collider, made by the ATLAS and CMS experiments in 2012. The newly-discovered boson is consistent with the Higgs boson of the Standard Model.

## 2.1 The Standard Model and the Higgs Mechanism

The Standard Model of particle physics (see References [79, 101, 106, 116]) describes the strong, weak, and electromagnetic forces of nature, and all fundamental particles that have been directly observed. Much of modern experimental high energy physics has been devoted to searching for deviations from the predictions of the Standard Model in order to reveal possible alternative descriptions of nature. However, the theory is an example of unprecedented accuracy in the effort to successfully predict the behavior of particles and interactions across a wide range of energy scales.

The Standard Model is a gauge theory that unifies the strong, weak, and electromagnetic forces. Therefore it is built on the symmetry groups of  $SU(3) \times SU(2)_L \times U(1)_Y$ . Each gauge symmetry gives rise to a force which is mediated by particles referred to as gauge bosons. The matter content of the Standard Model is described by representations of the symmetry group, which determine the charge of the particle under that symmetry.

One category of the matter content consists of fermions, and is further categorized into categories of leptons and quarks depending on the interaction of the particle with the strong force. Leptons are singlets of  $SU(3)$  and do not interact through the strong force, and quarks are triplets of  $SU(3)$  and do interact with the strong force. All charged fermions interact electromagnetically and all fermions interact weakly. In total, there are three generations of leptons and quarks. Each of these fermions is also associated to an anti-particle, a particle of the same mass but opposite charges.

Left-handed fermions are doublets of  $SU(2)_L$ , while right-handed fermions are the singlets of  $SU(2)_L$ . The  $SU(2)_L$  gauge bosons of the weak interaction only couple to the left-handed particles and right-handed anti-particles. The fundamental forces are carried by bosons (integer spin). The electromagnetic force is carried by massless, spin-1 photons, while the weak force is carried by the massive spin-1  $W$  and  $Z$  bosons. The strong force is carried by massless spin-1 particles called gluons. The properties of the particle content of the Standard Model are summarized in Figure 2.1.

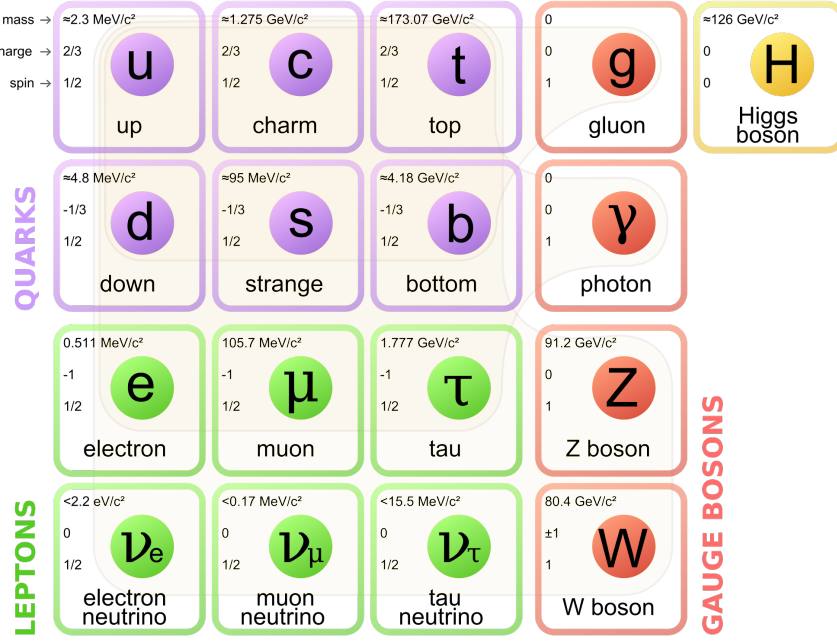


Figure 2.1: The particle content of the Standard Model [117].

### 2.1.1 The Electroweak Sector

The electroweak sector contains four gauge bosons, which are massless before electroweak symmetry is broken. The massless bosons are  $A_\mu^a$ , where  $a = 1, 2, 3$ , and

$B_\mu$  for  $SU(2)$  and  $U(1)$ , respectively. In order to construct a theory with local gauge invariance, the covariant derivative must be:

$$D_\mu = \left( \partial_\mu + igA_\mu^a \tau^a - i\frac{1}{2}g'B_\mu \right) \quad (2.1)$$

where  $\tau^a$  are the generators of the  $SU(2)$  gauge group in the adjoint representation and follow  $[\tau^a, \tau^b] = if^{abc}\tau^c$ , with  $f^{abc} = \epsilon^{abc}$ , the structure constants. For  $SU(2)$  the structure constants are equal to the totally anti-symmetric tensor  $\epsilon^{abc}$ . Mass terms are forbidden because they would not be gauge invariant.

The Electroweak Lagrangian can be organized into terms for the gauge boson kinetic energy, the fermion kinetic energy, the Higgs term, and the Yukawa term:

$$\mathcal{L}_{EW} = \mathcal{L}_g + \mathcal{L}_f + \mathcal{L}_h + \mathcal{L}_y. \quad (2.2)$$

The gauge boson kinetic energy term is

$$\mathcal{L}_g = -\frac{1}{4}(A_{\mu\nu}^a)^2 - \frac{1}{4}(B_{\mu\nu})^2, \quad (2.3)$$

where

$$X_{\mu\nu}^a = \partial_\mu X_\nu^a - \partial_\nu X_\mu^a + gf^{abc}X_\mu^b X_\nu^c \quad (2.4)$$

is the gauge boson field strength. The last term in the field strength, the self-coupling term arises in non-abelian gauge theories because the generators of the gauge group do not commute. Thus, the self-interaction term is necessary to maintain gauge invariance of non-abelian groups.

The next term, the fermion kinetic energy, is given by:

$$\mathcal{L}_f = \bar{E}_L(i\cancel{D})E_L + \bar{e}_R(i\cancel{D})e_R + \bar{Q}_L(i\cancel{D})Q_L + \bar{u}_R(i\cancel{D})u_R + \bar{d}_R(i\cancel{D})d_R. \quad (2.5)$$

In Equation 2.5,  $E_L$  represent the left-handed lepton doublets while  $e_R$  represents the right-handed lepton singlets. The left-handed quark doublets are represented by  $Q_L$  and the right handed singlets are represented by  $u_R$  and  $d_R$  for up and down-type quarks, respectively.  $\not{D} = \gamma^\mu D_\mu$ , where  $\gamma^\mu$  are the Dirac matrices.

### 2.1.2 The Higgs Sector

The next term in the Electroweak Langrangian from Equation 2.2 represents the Higgs sector. One possible way to generate mass terms for the electroweak bosons and the fermions without violating the  $SU(2)_L$  symmetry of the Standard Model is through the Higgs mechanism. This is done by adding an additional scalar field with spin-0 to the Lagrangian as a complex doublet. The scalar field will be represented by  $\phi$ , where:

$$\phi = \begin{pmatrix} \phi^+ \\ \phi^0 \end{pmatrix} = \begin{pmatrix} \phi_1 - i\phi_2 \\ \phi_3 - i\phi_4 \end{pmatrix}. \quad (2.6)$$

and the Lagrangian for the Higgs sector is written as:

$$\mathcal{L}_h = |D_\mu \phi|^2 + \mu^2 \phi^\dagger \phi - \lambda(\phi^\dagger \phi)^2 \quad (2.7)$$

Here  $\lambda$  must be positive so that the Higgs potential remains non-negative, even for large values of the field  $\phi$ . In the case that  $\mu^2 < 0$ , the potential has only a trivial minimum, but in the case that  $\mu^2 > 0$ , non-trivial minima exist. The set of these minima forms a surface given by:

$$\phi_{1,min} + \phi_{2,min} + \phi_{3,min} + \phi_{4,min} = v^2 = -\frac{\mu^2}{\lambda}, \quad (2.8)$$

Settling into this non-zero minima breaks Electroweak symmetry. In order to preserve the  $U(1)$  symmetry and break only the  $SU(2)$  symmetry, the first component of the scalar  $\phi, \phi^+$ , must be zero. Then the value of the field in the excited state may be written, after transforming to the unitary gauge as:

$$\phi = \begin{pmatrix} 0 \\ v \end{pmatrix}. \quad (2.9)$$

The field may be rewritten with a perturbation of the field components:

$$\phi = \begin{pmatrix} 0 \\ v + h \end{pmatrix}. \quad (2.10)$$

This transformation into the unitary gauge allows the potential term of the Lagrangian in Equation 2.7 to be rewritten as:

$$\begin{aligned} \mu^2 \phi^\dagger \phi - \lambda(\phi^\dagger \phi)^2 &= \frac{1}{2}\mu^2(v^2 + h^2 + 2vh) - \frac{1}{4}\lambda(v^4 + h^4 + 4vh^3 + 6v^2h^2 + 4v^3h) \\ &= v(\mu^2 - \lambda v^2)h + (\frac{1}{2}\mu^2 - \frac{3}{2})h^2 - v\lambda h^2 - \frac{1}{4}\lambda h^4 + const \\ &= \lambda v^2 h^2 - v\lambda h^3 - \frac{1}{4}\lambda h^4 + const \end{aligned} \quad (2.11)$$

In Equation 2.11, one may identify the mass term for the Higgs boson as  $m_H = v\sqrt{2\lambda}$ . The Higgs mass is therefore not determined by the Standard Model. Instead, it is dependent on the vacuum expectation value,  $v$ , and a free parameter. The value of  $v = 246$  GeV is constrained through the Fermi coupling constant. The fact that the Higgs mass is undetermined theoretically is a major reason for the difficulty in constructing an experiment to observe it.

Evaluating the kinetic term of the Langrangian from Equation 2.7 at the minimum of the potential ( $h = 0$ ) yields the effect of the Higgs mechanism on the gauge bosons.

$$\begin{aligned} |D_\mu \phi|^2 &\rightarrow \frac{1}{2} \begin{pmatrix} 0 & v \end{pmatrix} \left( g A_\mu^a \tau^a + \frac{1}{2} g' B_\mu \right) \left( g A_\mu^b \tau^b + \frac{1}{2} g' B_\mu \right) \begin{pmatrix} 0 \\ v \end{pmatrix} \\ &= \frac{v^2}{8} [g^2 (A_\mu^1)^2 + g^2 (A_\mu^2)^2 + (-g A_\mu^3 + g' B_\mu)^2]. \end{aligned} \quad (2.12)$$

Here the terms with squared fields are the form of masses for the vector bosons, so the non-zero vacuum expectation value of the Higgs field has generated the masses for the vector bosons. Using a transformation of basis, the physical  $W$  and  $Z$  bosons as well as the photon, can be written in terms of the original gauge fields  $A_\mu^a$  and  $B_\mu$ :

$$\begin{aligned} W_\mu^\pm &= \frac{1}{\sqrt{2}} (A_\mu^1 \mp i A_\mu^2) \\ Z_\mu &= \frac{1}{\sqrt{g^2 + g'^2}} (g A_\mu^3 - g' B_\mu) \\ A_\mu &= \frac{1}{\sqrt{g^2 + g'^2}} (g A_\mu^3 + g' B_\mu) \end{aligned} \quad (2.13)$$

In the new basis, the gauge boson masses can be read off as:  $m_W = gv/2$ ,  $m_Z = \frac{1}{2}v\sqrt{g^2 + g'^2}$ ,  $m_{photon} = 0$ . Thus the Higgs mechanism has generated masses for the vector bosons and fermions in the Standard Model while also leaving an additional massive boson, the Higgs boson, in the theory with an undetermined mass.

The remaining term for the Electroweak Lagrangian that has not been discussed is called the Yukawa term. The Yukawa interaction terms between the fermions and the Higgs are,

$$\mathcal{L}_y = -Y_d \bar{Q}_L \cdot \phi d_R - Y_u \epsilon^{ab} \bar{Q}_{La} \cdot \phi_b^\dagger u_R - Y_e \bar{E}_L \cdot \phi e_R + h.c. \quad (2.14)$$

where the matrices  $Y_u$ ,  $Y_d$ , and  $Y_e$ , are the Yukawa coupling constants,  $\epsilon^{ab}$  is the totally antisymmetric tensor, and *h.c.* denotes the hermitian conjugate. Substituting the  $\phi$  from Equation 2.9 into Equation 2.14 reveals the mass terms for the fermions. Both up and down-type fermions have masses  $m_{u,d} = \frac{1}{\sqrt{2}} Y_{u,d} v$ .

## 2.2 Higgs Boson Production and Decay at the LHC

One of the priorities of the Large Hadron Collider at the CERN laboratory was to discover the Higgs boson and precisely measure its properties. In that spirit, this section describes the production of the Higgs boson in a hadron collider as well as its important decay signatures. As the LHC collides protons, there are many initial states that may lead to the production of a Higgs boson, given the allowed vertices. The vertices allowed are found in the Standard Model Lagrangian as terms that contain three field terms, with at least one being the Higgs field. thus there are four allowed vertices for Higgs couplings, to the  $Z$ ,  $W$ , to fermions, and to the Higgs itself. The dominant production mode is via the gluon fusion process. In the lowest order, this process features the fusion of two gluons into a fermion loop that couples to the Higgs boson. Gluon fusion is illustrated as a Feynman diagram in subfigure (a) of Figure 2.2. The next-highest cross section is for vector boson fusion, a process that features two quarks in the intial state that emit  $W$ -bosons, which in turn fuse at a vertex yielding a Higgs boson. This process is shown in subfigure (c) of Figure 2.2. The production process that is the subject of this thesis contains the vertices found in subfigure (b) of Figure 2.2, and is called associated production. In this case, the leading order diagram is the case in which two fermions combine to form a vector boson, which

radiates a Higgs boson. The final state is then a Higgs boson and a vector boson. Finally, Higgs production in association with a pair of top quarks is the next-highest in cross section and is shown in subfigure (d) of Figure 2.2. The production cross sections important to the LHC running at  $\sqrt{s} = 8$  TeV are summarized in Figure 2.3.

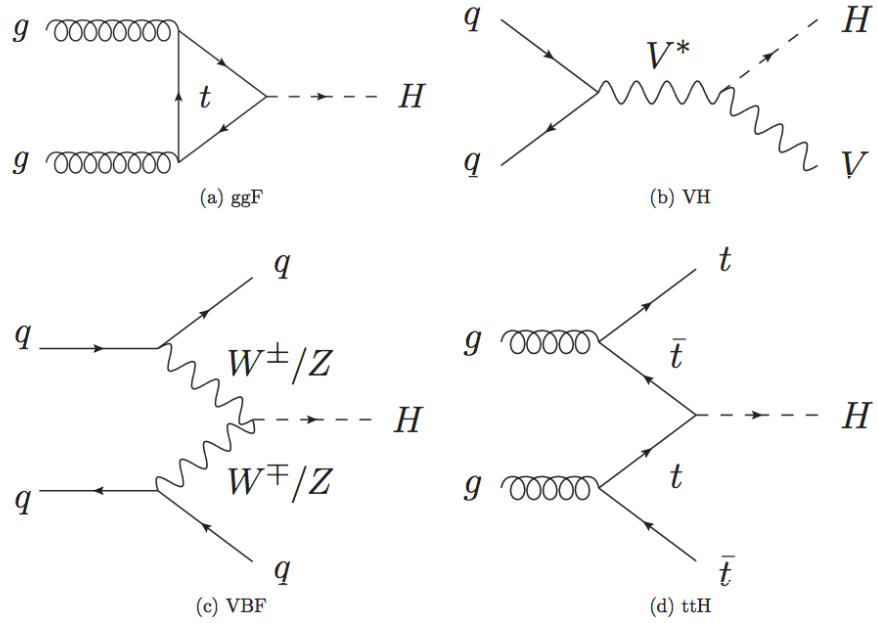


Figure 2.2: The four leading-order processes with the highest production cross sections for the Higgs boson in a pp collider such as the LHC. (a) The gluon-gluon fusion process, (b) Associated production with a vector boson, (c) The vector boson fusion process, and (d) Associated production with a pair of top quarks.

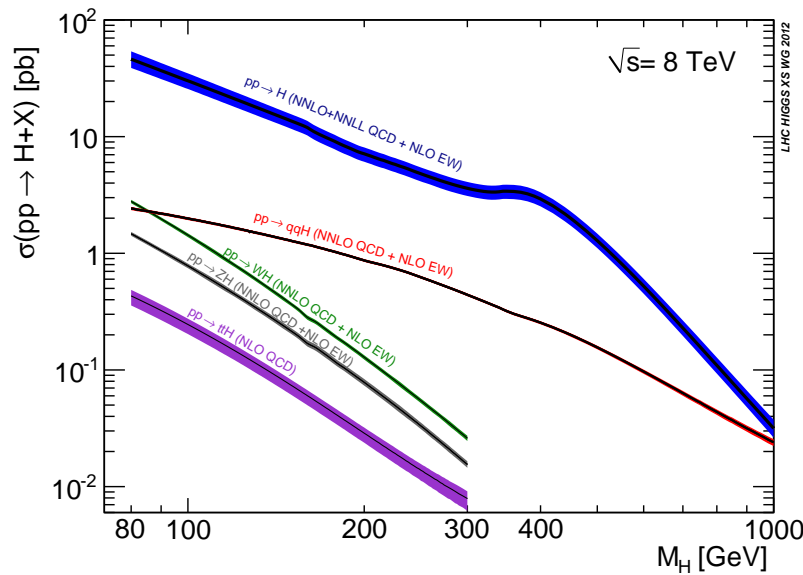


Figure 2.3: The production cross sections as a function of Higgs boson mass for a variety of production mechanisms for the LHC operating at  $\sqrt{s} = 8$  TeV [88].

The ensuing decay of the Higgs boson must of course use the same set of allowed vertices, and the branching ratios as a function of Higgs boson mass are shown in Figure 2.4. The partial widths are, at leading order [100]:

$$\Gamma(H \rightarrow ff) = \frac{G_F}{4\pi\sqrt{2}} m_f^2 m_H (1 - 4\frac{m_f^2}{m_H^2})^{\frac{3}{2}}, \quad (2.15)$$

$$\Gamma(H \rightarrow WW) = \frac{G_F}{8\pi\sqrt{2}} m_H^3 (1 - 4\frac{m_W^2}{m_H^2})^{\frac{1}{2}} (12\frac{m_W^4}{m_H^4} - \frac{m_W^2}{m_H^2} + 1), \quad (2.16)$$

$$\Gamma(H \rightarrow ZZ) = \frac{G_F}{16\pi\sqrt{2}} m_H^3 (1 - 4\frac{m_Z^2}{m_H^2})^{\frac{1}{2}} (12\frac{m_Z^4}{m_H^4} - \frac{m_Z^2}{m_H^2} + 1). \quad (2.17)$$

The branching ratio to fermions scales with the mass of the fermion, so heavier fermions are preferred. For a light Higgs, the dominant decay mode is through a pair of  $b$ -quarks, and this is the decay mode sought in this thesis. Decay through top quark pairs is disfavored at light Higgs masses because of the high mass of the top. Although it takes advantage of the high branching ratio, the experimental signature of  $b$ -quarks is more difficult to reconstruct in the detector and a mass measurement is more challenging than the  $H \rightarrow \gamma\gamma$  or  $H \rightarrow ZZ \rightarrow 4\ell$  channels.

## 2.3 Discovery of the Higgs boson at the LHC

In 2012, the ATLAS and CMS experiments reported the discovery of a new massive boson at CERN’s Large Hadron Collider. The ATLAS experiment reported a significance of 5.9 standard deviations, corresponding to a background fluctuation probability of  $1.7 \times 10^{-9}$  in Reference [39], while the CMS experiment reported a

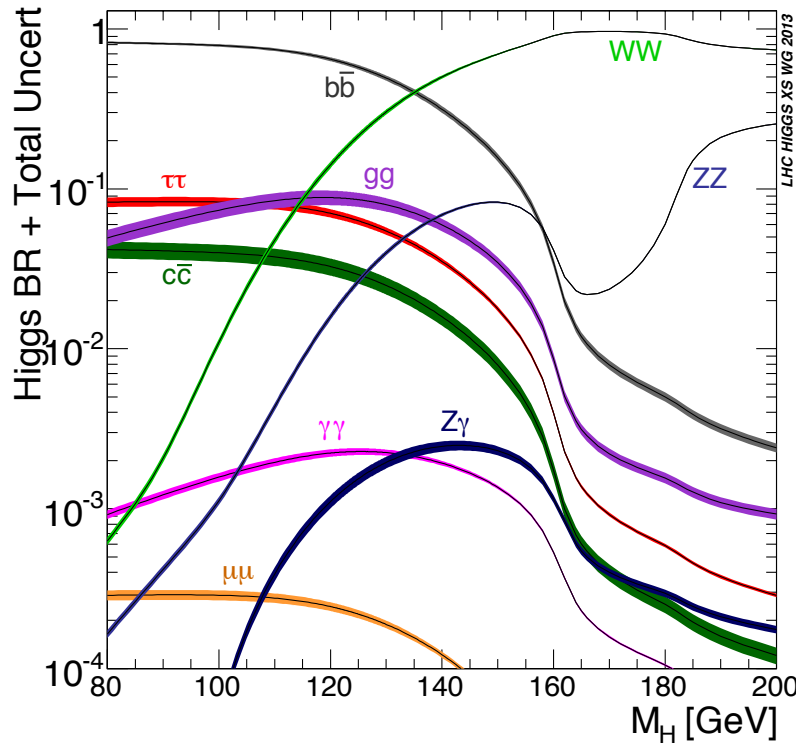


Figure 2.4: The branching ratio as a function of Higgs boson mass for a variety of decay modes [88].

significance of 5.0 standard deviations in Reference [62]. Each experiment combined data from several search channels, most notably the processes of  $H \rightarrow \gamma\gamma$ ,  $H \rightarrow ZZ$ , and  $H \rightarrow WW$ . The lack of an observation using either the associated production mode or the  $H \rightarrow b\bar{b}$  decay channel motivates the search presented in this thesis. Such a measurement contributes importantly to the verification that the Higgs couples to fermions as expected, and the Yukawa coupling to the  $b$ -quark may be probed.

Two of the most important Higgs discovery channels, and perhaps the most visually impressive, are the processes  $H \rightarrow \gamma\gamma$  and  $H \rightarrow ZZ$ . The result of the ATLAS search for the Higgs in the  $\gamma\gamma$  channel are shown in Figure 2.6. Figure 2.5 shows the results of the fully-leptonic  $H \rightarrow ZZ$  search as number of events as a function of the 4-lepton invariant mass. The ATLAS experiment measures the Higgs mass to be  $125.36 \pm 0.41$  GeV [43] while CMS measures a mass of  $125.03 \pm 0.31$  GeV [60]. Furthermore each experiment measures the rate of Higgs boson production and decays to be consistent with the Standard Model expectation across all observed processes. This is illustrated in Figure 2.7, which shows the ratio of the measured cross section times the branching ratio to the expected value for the Standard Model for a number of production mechanisms and decay modes. In this figure, the  $WH$  and  $ZH$  production measurements are from a previously ATLAS measurement which is superceded in part by the work of this dissertation. The remainder of this dissertation is dedicated to the ATLAS search for the  $H \rightarrow b\bar{b}$  decay when the Higgs is produced through associated production. More specifically, the process  $ZH \rightarrow \ell^+\ell^-b\bar{b}$  alone, and then the combination of the processes  $ZH \rightarrow \ell^+\ell^-b\bar{b}$ ,  $WH \rightarrow \ell\nu b\bar{b}$ , and  $ZH \rightarrow \nu\bar{\nu}b\bar{b}$ . The most recent ATLAS results for this search are found in Reference [29].

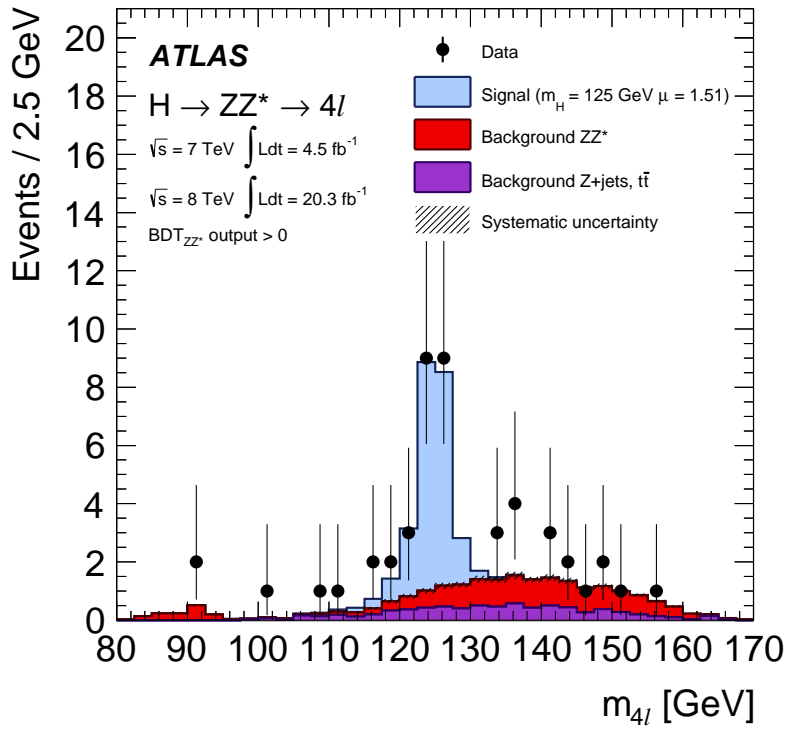


Figure 2.5: The four-lepton invariant mass from the ATLAS  $H \rightarrow ZZ$  analysis. The Higgs signal contribution is shown for  $m_H = 125$  GeV as the blue histogram. The expected background contributions,  $ZZ^*$  (red histogram) and  $Z + \text{jets}$  plus  $t\bar{t}$  (violet histogram), are shown for the combination of the 7 TeV and 8 TeV results [44].

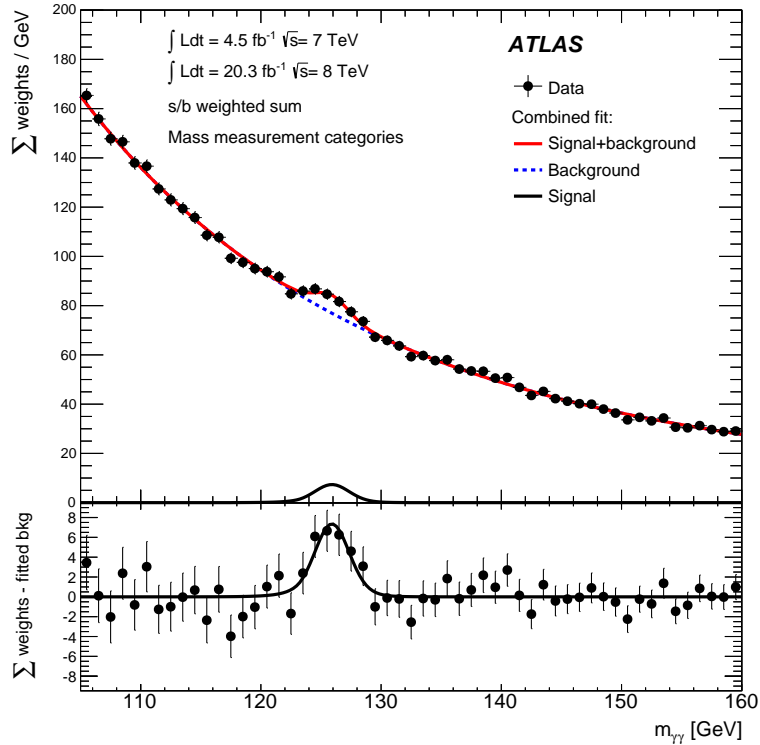


Figure 2.6: The di-photon invariant mass from the ATLAS  $H \rightarrow \gamma\gamma$  analysis. The Higgs signal contribution and background expectation are shown. The bottom panel shows the background-subtracted data and the expected Higgs signal contribution. The result corresponds to the combination of the 7 TeV and 8 TeV data [43].

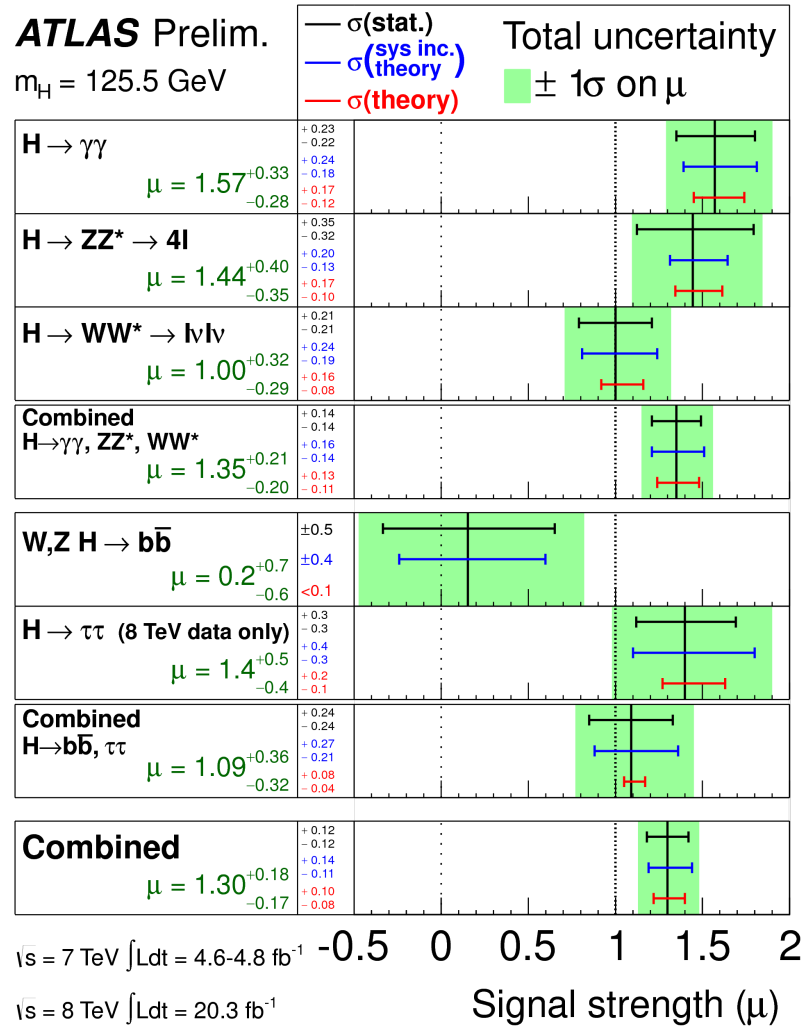


Figure 2.7: Higgs results from combinations of the 7 TeV and 8 TeV data with the ATLAS detector [111].

# Chapter 3

## The Large Hadron Collider

The Large Hadron Collider (LHC) uses superconducting magnet technology to accelerate beams of protons, and is located at the CERN laboratory in Geneva, Switzerland. With a design center-of-mass energy of  $\sqrt{s} = 14$  TeV and instantaneous luminosity of  $10^{34}$  cm $^{-2}$ /s, the LHC is both the highest energy and highest intensity proton accelerator in the world. During Run I of the LHC, from 2011-2012, the LHC produced integrated luminosities of  $5.3$  fb $^{-1}$  at  $\sqrt{s} = 7$  TeV and  $23.3$  fb $^{-1}$  at  $\sqrt{s} = 8$  TeV.

This chapter describes the accelerator complex that injects protons into the LHC in Section 3.1 and major design features of the LHC in Section 3.2, while more complete details are left to Reference [73] and References [49, 56, 55]. The method for calculating the luminosity is discussed in Section 3.3.1 and the calibration of the luminosity detectors is discussed in Section 3.3.2. Finally, details of the performance of the LHC during Run I are found in Section 3.3.3.

There are four main experiments on the LHC ring. The layout of the LHC ring and the location of each experiment is shown in Figure 3.1. The experiments are:

- ATLAS (“**A** Toroidal **L**H**C** Apparatu**S**”) [32] and CMS (“**C**ompact **M**uon **S**olenoid”) [61], are the two largest experiments. Both are considered general-purpose detectors in that the scope of possible measurements is vast. Priorities include the precision measurement of Standard Model processes, studying the source of electroweak symmetry-breaking, and probing for new physics at the TeV scale. These experiments are optimized to record the maximum integrated luminosity for proton-proton collisions and to reconstruct particles over a large range of energies.
- LHCb (“**L**arge **H**adron**C**ollider **b**eauty) [89] is optimized to study the properties of  $b$ -quarks and  $B$ -hadrons, in an attempt to observe greater CP-violation in the decays of  $B$ -hadrons. Such studies may elucidate the matter-antimatter asymmetry of the universe.
- ALICE (“**A** Large **I**on **C**ollider **E**xperiment”) [10] is optimized to study the properties of quark-gluon plasma, a dense, hot state of matter. As such, it is designed to study the lead-lead collisions produced by the LHC at  $\sqrt{s} = 2.76$  TeV/nucleon. In order to do so, it must cope with the extremely high flux of particles from these heavy-ion collisions.

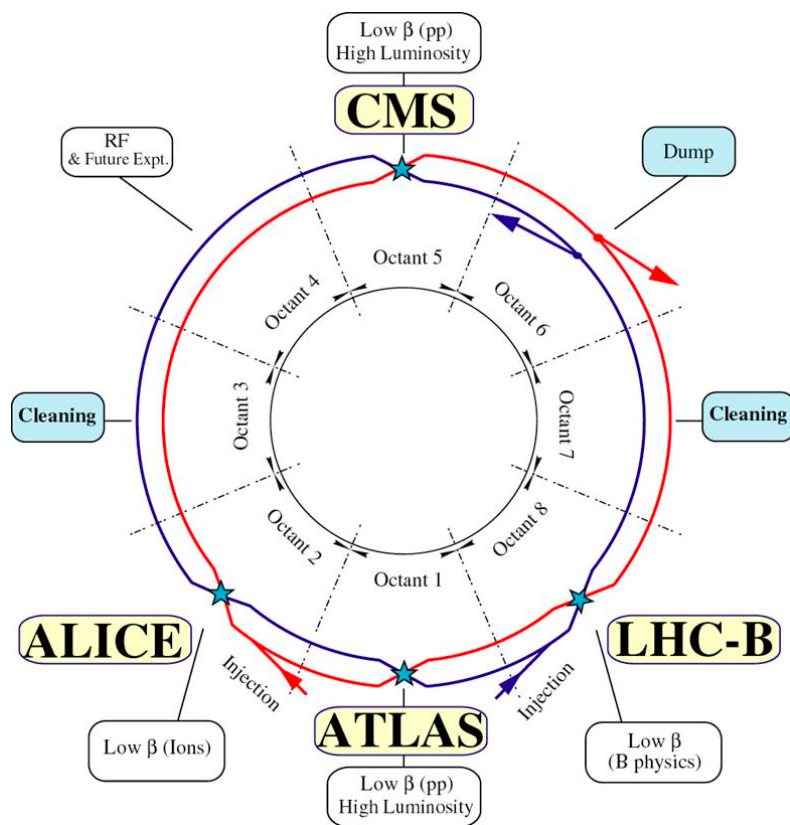


Figure 3.1: The layout of the major experiments on the LHC [73].

### 3.1 The Injection Chain for the LHC

Before protons enter the LHC for acceleration to an energy of 7 TeV, they accelerate to 450 GeV through additional machines at CERN. The process of acceleration to the LHC is called injection, and the Injection Chain refers to this set of accelerators that feed protons into the LHC. A layout of the Injection Chain is shown in Figure 3.2. Beginning at the Linac2, protons are accelerated to 50 MeV before they enter the Proton Synchrotron Booster (PSB) and reach an energy of 1.4 GeV. Next, the protons are accelerated to 25 GeV in the Proton Synchrotron (PS) and to the Super Proton Synchrotron (SPS), where they reach an energy of 450 GeV. The final input of protons to the LHC is formed by trains of 72 bunches each which are created from six input bunches in the PSB after multiple splittings in the PS [73].

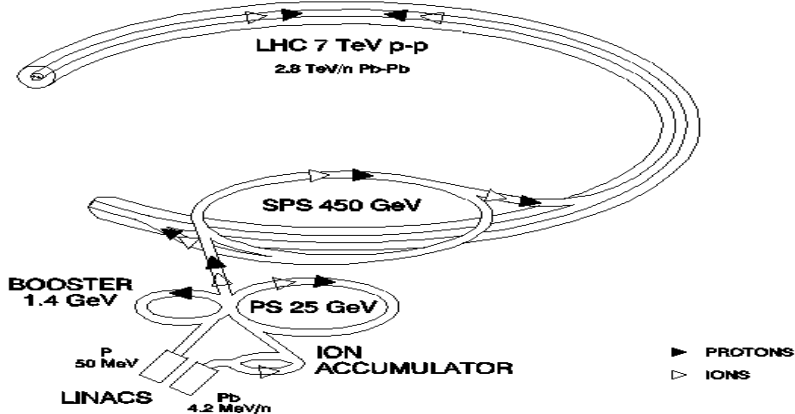


Figure 3.2: The LHC Injector Chain, showing the layout of the accelerator complex and the energy achieved for protons at the exit of each system [73].

## 3.2 The Design of the Large Hadron Collider

The LHC occupies a 26.7 km-long tunnel previously occupied by the LEP collider at CERN. This tunnel ranges from 70 m to 140 m underground. It consists of eight straight sections of beamline and eight sections in which dipole magnets bend the proton beam. Each dipole magnet must create a field of 8.3 T to bend a 7 TeV proton correctly. The magnetic field strength required is given by:

$$B[\text{T}] = \frac{p[\text{GeV}]}{0.3R[\text{m}]} \quad (3.1)$$

where  $B$  is the magnetic field in Tesla,  $p$  is the momentum of the accelerating particle, and  $R$  is the desired radius of curvature, in meters. To produce such a strong field, 11,850 A of current flow through NbTi cables that are cooled to 2 K to reach the superconductive phase. The cooling is achieved with 120 tons of liquid helium that circulate from the magnets to cryogenic refrigerators. Due to the spatial limitations of the LEP tunnel, which is only 3.7 m in diameter, the LHC cryostats must house both rings of protons, each traveling in an opposite direction. As such, the dipole magnets of the LHC have a *twin-bore*, or *two-in-one* design [52]. Since this field must be oriented in opposite directions for each beam and the space inside the cryostat is quite confined, the rings are coupled both mechanically and magnetically. This results in a complicated design, as shown in Figure 3.3. In total, the LHC has 1104 dipole magnets across its eight bending sections and 128 additional dipoles in other sections.

In addition to the dipoles, quadrupoles and other higher-order magnets are used to focus the beam and to bring it into collision at the interaction points (IPs). Near

each interaction point, for  $\sim 70$  m on either side, the two beams are steered into the same vacuum pipe. As it is important to minimize beam-beam interactions to avoid collisions at undesired locations, the beams are held in parallel orbits until the point of collision, where they cross with an angle of 286 mrad.

### LHC DIPOLE : STANDARD CROSS-SECTION

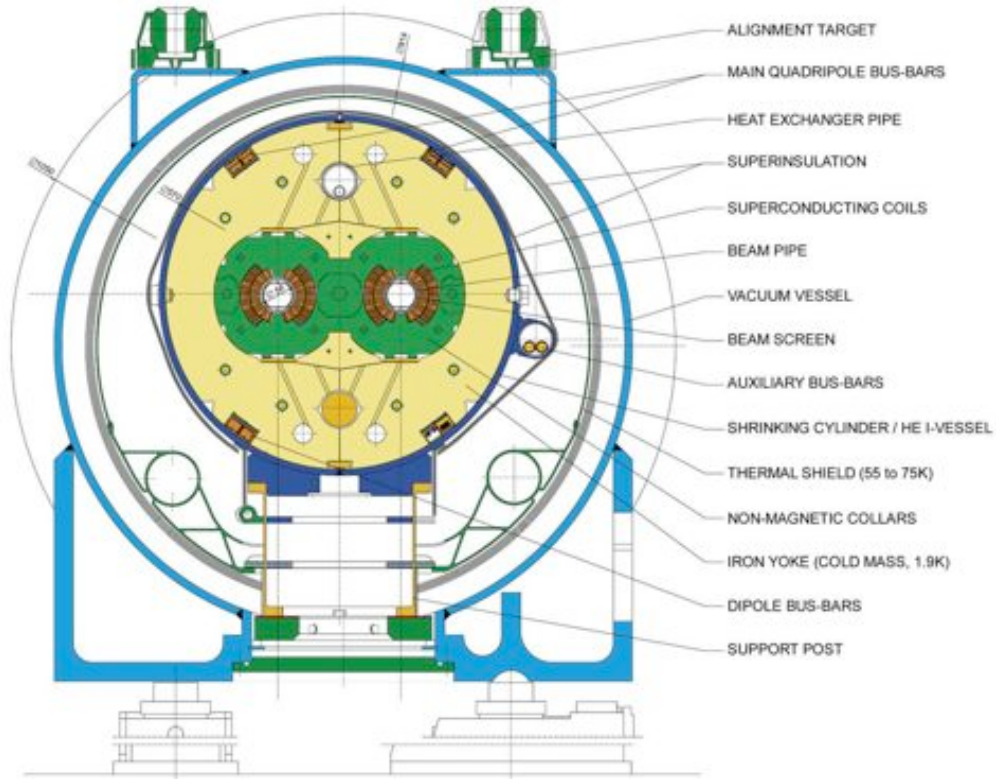


Figure 3.3: A cross-sectional view of an LHC dipole magnet [45].

The acceleration of charged particles in the LHC is achieved through eight radiofrequency (RF) cavities. Each cavity provides an electric potential gradient of 5 MV/m and operates at a frequency of 400 MHz. This field is capable of increasing the energy of the beam from 450 GeV to 7 TeV in approximately 20 minutes. Additionally,

these RF cavities must correct for the energy lost due to synchrotron radiation, which is 7keV/turn.

Each bunch entering the LHC has a design intensity of  $\sim 1 \times 10^{11}$  protons. As the LHC has 35640 RF-*buckets* of 2.5ns each, only every tenth bucket is designed to be filled with such a bunch of protons, while the other RF-buckets remain empty. These empty RF-buckets are partly a feature of the injection system and partly to allow time for abort signals to be passed in the case of a lost beam. In total, the design of the LHC calls for 2808 proton bunches per beam. In addition to a high intensity of protons and large number of bunches, the LHC must produce a narrow beamspot to achieve its design luminosity. At each interaction point, the beam is squeezed to a transverse size of 17  $\mu\text{m}$ .

The instantaneous luminosity of a synchrotron collider experiment with a Gaussian beam is a function of the above parameters:

$$\mathcal{L} = \frac{N_b n_b f_{rev} \gamma}{4\pi\epsilon_n \beta^*} F, \quad (3.2)$$

where  $N_b$  is the number of particles in each bunch,  $n_b$  is the number of bunches in each beam,  $f_{rev}$  is the revolution frequency,  $\gamma$  is the relativistic Lorentz factor,  $\epsilon_n$  is the normalized transverse beam emittance,  $\beta$  is the beta function at the collision point, and  $F$  is the geometric luminosity reduction factor due to the crossing angle at the collision point.

The above design parameters yield an instantaneous luminosity of  $10^{34}\text{cm}^{-2}s^{-1}$ . Several factors influence the ability of the LHC to achieve its design luminosity and energy, and as of Run I, the design luminosity and energy have not been obtained.

For one, synchrotron radiation from the bending protons and interactions between the beam and electron clouds heat the liquid helium that cools the magnets. If the helium temperature rises such that it cannot maintain the superconducting phase even changes phase to a gas, severe damage may occur. To reduce the risk of such incidents, the LHC was restricted to 3.5 TeV beams in 2011, and 4 TeV beams in 2012. Additionally, instabilities in the beam from beam-beam interactions proved difficult to overcome at the nominal bunch-spacing of 25 ns, and a spacing of 50 ns was used instead. The effects of these changes are discussed in Section 3.3.3.

### **3.3 The Luminosity Measurement**

An accurate measurement of the integrated luminosity collected by the physics experiments is necessary for the success of the LHC precision physics program. Cross section measurements of Standard Model processes and limits on the cross sections of new physics processes require a high degree of precision for the luminosity measurement because uncertainty on the luminosity can be a leading source of systematic error for some analyses.

For the ATLAS experiment, the method to calculate the luminosity involves multiple steps. Forward detectors (see Section 4.6) provide hit rates that are translated into measurements of the number of interactions per bunch crossing. Then, the forward detectors are calibrated with dedicated studies of the spatial properties of the proton beams, yielding a relation between the hit rates in the forward detectors, the shape of the proton beam, and the instantaneous luminosity. The procedure is described

below and discussed in more detail in References [22, 92].

### 3.3.1 Methodology

In addition to Equation 3.2, the luminosity of a proton-antiproton collider can also be expressed as:

$$\mathcal{L} = \frac{R_{inel}}{\sigma_{inel}} = \frac{\mu n_b f_{rev}}{\sigma_{inel}}, \quad (3.3)$$

where  $R_{inel}$  is the rate of inelastic collisions and  $\sigma_{inel}$  is the cross section for inelastic scattering. In the second equality, the rate of inelastic collision is expressed in terms of the quantities  $n_b$ ,  $f_{rev}$ , defined as before, and  $\mu$ , the average number of inelastic interactions per *bunch crossing* (BC). Given that  $n_b$  and  $f_{rev}$  are known LHC parameters, the instantaneous luminosity is then determined through a measurement of  $\mu$  and  $\sigma_{inel}$ . While  $\mu$  may be measured during normal data taking,  $\sigma_{inel}$  requires dedicated calibration runs, described below.

The strategy to measure the luminosity is first to measure a proxy to the  $\mu$  value, and then to calculate the value of  $\sigma_{inel}$  through calibration, using a technique called Van der Meer scans, which is described in Section 3.3.2. For the ATLAS experiment, the LUCID and BCM detectors are responsible for producing a measurement of the number of inelastic collisions per bunch crossing of the LHC. This value is called  $\mu_{vis}$ . The measurement of  $\mu_{vis}$  is not equivalent to  $\mu$  in Equation 3.3 because of non-unity detector efficiency. Thus,  $\mu_{vis} = \mu\epsilon$ , where  $\epsilon$  is the efficiency to detect and reconstruct

an inelastic collision. Then, Equation 3.3 may be rewritten as:

$$\mathcal{L} = \frac{\mu_{vis} n_b f_{rev}}{\sigma_{vis}}. \quad (3.4)$$

The measurement of  $\mu_{vis}$  is performed through two types of algorithms: *event counting* [34] and *hit counting* [22]. Event counting was used by the BCM and LUCID in early running, but at the time of higher-luminosity running in 2011 and 2012, the hit counting algorithm was preferred for LUCID, because the probability of a collision in any given bunch crossing was high [22]. This section will focus on the hit counting algorithm and leave the details of the event counting algorithms to Reference [34].

In a hit counting algorithm, the detector records the sum of the number of hits during a bunch crossing,  $N_{hits}$ , and assumes it follows a Binomial distribution, while the number of interactions in a bunch crossing follows a Poisson distribution. Under these assumptions, the probability to observe a hit in a detector channel during a bunch crossing is given by:

$$P(\mu_{vis}) = \frac{N_{Hit}}{N_{Ch} N_{BC}}, \quad (3.5)$$

where  $N_{Ch}$  is the number of channels in the detector (30 for LUCID) and  $N_{BC}$  is the number of bunch crossings. The measured value of  $\mu_{vis}$  is then:

$$\mu_{vis} = -\ln(1 - \frac{N_{Hit}}{N_{Ch} N_{BC}}) \quad [92]. \quad (3.6)$$

With the ability to translate hit rates into  $\mu_{vis}$ , the final step in this method of determining the luminosity is to determine the value of  $\sigma_{vis}$ .

### 3.3.2 Calibration of $\sigma_{vis}$ for Luminosity Determination

In order for  $\mu_{vis}$  to be used to monitor the luminosity, according to Equation 3.4,  $\sigma_{vis}$  must be calibrated for each detector and algorithm implemented. The primary means to perform this calibration in ATLAS is called a van der Meer scan [112], after Simon van der Meer, and measures the transverse size of the proton beams. First, note that the luminosity may also be written as a function of the characteristics of the colliding beams:

$$\mathcal{L} = \frac{n_b f_{rev} n_1 n_2}{2\pi \Sigma_x \Sigma_y}, \quad (3.7)$$

where  $n_b$  and  $f_{rev}$  are defined as before and  $n_1$  and  $n_2$  represent the number of protons in beam 1 and beam 2, respectively. The measurement of  $n_1$  and  $n_2$  is made from dedicated detectors called the DCCT and FCBT [48].  $\Sigma_x$  and  $\Sigma_y$  are related to the transverse sizes of the beams as they overlap in the collision region. For a Gaussian beam profile,  $\Sigma_x$  would be equivalent to the standard deviation of the beam's profile in the  $x$ -direction. In practice,  $\Sigma_x$  and  $\Sigma_y$  are measured by the van der Meer scans, which measure the interaction rate as a function of the separation of the two beams. A scan is performed over many possible distances between the beams, defined as  $\Delta x$  or  $\Delta y$ , both transverse to the beam's path.  $\Sigma_x$  and  $\Sigma_y$  can now be written as a function of how the collision rate depends on the beam separation:

$$\Sigma_x = \frac{1}{\sqrt{2\pi}} \frac{\int_{-\infty}^{+\infty} R_x(\Delta x) d(\Delta x)}{R_x(0)} \quad (3.8)$$

Here,  $R_x(\Delta x)$  is the measured rate at separation  $\Delta x$  and  $R_x(0)$  is the measured rate at minimal separation, where luminosity is maximized. As this quantity is a ratio

of rates, knowledge of the absolute rate is not required. Therefore a measurement of  $\sigma_{vis}$  may now be made. Using Equation 3.4 and Equation 3.7, one may write:

$$\sigma_{vis} = \frac{R'}{\mathcal{L}'} = \mu'_{vis} \frac{2\pi\Sigma_x\Sigma_y}{(n_1 n_2)'} \quad (3.9)$$

where  $R'$ ,  $\mathcal{L}'$ ,  $\mu'_{vis}$ ,  $n'_1$  and  $n'_2$  are the maximum values of the collision rate, luminosity, number of interactions, and the numbers of particles in each beam, respectively, when measured at zero separation.  $\sigma_{vis}$  is then fixed, and the luminosity for any bunch crossing is given by Equation 3.4. Summing over the total number of bunch crossings yields the desired result of the total instantaneous luminosity of the LHC. This method measures the luminosity with a systematic uncertainty of 2% in 2011 [22] and 2.5% in 2012 [92].

An example of the measurement of the interaction rate as a function of the horizontal beam separation,  $\Delta x$  is shown in Figure 3.4. Typically the measured quantity for  $R(\Delta x)$  in Equation 3.8 is  $\mu_{vis}/(n_1 n_2)$ , called the specific interaction rate. This quantity is used to eliminate sensitivity to the beam current, which may change over the course of a scanning run.

### 3.3.3 Performance During Run I

The data collected for this thesis are a subset of the Run I LHC dataset. This dataset consists of  $\sqrt{s} = 7$  TeV data in 2011 and  $\sqrt{s} = 8$  TeV data from 2012. The comparatively negligible amount of data collected in 2009 and 2010 is not included. As discussed in Section 3.2, several LHC parameters were different than the design parameters. These differences are detailed in Table 3.1.

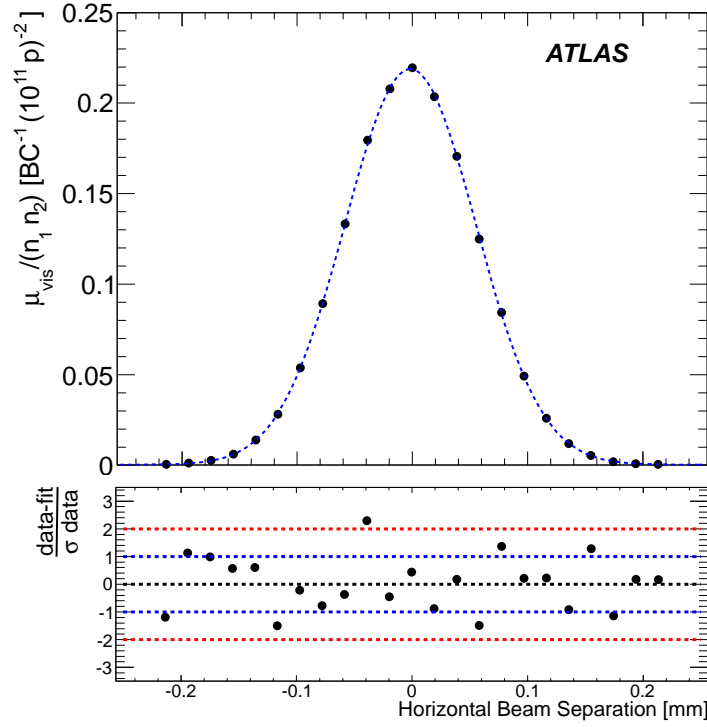


Figure 3.4: A measurement of the specific interaction rate as a function of the horizontal separation of the beams for a specific BCID. The residual deviation of the data from the Gaussian plus constant term fit, normalized at each point to the statistical uncertainty ( $\sigma_{data}$ ), is shown in the bottom panel. A value for  $\mu_{vis}$  is obtained from such data by combining the measurement with independent measurements of  $n_1$  and  $n_2$  [22].

Parameter	Units	Nominal (Design)	2011 (Data)	2012 (Data)
Beam Energy	TeV	7 TeV	3.5 TeV	4 TeV
Peak Instantaneous Luminosity	s <sup>-1</sup> cm <sup>-2</sup>	10 <sup>34</sup>	3.7x10 <sup>33</sup>	7.7x10 <sup>33</sup>
Max average collisions per crossing		19	17	37
Bunch Spacing	ns	25	50	50
Intensity per bunch	10 <sup>11</sup>	1.15	1.45	1.7
Number of filled bunches		2808	1380	1380
Normalized rms transverse emittance	μm	3.75	2.4	2.5
$\beta$	m	0.55	1.0	0.6
Stored Energy	MJ	362	110	140
Operating Temperature	K	1.9	1.9	1.9
Bending Radius	m	2803.98	2803.98	2803.98

Table 3.1: Differences between the design LHC parameters and those achieved during data taking in 2011 and 2012 [73, 94].

Despite these changes, the LHC produced high integrated luminosities in both years: 5.3 fb<sup>-1</sup> were collected in 2011, and 23.3 fb<sup>-1</sup> were collected in 2012. Graphs of the integrated luminosity as a function of calendar day are shown in Figures 3.5.

One feature of the change to 50 ns bunch spacing from 25 ns bunch spacing is that the average number of interactions per bunch crossing is higher. The design value for  $\langle \mu \rangle$  is 17, while in 2011 data taking  $\langle \mu \rangle$  reached 24 and in 2012  $\langle \mu \rangle = 20.7$ . The consequence of higher  $\langle \mu \rangle$  values is a phenomenon known as *pile-up*. Two categories of pile-up exist. The first is called *in-time pile-up*, and refers to the fact that at high beam intensities, several protons may interact in the same bunch-crossing. The second is called *out-of-time pile-up* and refers to the fact that the energy from multiple bunch crossings may be read out during the read out of a single bunch crossing, because the read-out window of many detectors is longer than the collision rate. Figure 3.6 shows the peak average number of interactions per

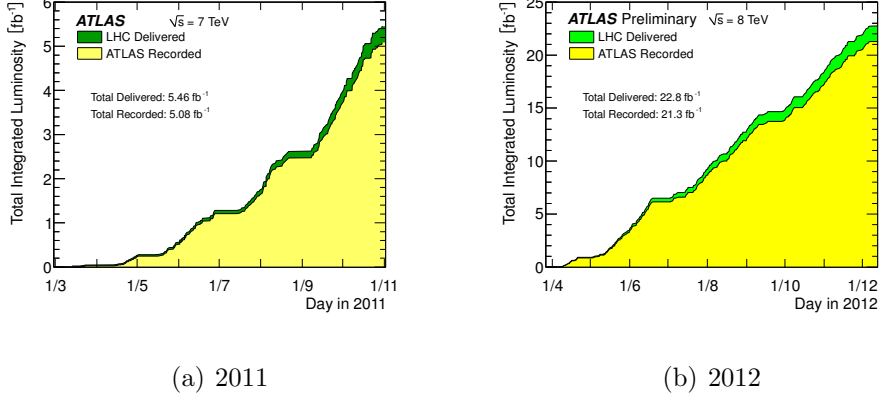


Figure 3.5: Integrated luminosity collected by the ATLAS experiment as a function of calendar day in 2011 (left) and 2012 (right). The green area represents the total integrated luminosity delivered by the LHC, and the yellow area represents the integrated luminosity recorded by the ATLAS detector. The difference is due to the safety precaution of keeping sensitive electronics in low-voltage mode before the beam is ensured to be stable [16].

bunch crossing observed by ATLAS as a function of calendar day from 2010 to 2012.

The amount of integrated luminosity collected as a function of the maximum average number of interactions per bunch crossing is shown in Figure 3.7.

The presence of pile-up complicates the reconstruction of all physics objects. As the number of interactions increases so does the number of charged particles, increasing the number of vertices and tracks, and increasing the amount of energy in the calorimeters. All the LHC experiments must be able to model pile-up well in order to produce precision physics measurements.

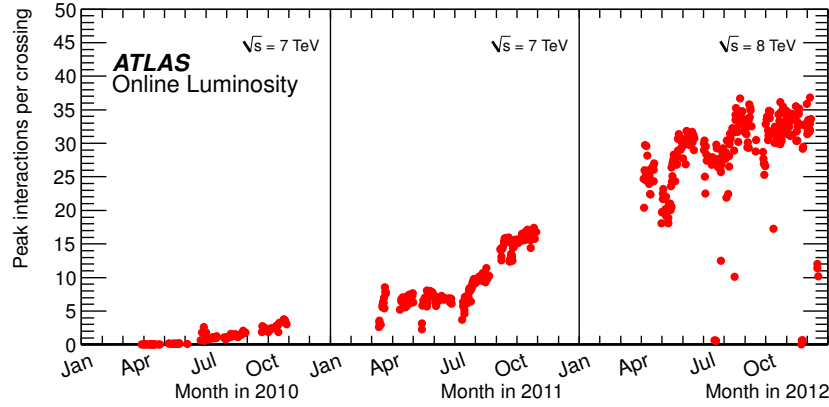


Figure 3.6: The peak value of the average number of interactions per bunch crossing as a function of calendar day, as recorded by ATLAS [16].

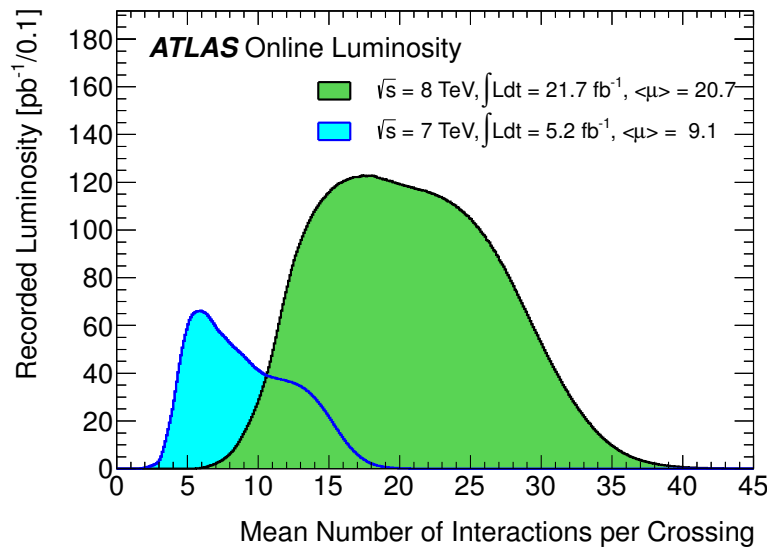


Figure 3.7: The integrated luminosity collected during Run I of the LHC as a function of the maximum average number of interactions per bunch crossing [16].

# Chapter 4

## The ATLAS Detector

The ATLAS Detector [32] (“**A Toroidal LHC ApparatuS**”) is a general-purpose, large-acceptance detector system with approximately hermetic coverage that is built around IP-5 of the LHC at CERN in Geneva, Switzerland. This chapter will introduce the major components of the ATLAS detector while leaving more detailed discussion to References [32, 14, 21]. An overview of the coordinate system used in ATLAS is given in Section 4.1. Then, the major components of the ATLAS detector are discussed: magnetic fields to bend charged particles (Section 4.2), a tracking system (Section 4.3), electromagnetic calorimeters (Section 4.4.1), hadronic calorimeters (Section 4.4.2), and a muon spectrometer (Section 4.5). Additional detectors dedicated to the measurement of the luminosity are discussed in Section 4.6, and finally, the trigger and data acquisition system is discussed in Section 4.7. These complimentary technologies allow ATLAS to meet the requirements to make high-resolution measurements of the properties of leptons, photons, and jets, as well as to identify both primary and secondary interaction vertices. Figure 4.1 details the

major components of the ATLAS detector. At the innermost layer of the detector lies the Inner Detector that is described in Section 4.3. The Inner Detector is immersed in a 2 T solenoidal magnetic field and consists of three major components: silicon pixels, silicon strips, and small-radius drift tubes. These components combine to precisely measure the trajectory of charged particles emerging from the collision point, and thus allow for the calculation of the momentum of these particles. Moving radially outward from the beam line, the next detector systems are the calorimeters. The electromagnetic calorimeter employs lead absorbers with liquid Argon for the active medium, and the hadronic calorimeter utilizes steel absorbers and scintillating tiles. Combined, these technologies measure the energy deposited by photons, electrons, and hadrons. At larger distance from the interaction point than these systems lies the muon spectrometer. This system consists of 4 technologies to measure the momentum of muons, which typically pass through the other components of ATLAS, and to trigger on these muons. The four technologies are monitored drift tubes (MDTs), resistive plate chambers (RPCs), thin gap chambers (TGCs) and cathode strip chambers (CSCs). Surrounding the detectors of the muon spectrometer is a toroidal magnetic field, described in Section 4.2.

As a general-purpose detector, ATLAS seeks to measure a wide variety of physical properties including both low-energy QCD processes and high-energy searches for new physics at the TeV scale. In order to achieve precise measurements across this range of energies, several benchmarks are set for the performance of the detector. These are outlined below, in Table 4.1. The measurement described in this thesis requires the identification of electrons, muons, and jets, as well as the reconstruction

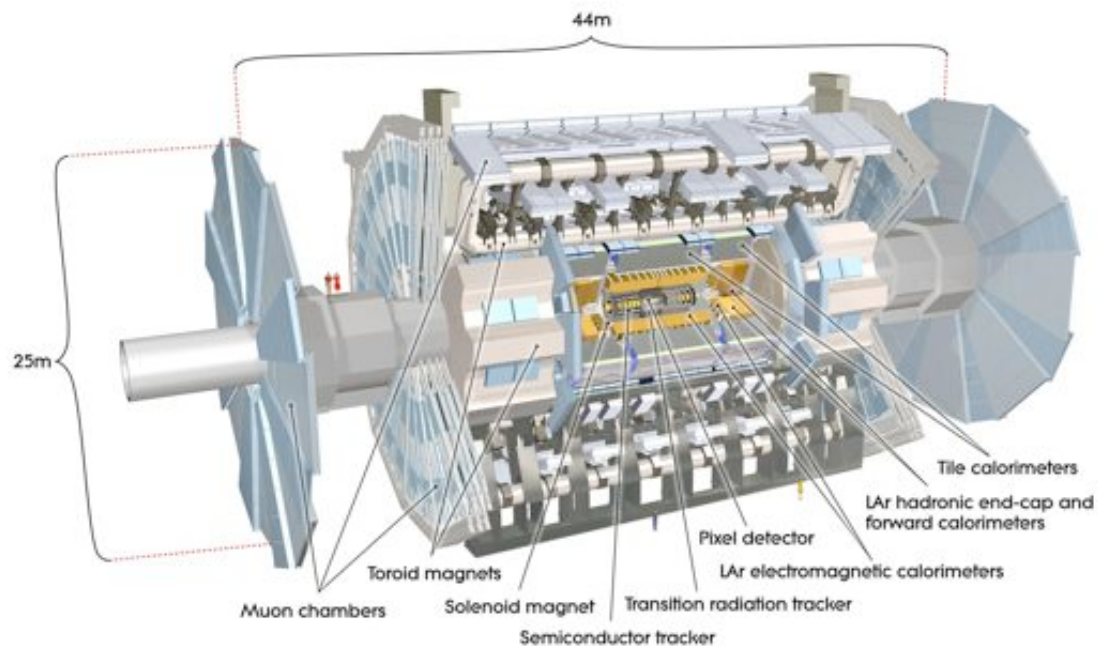


Figure 4.1: A schematic of the ATLAS detector [32].

of a quantity called missing energy, or  $E_T^{\text{miss}}$ , which is created as the opposite of the sum of all other energy in the event.

Detector	Resolution	Measurement Coverage	Trigger Coverage
Tracking	$\sigma_{pT}/pT = 0.05\% p_T \oplus 1\%$	$ \eta  < 2.5$	
Electromagnetic Calorimeter (electrons, photons)	$\sigma_E/E = 10\%/\sqrt{E} \oplus 0.7\%$	$ \eta  < 3.2$	$ \eta  < 2.5$
Hadronic Calorimeter (jets)			
Barrel and End-Cap	$\sigma_E/E = 50\%/\sqrt{E} \oplus 3\%$	$ \eta  < 3.2$	$ \eta  < 3.2$
Forward	$\sigma_E/E = 100\%/\sqrt{E} \oplus 10\%$	$3.1 <  \eta  < 4.9$	$3.1 <  \eta  < 4.9$
Muon Spectrometer	$\sigma_{pT}/pT = 10\% \text{ at } 1 \text{ TeV}$	$ \eta  < 2.7$	$ \eta  < 2.4$

Table 4.1: The performance goals of ATLAS detector's components [32]. Energy and momentum are listed in GeV and  $\oplus$  indicates summation in quadrature.

## 4.1 The ATLAS Coordinate System

ATLAS uses a cylindrical coordinate system with origin at the center of the detector, which coincides with interaction point 5 of the LHC. The  $z$ -axis runs through the beam line with the positive  $z$ -axis pointing toward the A side of the detector.  $\phi$ , the azimuthal angle in the  $x$ - $y$  plane, has a value of zero at the positive  $x$ -axis, which in turn points into the center of the LHC ring. The polar angle  $\theta$  is defined such that  $\theta = 0$  lies along the positive  $z$ -axis. An approximation to the rapidity:

$$y = \ln[(E + p_z)/(E - p_z)]/2, \quad (4.1)$$

called the pseudo-rapidity, or  $\eta$ , is defined as:

$$\eta \equiv -\ln \tan(\theta/2). \quad (4.2)$$

. Finally, a commonly-used angular distance is defined as:

$$\Delta R \equiv \sqrt{\Delta\eta^2 + \Delta\phi^2}. \quad (4.3)$$

Since the  $z$ -component of the energy of the colliding particles is not known and collisions in the ATLAS detector occur with approximately zero momentum in the plane perpendicular to the  $z$ -axis, it is often useful to project variables into this plane. The transverse momentum is defined as  $\mathbf{p}_T = (p_x, p_y)$  and the transverse energy as  $E_T = E \sin(\theta)$ . Finally, two additional coordinates are used for the description of tracks reconstructed by the Inner Detector. As a particle leaves the vicinity of the collision vertex, one can define the distance of closest approach that the reconstructed track makes with the vertex. The  $z$ -distance from the vertex to the track is defined as  $z_0$ . The distance in the transverse plane from the track's closest approach and the vertex is defined as  $d_0$ .

## 4.2 The Magnetic Field of the ATLAS Detector

The ATLAS magnetic field [32, 118] was designed to provide a field capable of providing sufficient bending power such that a measurement of muon momentum with 10% relative resolution at energies of 1 TeV would be possible with only the Muon Spectrometer 4.5. The magnetic system consists of a 2 T solenoid and a toroidal system of three additional magnets. A superconducting solenoid surrounds the inner detector and is aligned with the beam axis to produce a magnetic field of 2 T in the  $+z$ -direction and bend particles in the  $\phi$  direction. A second system produces a toroidal field with three magnets: one in the barrel region, and on each of the A

and C sides of the detector. The toroid is designed as eight separate coils separated by air in order to reduce the material budget and thus reduce the effect of muons undergoing multiple scatterings, which degrade resolution. In the barrel, the eight coils are arranged symmetrically in  $\phi$  beginning at  $\phi = 0$ . The endcap toroids also have eight-fold symmetry, but are rotated  $\pi/8$  relative to the barrel toroid coils. This toroidal field bends particles in the Muon Spectrometer in the  $\eta$  direction.

The superconducting solenoid has dimensions of 5.8 m in  $z$  and 2.5 m in  $R$ . It is made from 1154 windings of Al-stabilized NbTi, which is cooled to 4.5 K and runs with a current of 7.7 kA. In the barrel region, the toroid is 25.3 m long and has inner diameter of 9.4 m with an outer diameter of 20.1 m. Each of the three toroid magnets have eight coils consisting of 120 windings per coil. These windings are also made from Al-stabilized NbTi, and are cooled to 4.6 K while running at a current of 20.5 kA. Figure 4.2(a) details the layout and magnetic field strength of the magnet system.

### 4.3 The Inner Detector

The Inner Detector (ID) of ATLAS is designed to provide tracking coverage within  $|\eta| < 2.5$  to yield precise measurements of the momentum of charged particles as they are bent by a solenoidal magnetic field. These tracks are of particular importance to improve the measurement of the momentum of electrons and muons, and to identify photon conversions in the material of the ID. Additionally, the ID uses this tracking information to reconstruct the position of the partonic collision as well as the decays

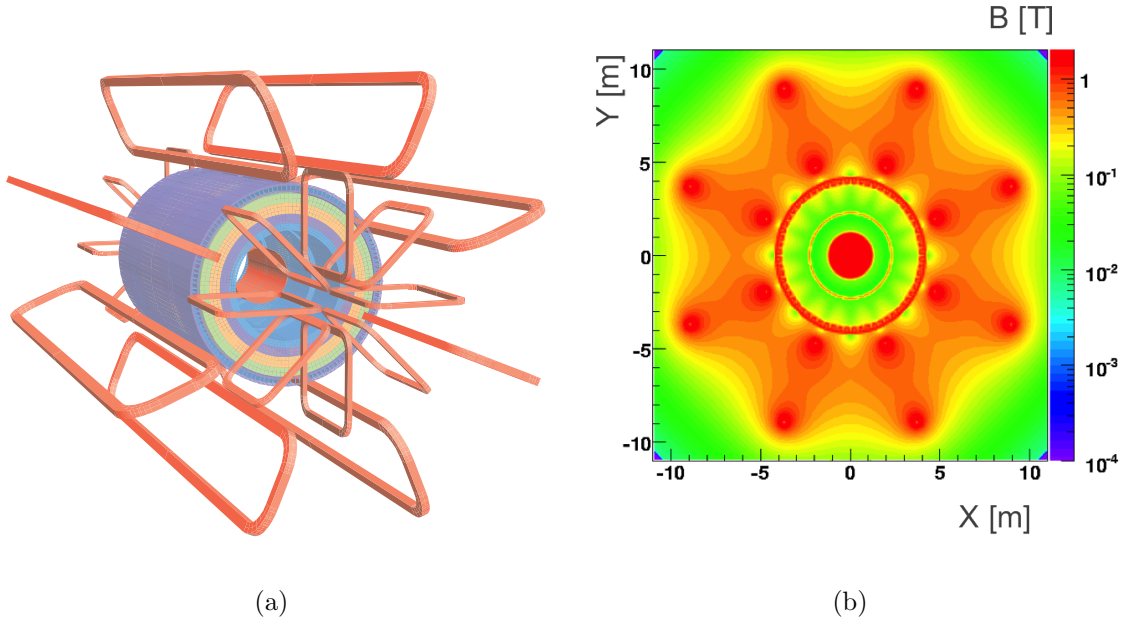


Figure 4.2: (Left) The layout of the ATLAS Magnet System. The orange, oval rings forming the outer layer of the cylinder represent the toroidal magnets of the Muon Spectrometer. The interior cylinder represents the four layers used to model the Tile calorimeter, which contains the solenoid windings. (Right) A cross-sectional view of the ATLAS magnetic field strength. The inner red circle with radius 1 m is the strength of the solenoid, while the outer, less homogeneous region with 8-fold symmetry is the strength of the toroid system. Return fluxes appear as the thin rings at  $R \sim 2.5$  m and  $R \sim 4$  m [32].

of longer-lived hadrons such as  $B$ -hadrons, Kaons, and  $\tau$  leptons.

More specifically, this system aims to have a resolution on the transverse momentum of  $\sigma_{p_T}/p_T = 0.05\% \times p_T \oplus 1\%$  for tracks of  $p_T > 500$  MeV. In achieving this goal, the ID must also be robust against radiation damage, as the LHC is capable of producing 1000 particles per collision every 25ns [32]. Furthermore, the ID was designed to minimize the material budget, which degrades resolution via multiple scattering effects and also impacts the measurement of energy in the calorimeters. Despite the effort to minimize the material budget of the detector services, the density of the sensors causes the ID to have a significant material for particles to traverse before reaching the calorimeters. Figure 4.3 details the amount of material present in the ID. The optimization of tracking resolution, given the concerns of material budget and radiation hardness, is the key design goal of the ID.

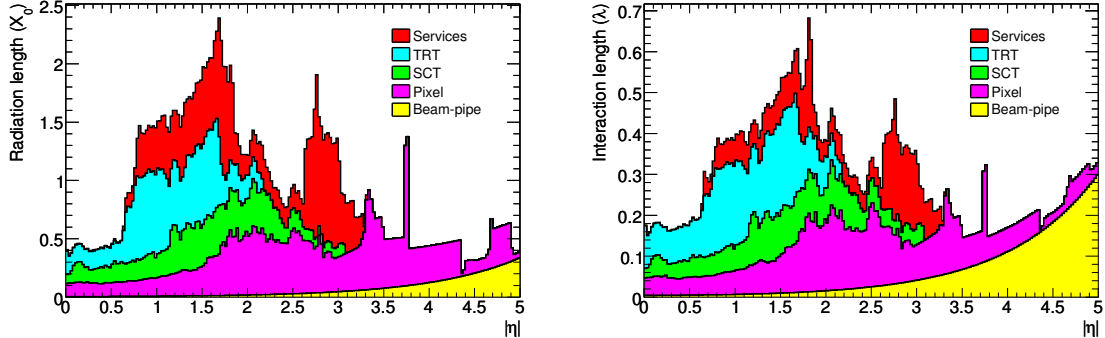


Figure 4.3: The material budget of the ATLAS Inner Detector traversed by a straight track, as measured at the exit of the Inner Detector envelope in terms of (left) radiation lengths  $X_0$ , and (right) interaction lengths  $\lambda_0$  [32].

The ID consists of three subsystems: the Pixel Detector, the Semiconductor Tracker, and the Transition Radiation Tracker. In its largest extent, the envelope of the ID ranges from a radius of 1150 mm and length 3512 mm in the  $\pm z$  direction. At the closest radius to the collision point is the Pixel Detector, which provides, on average, three high-resolution space-point measurements in  $\eta$  and  $\phi$ . At larger radii lies the Semiconductor Tracker (SCT). The SCT is made from silicon microstrips and usually provides eight space-point measurements along the particle's trajectory. In order to enhance the pattern recognition and improve momentum resolution over  $|\eta| < 2.0$  while maintaining a low material budget and cost, the final component of the ID, called the Transition Radiation Tracker (TRT) consists of many small, gaseous drift tubes [32]. A schematic of the ID is shown in Figure 4.4.

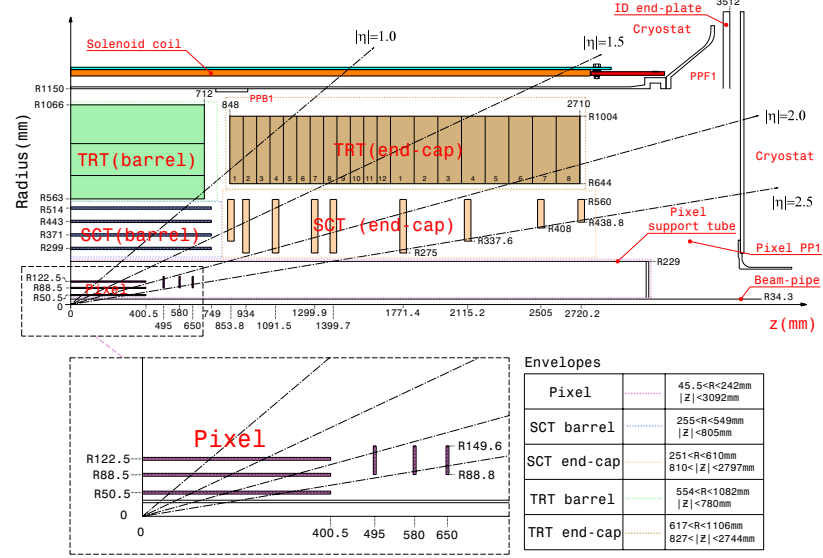


Figure 4.4: A schematic of the envelopes of the sub-detectors in a quarter-section of the ATLAS Inner Detector [32].

### 4.3.1 The Pixel Detector

As particles emerge from the interaction point, they first traverse the Pixel Detector. This system is responsible for providing high-precision measurements of space-points, which allow the reconstruction of charged particle tracks and vertices. The Pixel Detector is organized into three layers in two regions: a barrel region and an endcap region. The layer of the Pixel Detector closest to the beamline is denoted as the *B*-layer, and is crucial to the measurement described in this thesis because it allows for high-precision measurements of the secondary vertices that indicate the decay of long-lived particles such as *B*-hadrons. In the barrel region ( $|z| < 400.5$  mm), the sensors are arranged in three concentric cylindrical layers at  $R = 50.5$  mm,  $80.5$  mm, and  $122.5$  mm. In the endcap region they are arranged in three disks at  $|z| = 495$  mm,  $580$  mm, and  $650$  mm that are oriented transverse to the beamline. The endcap sensors span radial distances of  $88.8$  mm  $< |r| < 149.6$  mm.

The Pixel Detector consists of a total of 1744 sensors, each with 47232 silicon pixels of  $50\text{ }\mu\text{m}(R\phi) \times 400\text{ }\mu\text{m }(z/R)$ . Every silicon pixel is bump-bonded to a readout element, yielding a total of 80 million readout channels for the Pixel Detector. The intrinsic resolution of the Pixel Detector is  $10\text{ }\mu\text{m }(\phi)$  and  $115\text{ }\mu\text{m }(z, \text{or } R \text{ for the endcap region})$ . In order to reduce the effect of the large radiation dose received by the material of the Pixel Detector, the entire system is cooled to  $-7^\circ\text{C}$ .

### 4.3.2 The Semiconductor Tracker

To provide additional high-precision space-points for tracking, the ID has a second silicon-based technology called the Semiconductor Tracker (SCT). The SCT consists of four layers of silicon microstrips in the barrel region and nine layers in the endcap region in order to provide at least 8 additional space-time points in the R- $\phi$  plane for track reconstruction. In the barrel region the SCT planes are located from 299 mm  $< R <$  563 mm and cover the distance  $|z| <$  749 mm, while in the endcap region the planes cover 853 mm  $< |z| <$  2720 mm with radial size optimized to provide the same number of average hits over the full  $|\eta|$  coverage.

Each sensor of the SCT has an active area of 6.36x6.40 cm<sup>2</sup>, containing 768 readout strips with a pitch of 80  $\mu\text{m}$ . The total number of readout channels in the SCT is 6.2 million. In order to keep the number of readout channels lower, pairs of sensors are bonded together, creating doubly-long sensors of 12.8 cm. Two pairs of sensors are then arranged to overlap with a relative rotation of  $\pm 20$  mrad, which allows for measurement of the remaining coordinate that is not in the non-bending plane. The intrinsic resolution of the SCT space-point measurement is 7  $\mu\text{m}$  in  $\phi$  and 580  $\mu\text{m}$  in  $z$  ( $R$  for the endcap). This allows for the separation of tracks if the particles are separated in  $z$  by more than 200  $\mu\text{m}$ . As for the Pixel Detector, the SCT is also cooled to -7°C.

### 4.3.3 The Transition Radiation Tracker

Positioned outside the SCT, the Transition Radiation Tracker (TRT) is the outermost component of the Inner Detector. Designed to provide many additional space-points for tracking while being cost-effective and minimizing the material budget, the TRT consists of many gaseous drift tubes. The TRT is also divided into a barrel region in which the tubes run in the  $\pm z$  direction and an endcap region in which the tubes run radially. In the barrel region the tubes, with length 72 cm, cover 563 mm  $< R < 1066$  mm and  $|z| < 712$  mm. For the endcap regions, the tubes span from  $R = 644$  mm to  $R = 1004$  mm for  $848 \text{ mm} < |z| < 2710$  mm. In total, the TRT contains approximately 350,000 drift tubes and provides an additional 36 hits on a track that traverses the Inner Detector.

Each gaseous drift tube, or straw tube, has a diameter of 4 mm and contains a gold-plated W-Re wire with a 31  $\mu\text{m}$  diameter. Inside the tubes is a gas of mixture 70% Xe, 27% CO<sub>2</sub> and 3% O<sub>2</sub> with 5 to 10 mbar over-pressure. At the passing of a charged particle through this gas mixture, the gas ionizes and the drifting of an avalanche of electrons toward the anode wire produces a signal for the read-out electronics. The signal is converted from the time of arrival of the electrons to a drift radius inside the tube, yielding an intrinsic resolution per tube of  $\sim 130 \mu\text{m}$  in the bending plane. Because of the long length of the tubes, there is no significant measurement in the non-bending direction. Although this resolution is worse than that of the SCT and the Pixel Detector, the 36 additional hits are spread over a long track length, resulting in a significant improvement on the overall resolution of a reconstructed track.

Beyond its tracking capabilities, the TRT also provides electron identification through the exploitation of measurements of transition radiation. As the particles pass between media of different dielectric constants, radiation is emitted at intensities in proportion to the Lorentz factor. As lighter particles will have a higher Lorentz factor for a given energy than heavier particles, it is possible to discriminate between electrons and hadrons. To capitalize on this effect, the TRT read-out electronics have two threshold settings: a lower setting to detect radiation from hadrons or minimum ionizing particles, and a higher setting to indicate the presence of an electron or positron when transition radiation has been detected.

## 4.4 The ATLAS Calorimeter System

While the Inner Detector produces precise measurements of the momentum of charged particles passing through it, no measurement is possible for neutral particles such as photons or  $\pi^0$  mesons, which decay to photons. In order to measure the energy and direction of photons, as well as to better measure the energy and direction of electrons, hadrons and gluons which shower many particles as jets, a calorimeter is needed. Furthermore, the energy of neutrinos or other non-interacting particles can only be inferred from the total vectorial sum of the energy in the calorimeter system. The ATLAS calorimeter consists of three sampling calorimeters. The electromagnetic calorimeter (EM calorimeter) provides coverage within  $|\eta| < 3.2$ . This calorimeter is designed with high-granularity to distinguish between photons, electrons, pions through analysis of the shower shapes. The active medium is liquid Argon (LAr) with lead absorber plates to initiate the showers. At larger radius lies the hadronic

calorimeter (HCAL), which is designed with more coarse granularity sufficient to measure the total energies of charged and neutral hadrons for jet reconstruction. The HCAL utilizes tile scintillators with steel absorbers within  $|\eta| < 1.7$  and the endcap uses LAr as the active medium, with copper absorbers for  $1.5 < |\eta| < 3.2$ . For more forward trajectories, the Forward Calorimeter (FCAL) provides coverage from  $3.1 < |\eta| < 4.9$  using LAr with tungsten absorbers. Figure 4.5 details the layout of the ATLAS calorimeter systems and Table 4.2 describes the coverage, granularity, and radiation depth of each of the calorimeters.

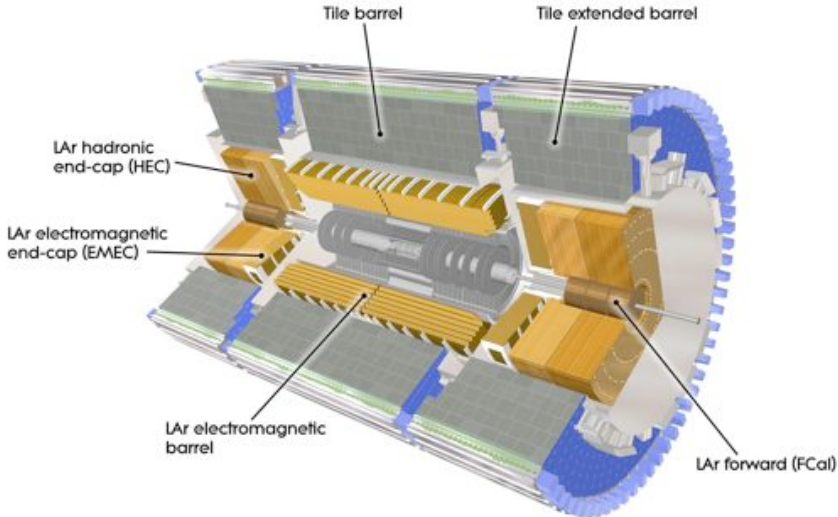


Figure 4.5: A schematic of the ATLAS calorimeter [32].

#### 4.4.1 The Electromagnetic Calorimeter

The EM calorimeter [25] is divided into a barrel region, within  $|\eta| < 1.7$  and an endcap region with coverage from  $1.7 < |\eta| < 3.2$ . A gap of 4 mm separates the two sections of the barrel at  $z = 0$ . The barrel region is 3.2 m long with inner and outer radii of  $\sim 1.470$  m and  $\sim 2.0$  m, respectively, while the endcap region is 63 cm long with inner and outer radii of 330 mm and 2098 mm, respectively. The construction of the EM calorimeter is novel in that an accordion shape was employed to interleave the absorber and electrodes, allowing for complete coverage in  $\phi$  because the readout electronics can be located at the back outer edge of the calorimeter. A schematic of this design and a photograph of a barrel module are shown in Figure 4.7. This accordion structure consists of folded layers of lead absorber plates with

EM calorimeter				
Barrel				
Num. Readout Channels	7808 (Presampler) + 101760 (Calo)			
Component	Layers	Coverage	Granularity ( $\Delta\eta \times \Delta\phi$ )	Depth
Presampler	1	$ \eta  < 1.52$	$0.025 \times 0.1$	10 mm
Layer 1	1	$ \eta  < 1.475$	$\sim 0.003 \times 0.1$	$4.3 X_0$
Layer 2	1	$ \eta  < 1.475$	$\sim 0.025 \times 0.025$	$16 X_0$
Layer 3	1	$ \eta  < 1.475$	$0.05 \times 0.025$	$2 X_0$
End-Cap				
Num. Readout Channels	1563 (Presampler) + 62208 (Calo)			
Component	Layers	Coverage	Granularity( $\Delta\eta \times \Delta\phi$ )	Depth
Presampler	1	$1.5 <  \eta  < 1.8$	$0.025 \times 0.1$	4 mm
Layer 1	1	$1.375 <  \eta  < 3.2$	$\sim 0.003 \times 0.1$	$4 X_0$
Layer 2	1	$1.375 <  \eta  < 3.2$	$\sim 0.025 \times 0.025$	$20 X_0$
Layer 3	1	$1.5 <  \eta  < 2.5$	$0.05 \times 0.025$	$2 X_0$
Hadronic Tile Calorimeter				
Num. Readout Channels	9852			
Component	Layers	Coverage	Granularity( $\Delta\eta \times \Delta\phi$ )	Depth
Layer 1,2	2	$ \eta  < 1.7$	$0.1 \times 0.1$	$4.1\text{-}5.6\lambda_0$
Layer 3	1	$ \eta  < 1.7$	$0.2 \times 0.1$	$1.8\text{-}3.3 \lambda_0$
LAr Hadronic End-Cap Calorimeter				
Num. Readout Channels	5632			
Component	Layers	Coverage	Granularity( $\Delta\eta \times \Delta\phi$ )	Depth
Low $\eta$ Layers	4	$1.5 <  \eta  < 2.5$	$0.1 \times 0.1$	$9.7\text{-}12.5\lambda_0$
High $\eta$ Layers	4	$2.5 <  \eta  < 3.2$	$0.2 \times 0.2$	$9.7\text{-}12.5\lambda_0$
Forward Calorimeter				
Num. Readout Channels	3524			
Component	Layers	Coverage	Granularity( $\Delta\eta \times \Delta\phi$ )	Depth
FCAL Layers	3	$3.1 <  \eta  < 4.9$	$\sim 0.2 \times 0.2$	$10.5\text{-}12.5\lambda_0$

Table 4.2: Calorimeter parameters.

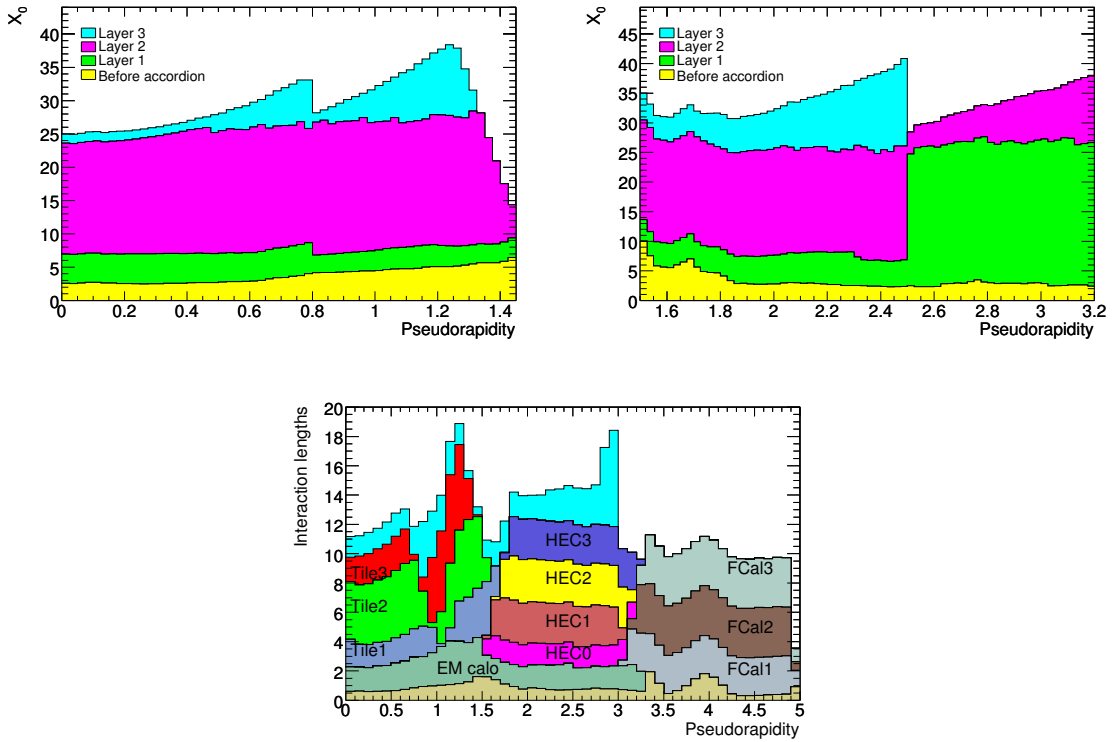


Figure 4.6: Cumulative amount of material in the calorimeter systems [32]. The amount of material in terms of radiation lengths  $X_0$  for the EM barrel (top right) and EM barrel (top left) . The amount of material in terms of nuclear interaction lengths for the different hadronic calorimeter layers, as well as the total EM calorimeter and the material before the calorimeter (bottom center).

kapton electrodes between each layer. The gaps between the electrodes and the lead absorbers are filled with liquid Argon, which acts as the active medium to produce a shower of electrons. As electrons and photons pass through a lead absorber layer, more electromagnetic showers are initiated. This radiation then ionizes the LAr upon passing through it, and the drift of the electrons from ionization toward the kapton electrodes induces a signal that is read out by capacitive coupling. The sampling time of the calorimeter is 25 ns and the readout window is 5 samples long. The energy measurement is approximately linear to the number of electrons arriving at the electrode, and the resolution is largely dependent on the total number of electrons collected in the readout window. The resolution scales with the inverse square root of the energy of incident particles. The relative resolution of the EM calorimeter is given by:

$$\frac{\sigma(E)}{E} = \frac{10\%}{\sqrt{E}} \oplus 0.7\%, \quad (4.4)$$

where E is the energy of a charged particle.

The EM calorimeter consists of three segmentations along the direction of shower development, and an additional sensitive layer called the presampler. The presampler covers the region  $|\eta| < 1.8$  and is instrumented with a thin layer of LAr, which allows for a derivation of an energy correction for energy lost in material upstream of the EM calorimeter. The first layer at larger radius than the presampler is optimized for precision direction measurements and particle discrimination between photons, electrons, and neutral pions, and thus has high granularity. The second layer is optimized to contain the energy of the electromagnetic shower, so has greater depth

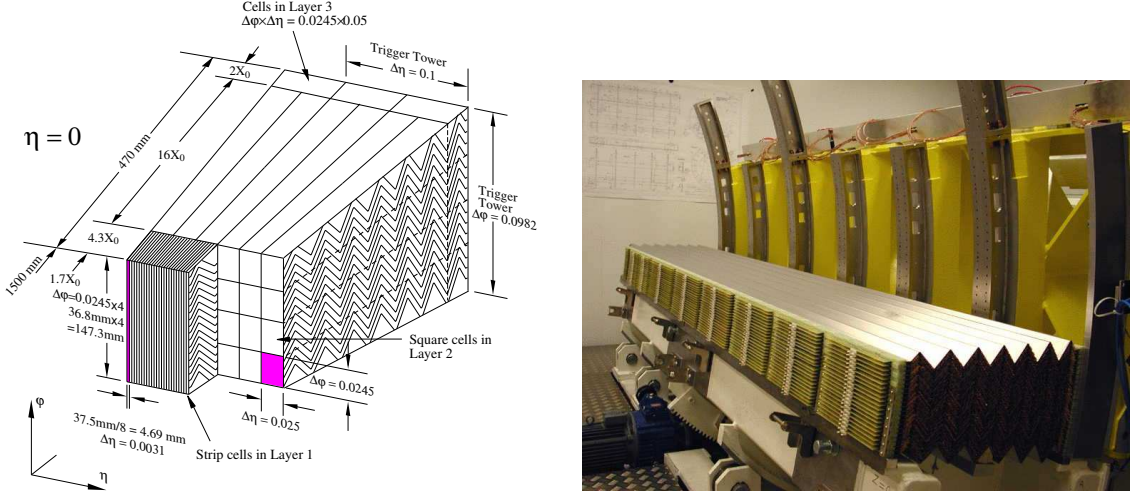


Figure 4.7: A sketch of the EM calorimeter geometry and readout granularity (left) and a photo of a partially stacked barrel module showing the accordion design [32].

but lower granularity than the first layer. Finally, the third layer is used to provide an additional energy measurement for particles passing through the EM calorimeter to the hadronic calorimeter. This provides a measurement to distinguish between electromagnetic and hadronic showers. In total, the depth of the EM calorimeter is  $22X_0$ , where  $X_0$  is one radiation length. A radiation length is the average distance traveled by a charged particle before it loses all but  $1/e$  of its energy.

The amount of material in the EM calorimeter is shown in Figure 4.6.

#### 4.4.2 The Hadronic Calorimeter

Beyond the EM calorimeter lies the Hadronic Calorimeter (HCAL), which consists of a central barrel, called the Tile Calorimeter (TileCal) [30], and an endcap system called the Hadronic Endcap Calorimeter (HEC) [25]. The TileCal is made from steel plates interleaved with polystyrene tile scintillators that are oriented such that

a vector normal to the the plane of the tile points in the  $z$ -direction. A signal is extracted via wavelength-shifting fibers, which carry the scintillation light to photomultiplier tubes. This system is further divided into a Barrel region ( $|\eta| < 1.0$ ) and an extended-barrel region ( $0.8 < |\eta| < 1.7$ ), which together have an inner and outer radius of 2.28 m and 4.25 m.

Further forward in  $|\eta|$ , the higher particle flux must be compensated for by utilizing a copper absorber rather than steel, and LAr is used as the active medium because it is more resistant to radiation damage than scintillating tile. This system covers the pseudorapidity region  $1.7 < |\eta| < 3.1$  and has inner and outer radii of 372 mm and 2030 mm. For a hadronic calorimeter, depth is measured in units of interaction lengths, or  $\lambda_0$ . The interaction length is defined as the mean path length traversed by a group of particles such that their number has been reduced by  $1/e$ . The depths of the TileCal and the HEC are optimized to contain the entire hadronic shower while also providing enough sampling layers to reach resolution goals and to allow for shower-shape analysis. With this optimization, the TileCal has a radial depth of  $7.4 \lambda_0$  and the HEC has a depth of  $10 \lambda_0$ . Furthermore, the granularity of each system is optimized to allow for adequate  $\eta$  and  $\phi$  measurements to meet goals for jet-direction measurements and studies of the shape of hadronic showers. The relative resolution of the Hadronic Calorimeter for single pions is measured in test beam data to be:

$$\frac{\sigma(E)}{E} = \frac{52\%}{\sqrt{E}} \oplus 3.0\% \oplus \frac{1.8GeV}{E}. [32] \quad (4.5)$$

### 4.4.3 The Forward Calorimeter

The highest  $|\eta|$  region,  $3.1 < |\eta| < 4.9$  is covered by the Forward Calorimeter (FCAL) [25]. This calorimeter serves two main purposes. First, it provides additional coverage, allowing jet and missing energy reconstruction to higher  $|\eta|$ . Secondly, it acts as a shield for the muon spectrometer, reducing the amount of background radiation in the spectrometer [32]. The FCAL consists of three layers of metal matrices in which small gaps filled with scintillator run linearly along the beamline. The first layer is optimized for electromagnetic measurements and made from copper absorber with LAr as the active medium. The final two layers are optimized for hadronic interactions, and utilize a tungsten absorber with LAr as the active medium. In total the FCAL has a depth of  $10\lambda_0$ .

## 4.5 The Muon Spectrometer

The Muon Spectrometer (MS) is the largest component of ATLAS by volume and coverage area, and instruments approximately  $5500\ m^2$ . As the outermost subsystem of ATLAS, it is devoted to the precision measurement of the direction and momentum of muons. All particles coming from the primary interaction except muons and neutrinos, which typically pass through the entire detector with no deposit of energy, have all their energy absorbed through interactions in the Inner Detector, Electromagnetic Calorimeter, or Hadronic Calorimeter. The MS provides coverage for precision momentum measurements for  $|\eta| < 2.7$  and the ability to trigger (see Section 4.7) on charged particles for  $|\eta| < 2.4$ . In addition to the large  $\eta$  coverage, the MS is designed

to provide an independent (from the Inner Detector) measurement of a muon’s momentum with resolution at least as good as 10% for a 1 TeV muon. This is achieved by tracking the muon over a long trajectory through the torodial magnetic field described in Section 4.2. This is in contrast to the shorter and more precise, but also more dense, tracking in the Inner Detector, which has worse reolution degradation at very high momentum.

The MS is built using four major technologies. For the triggering capability, Resistive Plate Chambers (RPC) are used in the barrel region  $|\eta| < 1.05$  and Thin Gap Chambers provide coverage in the endcap, for  $1.05 < |\eta| < 2.4$ . These chambers also provide the coordinate of the space-point in the non-bending direction,  $\phi$ . Providing the precision measurements in the bending plane ( $\eta$  in the barrel and R in the endcap), the Monitored Drift Tubes (MDT) are oriented such that the tubes run in the  $\phi$  direction and cover  $|\eta| < 2.7$ . In the most forward regions, the particle flux is high enough that resolution of hit position in MDT tubes would be significantly degraded, so Cathode Strip Chambers (CSC) are used instead. A summary of the coverage, number of channels, and number of chambers for each component of the MS is found in Table 4.3.

	Coverage	Num. Chambers	Num. Channels
<b>MDT</b>	$ \eta  < 2.7$ (2.0 inner layer)	1088	339,000
<b>CSC</b>	$2.0 <  \eta  < 2.7$	32	31,000
<b>RPC</b>	$ \eta  < 1.05$	544	359,000
<b>TGC</b>	$1.05 <  \eta  < 2.7$ (2.4 for trigger)	3588	318,000

Table 4.3: The parameters of the Muon Spectrometer [32].

The layout of the MS is shown in Figure 4.8. In the barrel region,  $|\eta| < 1.05$ , the MS is arranged into 16 sectors in  $\phi$ , following the symmetry of the toroidal magnetic field. Each  $\phi$ -sector of the barrel has three cylindrical layers, located at  $R = 5$  m, 7.5 m, and 10 m. The first layer is instrumented only with MDT, while the second layer consists of MDT chambers installed between two planes of RPC. The third layer features MDT chambers with one layer of RPC on the outside of the MDT chamber.

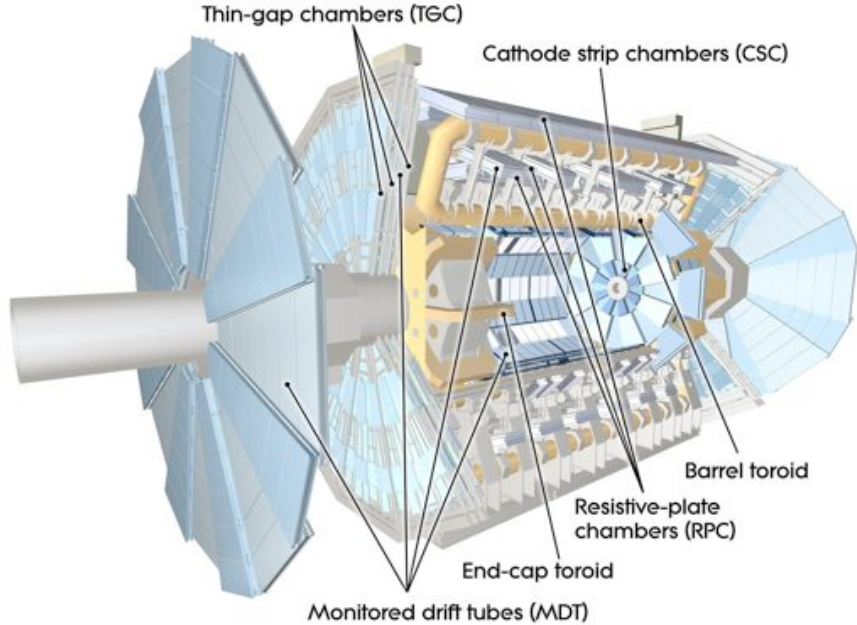


Figure 4.8: The layout of the ATLAS Muon Spectrometer [32].

In the endcap region,  $1.05 < |\eta| < 2.7$ , the MDT chambers are arranged into 16  $\phi$ -sectors, but the TGC are arranged into 12  $\phi$ -sectors. Here, three layers are also constructed at distances from the interaction point of  $z = 7.4$  m, 14 m, and 21.5 m. The TGC are mounted on each side of the middle layer of MDT chambers as well as the inner layer of MDT chambers. The  $|\eta| > 2.0$  region of the endcap is instrumented

with CSC. A detailed schematic of this layout is shown in Figure 4.9.

To achieve the design goal of 10% momentum resolution for a 1 TeV muon, the muon track must have a sagitta resolution of 50  $\mu\text{m}$ . This requires the chambers to have alignment to within 30  $\mu\text{m}$  and the toroidal field to be well understood. In order to align the chambers to this level of precision, optical alignment systems are installed between and within the detector chambers. For mapping the magnetic field, approximate 1800 Hall probes are installed throughout the toroidal field. These probes measure the field and serve to improve the simulation of the magnetic field used in track reconstruction. In addition to these two contributions to the momentum resolution, the intrinsic resolution of the tubes, multiple scattering of the muon in MS material, and fluctuations in the energy lost in upstream material each increase the resolution. Figure 4.10 describes the contributions to the momentum resolution as a function of the muon energy.

#### 4.5.1 The Monitored Drift Tubes

The Monitored Drift Tubes (MDT) [31] are the chambers responsible for producing precision spacepoints for pattern recognition in the Muon Spectrometer. In order to achieve the desired resolution of 10% for a 1 TeV muon, an MDT chamber must be capable of achieving a hit position resolution of 35  $\mu\text{m}$ . There are three layers of MDT in both the barrel region and the endcap region. In the barrel,  $|\eta| < 1.05$ , the layers are located at a distance from the beamline of  $R = 5 \text{ m}$ ,  $7.5 \text{ m}$  and  $10 \text{ m}$ . In the endcap,  $1.05 < |\eta| < 2.7$ , three layers, called wheels, are located at  $z = 7.4 \text{ m}$ ,  $14 \text{ m}$ , and  $21.5 \text{ m}$ . Each layer of MDT chambers has chambers of varying size depending on

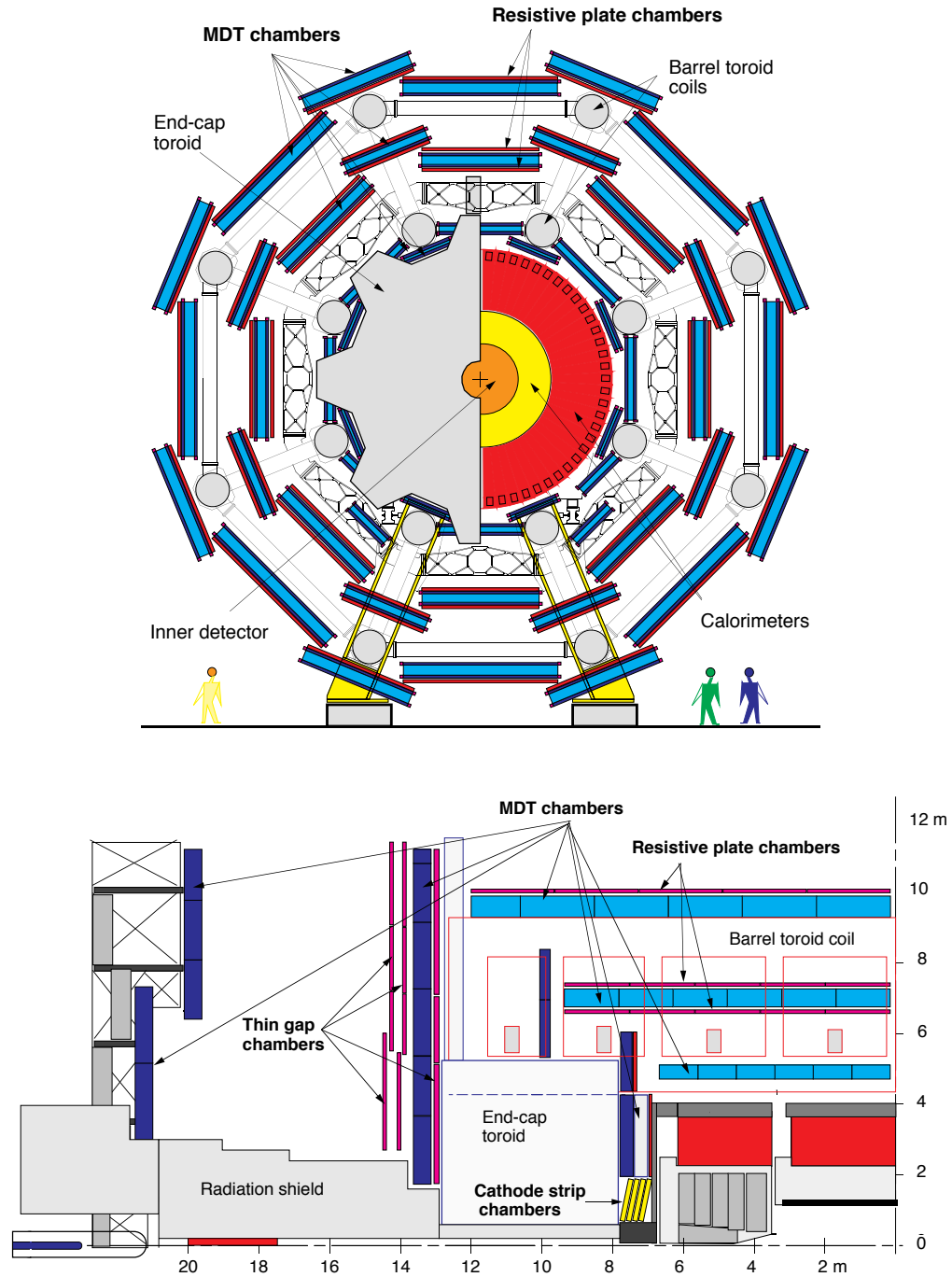


Figure 4.9: The layout of the muon spectrometer [31]. A cross-sectional view is shown on top, and a cut-away side view is shown on bottom.

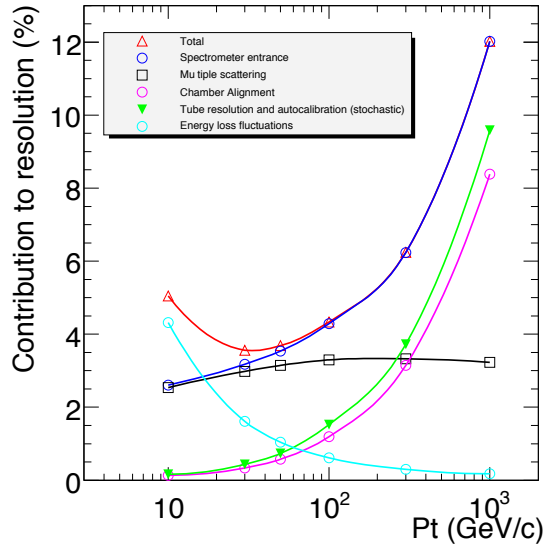


Figure 4.10: Primary contributions to muon stand-alone tracking resolution [21].

the location. A chamber of MDT consists of several layers of gaseous drift detectors, called tubes, which are 3 cm in diameter and of varying length depending on the geometry of the chamber. Each chamber has three individual layers of tubes, except the innermost barrel layer, which has four layers. This layout is shown in Figure 4.11.

Each 3 cm diameter tube is constructed from aluminum and filled with a gas mixture of Argon (93%), CO<sub>2</sub> (7%) and a trace amount of H<sub>2</sub>O, with a W-Re anode wire running the length of the tube. When a charged particle traverses a tube, the gas is ionized and electrons drift toward the anode. Through calibration, the time of arrival of electrons at the anode can be converted into a radius, which is the distance of closest approach of the track to the anode. A schematic of a muon traversing a tube and initiating an electron avalanche is shown in Figure 4.12. For a single tube, the resolution on a hit radius is approximately 80  $\mu\text{m}$ . The desired resolution of 35  $\mu\text{m}$

per chamber is achieved by having multiple layers of tubes per chamber.

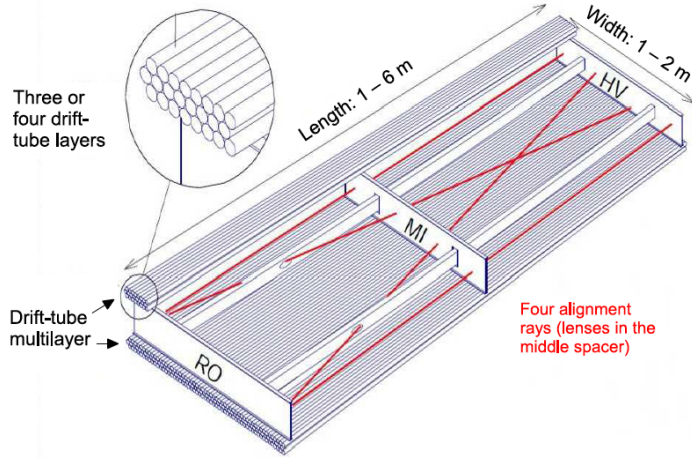


Figure 4.11: Layout of an MDT chamber [31]. Two multilayers, each with three layers of tubes are shown, along with the support structure and the optical alignment system.

### 4.5.2 The Cathode Strip Chambers

In the forward region closest to the interaction point, CSC are used because MDT would experience a buildup of ions in the high-flux environment that would degrade their resolution at hit rates above  $150 \text{ Hz/cm}^2$ . The CSC cover  $2.0 < |\eta| < 2.7$  and are located at  $z = 7 \text{ m}$  from the interaction point. Just as for the MDT and RPC, the CSC are arranged in 16  $\phi$ -sectors. There are four layers per chamber, yielding four  $\eta$  and  $\phi$  hits per track.

The CSC are multi-wire proportional chambers with anode wires running radially and both cathodes segmented into perpendicular strips for readout of hit coordinates in both  $\phi$  and  $\eta$ . The gas gap, with width 2.54 mm, consists of a mixture of  $\text{CO}_2$  (50%), Ar (30%) and  $\text{CF}_4$  (20%). The set of strips running perpendicularly to the

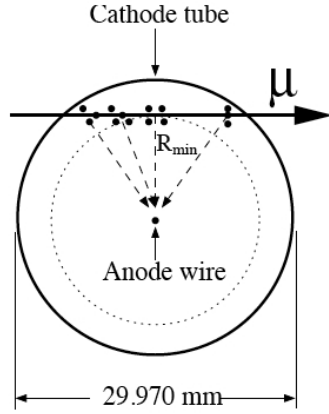


Figure 4.12: A schematic of an MDT tube while a traversing muon has ionized the gas. The first electrons to reach the wire are from the point of closest approach, or  $R_{min}$ , and form the leading edge of the hit signal [31].

wires has a pitch of 5 mm and allows for a measurement of  $\eta$  with resolution of  $60 \mu\text{m}$ , while the strips running parallel to the wires have a pitch of 16 mm and measure  $\phi$  with a resolution of 5 mm. The timing resolution of a CSC hit is 7 ns. A schematic of a CSC chamber is shown in Figure 4.5.2.

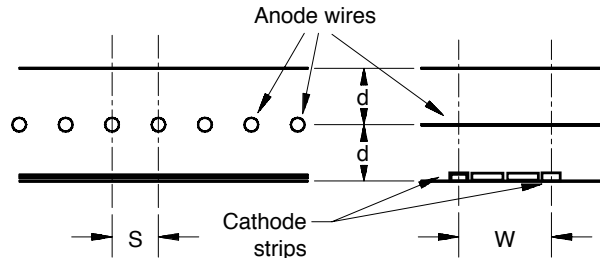


Figure 4.13: A schematic of a CSC chamber. [31].

### 4.5.3 The Resistive Plate Chambers

In the barrel region of the MS, the trigger and coordinate in the non-bending plane are provided by the Resistive Plate Chambers (RPC), which have coverage for

$|\eta| < 1.05$ . The RPC chambers are arranged into 16  $\phi$ -sectors and in three layers, two on either side of the middle layer of MDT at  $R = 7.5$  m and one on the inner side of the third layer of MDT at  $R = 10$  m. An RPC consists of two resistive Bakelite plates with a gaseous gap filled with  $C_2H_2F_4$ . The width of the gas gap is 2 mm and the voltage is held at  $\sim 4$  kV. Readout is performed via capacitive coupling with two sets of orthogonal strips, each with pitch of 30 mm, providing  $\eta$  and  $\phi$  information. A schematic of an RPC chamber is shown in Figure 4.14

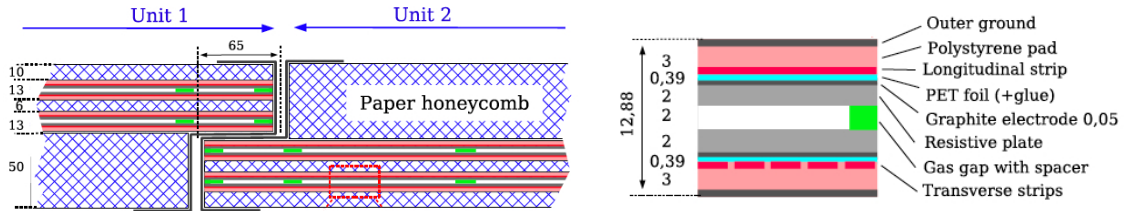


Figure 4.14: A schematic of an RPC chamber (left) and the material layers of an RPC gas gap (right). The right figure is a zoom-in version of the left figure. [31].

Each chamber consists of two detector layers, yielding a total of four  $\eta$  and four  $\phi$  hits for the middle layers of the RPC and two  $\eta$  and two  $\phi$  hits for the third layer. While the spatial resolution of the RPC is much larger than for the MDT at 10 mm, it is still adequate as a trigger, and the timing resolution of 7 ns is narrow enough to correctly identify the correct bunch-crossing of the collision.

#### 4.5.4 The Thin Gap Chambers

The TGC provide the triggering capability from  $1.05 < |\eta| < 2.4$  as well as the hit information in the non-bending plane. Due to the higher momentum of muons in the endcap and the higher particle flux in the endcap as compared to the barrel, a

higher-granularity and rate-tolerant technology is needed, relative to the RPC. The TGC are arranged into 12  $\phi$ -sectors in each endcap and mounted with two layers on the inside of the middle layer of MDT at  $z = 14$  m, and one layer on the outside of this layer for a total of 7 gas gaps. Additionally, one layer of TGC is installed on the inner layer of endcap MDT at  $z = 7.4$  m, but this layer does not provide trigger capabilities.

A TGC chamber is a multi-wire proportional chamber that extends radially from the beamline. Inside each chamber, a series of 50  $\mu\text{m}$  anode wires with pitch 1.8 mm is placed between two graphite cathodes with a gap of 2.8 mm that is filled with an n-pentane (45%) and CO<sub>2</sub> (55%) gas mixture. One side of the cathode is segmented into strips for readout. Each chamber consists of two or three gas gaps, yielding two or three wire hits and two strip measurements per muon. A schematic of the TGC gaps is shown in Figure 4.15.

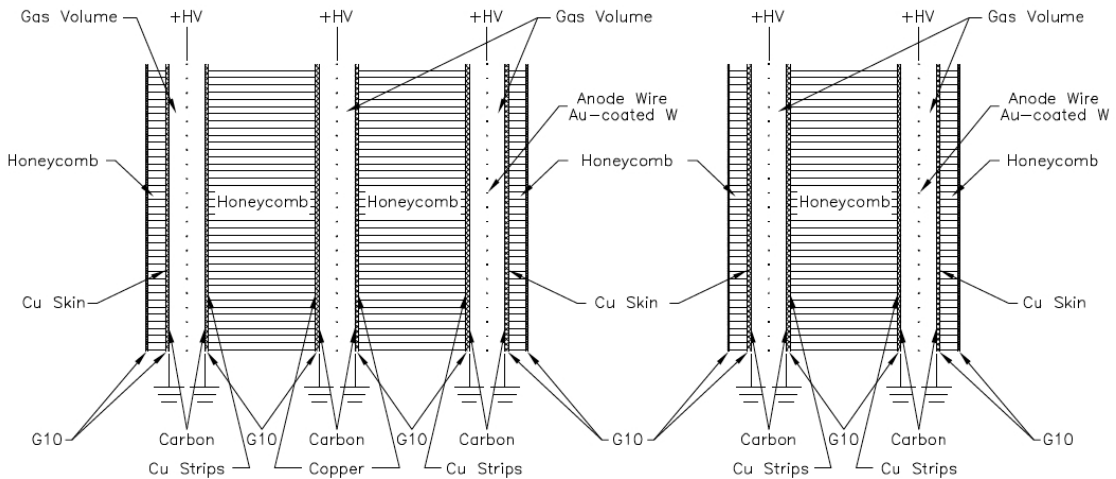


Figure 4.15: A schematic of TGC chambers, a TGC triplet (left) and doublet (right) [31].

The TGC are oriented such that the wires run in the  $\phi$  direction to measure  $\eta$  and the strips run in  $R$  to measure  $\phi$ . Although the TGC have worse spatial resolution than the MDT (2-6 mm in  $\eta$  and 3-7 mm in  $\phi$ , the small gap distance allows for an excellent timing resolution of 4 ns. This narrow timing resolution and fast response time allow the TGC to trigger in this high-rate environment.

## **4.6 Forward Detectors for Luminosity Measurement**

The importance of the luminosity measurement and a discussion of the method of luminosity determination is discussed in Chapter 3. In ATLAS, there are four systems contributing to the measurement of the luminosity: the Minimum Bias Trigger Scintillator (MBTS), the Beam Conditions Monitor (BCM), the Luminosity measurement using a Cerenkov Integrating Detector (LUCID), and the Zero Degree Calorimeter (ZDC). For the LHC Run I data collected in 2011 and 2012, the primary measurements of the luminosity were made with the BCM and LUCID, which are discussed below. Further detail for the MBTS and the ZDC may be found in Reference [22].

LUCID [113] provides the primary luminosity measurement for ATLAS. The measurement produced by LUCID is a flux of charged particles. LUCID detectors are located at  $\pm z = 17$  m and consist of 1.5 m long, 15 mm diameter aluminum tubes filled with  $C_4F_{10}$  gas. Upon the passage of particles through the gas, Cerenkov light is emitted and then reflected to the end of the tube, where it is read out through photo-multiplier tubes. The threshold for production of Cerenkov light in the gas is

2.7 GeV for pions and 9 MeV for electrons. By measuring the hit rate in the tubes, the luminosity can be calculated following the discussion in Chapter 3.

The BCM [72] provides a secondary luminosity measurement for ATLAS. Furthermore, it is capable of sending an abort signal to the LHC in the event that a beam begins to impact on a collimator, which may send a damaging rate of radiation into ATLAS. The BCM consists of two sets of detectors located at  $\pm z = 183.8$  cm and  $R = 55$  mm, just 20 mm farther than the edge of the beampipe. Each set of detectors consists of four diamond sensors, each  $1\text{ cm}^2$ , arranged in a vertical and a horizontal pair. A hit signal is produced through ionization as charged particles pass through the diamond layer, creating electron-hole pairs. The signal has a rise time of  $\sim 1$  ns, a width of  $\sim 3$  ns, and a baseline return time of  $\sim 10$  ns, so that pileup due to LHC collisions every 25 ns will not cause out-of-time pileup in the BCM. Thus, the BCM is capable of measuring the charged particle flux and therefore the luminosity.

## 4.7 Trigger and Data Acquisition

The ATLAS Trigger and Data Acquisition system (TDAQ) [32] is responsible for determining which events are considered valuable for further investigation, and for reading out the detector elements to store the event information for analysis. The acceptance of events for recording is performed in three levels of increasing complexity. The Level-1 Trigger, (L1), is hardware-based and uses custom electronics to provide a reconstruction algorithm that is much faster than the nominal physics object reconstruction discussed in Chapter 5, but has reduced granularity. The L1 trigger

is composed of the L1 Muon trigger for creating muon trigger objects, and the L1 Calo trigger, which creates trigger objects for  $\tau$  leptons, jets, photons, electrons, and  $E_T^{Miss}$ . In order to produce a trigger decision and read out the detector elements fast enough to avoid significant dead time, the L1 decision must be made within a  $2.5 \mu\text{s}$  window. The designed output rate of the L1 trigger is  $\sim 100 \text{ kHz}$ .

If an event is determined to have passed the L1 criteria, additional information about the event is read out via detector-specific read-out drivers (ROD) and analyzed with another set of simplified reconstruction algorithms called Level-2 (L2). For the L2 trigger, the decision window is limited to 40 ms and the designed output rate is 4 kHz. Once an event has passed the L2 criteria, the full detector information is taken from all RODs and the events are fully reconstructed in the third and final stage of the trigger process, called the Event Filter.

For the measurement presented in Chapter 7, the two key L1 triggers are the L1 Muon trigger for muons and the L1 Calo trigger for electrons. Additionally, a combination of other search channels presented in Chapter 11 utilizes an  $E_T^{Miss}$  trigger, also described below.

### 4.7.1 L1 Muon Trigger

The L1 Muon Trigger analyzes hit patterns in the fast RPC and TGC detectors and tests hypotheses for different  $p_T$  criteria by comparing the hit patterns to on-chamber *look-up tables*, after which a successful look-up will generate a L1-Accept. When a hit is generated in the *pivot plane* (the second layer of RPC or third layer of TGC) a straight line is calculated between the location of the hit and the interaction point.

This line defines a trigger *road*, and coincidences of hits in 3 of the 4 RPC planes in the barrel or 3 of the 4 planes of the TGC doublets in the last two TGC layers. If this coincidence requirement is passed, a straight-line fit is performed for these points and the slope of the line is compared to the slope of the line between the interaction point and the hit in the pivot plane. The look-up tables then define windows that relate the slope differences between these lines to different  $p_T$  windows. For example, a lower  $p_T$  muon will bend more in the magnetic field, giving larger slope differences, while a higher  $p_T$  muon will produce smaller differences between the slopes of the fits because it bends less. If the 3/4 coincidence is passed for the pivot and next-innermost layer of trigger chambers, the trigger algorithm also searches for hits in the other layer of TGC and RPC to test for higher  $p_T$  muons. In total, six thresholds exist yielding three low- $p_T$  triggers and three high- $p_T$  triggers. The definition of trigger roads and an indication of the differences between low- and high- $p_T$  trajectories is shown in Figure 4.16.

### 4.7.2 L1 Calo Trigger

The L1 Calo Trigger produces trigger signals for electrons, photons, jets,  $\tau$ -leptons, and  $E_T^{Miss}$  objects. This section will discuss the electron and  $E_T^{Miss}$  triggers. For the purposes of triggering, the calorimeter cells are grouped into longitudinal towers of  $0.1\eta \times 0.1\phi$ , which implies 7000 trigger towers for the entire system. Analog calorimeter signals are read out into the service cavern where they are digitized and associated to  $E_T$  values through fast look-up tables. Then a Cluster Processor (CP) is used to identify electron and photon candidates and a Jet/Energy Processor (JEP) is used to

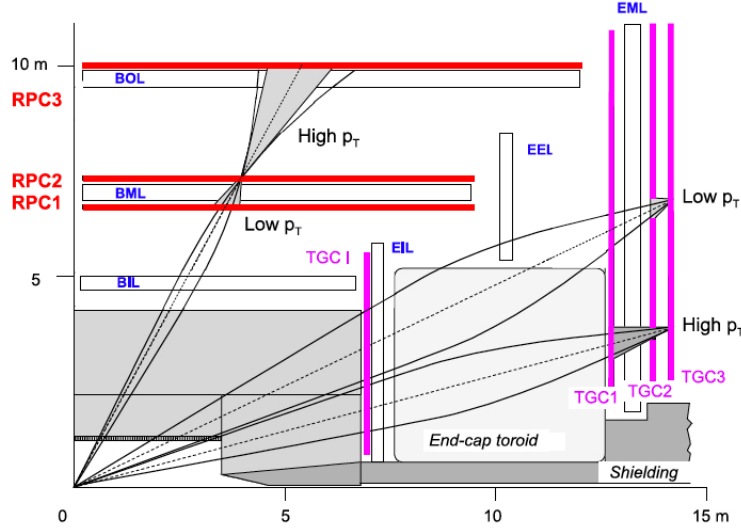


Figure 4.16: A diagram of the trigger logic for the L1 Muon Trigger [32].

calculate jet energies and  $E_T^{Miss}$ . The CP cannot distinguish electrons and photons at L1 because no tracking information is used. In order to define a trigger object, the CP algorithm searches in windows of  $4 \times 4$  trigger towers. For the central  $2 \times 2$  towers, the sum of the energy in the EM calorimeter in any of the four  $1 \times 2$  towers must pass a predefined threshold, and if it is successful, the 12 towers surrounding the  $2 \times 2$  towers are summed with the  $2 \times 2$  window to provide an estimate of the cluster's isolation. The local energy maximum in this window is defined as the L1 electron (or photon) candidate. A diagram of the  $2 \times 2 + 12$  trigger tower scheme is shown in Figure 4.17.

The JEP algorithm to identify  $E_T^{Miss}$  trigger objects sums the energy from EM calorimeter towers with equivalent windows of Hadronic Calorimeter towers to form sums of  $E_T$ ,  $E_x$  and  $E_y$ . A total of eight  $E_T^{Miss}$  trigger thresholds exist.

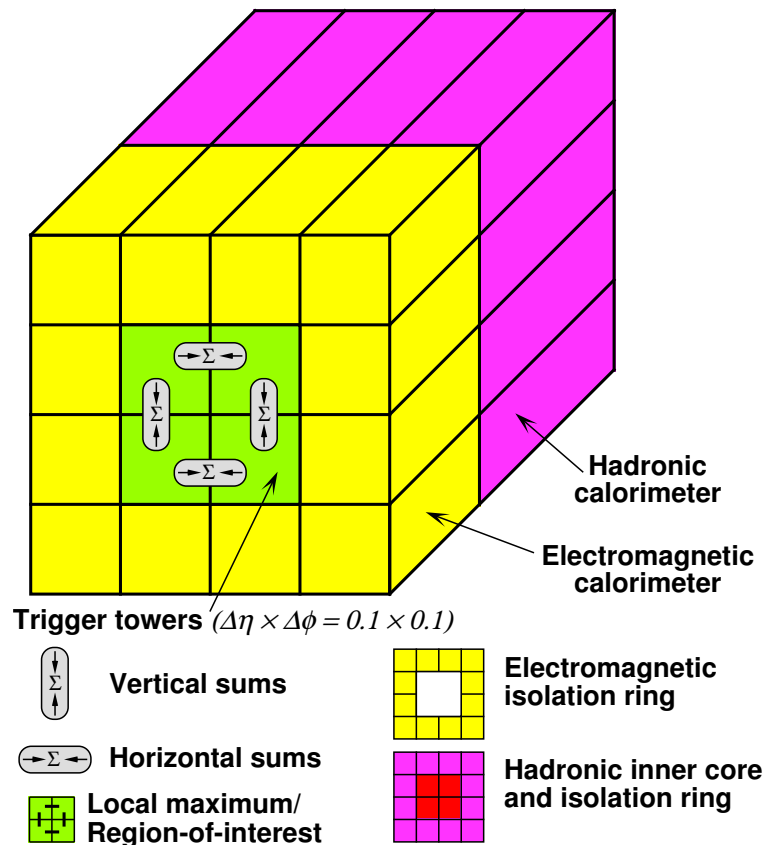


Figure 4.17: A diagram of the trigger logic for the L1 Calo Trigger Cluster Processor algorithm [32].

# Chapter 5

## Physics Object and Event Reconstruction in ATLAS

Electronic signals read out from the ATLAS detector are converted into physics *objects* used in physics analyses through a process called reconstruction. Reconstruction, more specifically, is the process of using software algorithms to determine a standard set of electrons, muons, jets, vertices, and missing energy ( $E_T^{\text{miss}}$ ) from the raw data. The same algorithms are run on both data and Monte Carlo simulation, which may reveal differences motivating corrections to the simulation. Such corrections and their systematic uncertainties are discussed in detail in Chapter 6. The  $ZH \rightarrow \ell^+ \ell^- b\bar{b}$  search is particularly challenging because the reconstructions of leptons, jets,  $b$ -jets, and  $E_T^{\text{miss}}$  are all required. This chapter provides a summary of the reconstruction algorithms for the objects essential to the measurement presented in this dissertation. Section 5.1 discusses Inner Detector track reconstruction and Section 5.2 discusses the reconstruction of primary vertices. Next, electrons are dis-

cussed in Section 5.3 followed by muons in Section 5.4. The reconstruction of jets is covered in Section 5.5,  $b$ -jet identification in Section 5.6, and finally  $E_T^{\text{miss}}$  is defined in Section 5.7.

## 5.1 Inner Detector Track Reconstruction

Tracks are reconstructed in the Inner Detector (ID). First, the components of the ID must generate space-points from hits, or from drift-circle measurements in the case of the TRT. Tracks are then built iteratively from these points. The ATLAS method for creating track objects from these space points consists of two algorithms, which are detailed in Reference [65]. The first algorithm is called *inside-out*. In the inside-out algorithm, track seeds are created by pairs of hits in two of the three layers of the Pixel Detector. From here, a Kalman Filter [75] is used to search for hits in the remaining pixel layer and the SCT. With the Kalman Filter, each space-point on the track is described by a state vector and a covariance matrix. At each point, energy loss and multiple scattering in material as well as magnetic field mismodeling must be considered, and possible locations for a hit in the next (increasing  $R$ -distance) active detector layer are predicted. The algorithm then searches in this region for hits and if a new hit is found, a new state vector and covariance matrix are calculated and the procedure is repeated to make a prediction for the next layer. In the case that a layer fails to produce a hit, the algorithm will continue to search farther out for hits in order to cover the possibility that a detector layer failed to register a hit, although the particle did indeed traverse it. Such lost hits are called *holes*. Kalman Filtering is mathematically equivalent to a minimization of a  $\chi^2$  fitting that accounts for energy

loss of the charged particle and the inhomogeneity of the magnetic field. As such, at each point of the track reconstruction the  $\chi^2$  is computed, and hits which significantly degrade the  $\chi^2$  of the fit are removed and the state vector and covariance matrix are recalculated.

Before the track is extrapolated into the SCT, ambiguities in which a hit may correspond to more than one track are removed. A procedure to remove such ambiguities is to introduce a *track score* to characterize the quality of the track, in addition to its  $\chi^2$ . The track score will penalize a track with holes and favor tracks with overlapping hits on different technologies, or multiple hits in the adjacent layers of the same technology. Hits that are shared between more than one track are then assigned to the track with the higher track score. Once a hit has been removed from a track, the track is refit and considered for further analysis. Additionally, a set of quality cuts is made and any tracks failing these requirements will be neglected when the algorithm proceeds to add TRT hits. With the introduction of TRT hits, a track may either be re-fit, including the TRT hits, or if the silicon-only track fit is better than the combined fit, the TRT tracks may be considered outliers and dropped for that track, reducing its track score.

The second algorithm for track reconstruction is called the *outside-in* algorithm. This algorithm is an essential complement to the inside-out algorithm because some long-lived particles such as kaons may not leave hits in the Pixel Detector, and electrons may convert to photons and this leave *holes* in the silicon detectors. These circumstances may cause a track seed to not be formed when there was indeed a

particle present. Additionally, bremmstrahlung in the detector material may cause a change in trajectory that prevents TRT hits from being added to a track constructed with the inside-out algorithm. To address these issues, the outside-in algorithm creates seeds from TRT hits.

First, a *segment-finding* algorithm is run, which takes TRT hit information and transforms it to the parameters of straight tracks via a Hough transform [71]. In the barrel region, this implies taking TRT hits in  $R$ - $\phi$  space and transforming them to  $\phi_0 - 1/p_T$  space, in which  $\phi_0$  is the initial direction of the track in  $\phi$  at the innermost radius of the TRT and  $p_T$  its transverse momentum. These segments are then used as track seeds for a Kalman filter that searches backward into the silicon detectors to add hits to the track.

## 5.2 Primary Vertex Reconstruction

Vertex reconstruction in ATLAS is performed in an iterative procedure called *adaptive vertex finding* [76]. Once tracks are reconstructed, those tracks with  $p_T > 400$  MeV that are consistent with the interaction region, according to  $d_0$  and  $z_0$  are selected. Among these tracks, the seed for Primary Vertex reconstruction is chosen as the  $z$  value that corresponds to the global maximum in the distribution of  $z_0$  values for all of the tracks in the event, and  $x = y = 0$ . Additional tracks are associated to the seed vertex by the fitter and the covariance matrix is updated until no tracks within  $7\sigma$  of the  $z$ -value of the seed are left. Then, a new seed is selected and the fit is repeated until all tracks are associated to a vertex or until no additional vertices

may be formed. The primary vertex in an event is defined as the vertex which has the maximum value for the sum of the squared transverse momentum of the tracks associated to that vertex,  $\Sigma p_T^2$ . Further details of vertex reconstruction may be found in Reference [27].

### 5.3 Electron Reconstruction

Electrons in ATLAS are reconstructed using information from both the ID and the Electromagnetic Calorimeter. References [42, 110] describe electron reconstruction in detail, while this section provides a summary of the critical features. In ATLAS, electron reconstruction has two steps: *cluster reconstruction* and *electron identification*. In cluster reconstruction, a candidate electron object is created from clusters in the EM calorimeter that are matched to reconstructed tracks from the ID. Once this candidate object is constructed, the electron identification step applies quality criteria to efficiently select true electrons and reject background from jets and photons. A baseline energy calibration is then performed using information from test-beam data. Then, a residual energy calibration is performed using  $Z \rightarrow ee$  events.

Cluster reconstruction is performed across the EM calorimeter coverage. The total energy measured by all three layers of the EM calorimeter is summed for a  $3 (\eta) \times 5 (\phi)$  window, called a *tower*, of calorimeter cells. Each tower has dimensions  $0.025 \times 0.025$  in  $\eta \times \phi$ . The algorithm, called a *sliding window* [114], searches over all  $3 \times 5$  windows in the EM calorimeter for a tower that is a local maximum and also has total energy of at least 2.5 GeV. Once such a tower has been found, it is considered a seed for

electron reconstruction. In Monte Carlo simulation of electrons from  $W$  and  $Z$  boson decays, this algorithm is 99% efficient in the creation of a seed for a 15 GeV electron. Where tracking is possible,  $|\eta| < 2.5$ , the position of the seed in  $\eta$  and  $\phi$  is matched to a track within 0.05 in both  $\Delta\eta$  and  $\Delta\phi$ , with additional allowance of  $\Delta\phi < 0.05$  in the bending direction to account for bremmstrahlung-induced direction changes. Next, the electron cluster is rebuilt from windows of  $3 \times 7$  towers in the barrel region and  $5 \times 5$  towers in the endcap region, and the cluster's total energy is calculated from four contributions:

- The estimated energy deposit in the material in front of the EM calorimeter
- The measured energy deposit, summed over all towers in the cluster
- The estimated external energy deposit outside the cluster
- The estimated external energy deposit beyond the EM calorimeter

The parameters which are estimated are calculated using a simulation of the energy depositions in both the active and inactive material in the pre-sampler and the other three layers of the EM calorimeter.

Once a cluster's energy is determined, the reconstruction step is over and the identification step must be implemented to reject photons and jets. In 2011 data-taking, electron identification involved a set of quality cuts that defined three categories with different levels of purity called *loose++*, *medium++*, and *tight++*. Several calorimeter and tracking variables that describe the shower shape and track characteristics are used for this categorization. The variables and thresholds used to define these

categories are discussed in detail in References [42], and not covered here. Instead, the focus is on a likelihood ratio technique first used for 2012 analyses called the electron likelihood tool [83]. The electron likelihood tool takes each input variable and creates a probability distribution function (PDF) for an electron hypothesis and for a background (photons, jets) hypothesis. By taking the product of these PDFs, a likelihood is created for each hypothesis:

$$\mathcal{L}_s(\vec{x}) = \prod_{i=1}^n P_{s,i}(x_i) \quad (5.1)$$

Then a discriminant is constructed to determine electron-like candidates from background-like candidates:

$$\delta\mathcal{L} = \frac{L_s}{L_s + L_b} \quad (5.2)$$

Electron detection efficiencies for identifying real and fake electrons are shown in Table 5.1 for a variety of the likelihood tool working points.

Menu	$20 < E_T < 50 \text{ GeV}$	
	Data Efficiency $Z \rightarrow ee$	Data Efficiency Background
VeryLooseLH	$97.77 \pm 0.14$	$3.028 \pm 0.019$
VeryLoose LH	$92.82 \pm 0.18$	$0.963 \pm 0.011$
Loose LH	$87.79 \pm 0.25$	$0.535 \pm 0.008$
Medium LH	$84.15 \pm 0.27$	$0.396 \pm 0.007$
Tight LH		

Table 5.1: Signal and background efficiencies for likelihood (LH) electron identification menus. The efficiencies shown are an average over all  $\eta$  and over electron  $20 < E_T < 50 \text{ GeV}$  [83].

## 5.4 Muon Reconstruction

The reconstruction of muons in the ATLAS detector may utilize combinations of the ID, the calorimeters, and the Muon Spectrometer (MS). For muons in the region  $|\eta| < 2.7$ , the MS is capable of providing an independent reconstruction of the muon. This is called a *Stand-Alone Muon*. Within the ID coverage,  $|\eta| < 2.5$ , an independent ID measurement exists. This object may be considered a muon candidate if it can be matched to a specific energy deposition in the calorimeters and is then called a *Calo Muon*. Additionally, the ID track could be matched to a segment of a track in the MS, called a *Segment-Tagged Muon*. Finally, a fit can be performed that combines a Stand-Alone muon and an inner detector track. This type of combination yields what is called a *Combined Muon*, a category which has the highest rejection power for fake muons as well as the best momentum resolution.

Several reconstruction algorithms exist to produce statistical combinations of tracking and energy-deposit information from these detectors. The algorithm used for reconstructing the muons used in this dissertation is called MuIDCombined and is discussed below, while information on other algorithms may be found in References [86, 98]. For the reconstruction of the MS track, which is an input to the MuIDCombined algorithm, the reconstruction algorithm is called MOORE. The MOORE algorithm [8] takes hits in the MDT,TGC,CSC, and RPC and builds a segment of a track in the non-bending ( $x$ - $y$ ) plane by looking for local maxima in this plane. A muon should leave many hits along the same  $\phi$  value since the torodial field does not bend in this direction. Next, a straight line is fit to the hits near the locally (in each

chamber near the  $\phi$ -section for each technology) to produce a *segment* in the bending plane ( $R$ - $z$ ). Finally, a fit is performed to all the hits lying on these segments. The fit returns the standard tracking parameters of  $(a_0, d_0, \phi, \cot\theta, q/p_T)$ . If a particular hit contributes to the  $\chi^2$  above a certain quality constraint, the hit is removed and the track is fitted again. This is a fully-described track using only the Muon Spectrometer, and the muon's parameters are expressed as calculated for the entrance point to the Muon Spectrometer.

The extrapolation of the track to the interaction point and the combination with an ID track is performed by the MuID algorithm. The first step of the MuID algorithm is to propagate the MOORE MS track back through the calorimeter material and solenoidal field to obtain an expression of the track parameters similar to those produced by an ID track. At this point the analyzer has a set of parameters for both the MS track and the ID track,  $P_{MS}$  and  $P_{ID}$ , as well as their covariance matrices  $C_{MS}$  and  $C_{ID}$ . The combined track parameters are obtained by solving for  $P$  in:

$$(C_{MS}^{-1} + C_{ID}^{-1}) \times P = C_{MS}^{-1} \times P_{MS} + C_{ID}^{-1} \times P_{ID} \quad (5.3)$$

And a  $\chi^2$  is calculated:

$$\chi^2 = (P - P_{MS})^T \times C_{MS}^{-1} \times (P - P_{MS}) + (P - P_{ID})^T \times C_{ID}^{-1} \times (P - P_{ID}) \quad (5.4)$$

For matches with a  $\chi^2$  above 0.001 a fit is performed which combines all of the ID and MS hits to create a track called a MuIDCombined track. No combined fit is performed otherwise, but in that case, the ID and MS-only tracks may still be used

in analyses.

## 5.5 Jet Reconstruction

The reconstruction of hadrons as jets is crucial for the analysis presented in this dissertation because the Higgs candidate decays to a pair of  $b$ -quarks, which hadronize and form jets. This section summarizes jet reconstruction as applicable to this analysis and leaves further discussion to Reference [32]. In ATLAS, jet reconstruction begins from topological clusters (or *topoclusters*) [114]. These clusters are three-dimensional groupings of cells in the calorimeters. A seed for creating such a cluster is chosen from the list of calorimeter cells with non-zero energy. The energy of each cell,  $E_{cell}$ , is calibrated to the electromagnetic scale using response information obtained from test-beam results of electrons and photons. The seed must have an energy that exceeds the root-mean-squared value of the expected noise in a calorimeter cell, which is measured in events with a random trigger, by a factor of four:  $E_{cell,seed}/\sigma_{noise} > 4$ . Once a seed is chosen, all cells that are directly neighboring the seed are included as a part of the cluster if  $E_{cell,neighbor}/\sigma_{noise} > 2$ , and the growth continues until all connecting cells surpassing that cell have been added. A final three-dimensional layer of nearest neighbors is added to the topological cluster, regardless of energy. A diagram of this scheme is shown in Figure 5.1.

These topological clusters are then considered as inputs to jet clustering algorithms, and their mass is taken to be zero. This analysis reconstructs jets with the anti- $k_t$  algorithm [57]. In the anti- $k_t$  algorithm, a distance parameter is defined be-

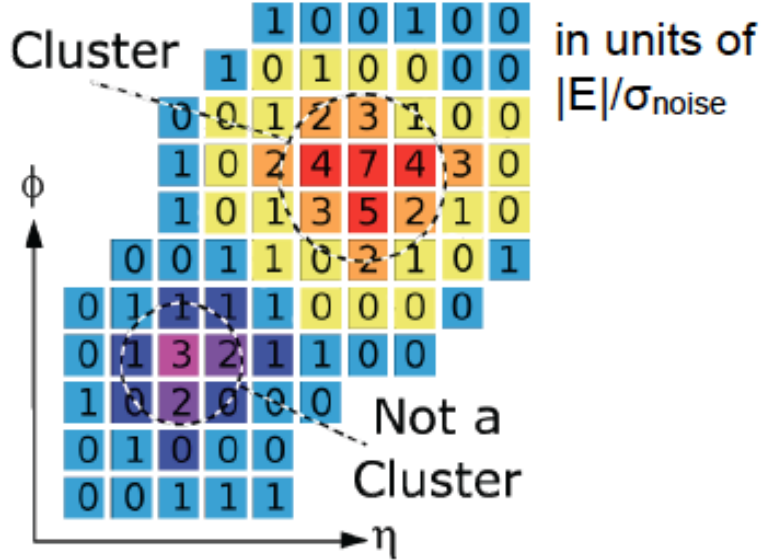


Figure 5.1: A drawing of several calorimeter cells demonstrating the creation of topoclusters from neighboring cells given the cell energy as a function of the noise threshold [73].

tween any two clusters:

$$d_{i,j} = \min(p_{T,i}^{-2}, p_{T,j}^{-2}) \frac{\Delta R_{i,j}^2}{R^2} \quad (5.5)$$

This algorithm iterates over each cluster,  $i$ , and attempts to merge it with each of the remaining clusters,  $j$ . The clusters are ordered by largest-to-smallest  $p_T$ . As long as  $d_{i,j}$  is smaller than  $d_i = p_{T,i}^{-2}$ , the cluster with the smallest  $d_{i,j}$  is merged with cluster  $i$ . Once two clusters are merged, the two original clusters are removed from the list of clusters and replaced with the new, combined, cluster. A jet is formed from the cluster  $i$  once no remaining clusters  $j$  can satisfy the  $d_{i,j}$  requirement. The algorithm then proceeds to reconstruct other jets from the next cluster with highest- $p_T$ .

The anti- $k_t$  algorithm is chosen because of specific experimental and theoretical advantages. From the theoretical perspective, it is insensitive to two non-perturbative effects: *soft radiation* and *collinear emission* [57]. Resiliency to soft radiation aids some theoretical calculations and also simplifies the calibration of the energy scale of jets. From the experimental perspective, this is equivalent to not allowing low-energy clusters to influence the properties of the jet, such as its shape, energy, and direction. Insensitivity to collinear emissions refers to the algorithm's ability to reconstruct a single jet from the same energy and constituents if the highest- $p_T$  particle changes after radiation, which in a collinear-unsafe algorithm may produce two nearby jets of smaller  $p_T$ .

### 5.5.1 Global Sequential Calibration

The jets used in this analysis are reconstructed using the anti- $k_t$  algorithm with a radius parameter of  $R = 0.4$ . The calorimeter is initially calibrated to the electromagnetic scale (EM scale), which means the reconstructed energy for a given calorimeter signal is correct if the particle were a photon or electron. Because different particles produce a different response in the calorimeter, hadronic jets must be calibrated to reach the correct energy scale. In ATLAS, calibration of the jets to the correct energy scale follows a calibration procedure called EM+JES [33]. With this scheme, jets receive a Monte Carlo-based  $\eta$ - and  $p_T$ -dependent correction to bring the jet from the EM scale to the hadronic scale. Additionally, a correction accounts for the presence of pileup by subtracting the expected amount of energy in a jet due to additional pileup interactions [24, 91].

To further improve the calibration of jets, an additional calibration scheme is applied, called the Global Sequential Calibration [67]. With this scheme, the jet’s  $p_T$  resolution is incrementally improved and the dependence of the jet’s response:

$$R = \langle p_T^{\text{reconstructed}} / p_T^{\text{true}} \rangle \quad (5.6)$$

on a number of different variables is reduced. The general strategy is to determine a jet property of interest,  $x$ , and to derive a correction to the jet response as a function of that variable:

$$C(x, p_T) = R^{-1}(x, p_T) \quad (5.7)$$

A list of variables used to correct the jet response is shown in Table 5.2. The improvement of the  $p_T$ -resolution of jets when the GSC calibration is used in addition to the EM+JES calibration is shown in Figure 5.2 for a simulation sample produced with  $\sqrt{s} = 10$  TeV.

Furthermore, ability of the GSC to improve the resolution of an invariant mass constructed from two jets is of particular importance for the analysis presented in this thesis. This feature is discussed in more detail in Section 7.3.

## 5.6 Identification and Calibration of $b$ -jets

In this search, the jets from the Higgs decay are  $b$ -jets, and thus the high-efficiency identification of  $b$ -jets, as well as the rejection of non- $b$ -jets, is paramount to the success of the analysis. The definition, in Monte Carlo simulation, of a  $b$ -jet for the purposes of this analysis is any jet that has a *truth*  $B$ -hadron with  $p_T > 5$  GeV

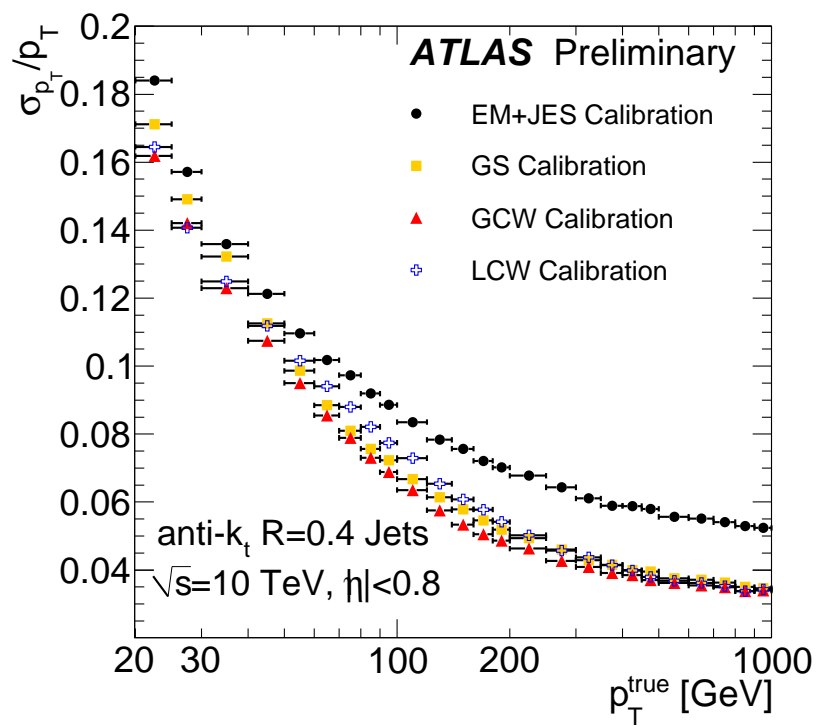


Figure 5.2: The relative resolution of jets as a function of  $p_T$  for several calibration methods. [23].

Jet Property	Order	Definition
$f_{\text{tile}0}$	1	fraction of energy deposited in the first layer of the Tile calorimeter
$f_{\text{em}3}$	2	fraction of energy deposited in the third layer of the EM calorimeter
$n_{\text{trk}}$	3	track multiplicity
$w_{trk}$	4	$p_T$ weighted average $\Delta R$ of tracks in the jet

Table 5.2: Ordered list of jet properties used in the GSC calibration.

within a radius  $\Delta R < 0.4$ . For the purposes of identification, the most important characteristic of a  $B$ -hadron is its relatively long lifetime,  $\sim 1.5$  ps. Converted to an average distance traveled before decay with  $\Delta d = c\gamma\Delta t$ , this implies that the hadron travels a macroscopic distance from the primary  $pp$ -collision vertex before it decays. For example, a 20 GeV  $B$ -hadron would travel 1.7 mm on average before decaying, while a 100 GeV  $B$ -hadron would travel 8.5 mm on average.

From the experimental perspective, then, a  $b$ -jet may be identified by reconstructing tracks that produce a vertex that is significantly displaced from the primary vertex. Such a vertex is called a *secondary vertex*.

Furthermore, given that the mass of the  $b$ -quark is 5 GeV,  $B$ -hadrons typically have heavier masses than others, and the resulting jets from their decay will have a greater angular spread due to this mass. In the ATLAS identification of  $b$ -jets, known as *b-tagging*, these two features are exploited through various algorithms. The algorithms pertinent to this analysis are described below, and further details are described in References [18, 77].

Two of the most important algorithms for  $b$ -tagging in this analysis are called *IP3D* and *JetFitter*. The IP3D algorithm uses a likelihood ratio technique to compare input values to predefined distributions from Monte Carlo simulation in order to define a  $b$ -jet hypothesis and a light jet hypothesis. The distributions are two-dimensional histograms of the transverse impact parameter significance and the longitudinal impact parameter significance ( $d_0/\sigma_{d_0}$  vs  $z_0/\sigma_{z_0}$ ) for all of the tracks in the jet. By creating two-dimensional histograms, correlations between the two variables are utilized. The one-dimensional histograms are shown in Figure 5.3 and compare 2011

data to Monte Carlo simulation, also showing the separation between light jets and  $b$ -jets.

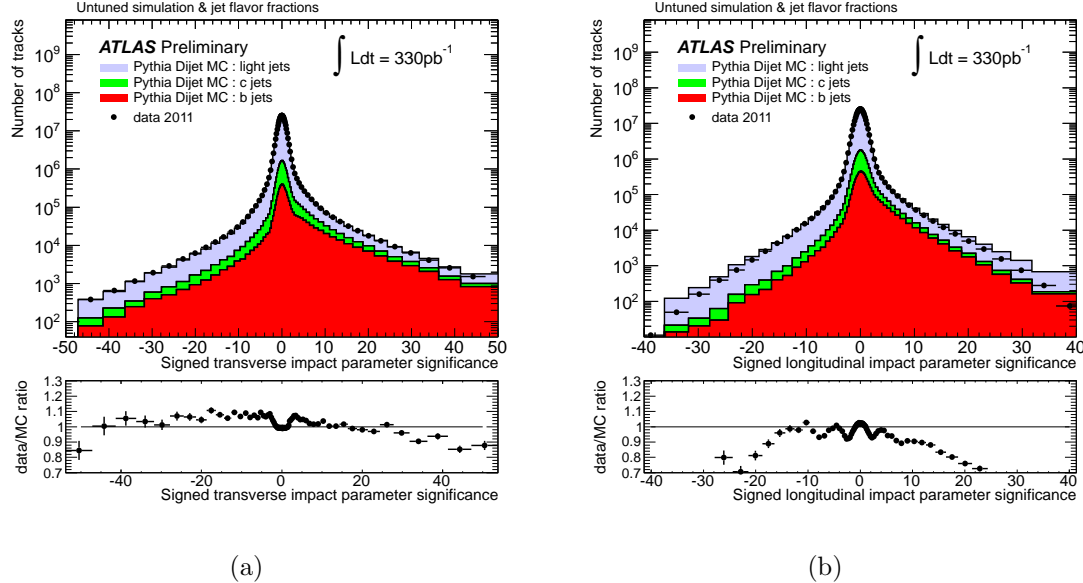


Figure 5.3: Histograms of the two input variables to the likelihood ratio analysis for the IP3D  $b$ -tagging algorithm. The negative impact parameters correspond to those tracks which are determined to cross the jet axis behind, rather in front of, the primary vertex. [18].

In the JetFitter algorithm, a *tertiary* vertex from the decay of a  $C$ -hadron to a strange hadron is the object of a search. It is assumed that the secondary vertex and tertiary vertex lie along the same flight path. Verifications of this assumption were performed in Monte Carlo simulation and, for example, a 60 GeV  $B$ -hadron was observed to have an average flight path of 4.3 mm and the daughter  $C$ -hadron had an average lifetime of 1.9 mm. The average longitudinal deviation from the original flight path of the  $B$ -hadron at the point of the tertiary vertex was found to be only 30  $\mu\text{m}$ . With this assumption validated, a Kalman filter is used to determine a single

flight path through the primary, secondary, and tertiary vertices, even if a given vertex has only one reconstructed track. Additionally, the algorithm does not require the tertiary vertex and will still identify a  $b$ -jet using only the fit to the primary and secondary vertices. The information collected through this flight-path determination and the location of the vertices along this path provides several variables which enter into a likelihood ratio technique. Some of these variables include:

- number of vertices with at least two tracks,
- total number of tracks at these vertices,
- number of additional single track vertices on the  $b$ -hadron flight axis,
- invariant mass of all charged particle tracks attached to the decay chain,
- fraction of energy of these particles divided by the sum of the energies of all charged particles matched to the jet,
- flight length significance,  $d/\sigma(d)$ , of the weighted average position divided by their errors of the displaced vertices.

The output of the JetFitter weight is shown in Figure 5.4 for a comparison between 2011 data and Monte Carlo simulation.

### 5.6.1 MV1 and MV1c $b$ -tagging Algorithms

In 2011, a more sophisticated algorithm was developed, called MV1, which utilizes a neural network to combine the results of the IP3D, JetFitter, and an additional tagger called SV1 that uses secondary vertex information. The result is a greater

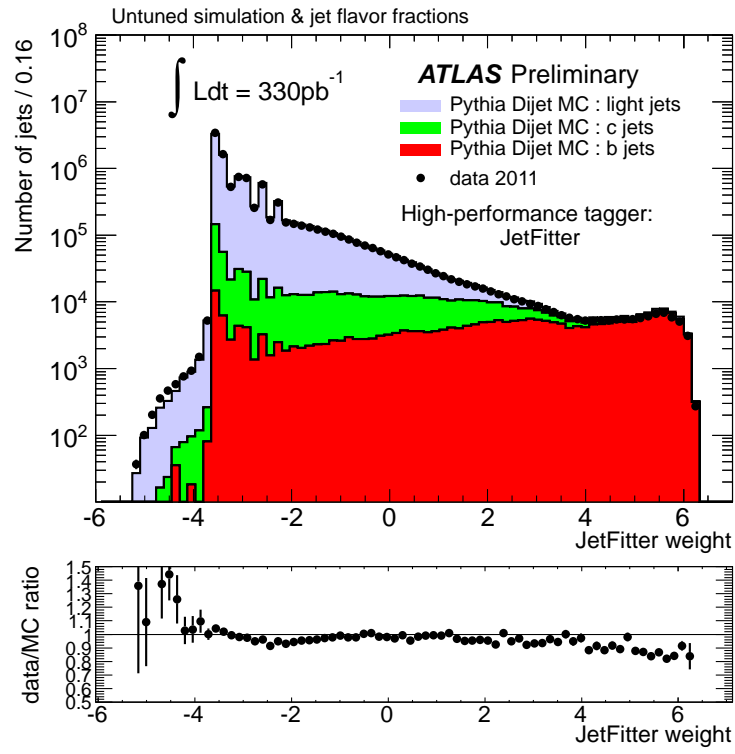


Figure 5.4: The output weight of the JetFitter  $b$ -tagging algorithm. Higher weights correspond to a greater likelihood of the candidate jet being a  $b$ -jet [18].

background rejection for a given  $b$ -tagging efficiency. A comparison of the rejection curves is shown in Figure 5.5. In this analysis, the rejection of  $c$ -jets is of particular importance, and a variation on the MV1 algorithm which has improved rejection for  $c$ -jets is used. This algorithm is called MV1c. A comparison of the two algorithms MV1 and MV1c is shown in Table 5.3.

In data, several calibration methods exist to determine the rejection power at given operating points of efficiency. Two common calibration methods are  $p_T^{rel}$ , which analyzes the kinematics of semileptonic  $b$ - and  $c$ -jets, *System8*, which produces a fully-constrained system of eight equations that are functions of the  $b$ -tagging efficiency and mistag efficiency on a variety of samples. Both are discussed in detail in Reference [26]. An additional calibration method is described in Reference [17] using dileptonic  $t\bar{t}$  decays coupled with a likelihood approach. Some differences in the observed tagging efficiencies for  $b$ -jets and jets of other flavors exist between data and Monte Carlo simulation. Corrections to the simulation are derived as functions of  $\eta$  and  $p_T$  and applied according to Section 6.2.3.

## 5.7 Missing Transverse Energy Reconstruction

Although the ATLAS detector has the interaction depth and radiation depth to absorb all electrons, photons, and jets, as well as the ability to precisely measure muons in the muon spectrometer, neutrinos completely escape direct detection. Despite this, the direction and energy of non-interacting particles such as neutrinos can be inferred from the other reconstructed objects by analyzing the energy and momentum in the plane transverse to the beam axis. This quantity is called missing

Name	w value	b-jet eff. (%)	$c\text{-jet RF}$ MV1c MV1	$\tau\text{-jet RF}$ MV1c MV1	$l\text{-jet RF}$ MV1c MV1
80 ‘Loose’ or ‘L’	0.4050	79.85	3.04 0.98	6.40 1.13	29.12 1.07
70 ‘Medium’ or ‘M’	0.7028	70.00	5.34 1.07	14.90 1.01	135.76 0.91
60	0.8353	59.99	10.45 1.31	33.92 1.35	453.53 0.70
50 ‘Tight’ or ‘T’	0.9237	49.99	26.22 1.9	120.33 2.6	1388.28 0.55

Table 5.3: The efficiencies for the available calibrated operating points for the MV1c algorithm and a comparison to the MV1 algorithm performance. These values have been determined in semileptonic  $t\bar{t}$  events with a jet  $p_T$  threshold of 20 GeV [15] RF stands for Rejection Factor which is the reciprocal of the efficiency.

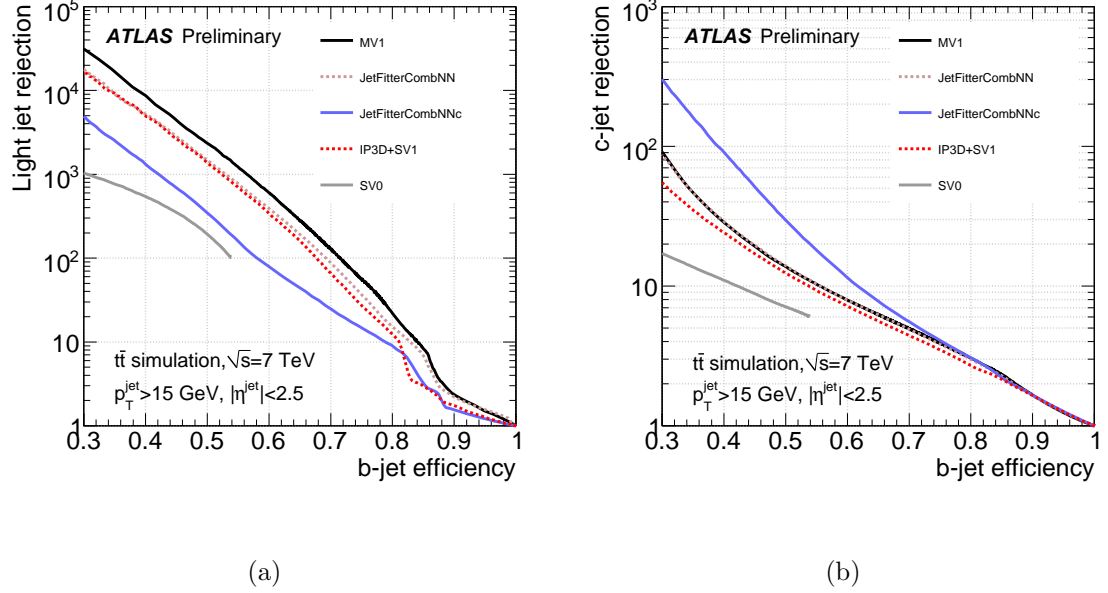


Figure 5.5: The rejection of light jets and charm jets as a function of  $b$ -tagging efficiency for a variety of tagging algorithms [26].

transverse energy ( $E_T^{Miss}$ ).  $E_T^{Miss}$ , because it depends on the reconstruction of all other objects in the event, may arise either from true non-interacting particles or from mismeasurements of the other objects. As such,  $E_T^{Miss}$  requires precise reconstruction and calibration of photons, electrons, muons, and jets. The definition of  $E_T^{Miss}$  is:

$$\vec{E}_T^{Miss} = - \sum_{electrons} E_T^e - \sum_{muons} p_T^\mu - \sum_{jets} p_T^{jet} - \sum_{soft} E_T \quad (5.8)$$

Which means that the vector  $E_T^{Miss}$  is constructed from the electron, muon, and jet reconstructed objects, and also from a sum of the other energy deposits in the calorimeter, which correspond to soft hadrons and other reconstructed calorimeter energy that is not already classified as one of the other objects. Further details on

the components of the  $\sum_{soft}$  term may be found in Reference [40].

# Chapter 6

## Data Samples and Monte Carlo Simulation

This chapter provides details on the data set used in this analysis, as well as the Monte Carlo simulation used to model the signal and background processes.

Section 6.1 discusses the set of data from the LHC analyzed for this study, while Section 6.2 summarizes the Monte Carlo generators used for event simulation. Important corrections to the Monte Carlo simulation are presented in Section 6.2.3. Further details on the modeling of simulation and background processes are left to Chapter 8.

### 6.1 Data Samples

The data used in this thesis correspond to the full integrated luminosity collected during data taking in 2011 and 2012. Events are only analyzed if they belong to a luminosity period that passes data quality requirements to ensure satisfactory func-

tioning of all detector components and the TDAQ. After passing these data quality requirements, events are said to belong to a *Good Run List* and are considered for further analysis. This analysis uses the following Good Run Lists for 2011 and 2012 data:

- For 2011  $\sqrt{s} = 7$  TeV: data11\_7TeV.periodAllYear\_DetStatus-v36-pro10-02\_CoolRunQuery-00-04-08\_All\_Good.xml
- For 2012  $\sqrt{s} = 8$  TeV: data12\_8TeV.periodAllYear\_DetStatus-v61-pro14-02\_DQDefects-00-01-00\_PHYS\_StandardGRL\_All\_Good.xml

After applying this requirement, the total integrated luminosity at  $\sqrt{s} = 8$  TeV is  $20.3 \text{ fb}^{-1}$  and the total integrated luminosity at  $\sqrt{s} = 7$  TeV is  $4.7 \text{ fb}^{-1}$ . A description of the luminosity measurement and its uncertainty may be found in Section 3.3. The data from the ATLAS detector were reconstructed using version 17.2 of ATHENA [13] and analyzed in the AOD format. The event triggers are discussed in Section 4.7 in general, and the specific triggers for this analysis are discussed in Section 7.4.2.

## 6.2 Monte Carlo Simulation

A variety of physics event generators are used to simulate the signal and background processes. Once the physical objects have been generated in Monte Carlo, they are passed through a GEANT4-based simulation of the ATLAS detector [4, 9]. A major constraint on the statistics of Monte Carlo simulation samples is the time taken to pass the events through the full simulation of the ATLAS detector. In order to decrease the simulation time and thus enable the generation of background samples

with higher numbers of events, many samples are instead generated using the ATLAS FastII simulation [104], which employs a simplified model of the ATLAS calorimeters. Extensive studies have been performed to validate the use of this simulation.

### 6.2.1 Signal Modeling

The signal processes of  $ZH \rightarrow \nu\bar{\nu}b\bar{b}$ ,  $WH \rightarrow \ell\nu b\bar{b}$ , and  $ZH \rightarrow \ell^+\ell^- b\bar{b}$ , where  $\ell = e, \mu, \tau$  are modeled using Monte Carlo-simulated events produced by the PYTHIA 8.165 [107] event generator configured with the AU2 tune [5], using the CTEQ6L1 PDF [102], interfaced to PHOTOS [81] for QED final-state radiation, and TAUOLA [115] for the simulation of  $\tau$  decays. The decay of  $V \rightarrow \tau\nu$  leptons is simulated to account for the small fraction of additional signal events selected due to leptonic  $\tau$  decays. Samples are generated in the Higgs boson mass range between 100 GeV and 150 GeV at intervals of 5 GeV. Detailed information on the cross sections and theoretical uncertainties of the signal processes is found in Section 8.1.

### 6.2.2 Background Modeling

The signature of the signal is characterized by two high- $p_T$   $b$ -tagged jets in association with zero, one or two leptons consistent with a  $W$ - or  $Z$ -boson signature. As such, the backgrounds to the  $ZH \rightarrow \nu\bar{\nu}b\bar{b}$ ,  $WH \rightarrow \ell\nu b\bar{b}$ , and  $ZH \rightarrow \ell^+\ell^- b\bar{b}$  processes include  $W$ +jets and  $Z$ +jets processes,  $t\bar{t}$ , single-top production, and diboson production ( $WW$ ,  $WZ$ ,  $ZZ$ ). Table 6.1 shows the different Monte Carlo generators for the most important background processes, along with their cross sections and total number of simulated events. An in-depth discussion of each background process

along with associated corrections and uncertainties on the modeling of the processes follows in Section 8.2.

Process	Generator	$\sigma \times BR$	$N_{\text{events}}$
Vector boson + jets			
$W \rightarrow \ell\nu$	SHERPA 1.4.1	12.07 nb	390M
$Z/\gamma^* \rightarrow \ell\ell$	SHERPA 1.4.1	66M	
$m_{\ell\ell} > 40$ GeV		1.24 nb	
$Z\gamma^* \rightarrow \nu\nu$	SHERPA 1.4.1	98M	
$m_{\nu\nu} > 5$ GeV		6.71 nb	
Top-quark			
$t\bar{t}$	PowHEG+PYTHIA	252.89 pb	100M
$t$ -channel	ACERMC+PYTHIA	87.76 pb	9M
$s$ -channel	PowHEG+PYTHIA	5.61 pb	6M
$Wt$ -channel	PowHEG+PYTHIA	22.37 pb	20M
Di-boson			
$WW$	PowHEG+PYTHIA8	52.44 pb	10M
$WZ$	PowHEG+PYTHIA8	15M	
$m_{\ell\ell} > 20$ GeV	one of the boson hadronically decaying	9.241 pb	
$ZZ$	PowHEG+PYTHIA8	15M	
$m_{\ell\ell} > 20$ GeV	one of the boson hadronically decaying	3.171 pb	

Table 6.1: Monte Carlo programs used for modeling the background processes, the cross sections times branching ratio (BR) used to normalize the different processes at  $\sqrt{s} = 8$  TeV, and the total number of generated events are shown.

### 6.2.3 Corrections for Reconstructed Objects

The above Monte Carlo generators cannot exactly reproduce the measurements of many observables in data. Corrections are derived by the combined performance groups of the ATLAS Collaboration, and these corrections are propagated to the Monte Carlo simulation used in this analysis. Most important for this analysis are corrections for the mismodeling of the efficiency to tag a jet as a  $b$ -jet. Additional corrections are made for the measurement of the trigger efficiencies, lepton reconstruction and identification efficiencies, and momentum and energy.

#### Vertex-Z Correction

The  $z$ -position of the primary vertex is not well-modeled by the Monte Carlo simulation. A correction is derived and applied to the generated position of the primary vertex in the Monte Carlo simulation such that the mean and standard deviation of the distribution of generated primary vertices matches that which is measured in data.

#### Trigger Efficiency Correction

In order to compare a measured number of events to a predicted cross section for a physical process, it is important that the trigger efficiency in data is well-modeled by the simulation. The trigger efficiencies are therefore measured, and residual mismodelings are corrected by weighting the Monte Carlo simulated events with a scale factor,  $SF_{trigger}$ , which corrects the simulated efficiencies to match those measured in data. For the 2-lepton analysis, single-lepton and di-lepton triggers are used.

For the case of these lepton triggers, the  $Z$  tag-and-probe technique is employed to measure the trigger efficiency. Details of the muon trigger studies are contained in Reference [12] and the electron studies are contained in Reference [19]. As an example of the scale factors for electron triggers, Figure 6.1 shows the ratio of data/MC for trigger efficiencies as a function of  $\eta$  for  $\sqrt{s} = 8$  TeV data.

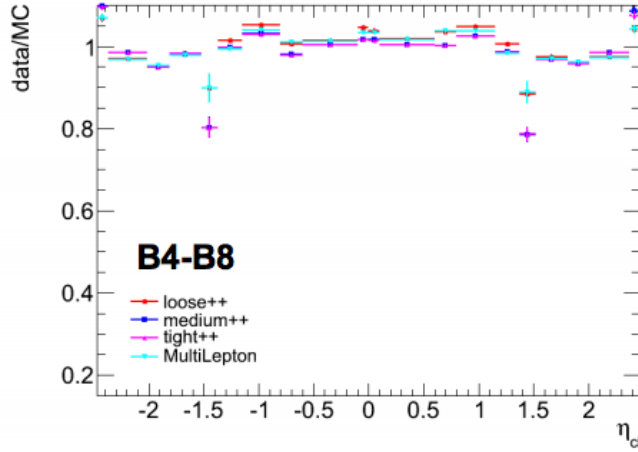


Figure 6.1: Scale factors for electron triggers as a function of  $\eta$ . The ratio of data/MC is applied to reweight the efficiency in Monte Carlo events to match the efficiency measured in data. [19].

## Muon Corrections

The Monte Carlo simulation is corrected for mismodeling of the identification and reconstruction efficiencies of muons, as well as for mismodeling of the muon momentum scale.

### Muon Reconstruction Efficiency Correction

A small discrepancy is observed between the efficiency to reconstruct MuID muons in Monte Carlo simulation and in data. The Monte Carlo simulation is corrected to

match the data. Using the tag-and-probe method with muonic decays of  $J/\Psi$  and  $Z$ -bosons, corrections are derived across a large range of  $p_T$ . In the tag-and-probe method, two oppositely-charged muons are selected such that the invariant mass is in a window of 10 GeV around the  $Z$ -boson mass. One of the muons is required to pass a desired reconstruction threshold (e.g. Combined Muon) and to have triggered the readout of the event. This muon is called the “tag” muon. The other is subject to less stringent reconstruction requirements (e.g. a Muon Spectrometer-only track) and called the “probe” muon. Next, the algorithm searches for a match between the probe muon and the reconstructed muons of the same reconstruction threshold as the tag muon. The measured efficiency is then defined as the number of successful matches over the total number of probe muons. Further details are found in Reference [28]. Figure 6.2 shows the reconstruction efficiency as a function of  $\eta$  for MuID muons of different reconstruction quality thresholds. The correction, called a *Scale Factor*, is shown at the bottom of the figure, as the ratio data/MC. This correction is applied as an  $\eta$ -dependent weight to the event in Monte Carlo simulation such that the data/MC ratio of efficiencies becomes 1. As an example of the improvement after the correction, Figure 6.3 displays the di-muon invariant mass in a window around the  $Z$ -boson mass both before and after the muon reconstruction efficiency weights are applied to the candidate events. Agreement between the simulation and the data is improved.

### **Muon Momentum Resolution and Scale Correction**

The scale and resolution of muon momentum measurements can be affected by several factors, including the uncertainty of the thickness of dead material traversed by the muon, mis-alignment and mis-calibration of the chambers, and imprecise knowl-

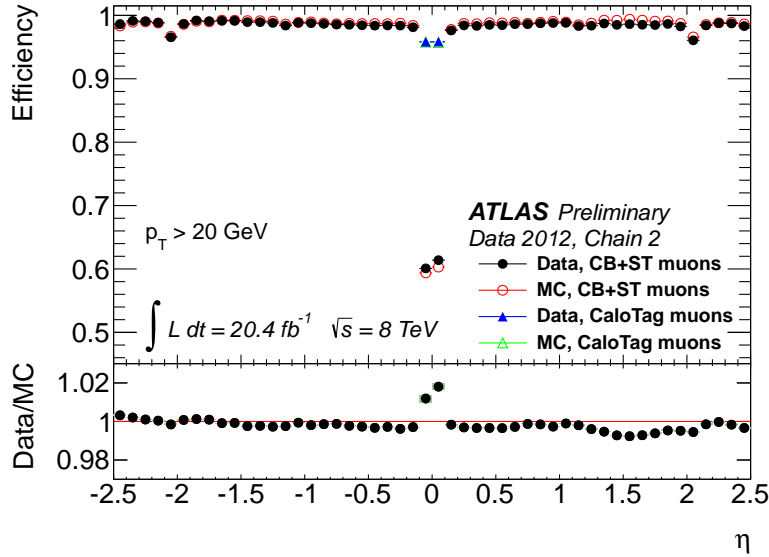


Figure 6.2: The reconstruction efficiency for Combined, Segment-Tagged, and Calo Muons. The bottom panel shows the ratio between measured and simulated efficiencies, which is used to weight events as a correction [28].

edge of the magnetic field. To correct possible mismodeling of the muon momentum scale and resolution, measurements are made of muonic decays of  $J/\Psi$  and  $Z$  bosons, using the line shape as a constraint. Information about the muon momentum resolution and scale can be obtained from the line shape's width and mean, respectively. In order to correct the muons' momenta, the Monte Carlo simulation's muons are smeared and scaled while being compared to the data using a maximum likelihood technique. The Monte Carlo parameters are adjusted until the likelihood is maximized. The procedure is repeated across 16  $\eta$  regions, and also separately for the different components of a track (Muon Spectrometer track, Inner Detector track, Combined track). Details of the analysis are left to Reference [28] and the resulting scale and resolution corrections are summarized below.

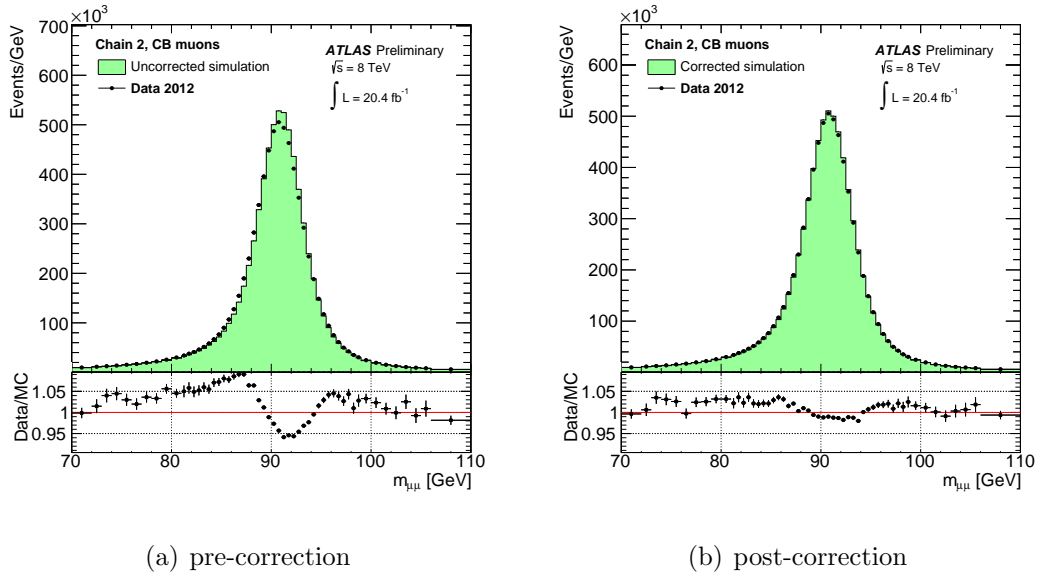


Figure 6.3: Di-muon invariant mass before and after the application of the correction for mis-modeling of the muon reconstruction efficiency [28].

The momentum scale and resolution of a muon can be corrected via:

$$p_T^{Cor,det} \rightarrow p_T^{det} \times s^{det}(\eta) \times (1 + \Delta(det)) \quad (6.1)$$

where  $\Delta(\det)$  is given by:

$$\Delta(det) = (1 + \Delta a^{det}(\eta)G(0,1) + \Delta b^{det}(\eta)G(0,1)p_T^{MC,det}) \quad (6.2)$$

Here,  $s^{det}$  is a correction to the momentum scale, and  $\Delta a(\eta)$  and  $\Delta b(\eta)$  are corrections to the constant and momentum-dependent terms of the resolution.  $G(0, 1)$  represents a normally distributed random variable with mean zero and standard deviation of 1. This correction is made independently to the Muon Spectrometer and Inner Detector momentum measurements. The correction to the Combined Muon is calculated as the average of the Muon Spectrometer and Inner Detector corrections, weighted by the inverse square of their resolutions.

Figure 6.4 shows the  $\Delta a^{MS}$  term of the correction. The  $\Delta b^{MS}$  and  $\Delta a^{ID}$  terms are determined to be small, and are negligible for this analysis. Figure 6.5 shows the momentum scale corrections for MuID Muon Spectrometer muons.

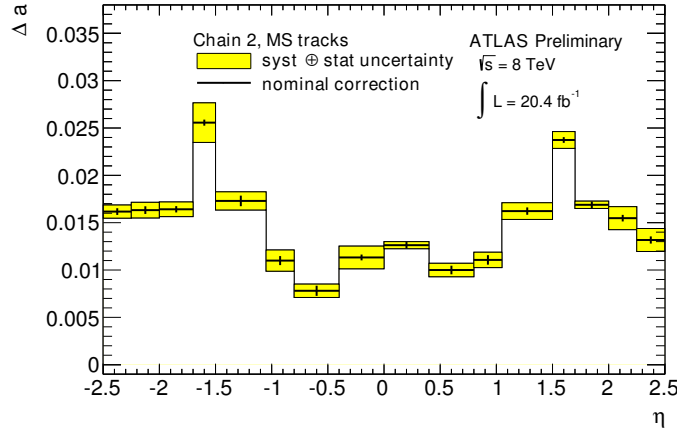


Figure 6.4: Corrections to the muon momentum resolution:  $\Delta a^{MS}$  [28].

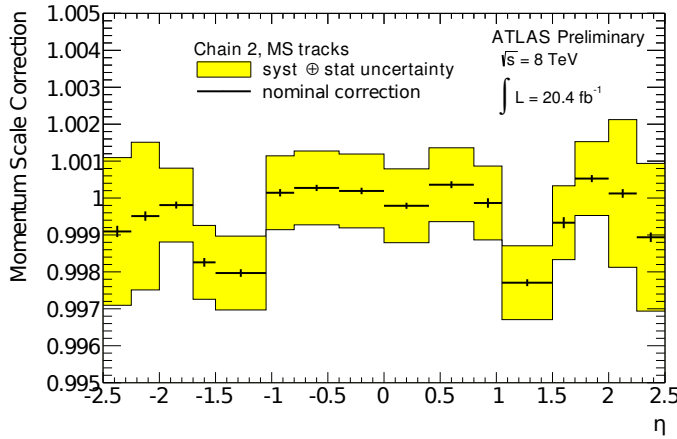


Figure 6.5: Corrections to the muon momentum scale for Muon Spectrometer track measurements [28].

## Electron Corrections

As for muons, observables dependent on electron quantities are not perfectly modeled by the Monte Carlo simulation. To improve the modeling of electrons in the Monte Carlo simulation, corrections are derived for the electron reconstruction efficiency, the electron identification efficiency, and the electron energy scale and resolution.

### Electron Identification and Reconstruction Efficiency Corrections

The electron reconstruction and identification efficiencies are also measured with a tag-and-probe method. This measurement is described in detail in Reference [20]. To study the electron reconstruction efficiency, the probe is defined as a cluster of cells in the EM calorimeter with  $E_T > 15$  GeV and the tag is a cluster of EM cells matched to an Inner Detector track with at least 1 hit in the Pixel Detector and at least 7 total hits in the Pixel and SCT. The tag must also be matched to an electron trigger object. The electron reconstruction efficiencies for a variety of algorithms is shown in Figure 6.6 as a function of  $\eta$ . The discrepancy between data and simulation is corrected by applying the data/MC efficiency ratio as a weight to Monte Carlo events in the same method as for muons.

The electron identification efficiency is measured the same technique, but in this case the probe is also required to be matched to a track in the Inner Detector as is the case for the tag in the measurement of the reconstruction efficiency. The  $J/\Psi$  provides information for electrons at lower  $p_T$  ( $7 < p_T < 20$  GeV) and the  $Z$ -boson resonance provides information for higher energies ( $p_T > 15$  GeV). Measurements of

the electron identification efficiency are shown in Figure 6.7 as a function of  $p_T$  and  $\eta$  for various thresholds of the likelihood method of electron identification. The scale factor applied as a correction to Monte Carlo simulation is shown in the bottom panel of each figure as the data/MC ratio.

### Electron Energy Resolution and Scale Correction

The energy scale and resolution of high-energy electrons is measured through studies of the  $J/\Psi$  and  $Z$ -bosons as well. Full details are available in Reference [36] and the results are summarized here.

The  $e\bar{e}$ -invariant mass distributions are fit with a Breit-Wigner distribution, which characterizes the  $Z$ -boson line shape, that is convoluted with a Crystal Ball function. The standard deviation of the Crystal Ball component models the  $p_T$ -independent term of the electron resolution. In order to provide an  $\eta$ -dependent correction, the measurement of the invariant mass is repeated in many  $\eta$  regions. To access the energy scale, the location of the peak of the  $Z$ -mass is measured, and a likelihood method is employed. The electron energy scale is corrected by an  $\eta$ -dependent factor,  $\alpha_\eta$ :

$$E_T^{measured} \rightarrow E_T^{true} \times (1 + \alpha_\eta) \quad (6.3)$$

where  $\alpha_\eta$  is determined by minimizing the negative log of the likelihood:

$$-\ln \mathcal{L} = \sum_{i,j}^{N_{i,j}^{events}} \ln \mathcal{L}_{i,j} \left( \frac{m_{ij}}{1 + (\alpha_i + \alpha_j)/2} \right), \quad (6.4)$$

In Equation 6.4,  $i$  and  $j$  are the  $\eta$  regions for the electrons under study, and  $m_{ij}$  is the measured invariant mass of the pair.  $\mathcal{L}_{i,j}(m)$  is a probability distribution function quantifying the compatibility of the measured event with a simulated  $Z$ -boson event. This correction alters the electron energy by  $\sim 2\text{-}5\%$ , depending on the  $\eta$  region in question.

In order to correct the mismodeling of the resolution of di-electron invariant masses, the energy is smeared according to:

$$E^{cluster} \rightarrow E^{cluster} \times (1 + f(0, \sigma)) \quad (6.5)$$

where  $f(0, \sigma)$  is a Gaussian of mean zero and standard deviation  $\sigma$ , where  $\sigma$  is equivalent to the fractional quadratic difference between the total energy resolution measured in Monte Carlo simulation and the total energy resolution measured in data. The di-electron invariant mass after the energy scale correction is shown in Figure 6.8 for electrons with  $|\eta| < 2.47$ . The measured and simulated energy resolutions are shown in the figure as  $\sigma_{data}$  and  $\sigma_{MC}$ , respectively.

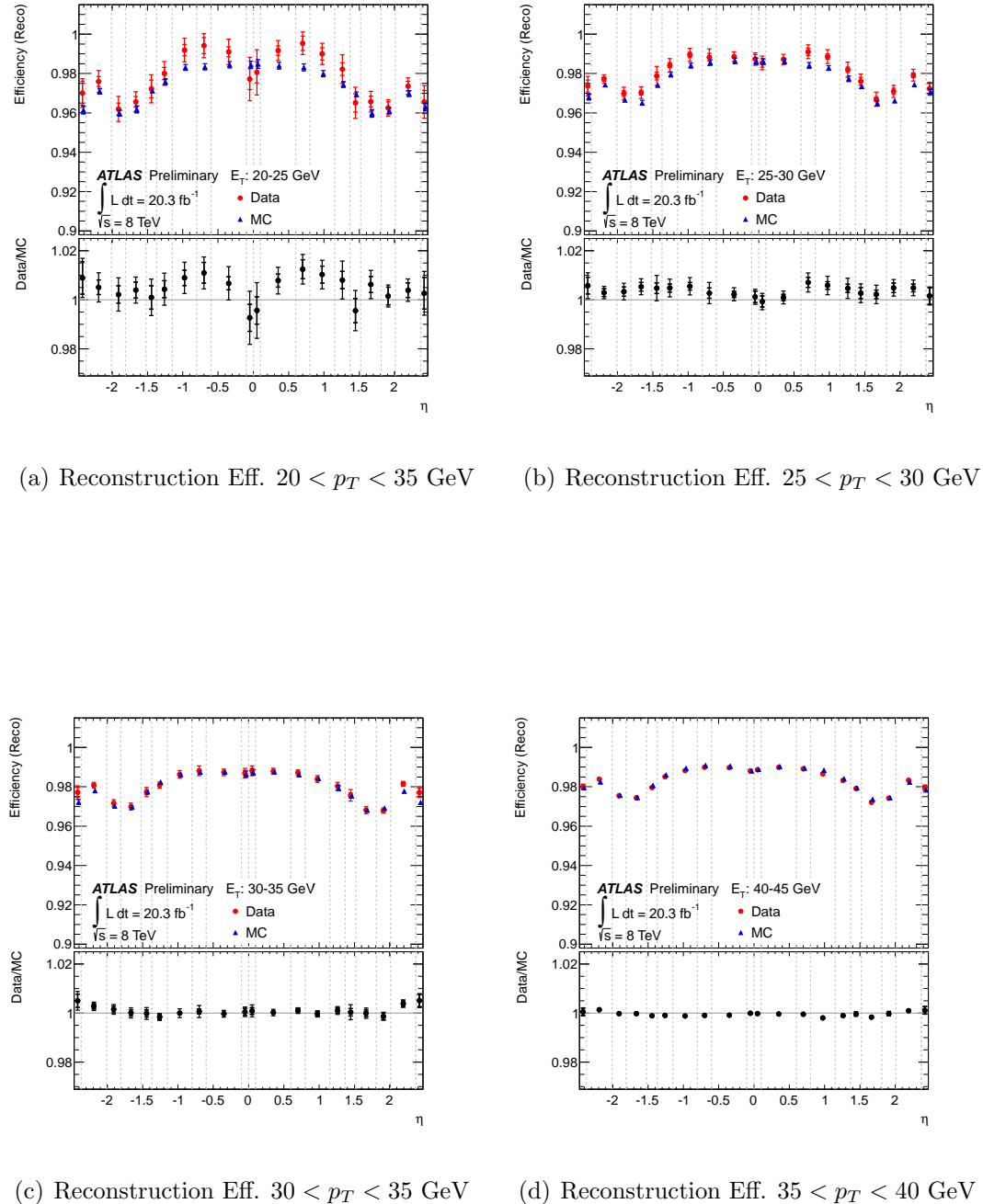
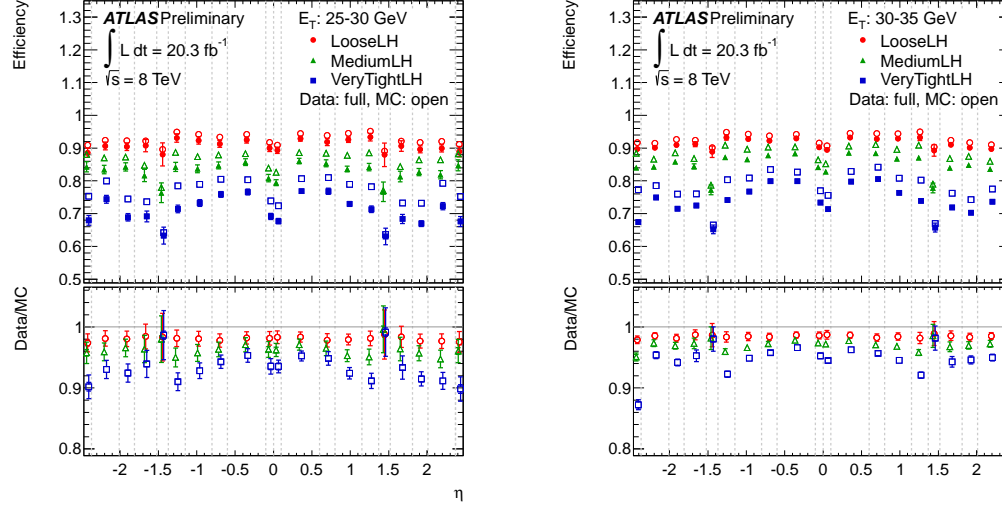
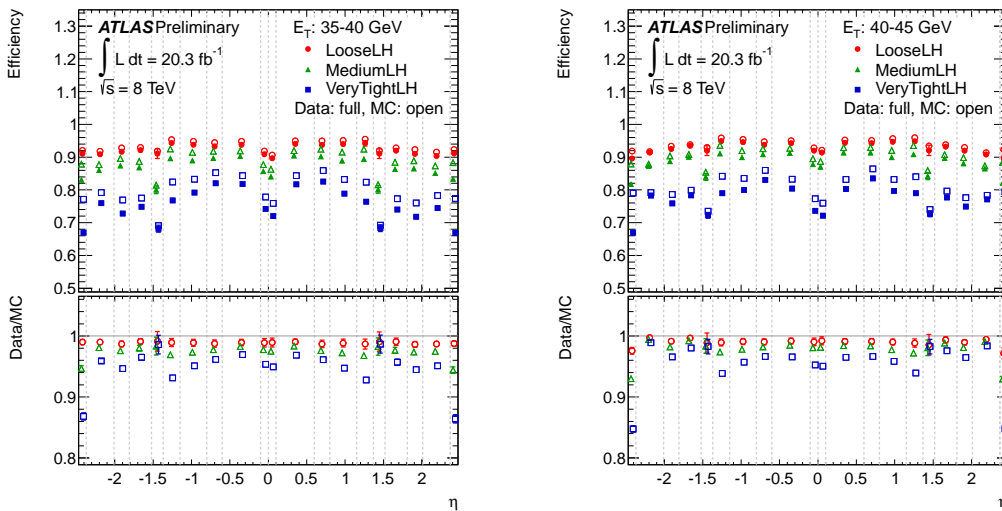


Figure 6.6: Reconstruction efficiency for electrons as a function of  $\eta$  in four  $p_T$  ranges. The bottom panel of each figure is the ratio of the efficiency in data to that in Monte Carlo simulation [20].



(a) Identification Efficiency,  $25 < p_T < 30 \text{ GeV}$  (b) Identification Efficiency,  $30 < p_T < 35 \text{ GeV}$



(c) Identification Efficiency,  $35 < p_T < 40 \text{ GeV}$  (d) Identification Efficiency,  $40 < p_T < 45 \text{ GeV}$

Figure 6.7: Identification efficiency for electrons as a function of  $\eta$  in four  $p_T$  ranges. The bottom panel of each figure is the ratio of the efficiency in data to that in Monte Carlo simulation [20].

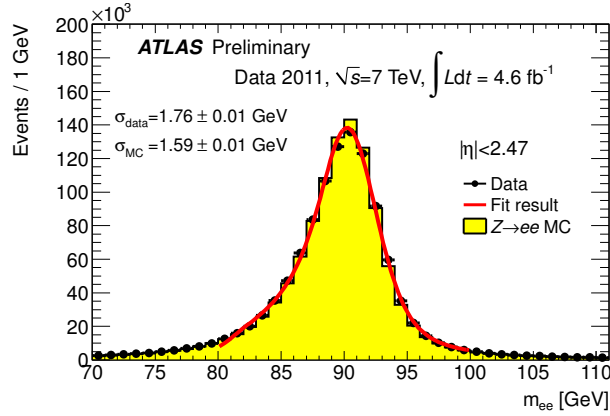


Figure 6.8: The di-electron invariant mass from events consistent with a  $Z$ -boson decay. Data and Monte Carlo simulation are shown, and the fit of a Breit-Wigner convoluted with a Crystal Ball function is shown in red [36].

## Jet Corrections

As jets are the reconstructed object resulting from the Higgs boson decay to  $b$ -quarks, jet energies and  $b$ -tagging must be well-modeled to yield a precise measurement for this analysis. The jet energy scale is calibrated with studies of pile-up effects and in-situ techniques described in Chapter 5. Therefore, this section will focus only on corrections for mismodelings related to the efficiency to tag a jet using the *MV1c* algorithm.

### **$b$ -tagging Corrections**

The most important correction to the Monte Carlo simulation for this analysis is the correction for the mismodeling of the efficiencies to  $b$ -tag jets using the *MV1c* tagger. Corrections are derived for each flavor of jet in the Monte Carlo simulation and applied in a  $p_T$ -dependent manner for each jet in the event on which the tagging algorithm is called. Reference [50] fully details the analysis to determine the scale factors for  $b$ -tagging efficiency measurements, as well as their corresponding systematic uncertainties. The efficiency measurements are made in a sample of di-leptonic top decays, and scale factors are calculated for five different bins of  $b$ -tagging efficiency. The method for the calculation of the  $b$ -tagging efficiency is to perform a maximum likelihood fit to the data, where the likelihood (for the 2-jet case) is defined as:

$$\begin{aligned}\mathcal{L}(p_{T,1}, p_{T,2}, w_1, w_2) = & [ f_{bb} \text{PDF}_{bb}(p_{T,1}, p_{T,2}) \text{PDF}_b(w_1|p_{T,1}) \text{PDF}_b(w_2|p_{T,2}) \\ & + f_{bl} \text{PDF}_{bl}(p_{T,1}, p_{T,2}) \text{PDF}_b(w_1|p_{T,1}) \text{PDF}_l(w_2|p_{T,2}) \\ & + f_{ll} \text{PDF}_{ll}(p_{T,1}, p_{T,2}) \text{PDF}_l(w_1|p_{T,1}) \text{PDF}_l(w_2|p_{T,2}) \\ & + 1 \leftrightarrow 2 ]/2,\end{aligned}$$

where:

- $f_{bb}, f_{bl}$  and  $f_{ll} = 1 - f_{bb} - f_{bl}$  are the fraction of events with two jets with a certain flavor (where  $b$  indicates a  $b$ -jet and  $l$  indicates any non  $b$ -jet).
- $\text{PDF}_f(w|p_T)$  is the probability density function for the  $b$ -tagging weight for a jet of flavor  $f$ , conditionally dependent on  $p_T$ <sup>1</sup>.
- $\text{PDF}_{f_1 f_2}(p_{T,1}, p_{T,2})$  is the two-dimensional PDF for  $[p_{T,1}, p_{T,2}]$  for the flavor combination  $[f_1, f_2]$ .

Each of the probability distribution functions  $\text{PDF}_f(w|p_T)$  is implemented as a N-bin histogram, for N bins of the jet  $p_T$ . The flavor fractions, the  $b$ -weight probability distribution functions for the non  $b$ -jets, and the 2-D kinematic probability distribution functions are obtained from Monte Carlo simulation and fixed. The remaining distribution of interest,  $\text{PDF}_b(w|p_T)$ , must then be parametrized such that it is a function of only the content in each of the N bins, so that it can be fully determined from data. Therefore,  $\text{PDF}_b(w|p_T)$ , for each  $p_T$  bin, is a binned histogram with one

---

<sup>1</sup>This means that, regardless of the  $p_T$  bin the jet falls in, the integral of the PDF over the  $b$ -tagging weight variable is one.

bin for each interval of interest in the tagging weight,  $w$ , where the content of each bin corresponds to the b-tagging efficiency for that  $w$  interval:

$$\epsilon_b(p_T) = \int_{w_{lower}}^{w_{upper}} dw' \text{PDF}_b(w', p_T).$$

The likelihood is then optimized over the data, yielding a result for  $\epsilon_b$ . This procedure may be repeated to obtain the efficiency to tag jets of any flavor. Finally, the efficiency measured in data with this method is compared to the efficiency measured in Monte Carlo simulation to produce a scale factor to match the simulated *MV1c* weight distribution in Monte Carlo simulation to that measured in the data. Figure 6.9 contains examples of the scale factors applied to the jets in Monte Carlo simulation.

Further details of the calibration of the *MV1/MV1c* taggers for  $c$ , light, and  $\tau$  jets are in Reference [50].

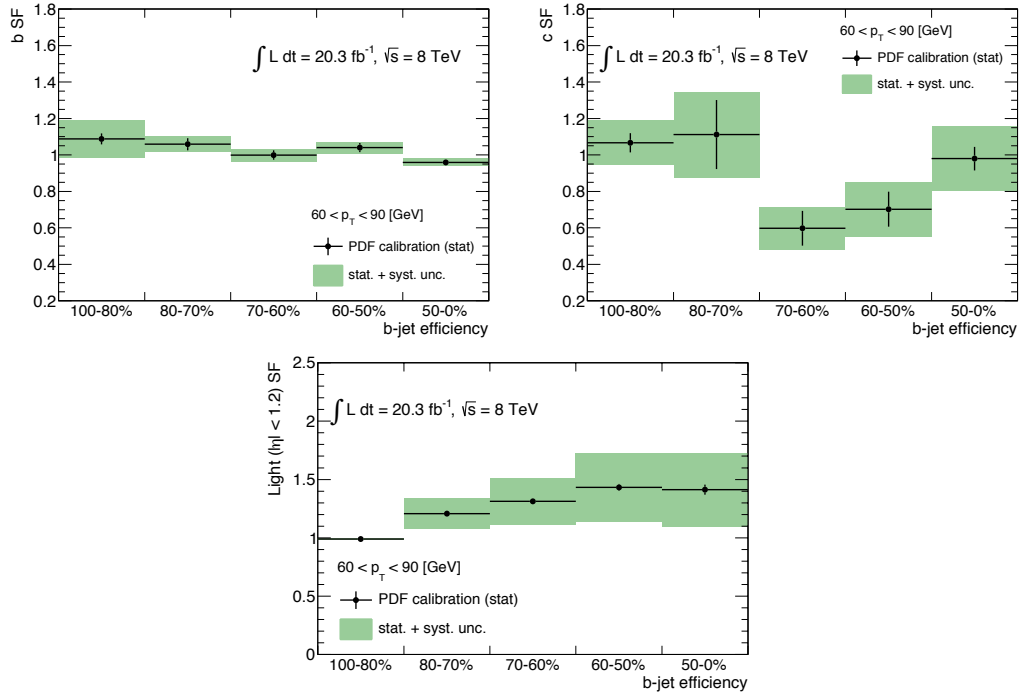


Figure 6.9: Scale factors for the  $MV1c$   $b$ ,  $c$ -jet and  $l$ -jet calibrations for a representative jet  $p_T$  bin ( $|\eta| < 1.2$ ). Error bars refer to statistical uncertainties, while the total error bands also include systematic uncertainties.

# Chapter 7

## Analysis Strategy and Event Selection

This chapter provides an overview of the analysis, as well as definitions of the physics objects used in the analysis and an explanation of the event selection. Section 7.1 provides an overview of the overall strategy for the search. A discussion of the selection of physics objects used in the search is presented in Section 7.2. Section 7.3 covers methods to improve the  $m_{b\bar{b}}$  invariant mass resolution, the key variable of the analysis. Finally, Section 7.4 discusses how groups of reconstructed objects are used to categorize events into analysis regions for signal and background studies.

### 7.1 Analysis Strategy

The goal of the analysis is to observe the  $ZH \rightarrow \ell^+\ell^- b\bar{b}$  process: the production of the Standard Model Higgs boson associated with a  $Z$ -boson where the Higgs

decays via the  $b\bar{b}$  channel and the  $Z$ -boson decays via a pair of leptons. The boson discovered in July 2012 and discussed in Chapter 2 is consistent with the Standard Model couplings to  $W$  and  $Z$  bosons, as well as to top quarks,  $\tau$  leptons, and photons. Measuring the coupling of the boson to the  $b$  quark is an important step to determine the boson's consistency with the properties of the Standard Model Higgs.

**Analysis Overview** To search for the Higgs boson in the  $ZH \rightarrow \ell^+\ell^-b\bar{b}$  channel, a profile likelihood fit is performed. This fit is discussed in detail in Chapter 9. The goal of the profile likelihood fit is to extract a parameter,  $\mu$ , which is called the normalized signal strength. This parameter represents the following ratio:

$$\mu = \frac{\sigma \times BR}{\sigma_{SM} \times BR_{SM}} \quad (7.1)$$

where  $\sigma$  and  $BR$  refer to the cross section and branching ratio for the  $ZH \rightarrow \ell^+\ell^-b\bar{b}$  process and the subscript  $SM$  indicates that the quantities in the denominator are the values of the cross section and branching ratio given by the Standard Model. Therefore any deviation of  $\mu$  from 1 indicates a deviation from the Standard Model.

In order to select events and produce the measurement, several steps are performed and listed below. These steps serve as an outline for the remainder of this thesis.

- Event Selection: In Chapter 6, a set of quality requirements is imposed on the data collected in 2011 and 2012 as well as on the Monte Carlo simulations. Corrections are also made to the simulation based on observed differences between the data and the simulations.
- Physics Object Selection: Leptons, jets, missing transverse energy, and  $b$ -tagged

jets are first reconstructed according to Chapter 5 and then further quality and kinematic requirements are imposed in this chapter.

- Modeling of Signal and Background Processes: Chapter 8 discusses the modeling of the  $ZH \rightarrow \ell^+ \ell^- b\bar{b}$  signal as well as the other processes that are the major backgrounds to this signal. Corrections must be made for known discrepancies between the data and Monte Carlo simulation, and systematic uncertainties are estimated to characterize the knowledge of the background model.
- Profile Likelihood Fit: The mathematical model of the profile likelihood fit is discussed in Chapter 9. The model is based upon a bin-by-bin likelihood of observing a number of events given the background expectation for that distribution. The number of signal and background events in each of these bins is modeled as a Poisson distribution that is parametrized as a function of the uncertainties calculated in the previous item above.
- $ZH \rightarrow \ell^+ \ell^- b\bar{b}$  Validation with the Diboson observation: In this step of Chapter 10, the analysis is validated through the search for a known Standard Model process, the decay of the  $Z$ -boson to a pair of  $b$ -quarks.

After these items are discussed, the result of the  $ZH \rightarrow \ell^+ \ell^- b\bar{b}$  analysis is presented in Chapter 10. Finally, a combined measurement of the  $ZH \rightarrow \ell^+ \ell^- b\bar{b}$ ,  $WH \rightarrow \ell\nu b\bar{b}$ , and  $ZH \rightarrow \nu\bar{\nu} b\bar{b}$  channels is presented in Chapter 11.

## 7.2 Physics Object Selection

This section describes the requirements for each reconstructed object that enters into the  $ZH \rightarrow \ell^+\ell^- b\bar{b}$  search. Sections 7.2.1 through 7.2.2 describe the selection of electrons and muons. Section 7.2.3 describes the jet selection, and then Section 7.2.4 describes how ambiguities related to overlapping objects are resolved. The next section is Section 7.2.5, which discusses the selection of  $b$ -jets. Finally, Section 7.2.5 is a description of a procedure called “truth-tagging”, which increases the number of events available to model the contribution of mis-tagged light jets to the doubly  $b$ -tagged signal regions.

### 7.2.1 Lepton Definition

Three different categories of leptons are defined for the identification of leptonically-decaying bosons.

- *Loose* leptons include electrons reconstructed with the VeryLoose Electron Likelihood selection, and MuID muons reconstructed as Combined, Stand-Alone, or Calo-Muons. Loose leptons are required to have  $p_T > 7$  GeV, except when the muon is a Calo-Muon and the requirement is 0 GeV. The kinematic requirements are described in Table 7.1. In the case that a Calo-Muon and a Combined muon are overlapping within a  $\Delta R < 0.1$ , the Combined Muon is kept and the Calo-Muon is discarded to avoid double-counting. Additionally, these leptons must satisfy a track isolation requirement that is designed to reject multijet

background. The isolation requirement is defined as:

$$iso_{track}(\ell) = \frac{1}{p_T^\ell} \sum_{trk} p_T^{trk} \text{ for } \Delta R(\ell, trk) < 0.2. \quad (7.2)$$

- *Medium* leptons consist of leptons in the Loose category except that Stand-Alone and Calo-Muons are rejected. Furthermore, the  $E_T$  cut for electrons and  $p_T$  cut for muons is increased to 25 GeV, while the  $|\eta|$  range is restricted to  $|\eta| < 2.5$ .
- *Tight* leptons are taken from the set of Medium leptons, and impose more stringent isolation requirements to reject multijet background. The additional requirement is on the calorimeter isolation, which is a ratio of the energy measured in a cone of topological clusters (TC) around the lepton to the energy of the lepton itself:

$$iso_{calo}(\ell) = \frac{1}{p_T^\ell} \sum_{calo} E_T^{TC} \text{ for } \Delta R(\ell, TC) < 0.3. \quad (7.3)$$

### 7.2.2 Additional Lepton Selection Information

The likelihood tool used to identify electrons as VeryLoose or VeryTight above is described in Section 5.3. The muon categories of Combined, Stand-Alone, and Calo-Muon are described in Section 5.4. The track requirements for categorizing a muon in the Loose lepton category are described below:

- *B-layer hits*: At least 1 hit is required on the innermost layer of the pixel detector if the track crosses an active layer,

Flavor Type	Electrons		Muons		
	Author 1 or 3	Comb/Seg-Tag	Calo	Stand Alone	
Loose Category					
Quality	VeryLoose LH	Tight MuID & MCP hit requirements			
$ \eta $	< 2.47	< 2.7	< 0.1	> 2.5, 2.7	
$E_T$ (GeV)	> 7	> 7	> 20	> 7	
$ d_0 $ (mm)	–	< 0.1	< 0.1	NA	
$ z_0 $ (mm)	–	< 10	< 10	NA	
$isotrack$	< 0.1	< 0.1	< 0.1	NA	
Medium Category					
$E_T$ (GeV)	> 25	> 25		NU	
$ \eta $	–	< 2.5			
Tight Category					
Quality	VeryTight LH	–			
$isotrack$	< 0.04	< 0.04		NU	
$isocalo$	< 0.04	< 0.04			

Table 7.1: Loose, Medium and Tight lepton definitions. NU stands for ‘Not Used’ and NA stands for ‘Not Applicable’. Stand Alone muons are reconstructed entirely from the Muon Spectrometer with no Inner Detector information and hence no  $d_0$ ,  $z_0$  or isolation requirements are imposed.

- *Pixel hits*: At least 1 hit,
- *SCT hits*: At least 4 hits are required across the layers of the SCT,
- *Pixel or SCT holes*: Less than 3 total holes across the Pixel or the SCT are allowed,
- *TRT hits*: For  $0.1 < |\eta| < 1.9$ , at least 6 hits are required in the TRT, and the ratio of TRT outliers to hits must be less than 0.5.

### 7.2.3 Jet Selection Criteria

Jets are reconstructed using the anti- $k_t$  algorithm [57] with a radius parameter  $R = 0.4$  as described in Section 5.5. Two categories of jets are defined. The first, called *signal* jets are used to reconstruct the Higgs boson candidate. These jets are required to be within  $|\eta| < 2.5$  and have  $p_T > 20$  GeV. The leading jet in each event must have  $p_T > 45$  GeV, a requirement that was optimized for background rejection. In order to reduce the contribution of jets from pile-up events, the tracks within the jet are matched to reconstructed vertices, and jets are rejected if too much energy within the jet originates from a pile-up vertex. This is captured by the jet vertex fraction (JVF), which is defined as the ratio of sum of the  $p_T$  of the tracks matched to the jet that originate from the primary vertex to the total sum of the  $p_T$  of the tracks matched to the jet. This ratio must be greater than 0.5 for jets with  $p_T < 50$  GeV and  $|\eta| < 2.4$ . The JVF cut is not applied above 50 GeV because it is intended to only reject pile-up jets, and the cutoff at  $|\eta| < 2.4$  is to ensure the jet falls completely within the acceptance of the Inner Detector. The second category of

jets, called *veto* jets, are a looser category designed to identify events with additional hadronic activity, such as additional jets from  $t\bar{t}$  background. Events with veto jets are rejected. Veto jets are only used in the event selection for the combined analysis in Chapter 11. These jets include those reconstructed within  $2.5 < |\eta| < 4.5$  and have  $p_T > 30$  GeV. The kinematic requirements for jets are summarized in Table 7.2.

Type	Signal Jet	Veto Jet
$p_T$ (GeV)	$\text{jet}_{i=1} > 45$ $\text{jet}_{i>1} > 20$	$> 30$
$ \eta $	$< 2.5$	$2.5 - 4.5$
$ _{\text{JVF}}$	$> 0.5^*$	—

Table 7.2: Selection used to define orthogonal sets of central and veto jets. \*The JVF cut is only required for jets with  $p_T < 50$  GeV and  $|\eta| < 2.4$ .

To achieve a better understanding of the modeling of  $Z$ -jet backgrounds and the application of  $b$ -tagging scale factors to jets in the Monte Carlo simulation, the flavor of the jet in question must be determined. The flavor of reconstructed Monte Carlo jets is defined at the hadron-level. A jet is labeled as a  $b$ -jet if there is a  $B$ -hadron with  $p_T > 5$  GeV within a cone of 0.4 about the jet axis. Jets unmatched to a  $B$ -hadron are labeled  $c$ -jets if there is a  $C$ -hadron within the same cone. The remaining jets are labeled as  $\tau$  jets if there is a  $\tau$ -lepton within the same cone, and finally all other jets are labeled as light jets.

#### 7.2.4 Removal of Overlapping Objects

It is important to avoid the double-counting of energy deposits in the calorimeter as both leptons and jets, and also to avoid categorizing an electron as a muon in the

case that only an inner detector track exists. To harmonize the selection of physics objects for analysis, an overlap removal procedure resolves ambiguities that arise from the presence of these overlapping objects. Loose electrons within  $\Delta R < 0.4$  of signal jets are kept, while the jet is rejected. Loose muons overlapping with signal jets within  $\Delta R < 0.4$  are kept if  $N_{trk} < 4$ <sup>1</sup>, but the jet is kept if  $N_{trk} \geq 4$ . This increases the acceptance for the  $ZH \rightarrow \ell^+ \ell^- b\bar{b}$  signal by not rejecting leptons from the  $Z$ -boson decay that randomly fall inside of a jet. Loose muons overlapping with loose electrons within  $\Delta R < 0.2$  are kept and the electron is rejected if the muon is a Calo Muon. Otherwise, the muon is rejected and the electron is kept. This is because the Calo Muon identification procedure determines if a calorimeter energy deposit is more likely due to a muon than an electron.

### 7.2.5 $b$ -jet Tagging Requirements

Since the Higgs candidate in this analysis decays to a pair of  $b$ -quarks, the search sensitivity is increased when requiring the jets in the final state to be  $b$ -tagged. Jets which originate from  $b$ -quarks are identified using algorithms which exploit the long lifetime of  $B$ -hadrons. The  $b$ -tagging algorithm MV1c [26, 35, 38] described in Section 5.6.1 is used to categorize the jets in the event into categories for background control regions and signal regions. The output of the MV1c algorithm is a weight  $w$ , and a higher weight corresponds to a higher likelihood that the candidate jet is a  $b$ -jet. Three thresholds of  $b$ -tagging are utilized for the analysis:

- A Loose  $b$ -tag,  $0.4050 < \text{MV1c weight} \leq 0.7028$ ,

---

<sup>1</sup> $N_{trk}$  is the number of tracks with  $p_T > 5$  GeV inside of the jet

- A Medium  $b$ -tag,  $0.7028 < \text{MV1c weight} \leq 0.9237$ ,
- A Tight  $b$ -tag,  $\text{MV1c weight} > 0.9237$ .

The signal regions are required to have exactly two  $b$ -tagged jets that meet at least the Loose tagging threshold.

### Truth-Tagging

The MV1c algorithm has powerful rejection against non- $b$ -jets. It is therefore difficult to produce enough events with Monte Carlo simulation to have reasonable statistical power after requiring 2  $b$ -tags for events without true  $b$ -jets. A sufficient number of events is necessary to produce reliable background templates for  $W$  and  $Z+\text{jets}$  processes, which have the greatest contribution to the final event yield. In order to increase the number of events in these templates, a method known as ‘truth tagging’ is used to create pseudo 2-tagged events to populate the ‘2-tagged’ control regions in the cases that neither of the two leading  $p_T$  jets is actually matched to a truth-matched  $b$ -jet. Truth tagging is a method by which a random MV1c value above the loose operating point is generated for a given jet. This is done by creating a random efficiency obtained from sampling a cumulative distribution that is built from the tagging efficiency above the loose operating point, and then assigning the MV1c value corresponding to the random efficiency generated to the jet in question. The efficiencies used to build the cumulative distribution depend on the physical process, and are parametrized as a function of the flavor,  $p_T$  and  $\eta$  of the given jet as well as the process type. The efficiency maps are shown in Reference [109]. After the generation of a random MV1c value, every jet will, by construction, satisfy the loose

$b$ -jet cut, so to correct for this bias, the event must be weighed down by the efficiency of the jet to pass the loose operating point. In events where one of the leading two jets is truth-matched to a  $B$ -hadron, this procedure is not used; instead, the original MV1c weight of each jet is directly used.

### Biases from Truth Tagging

Although truth-tagging dramatically increases the available statistics for the  $Z + \text{jets}$  samples, this method ignores correlations in the tagging efficiencies of jets in the same event. For events with two  $c$ -jets, a bias in the tagging efficiency as a function of  $\Delta R(cc)$  is observed and merits a correction. Figure 7.1 shows the  $\Delta R(cc)$  distribution and the correction. Half the correction is used as a systematic uncertainty. Further details on the biases observed in truth-tagging are given in Reference [109].

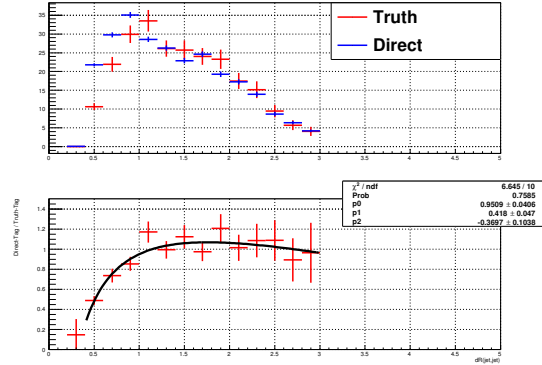


Figure 7.1: The truth tagging  $\Delta R$  correction derived from the ratio truth to directed tagged events using  $W + cc$  and  $Z + cc$  in 2 and 3-jet events (top). The correction itself is obtained from a fit to the ratio (bottom):  $0.9509 + 0.418 \times \ln(\Delta R) - 0.3697 \times \ln^2(\Delta R)$ .

## Biases from Generators

The scale factors to correct the flavor tagging efficiency in Section 6.2.3 were derived with respect to PYTHIA6 for  $b$ -jets and  $c$ -jets. As shown in Figure 7.2 for the exclusive 70% MV1c operating point, the efficiency for jets truth-matched to a  $b$ -jet or  $c$ -jet is different for each of the three generators used in this analysis (PYTHIA6, PYTHIA8, and SHERPA). Half the correction is used as a systematic uncertainty, which is decorrelated for  $b$ - and  $c$ -jets as well as for the PYTHIA8, and SHERPA. A correction is not applied to light jets since both the generator effect and the light-jet contribution are small. More details are given in Reference [109].

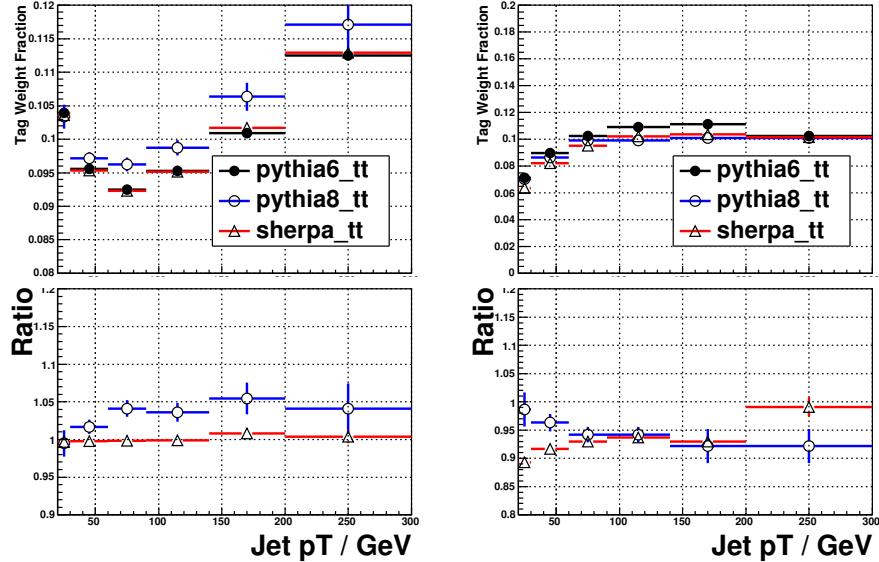


Figure 7.2:  $b$ -jet (left) and  $c$ -jet (right) tagging efficiency for the jets between the 70% and 60% operating points ( $0.7028 < \text{MV1c} < 0.8353$ ) in  $t\bar{t}$  events produced by PYTHIA6 (Black), PYTHIA8 (Blue) and SHERPA (Red). The ratio is the Monte Carlo to Monte Carlo scale factor.

### 7.2.6 Missing Energy Selection

$E_T^{\text{miss}}$  enters the analysis to reject top background in the 2-lepton channel because  $t\bar{t}$  events have real  $E_T^{\text{miss}}$  from neutrinos while  $ZH \rightarrow \ell^+\ell^- b\bar{b}$  events do not. The measurement of the  $E_T^{\text{miss}}$  follows Section 5.7, based on the MetRefFinal\_Eflow algorithm. The corrections to leptons and jets discussed in Chapter 6 are applied before the  $E_T^{\text{miss}}$  is calculated.

## 7.3 Improvements to the $m_{b\bar{b}}$ Resolution

Final state radiation and the complicated task of reconstructing  $b$ -jets degrades the resolution of the Higgs resonance. Since the search presented in this thesis depends upon observing a significant number of candidate events above the background in bins of  $m_{b\bar{b}}$ , improvements to the  $m_{b\bar{b}}$  resolution of the Higgs boson candidate provide greater significance to the search. Three methods of improving the  $m_{b\bar{b}}$  are utilized. Firstly,  $m_{b\bar{b}}$  resolution is improved by 6.4% [37] by adding the energy from muon reconstructed within jets (and not belonging to the  $Z$ -boson decay) to the total energy of the jet, after subtracting the muons energy deposit in the calorimeter. Muons are considered for this correction if they have  $p_T > 4$  GeV and are within  $\Delta R < 0.4$  of the  $b$ -tagged jet. No statistically significant advantage is found from adding multiple muons found within jets, so only the highest  $p_T$  muon is considered for this correction.

Secondly, a correction that improves the  $m_{b\bar{b}}$  resolution by incorporating information about the underlying jet  $p_T$  spectrum of  $ZH \rightarrow \ell^+\ell^- b\bar{b}$  signal events is added.

This correction, called the  $p_T$ -reco correction, improves the invariant mass resolution by  $\sim 6\%$ , though the background is also shaped, yielding a reduced improvement of  $\sim 3\%$  (depending on the channel) on the final sensitivity of the search [37]. Figure 7.3 shows the value of the  $p_T$ -reco correction as a function of the reconstructed jet  $p_T$ . The red points are the values of the correction for jets calibrated with the Global Sequential Calibration, which is used in this analysis. This correction is applied for the 0-lepton and 1-lepton searches discussed in Chapter 11, but this information is exploited differently for the 2-lepton channel by combining it with the kinematics of other objects in the final state.

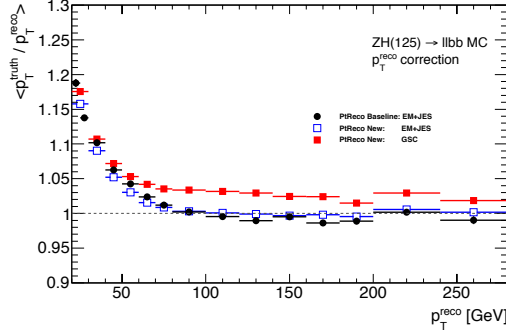


Figure 7.3: Three versions of the  $p_T$ -reco correction are shown. The black points show the correction applied to EM+JES jets with a baseline selection. The blue uses the object selection detailed in this chapter, also with EM+JES jets, and the red points are the correction values for Global Sequential Calibration jets.

### 7.3.1 Kinematic Likelihood Fit

For the  $ZH \rightarrow \ell^+\ell^- b\bar{b}$  search, the final-state topology is fully reconstructed as two leptons and two jets. Therefore the only true  $E_T^{\text{miss}}$  in the event comes from semileptonic decays of  $b$ -jets and any transverse momentum of the colliding partons. The true  $E_T^{\text{miss}}$  determines the resolution to which the sum of the transverse momentum of

any given event will be zero. The kinematic likelihood fit adjusts the  $p_T$  of the jets so that the hadronic energy in the event is balanced against the more-precisely measured leptons coming from the  $Z$ -boson decay. A likelihood model is parametrized by 12 parameters:

- energies of 2 electrons or inverse transverse momenta of 2 muons and the energies of 2 jets,
- pseudorapidity and azimuthal angles of the 2 leptons and 2 jets,
- transverse momentum of the  $\ell\ell b\bar{b}$  system,
- reconstructed dilepton mass  $m_{\ell\ell}$ ,

and 3 constraints for the variation of these parameters,

- the  $m_{\ell\ell}$  is constrained to follow a Breit-Wigner (BW) distribution around a pole mass and width of the  $Z$  boson,
- the  $\sum P_{x,y}^{\ell\ell b\bar{b}}$  is constraint to be zero with a width of  $\sim 9\text{GeV}$  obtained from  $ZH$  Monte Carlo events,
- assume parameters to follow Gaussian distributions (except for the jets, for which dedicated asymmetric transfer functions are derived).

Given the fit parameters and constraints defined above, the probability density function is defined as

$$\begin{aligned}\mathcal{L} &= \prod_i f(y_i^{obs}, y_i^{pred}) \\ &= G(\Omega_\ell^n; \Omega_\ell^0, \sigma_\Omega) L^j(P_T^n; P_T^0, \eta_j^0) L_{truth}^j(P_T^n; \eta_j^0) \\ &\quad \prod_{i=j} G(\phi_i^n; \phi_i^0, \sigma_\phi) \\ &\quad \prod_{i=x,y} G\left(\sum p_i^n; \sum P_i, \sigma_{\sum p_i}\right) \\ &\quad \mathcal{B}(m_{\ell\ell}^n; M_Z, \Gamma_Z),\end{aligned}$$

The likelihood is a product of:  $G(\Omega_\ell^n; \Omega_\ell^0, \sigma_\Omega)$ , a Gaussian constraint on the lepton energy, where  $\Omega$  is either the  $E$  for electrons or  $1/p_T$  for muons,

$L^j(P_T^n; P_T^0, \eta_j^0)$ , the likelihood of the jet response, or detector transfer function,  $L_{truth}^j(P_T^n; \eta_j^0)$ , the  $p_T$  reco correction described above,  $G(\phi_i^n; \phi_i^0, \sigma_\phi)$ , a Gaussian constraint on the  $\phi$  of the jets,  $G\left(\sum p_i^n; \sum P_i, \sigma_{\sum p_i}\right)$ , a Gaussian constraint on the total transverse energy in the event, and  $\mathcal{B}(m_{\ell\ell}^n; M_Z, \Gamma_Z)$ , which represents a Breit-Wigner distribution to characterize the  $Z$ -boson resonance. A test statistic is constructed from the negative log of the likelihood:

$$\begin{aligned}-2 \ln(\mathcal{L}) &= \sum_{i=j} \left( \frac{(\phi_i^n - \phi_i^0)^2}{\sigma_\phi^2} \right) + \frac{(\Omega_\ell^n - \Omega_\ell^0)^2}{\sigma_\Omega^2} - 2 \ln(L^j) - 2 \ln(L_{truth}^j) \\ &\quad + \sum_{i=x,y} \frac{(\sum p_i^n - \sum P_i)^2}{\sigma_{\sum p_i}^2} + 2 \ln((m_{\ell\ell}^2 - M_Z^2)^2 + M_Z^2 \Gamma_Z^2)\end{aligned}$$

where  $M_Z$  and  $\Gamma_Z$  are the  $Z$  boson mass and width respectively. Finally this statistic is minimized, yielding improved jet kinematics on an event-by-event basis.

The kinematic likelihood fit provides a further improvement in the  $m_{b\bar{b}}$  resolution of 10% above that of using only the  $p_T$ -reco correction and muon-in-jet corrections. With this correction, an additional 4% achievement is gained in the sensitivity of the  $ZH \rightarrow \ell^+ \ell^- b\bar{b}$  search.

Figure 7.4 shows the invariant mass,  $m_{b\bar{b}}$  before and after the correction is applied. Further details are found in Reference [41].

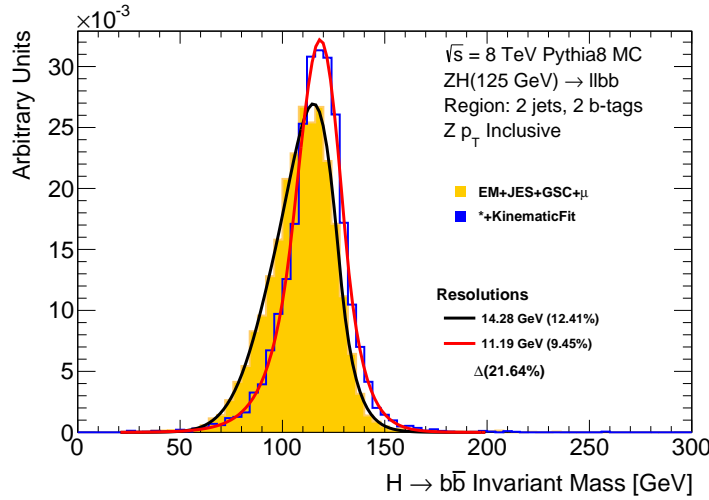


Figure 7.4: Dijet invariant mass before and after applying a kinematic likelihood fit in  $ZH$ ,  $m_H = 125$  GeV signal Monte Carlo-simulated events showing a  $\sim 22\%$  resolution improvement.

## 7.4 Event Selection

The following section discusses how groups of reconstructed objects are used to categorize events into analysis regions for signal and background studies. Event-level cleaning cuts are discussed in Section 7.4.1, and the triggers used to select events are discussed in Section 7.4.2. Section 7.4.3 and Section 7.4.4 detail the lepton and jet

categories for the analysis. Finally, Section 7.4.5 provides a detailed discussion on the categorization of events for further analysis.

### 7.4.1 Event Cleaning

The data are required to satisfy the Good Run List requirements from Section 6.1. Additionally, a series of standard cleaning cuts are applied to avoid random event problems in the detector, during reconstruction, or due to activity in the detector from non-collision background. The applied event cleaning cuts are:

**On data:**

**Incomplete Events:** remove events that have Core EventInfo error flag (  
 $\text{coreFlags} \& 0x40000 != 0$  in D3PD),

**LAr Error Flag:** remove events that have noise bursts in the electromagnetic calorimeter, or corrupted calorimeter data,

**TileCal Error Flag:** remove events that have incomplete event information from the hadronic (Tile) calorimeter,

**Corrupted Tile Events:** remove events with corrupted data from the hadronic (Tile) calorimeter,

**Hot Tile Cells:** remove events with jets (after overlap removal with other objects and before JVF requirement) pointing to noisy hadronic calorimeter cells in the runs : 202660, 202668, 202712, 202740, 202965, 202987, 202991, 203027, 203169,

**On simulations:**

**Incomplete Events:** reject Monte Carlo events that have no truth particles,

**On both data and simulations:**

**Vertex Selection:** Require that the first primary vertex contains at least 3 tracks,

**MET Cleaning:** Reject any data or Monte Carlo event containing a looser bad jet with  $p_T > 20 \text{ GeV}$ ,  $|\eta| < 4.5$  (after overlap removal and before JVF cut).

This removes events with badly mismeasured jets, beam backgrounds, and cosmic rays.

### 7.4.2 Trigger Selection

The 2-lepton channel uses both single and dilepton triggers for maximum efficiency to detect the leptons from the  $ZH \rightarrow \ell^+ \ell^- b\bar{b}$  process. The single-lepton triggers increase the efficiency to detect signal events in cases where one lepton may fall outside of the trigger or kinematic acceptance. Table 7.3 below details the triggers used for muons and electrons in 2012 data.

Trigger Object	Data Period	Trigger Names	$iso_{track}$	Luminosity ( $\text{fb}^{-1}$ )
single electron	A-L	EF_e24vhi_medium1	✓	
		EF_e60_medium1		20.2769
single muon	A-L	EF_mu24i_tight	✓	
		EF_mu36_tight		
di-electron di-muon	A-L	EF_2e12Tvh_loose1		20.2769
		EF_2mu13		

Table 7.3: Trigger table used in the 2012 data analysis. The digits exceed the precision on the measurement of the luminosity, but they are reported here for future reference, since these are the numbers used to normalize the Monte Carlo predictions.

### 7.4.3 Lepton Selection

The leptons selected in Section 7.2.1 are used to reconstruct the  $Z$ -boson according to Table 7.4. One Loose and one Medium lepton are required. Tight leptons are only used in the selection for the 1-lepton channel discussed in Chapter 11.

Analysis	Loose Lepton	Medium Lepton	Tight Lepton
2-lepton	1	1	–

Table 7.4: Signal lepton selection from the 3 inclusive lepton definitions.

### 7.4.4 Jet Selection

The jets defined in Section 7.2.3 are used to select events compatible with a Higgs decay and define analysis categories in order to isolate regions with a large signal to background ratio. For this thesis, one analysis region consists of events with exactly 2 signal jets, and another region consists of events with 3 or more signal jets. Any number of veto jets may enter the analysis. The use of veto jets is discussed in the context of the 0-lepton and 1-lepton channels in Chapter 11.

Events are categorized by the number of signal jets present in the event and are further divided by the number of  $b$ -jets present as shown in Figure 7.5. Three exclusive 2  $b$ -tag categories are used in this analysis:

- One Loose  $b$ -tag and one Loose, Medium, or Tight tag, labeled “LL”
- One Medium  $b$ -tag and one Medium or one Tight  $b$ -tag, labeled “MM”
- Two exclusive tight  $b$ -tags, labeled “TT”

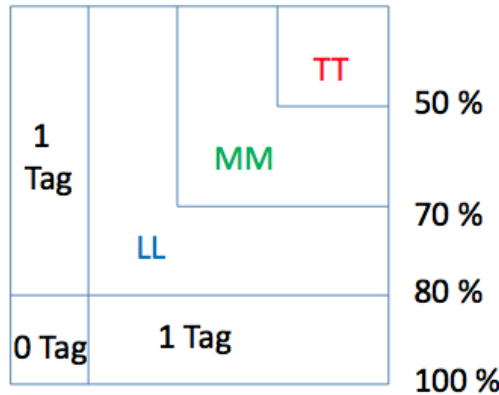


Figure 7.5: A graphical representation of the exclusive  $b$ -tagging categories used in the analysis.

The  $b$ -tagged jets must be the two jets that are the highest in  $p_T$ . If one of the leading two jets in  $p_T$  is not  $b$ -tagged, as is the case in a small fraction of signal events, the event is rejected. The single- $b$ -tag regions are inclusive in the operating points given. For events with three signal jets (3-jet events), the event is rejected if the lowest  $p_T$  jet passes the loose  $b$ -tag cut given in Section 7.2.5.

#### 7.4.5 Kinematic Requirements to Define Analysis Regions

Once definitions of the physics objects are set as in the previous subsections and the quantity of these objects is set as in Section 7.4, further kinematic requirements are placed on each channel to discriminate signal events from the major backgrounds. This section discusses these kinematic requirements, and defines the final analysis regions that are used as input to the profile likelihood fit described in Chapter 9. The  $ZH \rightarrow \ell^+\ell^- b\bar{b}$  search is divided into several regions of  $p_T^Z$  as regions have shown the signal to background ratio increases with the boost of the associated vector boson. In total, five bins of  $p_T^Z$  are chosen. In addition to splitting by  $p_T^Z$ , a cut is placed

on the maximum allowed  $\Delta R$  between the jets from the Higgs candidate. This cut varies depending on the  $p_T^Z$  bin under study to take advantage of the fact that a more-boosted Higgs candidate will yield two  $b$ -jets closer in  $\Delta R$  than jets from background processes. These  $\Delta R$  cuts range from  $\Delta R < 3.4$  at low  $p_T^Z$  to  $\Delta R < 1.4$  at high  $p_T^Z$ . Both the  $p_T^Z$  categorization and  $\Delta R$  cut values were optimized by maximizing the significance  $S/\sqrt{B}$  in the range  $80 < m_{b\bar{b}} < 140$ . The full list of kinematic cuts is summarized in Table 7.5. Some variables of interest are:

- The  $E_T^{\text{miss}}$  is used to reject top pair background in the 2-lepton channel,
- $Z$  is the vector boson, constructed from the vectoral sum of the two leading  $p_T^{\text{leptons}}$ ,
- $H$  is the Higgs candidate, constructed from the vectoral sum of the two leading  $p_T$  jets,

Variable	Dijet Mass Analysis				
	Selection				
$p_T^Z$ (GeV)	0-90	90-120	120-160	160-200	> 200
$\Delta R(jet_1, jet_2)$	0.7-3.4	0.7-3.0	0.7-2.3	0.7-1.8	< 1.4
Applied for all $p_T^Z$ and $\Delta R$ bins					
$m_{\ell\ell}$ (GeV)	83-99				
$E_T^{\text{miss}}$ (GeV)	< 60				

Table 7.5: Event kinematic selection for the signal regions.

With these kinematic selections, a total of 55 analysis regions have been created to study the  $m_{b\bar{b}}$  shape. For each of the 5 bins of  $p_T^Z$  the region is split into regions of

either 2 or 3 signal jets. Each of these 10 regions is then split by the  $b$ -tagging selection into a further 5 regions (0-tag, 1-tag, LL, MM, and TT), resulting in 50 analysis regions. Additionally,  $t\bar{t}$ -enriched regions are created by requiring the  $Z$ -boson candidate to consist of differently-flavored leptons. More precisely, this forces the selection to have one electron and one muon, rejecting much of the  $Z$ +jets background while efficiently selecting fully-leptonic  $t\bar{t}$  events that have one electron and one muon in the final state. This region combines the 2 and 3 jet categories and is inclusive across the 2-tag categories. These regions are called the top  $e - \mu$  control region and are split into 5  $p_T^Z$  bins for a total of 5 analysis regions. As discussed further in Chapter 9, some of these regions are combined or eliminated to make the statistical model both more robust and efficient, so the final number of regions in the profile likelihood fit is less than 55.

# Chapter 8

## Characterization of Signal and Background Processes

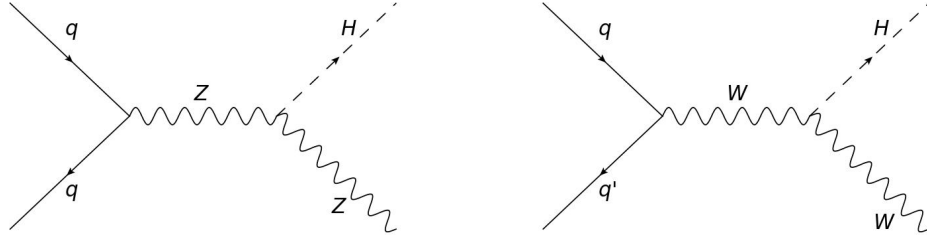
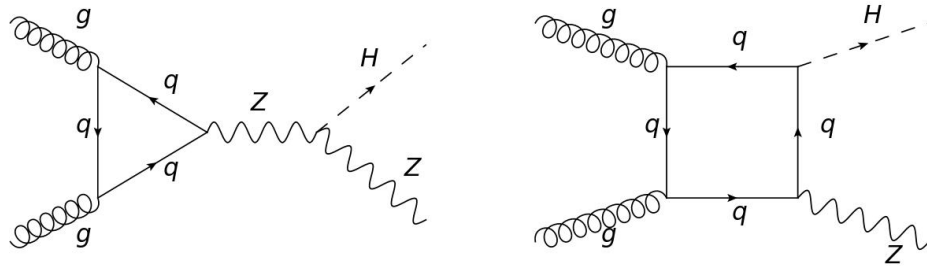
In Chapter 7, the kinematic regions into which all events in the searches are categorized, are defined. Before discussing the statistical model used to extract the measurement of the strength of the Higgs boson signal, this chapter discusses each of the signal and background processes in full detail, including any corrections and systematic uncertainties associated with the modeling of each process. Section 8.1 covers the modeling and theoretical uncertainties associated with the signal processes for  $ZH \rightarrow \ell^+ \ell^- b\bar{b}$ ,  $WH \rightarrow \ell\nu b\bar{b}$ , and  $ZH \rightarrow \nu\bar{\nu} b\bar{b}$ . Section 8.2 covers the modeling of the background processes:  $Z + \text{jets}$ ,  $t\bar{t}$  pair production, single-top, diboson, and multijets. The systematic uncertainties that enter into the profile likelihood fit model presented in Chapter 9 are discussed in detail here. These uncertainties are estimated, when possible, from data in kinematic regions enriched in a given background, and estimated through comparisons of various alternative Monte Carlo generators when

a data-driven approach is not possible. When a systematic uncertainty is labeled for inclusion in the fit model, it receives a special font. For example, the systematic uncertainty associated with the uncertainty in the modeling of the  $\Delta\phi$  distribution in the  $Z + \text{jets}$  processes is denoted by  $\text{ZDPhi}$ .

## 8.1 Signal Modeling and Theoretical Uncertainties

This section discusses the signal modeling for all processes described in the combination presented in Chapter 11, although the details of the 0-lepton and 1-lepton channels will be left to that chapter. The signal processes  $ZH \rightarrow \ell^+ \ell^- b\bar{b}$ ,  $WH \rightarrow \ell \nu b\bar{b}$  and  $ZH \rightarrow \nu\bar{\nu} b\bar{b}$ , where  $\ell = e, \mu, \tau$  are modeled using Monte Carlo events produced by the PYTHIA 8.165 [107] event generator configured with the AU2 tune [5], using the CTEQ6L1 PDF [102] set of parton distribution functions (PDF), interfaced to PHOTOS [81] for QED final-state radiation, and TAUOLA [115] for the simulation of  $\tau$  decays. The decays of  $Z \rightarrow \tau\tau$  and  $W \rightarrow \tau\nu$  are also simulated in order to account for the small fraction of additional signal events selected due to the decay  $\tau \rightarrow \nu_\tau l \nu_l$  where  $l$  is either an electron or muon. Signal samples are generated in the Higgs boson mass range between 100 GeV and 150 GeV at 5 GeV intervals.

Two production modes are considered, shown below in Figures 8.1 and 8.2. The most significant process for both  $ZH$  and  $WH$  production is the quark initiated process, but for  $ZH$  production, approximately 15% of the total cross section is from the gluon-initiated second-order process in Figure 8.2.


 Figure 8.1: Leading order Feynman diagrams for quark-initiated  $VH$  production.

 Figure 8.2: Leading order Feynman diagrams for gluon-initiated  $ZH$  production.

The total cross section for the signal processes as a function of the Higgs mass are given by Reference [88], and the branching ratio for the Higgs decay to  $b\bar{b}$  is given by References [70] and [88]. Central values of the cross section have been calculated at next-to-next-to-leading order (NNLO) in QCD corrections in Reference [54], and next-to-leading order in electroweak (EW) corrections in Reference [59]. For the branching ratios for the decay of the  $W$  and  $Z$ -bosons, values are taken from the Particle Data Group [96]. At  $\sqrt{s} = 8$  TeV, the total cross section for  $ZH$  production is 0.415 pb, and for  $WH$  production it is 0.705 pb.

### 8.1.1 $p_T^V$ -dependent NLO Electroweak Correction

Although the signal cross section is calculated to NLO in the EW corrections, the fact that the analysis is performed in bins of  $p_T^V$  motivates a  $p_T^V$ -dependent NLO EW correction rather than a correction that averages over  $p_T^V$ . In order to derive the correction, the HAWK Monte Carlo program [69, 58] is used to calculate differential cross sections for the  $WH$  and  $ZH$  processes as a function of  $p_T^V$ .

Since the inclusive cross section for the signal processes is calculated at NLO in the EW corrections, the  $p_T^V$  correction derived here is the difference between the inclusive (across all  $p_T^V$ ) and the differential cross section predictions from HAWK. The resulting correction is shown in Figure 8.3 and the values are given in Table 8.1. A systematic uncertainty is taken from an estimate of the next-highest order correction (NNLO), which is of the scale  $\Delta_{NLO}^2$ . This systematic uncertainty is called `TheoryVHPt`, and is taken to be  $\max(2\%, \Delta_{NLO}^2)$  to ensure that it is non-vanishing.

### 8.1.2 Uncertainties on the Inclusive Cross Section

For the theoretical production cross section, the systematic uncertainties can be divided into one of two categories, either renormalization and factorization scale uncertainties or PDF uncertainties. Both types of uncertainty were studied in detail in Reference [87] and the results are summarized below in Table 8.2 for the  $WH$  process, Table 8.3 for the quark-initiated  $ZH$  process, and Table 8.4 for the gluon-initiated  $ZH$  process. Since the analysis is performed in both a 2-jet and 3-jet signal region, an additional uncertainty to account for the lack of knowledge of the ratio between the number of events in each region is included when scaling the  $ZH$  cross section

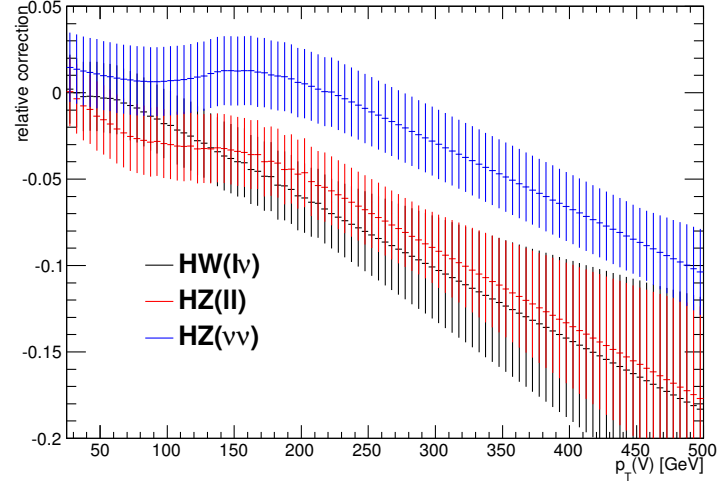


Figure 8.3: Relative NLO electroweak corrections to signal cross sections and the size of the associated uncertainties are shown as a function of  $p_T^V$  as calculated from the HAWK Monte Carlo generator.

$WH \rightarrow \ell\nu H$	[0,90]	[90-120]	[120-150]	[150-200]	> 200
$\Delta_{\text{EW}}$	-7.1%	-8.6%	-9.9%	-11.4%	-14.7%
$\delta_{\text{EW}}$	-0.4%	-2.0%	-3.4%	-5.0%	-8.6%
uncertainty	2.0%	2.0%	2.0%	2.0%	2.6%
$ZH \rightarrow \ell\ell H$	[0,90]	[90-120]	[120-150]	[150-200]	> 200
$\Delta_{\text{EW}}$	-6.7%	-8.0%	-8.3%	-9.0%	-12.2%
$\delta_{\text{EW}}$	-1.6%	-3.1%	-3.3%	-4.2%	-7.5%
uncertainty	2.0%	2.0%	2.0%	2.0%	2.2%
$ZH \rightarrow \nu\nu H$	[0,90]	[90-120]	[120-150]	[150-200]	> 200
$\Delta_{\text{EW}}$	-4.1%	-4.4%	-4.0%	-4.1%	-6.4%
$\delta_{\text{EW}}$	+1.0%	+0.7%	+1.1%	+1.1%	-1.4%
uncertainty	2.0%	2.0%	2.0%	2.0%	2.0%

Table 8.1: For all three 8 TeV processes  $WH \rightarrow \ell\nu b\bar{b}$ ,  $ZH \rightarrow \ell\ell b\bar{b}$ , and  $ZH \rightarrow \nu\nu b\bar{b}$ , the full NLO EW correction is quoted first ( $\Delta_{\text{EW}}$ ) and then the only difference from the inclusive to the differential cross section ( $\delta_{\text{EW}}$ ). The latter is the one which needs to be applied on top of the inclusive NNLO QCD+NLO EW cross section. The results are quoted in intervals of  $p_T^W$  (for  $WH$ ) or  $p_T^Z$  (for  $ZH$ ), using the  $p_T$  intervals defined for the analyses.

from leading order to next-to-leading order. The uncertainties on the inclusive cross section are denoted `TheoryQCDscale` and `TheoryPDF` in the statistical model.

$m_H$ (GeV)	7 TeV			8 TeV		
	$\sigma(WH)$ (pb)	Scale (%)	PDF+ $\alpha_s$ (%)	$\sigma(WH)$ (pb)	Scale (%)	PDF+ $\alpha_s$ (%)
115	0.7517	$\pm 0.9$	$\pm 2.4$	0.9266	$\pm 1.0$	$\pm 2.3$
120	0.6617	$\pm 0.9$	$\pm 2.6$	0.8052	$\pm 1.0$	$\pm 2.5$
125	0.5785	$\pm 0.9$	$\pm 2.6$	0.7046	$\pm 1.0$	$\pm 2.3$
130	0.5059	$\pm 0.9$	$\pm 2.6$	0.6169	$\pm 0.9$	$\pm 2.4$
135	0.4431	$\pm 1.0$	$\pm 2.6$	0.5416	$\pm 1.0$	$\pm 2.5$

Table 8.2: NNLO QCD + NLO EW inclusive cross sections and related uncertainties for  $WH$  production quoted from the CERN Yellow Report [87].

$m_H$ (GeV)	7 TeV			8 TeV		
	$\sigma(ZH)$ (pb)	Scale (%)	PDF+ $\alpha_s$ (%)	$\sigma(ZH)$ (pb)	Scale (%)	PDF+ $\alpha_s$ (%)
115	0.4345	$\pm 2.6$	$\pm 2.7$	0.5358	$\pm 2.8$	$\pm 2.5$
120	0.3808	$\pm 2.8$	$\pm 2.8$	0.4710	$\pm 3.0$	$\pm 2.5$
125	0.3351	$\pm 2.9$	$\pm 2.7$	0.4153	$\pm 3.1$	$\pm 2.5$
130	0.2957	$\pm 3.0$	$\pm 2.8$	0.3671	$\pm 3.3$	$\pm 2.5$
135	0.2616	$\pm 3.2$	$\pm 2.8$	0.3259	$\pm 3.5$	$\pm 2.7$

Table 8.3: NNLO QCD + NLO EW inclusive cross sections and related uncertainties for  $ZH$  production quoted from the CERN Yellow Report [87].

### 8.1.3 Uncertainties on the Signal Acceptance

The factorization and renormalization uncertainties for the acceptance of the signal processes are evaluated at truth level using Monte Carlo simulations generated with PowHEG [90] and showered with PYTHIA8. The renormalization ( $\mu_R$ ) and factorization ( $\mu_F$ ) scales were varied independently by factors of 2 and 0.5 in all possible combinations while maintaining  $0.5 \leq \mu_R/\mu_F \leq 2.0$ . Each sample was normalized to

$m_H$ (GeV)	qqZH			ggZH		
	$\sigma$ (pb)	Scale (%)	PDF+ $\alpha_s$ (%)	$\sigma$ (fb)	Scale (%)	PDF+ $\alpha_s$ (%)
115	0.4995	$\pm 1.0$	$\pm 2.3$	36.34	$\pm 50.0$	$\pm 19.0$
120	0.4366	$\pm 1.0$	$\pm 2.5$	34.39	$\pm 50.0$	$\pm 12.8$
125	0.3828	$\pm 1.0$	$\pm 2.3$	32.46	$\pm 50.0$	$\pm 16.9$
130	0.3365	$\pm 1.0$	$\pm 2.4$	30.60	$\pm 50.0$	$\pm 14.2$
135	0.2971	$\pm 1.0$	$\pm 2.5$	28.79	$\pm 50.0$	$\pm 16.4$

Table 8.4: NNLO QCD + NLO EW inclusive cross sections and related uncertainties for  $qq \rightarrow ZH$  and  $gg \rightarrow ZH$  production at 8 TeV derived from the CERN Yellow Report [87].

the nominal cross section to avoid double counting the uncertainties on the inclusive cross section.

After performing a full truth-level event selection, the difference in inclusive yields compared to the nominal  $\mu_R = \mu_F = 1$  sample is used to determine the acceptance uncertainty. In order to treat correlations in the acceptance scale uncertainty between the 2-jet and 3-jet analysis regions, the “Stewart-Tackmann method” [78][108] is used. Following this method, the uncertainty in the 2-jet region consists of two components. The first component is the inclusive 2+3-jet acceptance uncertainty (`TheoryAcc_J2`); the second component is the absolute 3-jet exclusive normalization uncertainty relative to the nominal 2-jet acceptance. This second component is called `TheoryAcc_J3`. In the 3-jet region, there is only one uncertainty from the Stewart-Tackmann procedure that applies, and it is `TheoryAcc_J3`. The uncertainty `TheoryAcc_J3` is anti-correlated between the 2-jet and 3-jet regions so that the total yield of the 2-jet region plus the 3-jet region is preserved when varying that parameter in the profile likelihood fit. The values for the uncertainties are given in Table 8.5.

The uncertainty due to the parton distribution functions (PDF) is calculated from samples generated with PowHEG and showered with PYTHIA8 using the MSTW2008 NLO68CL [93] and NNPDF23\_NLO\_AS\_0120 [63] PDF set central value members, as recommended by the PDF4LHC [53] Working Group. After performing a full truth-level analysis, the varied sample yields are compared to the nominal sample made with the CT10NLO [85] central value PDF set members to derive uncertainties on the acceptance yields stated in Table 8.5 (TheoryAccPDF). Comparing different PDF sets rather than comparing individual PDF errors within the same set provides a more conservative estimate of the uncertainty.

Process	PDF		Scale		
	2-jet [%]	3-jet [%]	2+3-jet [%]	3-jet rel. 2-jet [%]	3-jet rel. 3-jet [%]
$WH$	$\pm 3.5$	$\pm 2.8$	$\pm 3.0$	$\mp 1.1$	$\pm 4.2$
$qq \rightarrow ZH$	$\pm 3.0$	$\pm 5.0$	$\pm 3.4$	$\mp 0.9$	$\pm 3.6$
$gg \rightarrow ZH$	$\pm 2.1$	$\pm 3.4$	$\pm 1.5$	$\mp 1.8$	$\pm 3.3$

Table 8.5: Inclusive acceptance uncertainties derived from scale and PDF variations.

### 8.1.4 QCD Uncertainties on the Signal $p_T^V$

The factorization and renormalization scale uncertainties for the  $p_T^V$  shape of the signal (`TheoryVPtQCD`) are calculated by comparing a number of different Monte Carlo simulations as in Section 8.1.3. In this case, a linear fit was made to the  $p_T^V$  distribution that forms an envelope around the most-discrepant Monte Carlo relative to the nominal Monte Carlo simulation.

As an example, Figure 8.4 shows the  $p_T^V$  distribution for  $qq \rightarrow WH$  (a),  $qq \rightarrow ZH$  (b), and  $gg \rightarrow ZH$  (c) for 2-jet events.

The functional form for the linear fit is

$$f(p_T^V) = 1 \pm \left( a + b \frac{p_T^V}{400 \text{ GeV}} \right) \quad (8.1)$$

with  $a$  and  $b$  given in Table 8.6 for each of the processes.

Process	Region	$a$	$b$
$qq \rightarrow VH$	2-jet	-0.02	0.10
$qq \rightarrow VH$	3-jet	-0.03	0.13
$gg \rightarrow ZH$	2+3-jet	-0.05	0.25

Table 8.6: Parameters for the linear fit of Equation 8.1 for the  $p_T^V$  shape uncertainty for renormalization and factorization scales.

To measure the contribution of the PDF uncertainty to the  $p_T^V$  uncertainty, additional Monte Carlo samples are generated with PowHEG and showered with PYTHIA8 using the MSTW2008NLO68CL [93] and NNPDF23\_NLO\_AS\_0120 [63] PDF set central value members, as recommended by the PDF4LHC [53] Working Group. After performing a full truth-level analysis, and comparing the resulting  $p_T^V$  distribution to the nominal sample made with the CT10NLO [85] PDF set, no additional uncertainty

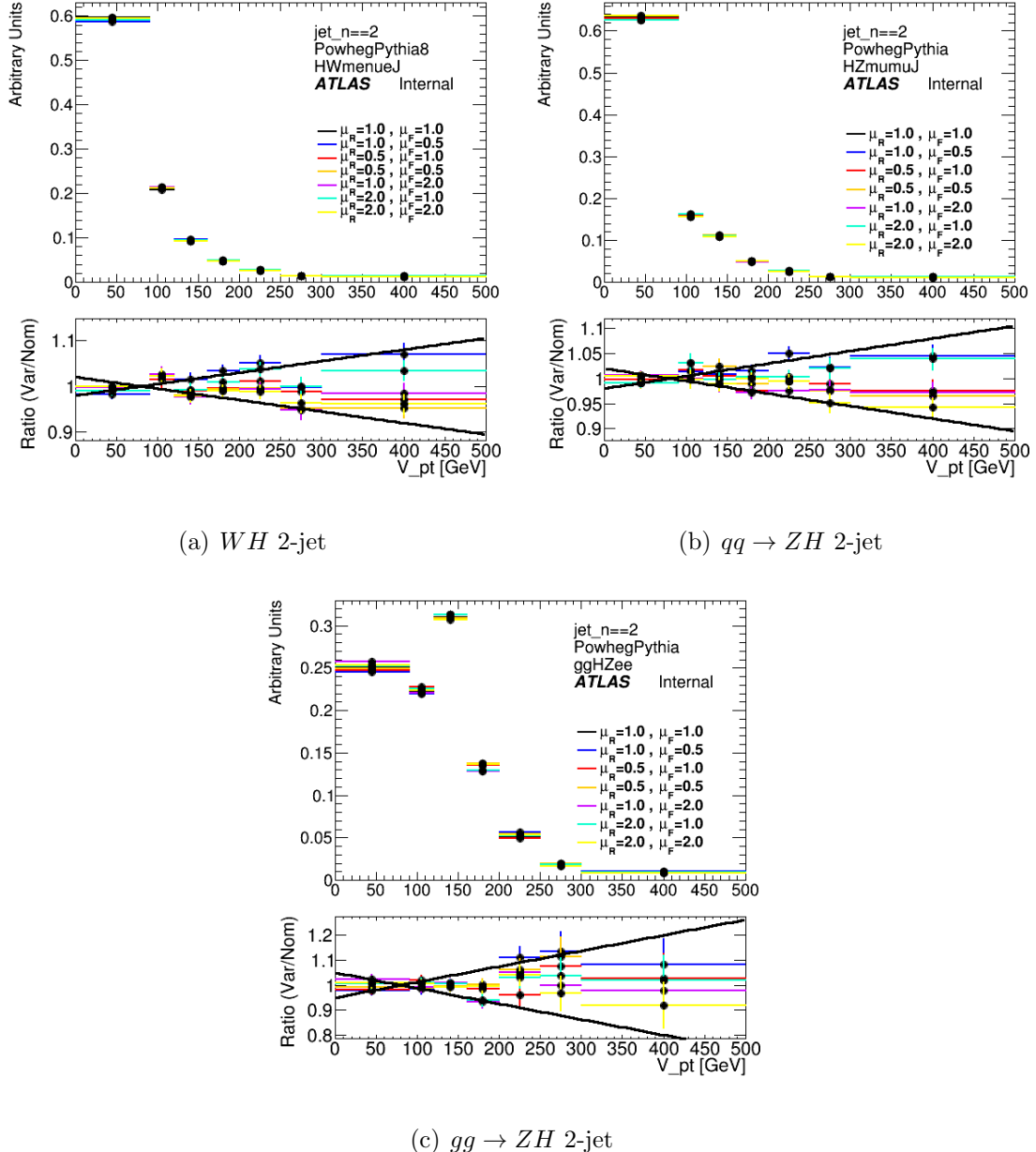


Figure 8.4: Normalized  $p_T^V$  distributions after truth-level selection for  $WH$ ,  $qq \rightarrow ZH$ , and  $gg \rightarrow ZH$  scale uncertainty studies on the 1<sup>st</sup>, 2<sup>nd</sup>, and 3<sup>rd</sup> row respectively.

was found. Figure 8.5 shows a comparison between the  $p_T^V$  distributions made from the nominal and varied PDF sets. The bottom panel in each figure shows the ratio in each bin.

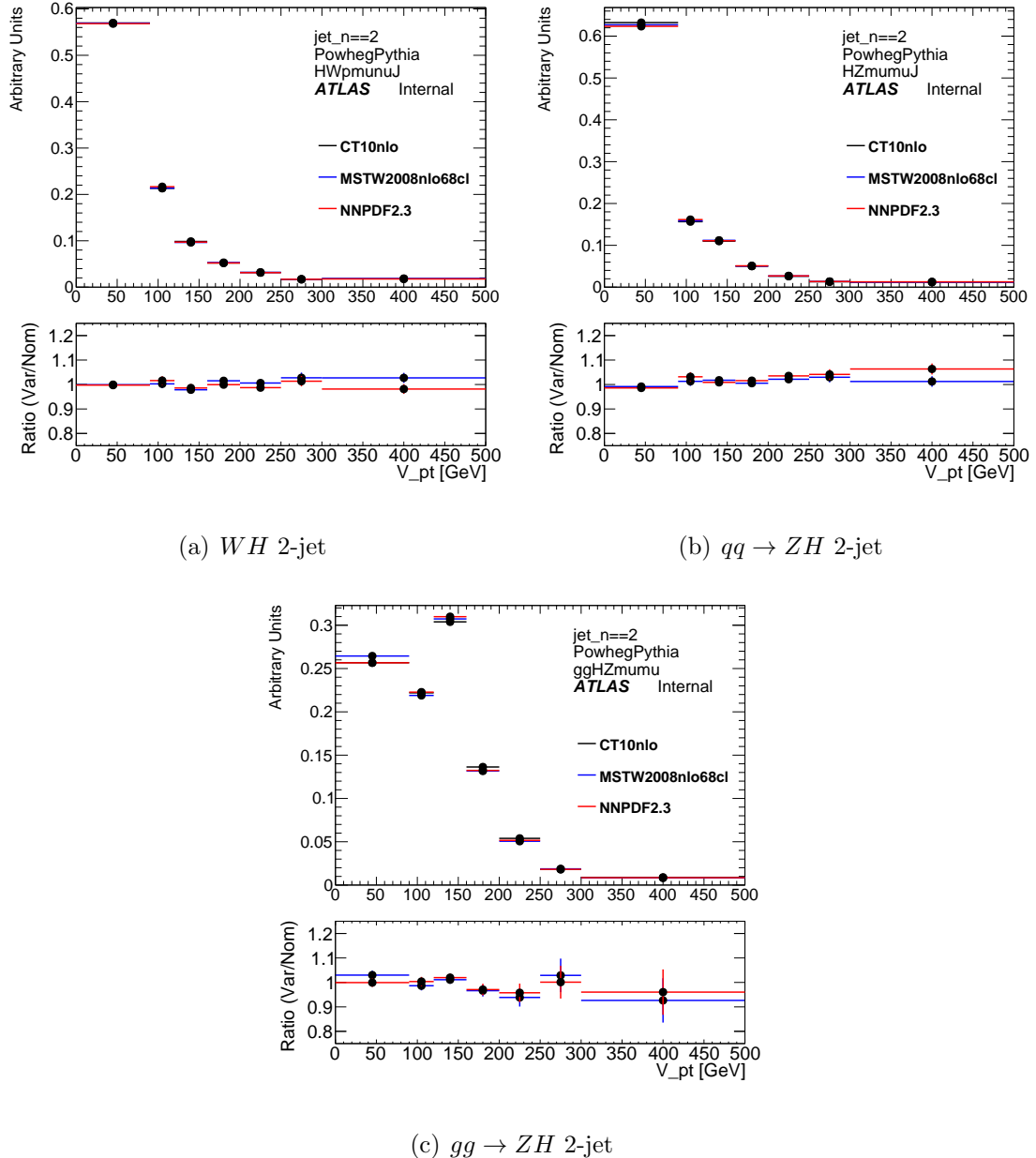


Figure 8.5: Normalized  $p_T^V$  distributions after truth-level selection for  $WH$ ,  $qq \rightarrow ZH$ , and  $gg \rightarrow ZH$  PDF uncertainty studies.

## 8.2 Modeling of the Background Processes

This section provides details on the modeling of all background processes relevant to the 2-lepton channel. The most important backgrounds by total yield to the signal regions are  $Z$ +jets and  $t\bar{t}$  pair production. These backgrounds account for, at a minimum, 95% of the total background in any analysis region, as will be shown in Chapter 9. Section 8.2.1 discusses the modeling and uncertainties related to the  $Z$ +jets background, and Section 8.2.2 discusses the modeling and uncertainties corresponding to the  $t\bar{t}$  process. In addition to these two backgrounds, the production of diboson pairs -  $WW$ ,  $WZ$ , and  $ZZ$  - are important because hadronically-decaying  $Z$ -bosons create a peak in the invariant mass spectrum that is overlapping with the peak of the Higgs boson. These backgrounds are discussed in Section 8.2.3. Finally, the remaining sections of this chapter discuss the contributions from single-top processes, QCD multijet production, and  $W$ +jets production.

### 8.2.1 Modeling of the $Z$ +jets Background

The  $Z$ +jets processes are modeled with the SHERPA event generator [80], and three separate and exclusive categories of samples are generated: one with  $\geq 1$   $b$ -quark, one with  $\geq 1$   $c$ -quark, and one with  $\geq 1$   $l$ -quark (light-flavor quark). This is done to increase the statistics for the heavy-flavor samples. Aside from reducing the statistical uncertainty in the analysis, another motivation for splitting the generation of these processes is to allow detailed studies of the modeling of important kinematic variables in the  $VH$  system in a flavor-dependent manner. As each process has different kinematic properties, such as the shape of the  $\Delta\phi$  distribution between the Higgs

candidate's jets or the  $p_T^V$  distribution, studying them independently allows for more precise corrections to be made to the simulation. Furthermore, since the analysis relies on the  $b$ -tagging of jets to define the analysis regions, the modeling of the flavor fractions in each analysis region must be well-understood. In order to study the quality of the modeling, a kinematic region is selected that is relatively pure in  $Z$ +jets, and also rejects the signal-rich and diboson-rich region from  $100 \text{ GeV} < m_{b\bar{b}} < 150 \text{ GeV}$ . Otherwise, the kinematic cuts of this control region are identical to those presented in Section 7.4.5. The composition of these control regions in terms of the contributions of  $Z$ +light flavor jets,  $Z$ +heavy flavor jets, and top pair production backgrounds is given in Table 8.7.

process	0tag (%)	tag (%)	2tag (%)
$Z$ +light flavor	85	46	12
$Z$ +heavy flavor	12	50	69
$t\bar{t}$	0.07	1.5	12

Table 8.7: Sample composition for  $Z$ +jets modeling studies using the selection described in Section 8.2.1.

The following sections discuss two corrections to the simulation for mismodeling of the  $Z$ +jets background: one for the  $\Delta\phi$  distribution, and one for the  $p_T^Z$  distribution. Corresponding systematic uncertainties are derived for these corrections. Additionally this section discusses uncertainties for the ratio of events in the 2-jet and 3-jet analysis regions, for the fraction of events of each flavor in the sample, and for the  $m_{b\bar{b}}$  shape.

## 2-jet to 3-jet Ratio, Flavor Fractions

In order to understand the limitations of the Monte Carlo description of the number of jets and fractions of each jet flavor in the  $Z$ +jet background contribution, comparisons between the data and Monte Carlo simulation are made separately for the 2-jet and the 3-jet categories. To constrain the uncertainty on the  $Z$ +light jet component, the region with 0  $b$ -tags is studied.

The ratio of the yields in data and Monte Carlo simulation for the 0-tag 2-jet and 0-tag 3-jet regions at low and high  $p_T^Z$  are given in Table 8.8. A value of 5% is taken for the  $Z$ +light normalization uncertainty (`Z1Norm`) as well as for the uncertainty on the ratio of 2-jet to 3-jet production (`Z1Norm_3J`). The normalizations for the other jet flavors (jet flavors = cl, cc, bl, bc, bb), are determined from the profile likelihood fit.

$p_T^Z$	N Jet	Data/MC
$p_T^Z < 120 \text{ GeV}$	2	$1.018 \pm 0.002$
	3	$0.994 \pm 0.004$
$p_T^Z > 120 \text{ GeV}$	2	$1.016 \pm 0.005$
	3	$1.014 \pm 0.007$

Table 8.8: Yield ratios for 2-lepton 0tag events used to derive the 3/2-jet ratio systematic.

To estimate the uncertainty on the 2-jet to 3-jet production ratios for the  $Z$ +heavy processes, the SHERPA Monte Carlo prediction for the event yield in these categories is compared to the yield from ALPGEN . This comparison is considered to produce a robust estimate of the uncertainty because the two generators use different characterizations for the underlying event, parton showering, and hadronization. The region

studied is the 2-tag region, combining the LL, MM, and TT categories.

The yield ratios in the 2-jet and 3-jet categories for the  $Z+$ heavy processes are shown in Table 8.9. The process with the two final state jets of flavor  $b$  and  $c$  ( $bc$ ) is taken to have the same uncertainty as the process with two final state jets of flavor  $b$  and  $b$  ( $bb$ ). The systematic uncertainty on the relative fractions of the flavor composition in the heavy flavor samples is obtained through the same SHERPA and ALPGEN comparison. Table 8.10 shows the comparison of the relative heavy flavor fractions in the 2-tag region for each generator.

In summary, the systematic uncertainties are:

- Uncertainties on the modeling of the 3/2-jet ratio

$Z+l$ : 5% (`ZlNorm_3J`)

$Z+cl$ : 26% (`ZclNorm_3J`)

$Z+(cc,bl,bc,bb)$ : 13% (`ZbbNorm_3J`)

- Uncertainty on the relative heavy flavor composition in  $Z+2$ -jet and  $Z+3$ -jet events

$Z+bl$  to  $Z+bb$ : 10% (`ZblZbbRatio`)

$Z+bc$  to  $Z+bb$ : 20% (`ZbcZbbRatio`)

$Z+cc$  to  $Z+bb$ : 20% (`ZccZbbRatio`)

## **$\Delta\phi$ Correction**

The variable  $\Delta\phi$  is sensitive to final state radiation from the  $b$ -quark and its hadronization process. Figure 8.6 shows that the shape of this distribution is not

$p_T^Z$	N Jet	ALPGEN	SHERPA	% difference
yield of bl / yield of bb				
$p_T^Z > 0$ GeV	2+3	0.207	0.225	-7.6
$p_T^Z > 120$ GeV	2+3	0.241	0.238	1.4
$p_T^Z > 0$ GeV	2	0.196	0.212	-7.4
$p_T^Z > 0$ GeV	3	0.243	0.270	-9.9
yield of cc / yield of bb				
$p_T^Z > 0$ GeV	2+3	0.161	0.146	9.9
$p_T^Z > 120$ GeV	2+3	0.110	0.133	-17.5
$p_T^Z > 0$ GeV	2	0.155	0.144	-7.2
$p_T^Z > 0$ GeV	3	0.178	0.151	17.7

Table 8.9: ALPGEN and SHERPA heavy-flavor jet multiplicity yield comparison in 2-lepton 2tag events used to derive the 3/2-jet ratio systematic.

Jet Flavors	ALPGEN	SHERPA	difference (%)
bb,bc,cc	0.318	0.280	13.3
bl	0.394	0.357	10.3
cl	0.480	0.382	25.7

Table 8.10: Yield ratios for 2-lepton 2tag events in ALPGEN and SHERPA . These ratios are used to derive the heavy-flavor fraction systematic.

well-modeled by the Monte Carlo in the 0-tag analysis region, but in the 1-tag and 2-tag region, no statistically significant shape discrepancy is observed. Overall normalization discrepancies are adjusted during the profile likelihood fit. This motivates a shape correction to be applied to the  $Z$ +light samples, but not to the  $Z$ +heavy flavor samples. The correction is derived by fitting a function  $a(1+bx)$  to the ratio of the non- $Z$ -background-subtracted data over the  $Z$ +jets simulation in the 0tag region. An example of the correction fit is shown in Figure 8.7 in the region with  $p_T^Z < 120$  GeV. The correction is derived separately for two ranges of  $p_T^Z$ . A corresponding systematic uncertainty of half this correction value is called **ZDPhi** and is considered in the statistical model for the  $Z$ +light background. For the  $Z$ +heavy flavor backgrounds, the low statistics in the data prevent the observation of a significant discrepancy in the modeling of the  $\Delta\phi$  distribution. Therefore no correction is made to the  $Z$ +heavy flavor samples, and 100% of the correction value applied to the  $Z$ +light sample is taken as the systematic uncertainty for these samples. The correction values applied to the  $Z$ +light sample and used as a systematic uncertainty on the  $Z$ +light and  $Z$ +heavy flavor samples are:

- $0.863(1 + 0.0863\Delta\phi)$  for  $p_T^Z < 120$  GeV,
- $0.933(1 + 0.0316\Delta\phi)$  for  $p_T^Z > 120$  GeV.

### $p_T^Z$ Correction

Given that the analysis is performed in 5 bins of  $p_T^Z$  it is important that this distribution is well-modeled by the Monte Carlo. After the application of the  $\Delta\phi$

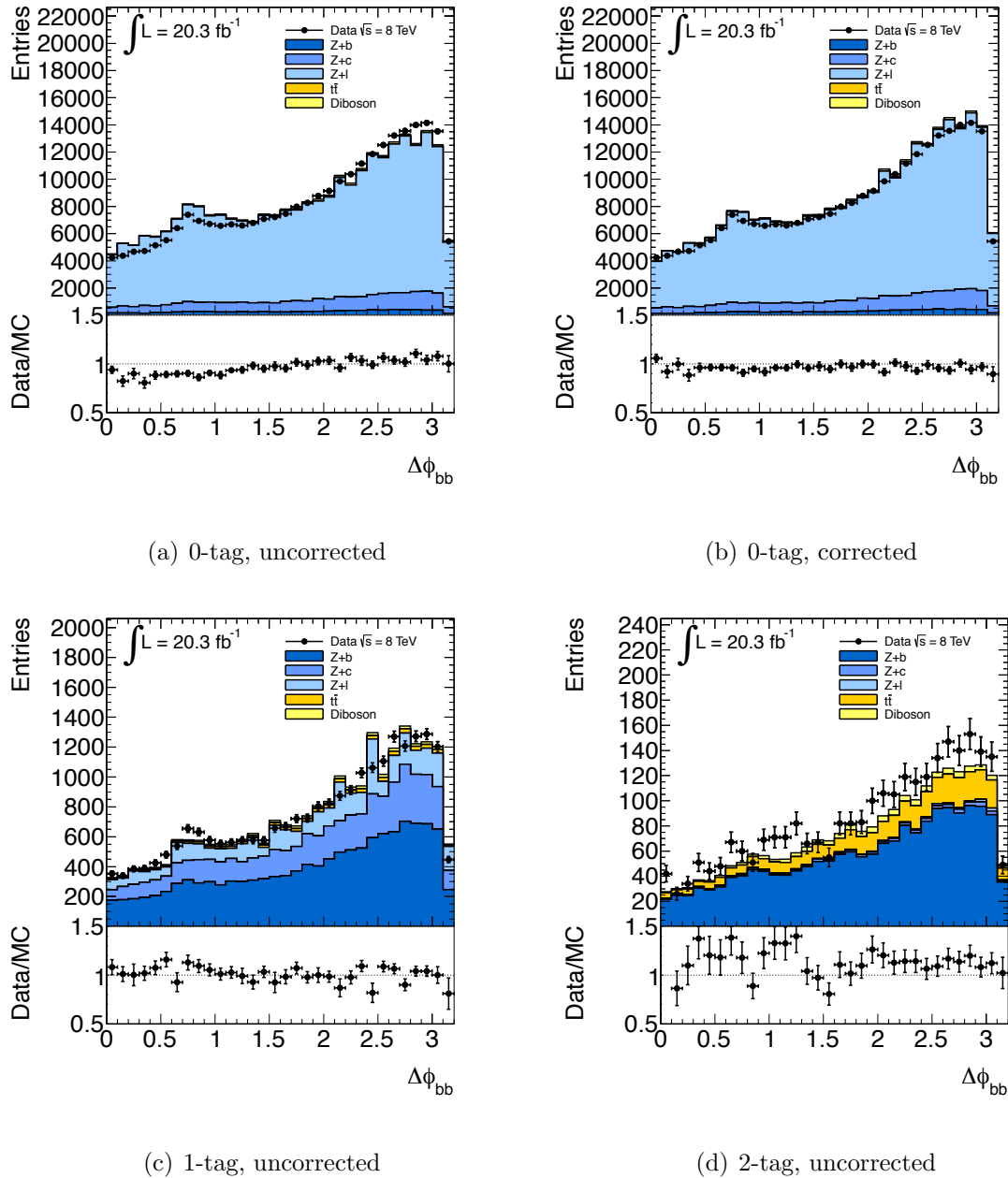


Figure 8.6: The  $\Delta\phi$  distribution in the 0tag, 1tag, and 2tag regions. Subfigure (a) shows the 0tag region before correction, while (b) shows the same region after the correction has been applied.

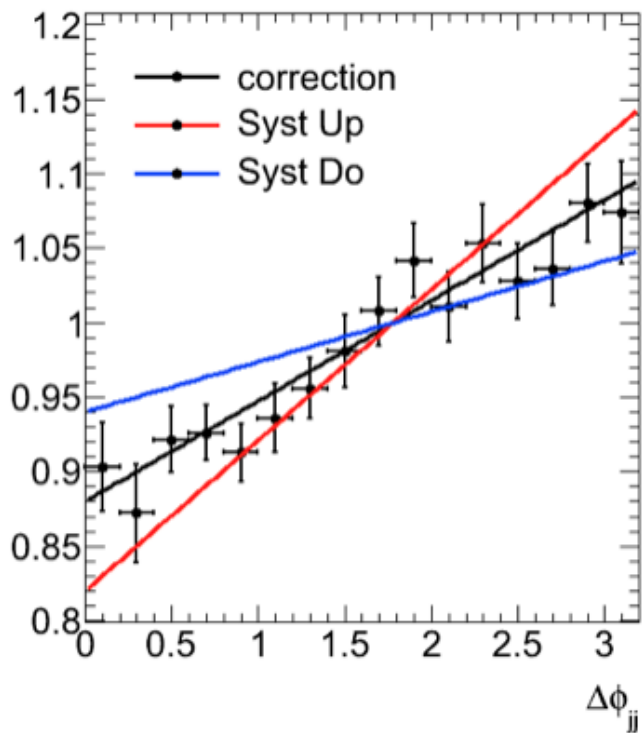


Figure 8.7:  $\Delta\phi$  correction for the  $Z+jets$  background. The data points represent the ratio of data/MC in the 0-tag analysis region for the 2-lepton analysis, where the contribution from the non- $Z+jets$  backgrounds have been subtracted from both data and the MC before taking the ratio. The black line is a linear fit to this ratio, which defines the correction. Systematic variations of 150% and 50% of the correction value are shown as red and blue lines, respectively.

correction, the modeling of the  $p_T^Z$  distribution is studied. Figure 8.8 shows the  $p_T^Z$  distribution. The yield of the Monte Carlo processes other than  $Z + \text{jets}$  is subtracted, and the data points are the data values in each bin after the same subtraction of non- $Z + \text{jets}$  background is performed. The underlying assumption is that any mismodeling of the  $p_T^Z$  distribution for non- $Z + \text{jets}$  background has a negligible effect, given the purity of this control region. Figure 8.8 indicates that the mismodeling of the  $p_T^Z$  distribution worsens as more  $b$ -tags are required. This motivates a correction to be derived and implemented only in the region with 2  $b$ -tags that contain much of the  $Z + bb$  and  $Z + cc$  yield, but a systematic uncertainty is calculated for all regions. The correction is derived by fitting the bottom panel of the 2-tag region in Figure 8.8 with the function  $a + b \log(p_T^Z)$ , combined with a constant correction for  $p_T^Z < 10 \text{ GeV}$ . Each event in Monte Carlo is scaled with the correction value, which is parametrized according to the functional form below:

- $1.40 - 0.0975 \log(10.0) = 1.30$  below  $10 \text{ GeV}$
- $1.40 - 0.0975 \log(p_T^Z)$  above  $10 \text{ GeV}$

A systematic uncertainty of half this correction value is called ZPtV and is considered in the statistical model for  $Z + \text{light}$  and  $Z + \text{heavy}$  flavor.

### Systematic Uncertainty on the $m_{b\bar{b}}$ Shape

Since the analysis relies on the modeling of the  $m_{b\bar{b}}$  distribution, it is important to have a prior measurement on the uncertainty of the  $m_{b\bar{b}}$  shape for each background process. In order to measure the uncertainty on  $m_{b\bar{b}}$  shape in the 2-lepton channel,

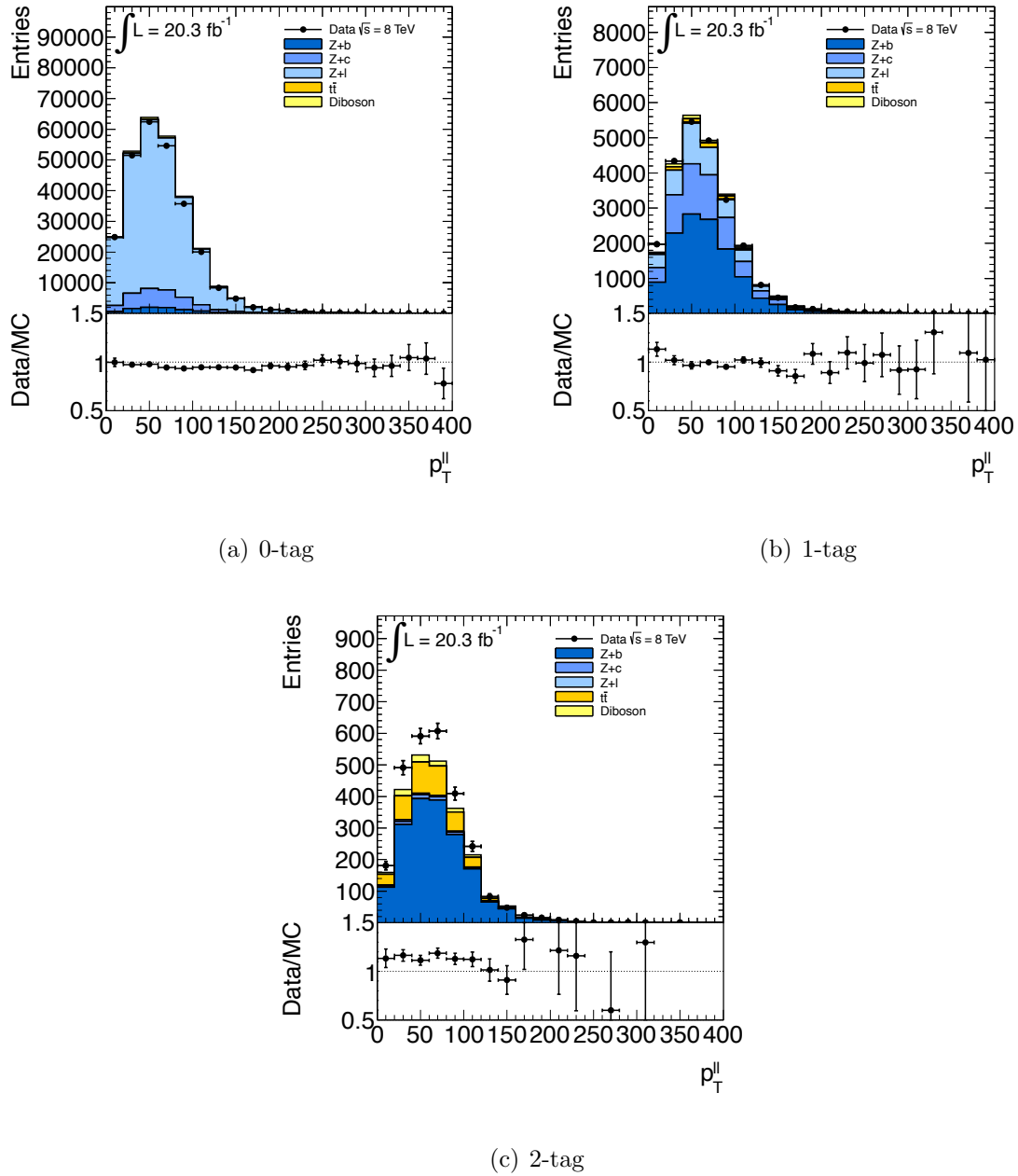


Figure 8.8: A data-driven  $p_T^Z$  correction is derived from data to Monte Carlo ratios for  $Z+\text{heavy flavor}$  events, motivated by the observed increase in the shape discrepancy with increasing number of  $b$ -tags. The overall normalization discrepancies are accounted for during the profile likelihood fit.

the three tagging regions (LL, MM, TT) are combined to yield greater statistics to make a comparison between the data and Monte Carlo simulation. Furthermore, the region of  $80 < m_{b\bar{b}} < 140$  GeV is excluded to avoid contamination from the signal process. A systematic uncertainty on this distribution is set by using the functional form of  $a(m_{b\bar{b}} \times 10^{-3} - b)$  to form an envelope for the ratio of data over the Monte Carlo prediction. The systematic is called **ZMbb** and applied to all  $Z + \text{jets}$  events, but  $Z + \text{light}$  is decorrelated from the other jet flavors.

Figure 8.9 shows the comparison of data to Monte Carlo simulation in the 0-tag, 1-tag, and 2-tag regions of the 2-lepton analysis.

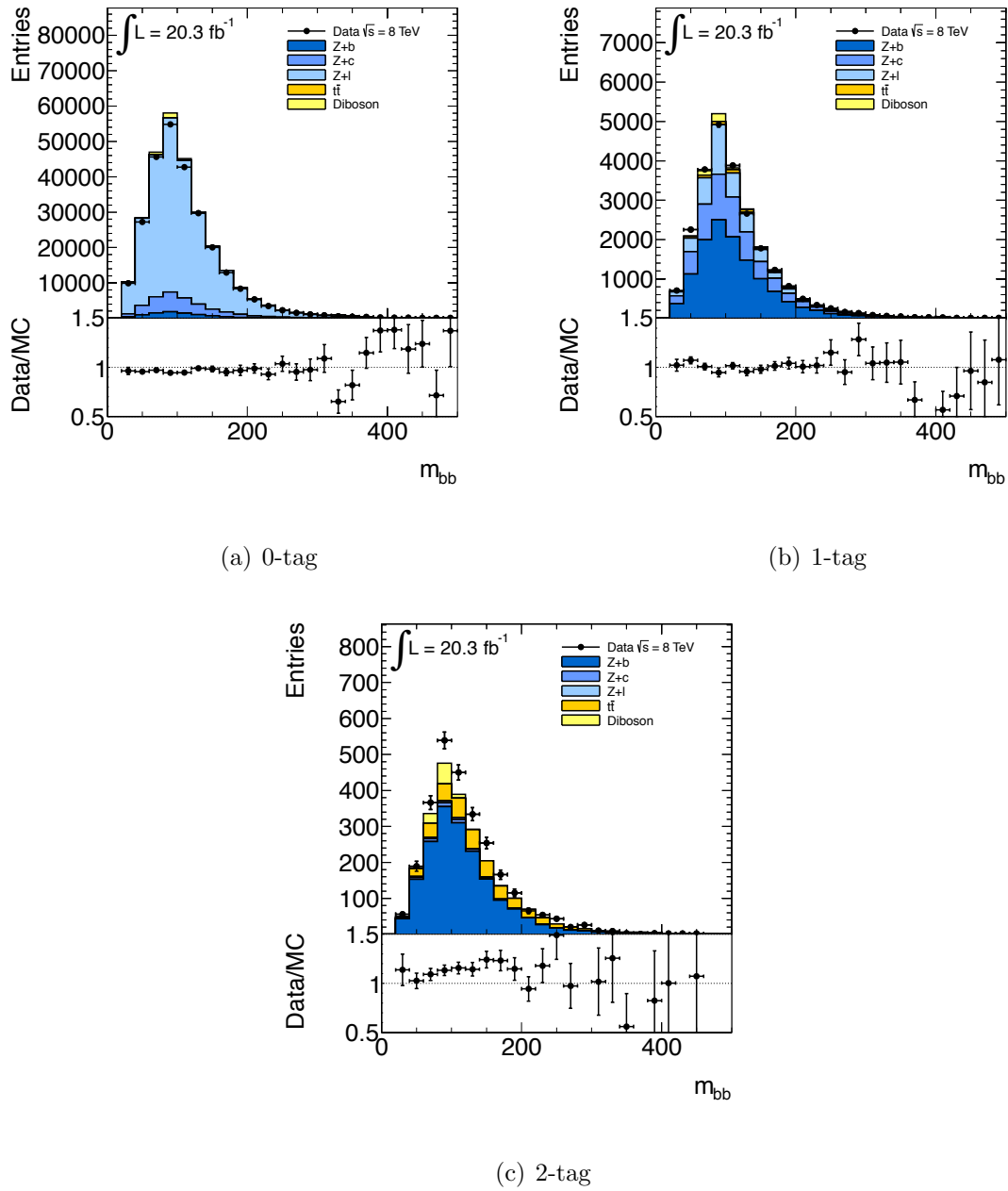


Figure 8.9:  $m_{jj}$  distribution in  $Z$ +jets events from which a systematic uncertainty on the Monte Carlo modeling of the  $m_{b\bar{b}}$  shape has been derived. Furthermore, the 0-tag control region is used to set the uncertainty on the normalization of  $Z$ +light jet events.

### 8.2.2 Modeling of the $t\bar{t}$ Background

After  $Z$ +heavy flavor processes, the production of  $t\bar{t}$  pairs is the background process that contributes the greatest number of events to the signal regions of the analysis. The production of  $t\bar{t}$  pairs is generated with PowHEG [105, 97, 99] and interfaced to PYTHIA for the parton showering and hadronization. An event filter requires at least one of the  $W$ -bosons from the two top decays to be leptonic in order to increase the statistics in the analysis regions. The parton showering and hadronization is generated according to the *Perugia2011C* tune and uses the CTEQL1 PDF set. As for all of the backgrounds in this analysis, the features of the top background which are most important to model accurately are the  $p_T^V$  distribution, the relative normalizations of the 2-jet and 3-jet analysis regions, and the shape of the  $m_{jj}$  distribution. For the 2-lepton analysis, a top-enriched control region was defined in Section 7.4.5 by requiring one electron and one muon rather than two leptons of the same flavor.

#### Top $p_T$ Correction

To provide the most accurate description of the  $p_T$  distribution of the top background contributing to the analysis regions used in the profile likelihood fit, the results of a dedicated study on differential top cross sections are incorporated [47]. Figure 8.10 displays this measurement of the differential top-quark-pair cross section as a function of the average  $p_T$  of the top quarks in the event. The comparison of the data to several Monte Carlo simulations shows that the distribution of the top  $p_T$  is harder in the simulation than in the data. From that study, a correction was derived to correct the  $p_T$  distribution in simulation to agree with the distribution in data.

The correction scales events by a scale factor that is a function of the average  $p_T$  of the top quarks in the event. The full details of the correction are left to Reference [7] and the scale factors are summarized in Table 8.11. A systematic uncertainty on the shape of the  $p_T^Z$  distribution from the  $t\bar{t}$  background is taken to be half the correction value and called TopPt. Although the 2-lepton channel's  $e - \mu$  control region does not have sufficient statistics to observe significant improvements from this correction, the 1-lepton channel presented in Chapter 11 suggests that modeling is improved.

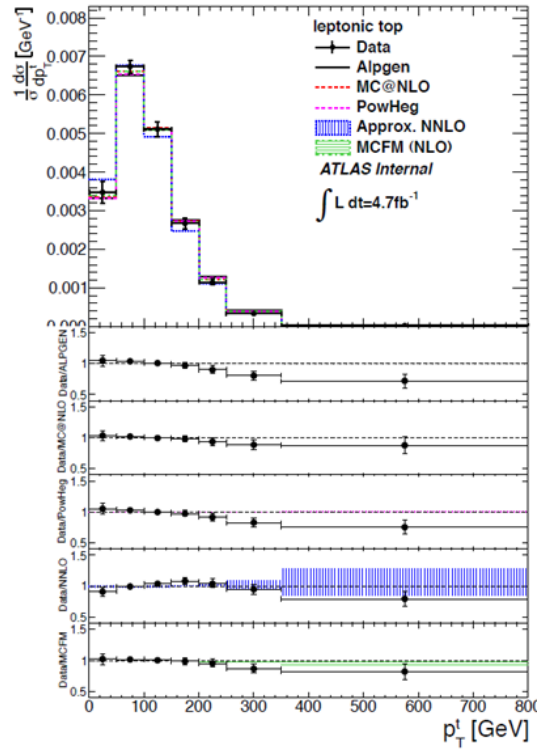


Figure 8.10: The top  $p_T$  differential cross section with the 7 TeV dataset is shown for several Monte Carlo Simulations. Disagreement between data and Monte Carlo motivates correcting the  $p_T$  of the top quarks to improve the modeling of the top background for the analysis presented in this thesis.

### Uncertainty on the 2-jet to 3-jet Ratio

As it is difficult to create a relatively pure control region for  $t\bar{t}$  background in the data for the 0-lepton and 1-lepton analyses presented in Chapter 11, the uncertainty on the 2-jet to 3-jet yield ratios for those channels is made with a comparison of Monte Carlo generators. To aid in the combination of the channels, the 2-lepton channel also estimates the uncertainties in the same way. The Monte Carlo generators used for systematic studies are:

- PowHEG+PYTHIA8 with the CTEQL1 PDF PDFs is the nominal sample,
- PowHEG+PYTHIA8 interfaced with the HERA PDF set instead of CTEQL1 PDF,
- ALPGEN, which is only a leading-order (LO) generator (POWHEG is NLO),
- PowHEG+HERWIG to test a different hadronization model than PYTHIA,
- aMC@NLO, to compare the effects of different matrix element calculations.

The ratio of the yield of 3-jet events to the yield of 2-jet events was compared for each of the generators and the results are shown in Table 8.12. A systematic uncertainty on this ratio is taken from the largest difference between any generator

top $p_T$ (GeV)	0-50	50-100	100-150	150-200	200-250	250-350	350-
Weight	$1.05^{+0.09}_{-0.08}$	$1.03^{+0.03}_{-0.03}$	$1.0^{+0.04}_{-0.04}$	$0.98^{+0.05}_{-0.05}$	$0.92^{+0.06}_{-0.07}$	$0.80^{+0.07}_{-0.07}$	$0.75^{+0.12}_{-0.12}$

Table 8.11: The event weight for the top  $p_T$  correction from the unfolding measurement. The values are corrections to the differential cross section in bins of the transverse momentum of the top quark.

and the nominal sample. In this case the largest difference (20%) comes from the ALPGEN generator. In the profile likelihood fit this uncertainty is represented by `ttbarNorm_J3`.

### Residual $p_T^Z$ Uncertainty

After correcting the  $p_T$  of the top quarks in the event according to the method outlined in the previous section, the  $p_T^V$ -distribution may still have some residual mismodeling, and this must be accounted for since the analysis is split into many regions of  $p_T^V$ . This uncertainty is derived through the same comparison of generators as shown above for the other  $t\bar{t}$  uncertainties. The yield in the high- $p_T^V$  region is compared to the yield in the low- $p_T^V$  region for each generator. The split is again performed in only two regions of  $p_T^V$  in order to allow sufficient statistical power for a comparison of generators at high- $p_T^V$ . A systematic uncertainty is derived by taking the relative difference between the nominal sample and the ALPGEN generator, which has the largest disagreement with the nominal sample. The size of the uncertainty is 8% and in the profile likelihood fit, it is represented by `ttbarHighPtV`. Table 8.13 shows the ratio of the number events in the 2-tag 2+3 jet analysis region with  $p_T^V > 120$  GeV to the number of events with  $p_T^V < 120$  GeV for the generators listed above. The numbers in Table 8.13 correspond to the case where  $p_T^V$  is  $p_t^W$ , because the analysis in Chapter 11 is more sensitive to the top background. The assumption that these uncertainties also cover the case where  $p_T^V = p_T^Z$  is validated by the results of Chapter 9.

Generator	3-jet/2-jet	ratio to PowHEG+PYTHIA
PowhegPythia with top $p_T$ reweighting	1.854	1.00
MC@NLO	1.872	1.01
PowhegHerwig	1.890	1.019
PowhegPythia with HERAPDF	1.841	0.99
AlpgenPythia	1.481	0.80

Table 8.12:  $t\bar{t}$  3-to-2-jet uncertainty, derived from the largest difference to the nominal Monte Carlo. This is ALP-GEN+PYTHIA for the 3-to-2-jet uncertainty.

Generator	Yield (high $p_T^Z$ )/(low $p_T^Z$ )	ratio to PowHEG+PYTHIA
PowhegPythia with top $p_T$ reweighting	0.193	1.00
MC@NLO	0.207	1.07
PowhegHerwig	0.191	0.99
PowhegPythia with HERAPDF	0.197	1.02
AlpgenPythia	0.208	1.08

Table 8.13:  $t\bar{t} p_T^V$  uncertainty, taken from the largest difference to the nominal Monte Carlo. This is ALPGEN+PYTHIA. The cutoff between high and low  $p_T^Z$  regions is 120 GeV.

### Systematic Uncertainty on the $m_{b\bar{b}}$ Shape

An uncertainty on the  $m_{jj}$  shape for the  $t\bar{t}$  pair production background is estimated by studying the  $m_{jj}$  distribution in all of the generators listed above, as done for the 3-jet to 2-jet ratio uncertainty. In the case of the  $m_{jj}$  distribution ALPGEN again produces the greatest difference with respect to the nominal Monte Carlo simulation. Because the  $m_{jj}$  shape may be different in the 2-jet and the 3-jet regions, and also in different “ $p_T^Z$ ” regimes, the shape is studied separately in each of the four regions. The split between the  $p_T^V$  regions is at 120 GeV, which allows sufficient statistics for the higher  $p_T^V$  range to be studied. Figure 8.11 shows the  $m_{jj}$  distribution in each region, compared for a variety of Monte Carlo generators. To parametrize the uncertainty as a continuous function of  $m_{jj}$ , a linear fit is made to ratio of the nominal Monte Carlo to ALPGEN. The results of this linear fit are shown in Table 8.14. In the profile likelihood fit, this uncertainty is represented by `TtbarMBBCont`.

Analysis Region	constant term	slope(for $m_{jj}$ in GeV)
2-jet $p_T^Z < 120$ GeV	-0.008	$1.26^{-4}$
2-jet $p_T^Z > 120$ GeV	-0.049	$3.05^{-4}$
3-jet $p_T^Z < 120$ GeV	+0.011	$-3.56^{-5}$
3-jet $p_T^Z > 120$ GeV	+0.030	$-2.56^{-4}$

Table 8.14: Parameter values for the  $m_{jj}$  shape systematic uncertainties for the  $t\bar{t}$  process in four analysis regions. These parameters are for a linear fit of the form  $\Delta(m_{jj}) = \text{constant term} + \text{slope} \times m_{jj}$

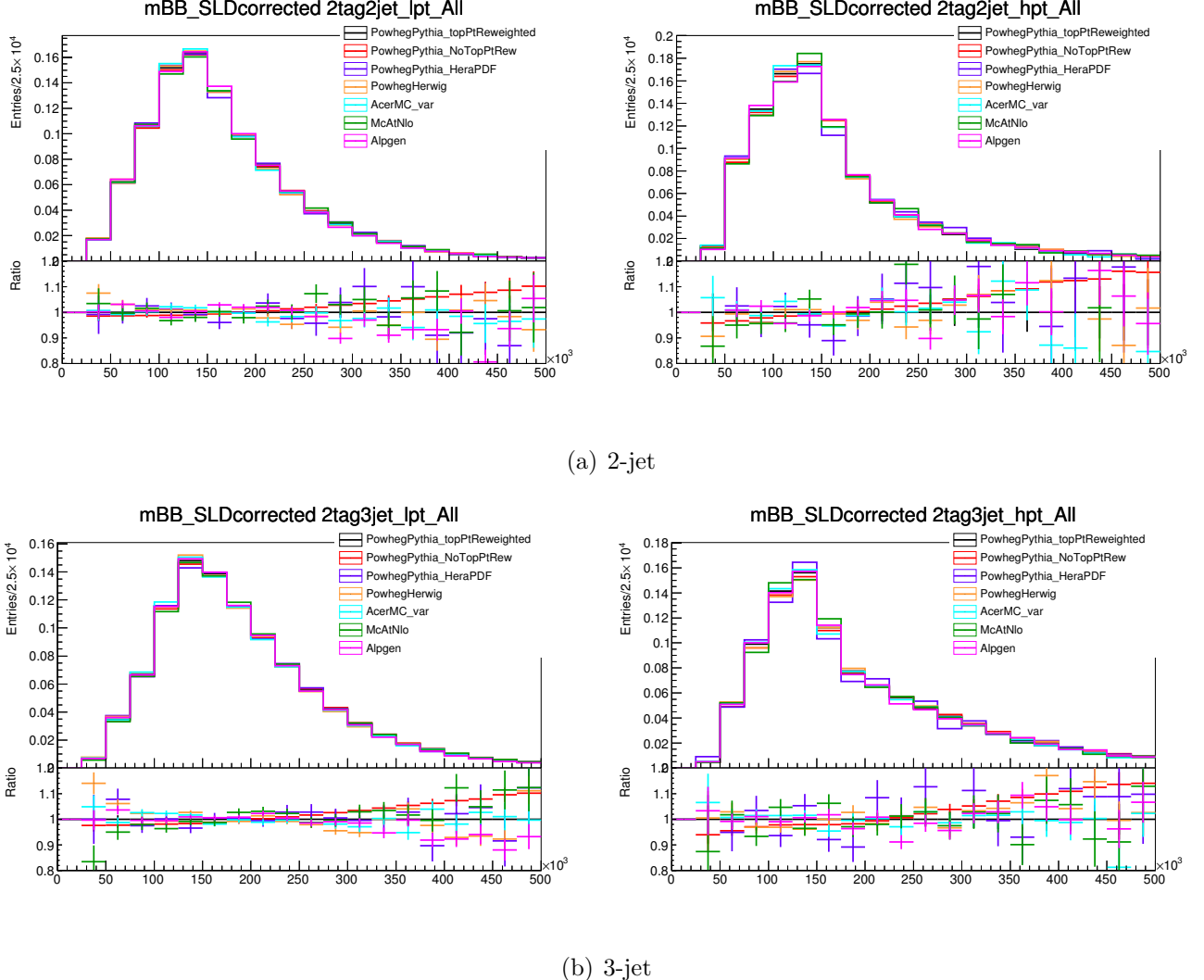


Figure 8.11: 2-jet and 3-jet 2-tag MC comparisons for the  $t\bar{t}$   $m_{b\bar{b}}$  systematic uncertainty. The largest difference is between PowHEG+PYTHIA and ALPGEN+PYTHIA and is taken as the systematic uncertainty.  $p_T^V < 120$  GeV is shown on the left and  $p_T^V > 120$  GeV is shown on the right.

### 8.2.3 Modeling of the Diboson Background

The diboson process that contributes to the  $ZH \rightarrow \ell^+\ell^- b\bar{b}$  search is  $ZZ$  production with one leptonically-decaying  $Z$ -boson and the other decaying to a pair of  $b$ -quarks. The contribution from  $WW$  is highly rejected due to the requirement of  $83 < m_{\ell\ell} < 99$  GeV and the two  $b$ -tag requirement. Contributions from  $WZ$  processes are highly suppressed in the event selection. The  $W \rightarrow l\nu Z \rightarrow q\bar{q}$  process can only contribute if another jet in the event is reconstructed as a lepton and also fulfills the invariant mass cut on the  $Z$  mass window. The  $Z \rightarrow ll W \rightarrow q\bar{q}$  may contribute if the two jets from the hadronic  $W$  decay are both tagged as  $b$ -jets, which becomes increasingly unlikely for tighter  $b$ -tagging requirements given the rejection power of the MV1c  $b$ -tagging algorithm.

The diboson backgrounds are simulated with PowHEG which provides a next-to-leading-order (NLO) estimate of the cross sections, relying on the CT10NLO PDF set and interfacing with the PYTHIA8 parton shower and hadronization model. The Monte Carlo samples for the diboson processes are listed in Table 8.15, as are the cross sections calculated at  $\sqrt{s} = 8$  TeV. Studies conducted using the HERWIG generator have shown that the contributions of the diboson processes not included in Table 8.15 are less than 1% of the total, and they are not considered for this analysis. Since the PowHEG cross sections do not include the contributions from the gluon-gluon initiated processes, this contribution is computed and added to the cross section value using the MCFM software, in which the factorization and renormalization scales of the processes are set to half the invariant mass of the bosons decay products, and the

CT10nlo PDF set is used.

Process	Generator	Cross Section ( $\sqrt{s} = 8$ TeV) [pb]
$Z \rightarrow ll$	POWHEG+PYTHIA8	1.207
$Z \rightarrow ll$		1.594
$W \rightarrow l\nu$		4.870
$WW$		52.4

Table 8.15: Monte Carlo generator used for the modeling of the diboson processes and correspondent cross sections.

Three sources of uncertainty are considered on the modeling of the diboson processes:

- Perturbative uncertainties on the fixed-order NLO cross section computation,
- Uncertainties on the coupling  $\alpha_S$  and the parton distribution functions (PDFs),
- Uncertainties on the  $m_{jj}$  distribution from parton showering and hadronization models.

### Uncertainties on the 2-jet to 3-jet Ratio

Uncertainties on the relative normalizations of the 2-jet to 3-jet ratio from the renormalization and factorization scale uncertainties are calculated using MCFM. Since MCFM does not provide the cross section computation at higher order than NLO, the 3-jet region corresponds to the inclusive cross section  $\sigma_{\geq 3}$  for  $VV+1$  jet, while the 2-jet region corresponds to the exclusive cross section  $\sigma_2$  for  $VV+0$  jets.

In order to estimate uncertainties in the yield of the 2-jet region compared to the 3-jet region, the “Stewart-Tackmann” method is applied, as it was for the sig-

nal process. Under this method, the uncertainty in the 2-jet region consists of two components. The first component is the inclusive 2+3-jet normalization uncertainty (`VVJetScalePtST2`), and the second component is the uncertainty on the exclusive 3-jet normalization relative to the 2-jet normalization, and is called `VVJetScalePtST1`. The uncertainty in the 3-jet region only has one component, `VVJetScalePtST1`. The `VVJetScalePtST1` parameter in the profile likelihood fit is anti-correlated between the 2-jet and 3-jet regions so that the total number of events in the 2-jet region plus the 3-jet region is conserved.

Because of the  $p_T^V$ -dependence of the diboson cross section, the uncertainties on the normalizations in the 2-jet and 3-jet regions are calculated as a function of  $p_T^V$ . As a result, this systematic uncertainty allows the shape of the  $p_T^V$  distribution to change during the profile likelihood fit.

Tables 8.16, 8.17, and 8.18 summarize the systematic uncertainties for the 2-jet to 3-jet ratios as calculated from the terms of the Stewart-Tackmann method [108]

$p_T^V$ bins [GeV]	0-90	90-120	120-160	160-200	> 200
$Z \rightarrow ll$ $Z \rightarrow q\bar{q}$	3%	5%	7%	10%	13%
$Z \rightarrow ll$ $W \rightarrow q\bar{q}$	3%	8%	13%	19%	29%
$W \rightarrow l\nu$ $Z \rightarrow q\bar{q}$	3%	8%	12%	19%	28%
$WW$	3%	6%	9%	13%	19%

Table 8.16: Perturbative systematics on  $\sigma_2$  from the  $C_1$  term of the covariance matrix across the different  $p_T^V$  bins.

### Cross Section Uncertainties from PDF and $\alpha_S$

The uncertainties on the PDF and  $\alpha_S$  are derived by taking the envelope of the error bands provided by the CT10 and MSTW2008 PDF sets, evaluated for two

$p_T^V$ bins [GeV]	0-90	90-120	120-160	160-200	> 200
$Z \rightarrow ll Z \rightarrow q\bar{q}$	2%	4%	6%	8%	11 %
$Z \rightarrow ll W \rightarrow q\bar{q}$	2%	6%	9%	13%	21%
$W \rightarrow l\nu Z \rightarrow q\bar{q}$	3%	6%	0%	14%	22%
$WW$	2%	4%	6%	9%	13%

Table 8.17: Perturbative systematics on  $\sigma_2$  from the  $C_2$  term of the covariance matrix across the different  $p_T^V$  bins.

$p_T^V$ bins [GeV]	0-90	90-120	120-160	160-200	> 200
$Z \rightarrow ll Z \rightarrow q\bar{q}$	-10%	-12%	-14%	-15%	-16%
$Z \rightarrow ll W \rightarrow q\bar{q}$	-12%	-13%	-14%	-16%	-18%
$W \rightarrow l\nu Z \rightarrow q\bar{q}$	-12%	-13%	-15%	-16%	-17%
$WW$	-11%	-12%	-14%	-15%	-17%

Table 8.18: Perturbative systematics on  $\sigma_{\geq 3}$  from the  $C_2$  term of the covariance matrix across the different  $p_T^V$  bins.

different  $\alpha_S$  central values of 0.117 and 0.119. This set of uncertainties does not show a significant dependence with respect to  $p_T^V$ , and therefore the errors are considered as normalization systematics on the cross sections of the diboson backgrounds. The systematic errors are derived separately for the 2-jet and 3-jet categories, and do not depend on the decay of the vector boson, only on the  $V$ -boson pair produced. The full list of PDF+ $\alpha_S$  uncertainties for the diboson processes is shown in Table 8.19. They are represented in the profile likelihood fit model by `VVJetPDFAlphaPt`.

Process	PDF+ $\alpha_S$ (2-jet)	PDF+ $\alpha_S$ (3-jet)
$ZZ$	3%	3%
$WZ$	4%	2%
$WW$	3%	2%

Table 8.19: PDF+ $\alpha_S$  systematic uncertainties for the  $ZZ$ ,  $WZ$  and  $WW$  processes, in the 2-jet and 3-jet analysis regions.

### Systematic Uncertainty on the $m_{b\bar{b}}$ Shape

To estimate the systematic uncertainty on the shape of the  $m_{jj}$ , two different parton shower and hadronization models for the final state  $b$ -quarks are studied. The analysis uses PowHEG interfaced with PYTHIA8 as the nominal Monte Carlo simulation, and for this estimate, the prediction from the HERWIG diboson simulation is studied. HERWIG provides a leading-order cross section calculation with a leading-log parton shower. However, the HERWIG sample does not provide separate estimates for the different decay modes of the diboson pair, so the uncertainties are derived inclusively for each sample:  $WW$ ,  $WZ$ ,  $ZZ$ . The  $m_{jj}$  distribution is produced for both the PowHEG+PYTHIA8 simulation and the HERWIG simulation and each is normalized to unit area to compare the shapes of the distribution. A systematic uncertainty on the  $m_{jj}$  shape in the  $WZ$  and  $ZZ$  processes is estimated by parametrizing the ratio between the two simulations according to:

$$\Delta(m_{jj}) = a + \frac{b}{1 + e^{-c(m_{jj}-d)}} \quad (8.2)$$

and for the  $WW$  process, a linear fit is sufficient:

$$\Delta(m_{jj}) = a + b(m_{jj}) \quad (8.3)$$

An example of this parametrization is shown in Figure 8.12 and Table 8.20 summarizes the parameters of the fit for each diboson process. In the profile likelihood fit, the diboson  $m_{jj}$  shape systematics are represented by `VVMbb_ZZ`, `VVMbb_WZ`, and `VVMbb_WW`.

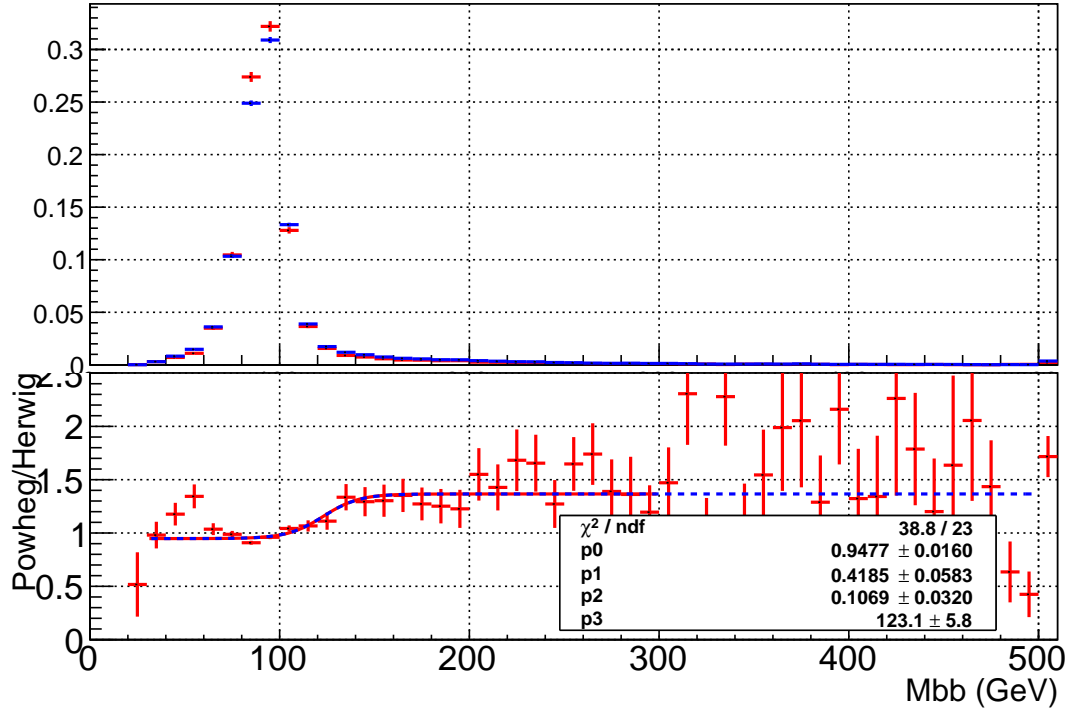


Figure 8.12: POWHEG+Pythia8 and Herwig comparison for the ZZ diboson process. The systematic uncertainties from the parton shower and hadronization model are estimated by taking fitting the ratio of the different predictions with Equation 8.2. The POWHEG+Pythia8 simulation is shown in blue, and Herwig shown in red.

Process	a	b	c	d
ZZ	-0.0523	0.4185	0.1069	123.1
WZ	-0.1752	0.6231	0.0661	121.4
WW	-0.1306	0.0008	–	–

Table 8.20: Parameter values for the  $m_{jj}$  shape systematic uncertainties for the ZZ, WZ and WW processes. These parameters correspond to Equation 8.2 and Equation 8.3

### 8.2.4 Modeling of the Single-Top Background

For the single-top processes,  $s$ -channel and  $Wt$ -channel are generated with PowHEG+PYTHIA and the  $t$ -channel simulated with ACERMC+PYTHIA. All single-top channels use CTEQL1 PDF and the *Perugia2011C* tune. The  $Wt$  process has a top quark and a  $W$ -boson in the final state, a topology which can yield a number of events in each analysis region of the same order of magnitude as the signal process. Because the statistics of the Monte Carlo samples for the phase space of the 2-lepton analysis are relatively small, the systematic uncertainties for the modeling of the single-top processes contributing to the 2-lepton analysis are taken from the 1-lepton analysis region presented in Reference [109]. Given that the single-top background accounts for less than 0.5% of the total at low- $p_T^Z$  and negligibly at high- $p_T^Z$  in any of the analysis regions, it is assumed that any difference in the systemic uncertainties between the 1-lepton topology and the 2-lepton topology will be negligible compared to the size of the uncertainty. This is verified in the analysis of the fit results shown in Chapter 9. Details of the derivation of the systematics related to the single-top background are found in Reference [109] and not repeated here as they have no impact on the final result.

### 8.2.5 QCD multijet and Non-collision Background

For the 2-lepton analysis, QCD multijet background may enter the signal regions when a jet is reconstructed as a charged lepton. This process is called “faking” a lepton. Additionally, semi-leptonic decays of  $c$ -jets and  $b$ -jets may produce a real lepton that passes the object selection requirements and causes the event to enter into the 2-lepton signal region. In order to estimate the multijet background with a data-driven approach, the requirement that the leptons in the event are isolated,  $iso_{track} < 0.1$  where,

$$iso_{track}(\ell) = \frac{1}{p_T^\ell} \sum_{trk} p_T^{trk} \text{ for } \Delta R(\ell, trk) < 0.2. \quad (8.4)$$

is reversed, yielding an orthogonal sample to the signal region and enhancing the number of fake leptons and leptons from semi-leptonic decays in the sample. Other than the reversal of the track isolation, the same kinematic selection is applied and events are categorized into the 0-tag, 1-tag, and 2-tag signal regions. Once a template has been derived in this way, a fit must be performed to determine a scale factor for the template because the efficiency of selecting a lepton with the reversed isolation requirement is unknown. The fit is performed to scale the multijet template to the di-lepton mass in the range of  $40 < m_{\ell\ell} < 120$  GeV. While the multijet scale is allowed to float, all other backgrounds are held to their Standard Model expectation. An example of the template is shown in Figure 8.13 for the 1-tag control region.

Fitting the multijet template in the electron channel yields an estimate for the multijet contribution in that control region. As the  $t\bar{t}$  background contributes significantly in the 2-tag region and is known to have a non-unity scale factor in the profile

likelihood fit, the scale factor estimate for the multijet background may not be robust in that region. As a result, the scale factors for the 0-tag region are applied to the 1-tag and 2-tag regions as well, but an uncertainty of 100% of that value is taken as a systematic uncertainty when it enters the profile likelihood fit as `MJ_L2`. Separate templates are made for the top  $e - \mu$  control region to account for the different shape of the final distributions in that control region. For the muon channel, Figure 8.14 indicates that the multijet contribution is negligible, which is as expected, because the rate to fake a muon with a jet or  $\pi^0$  is small.

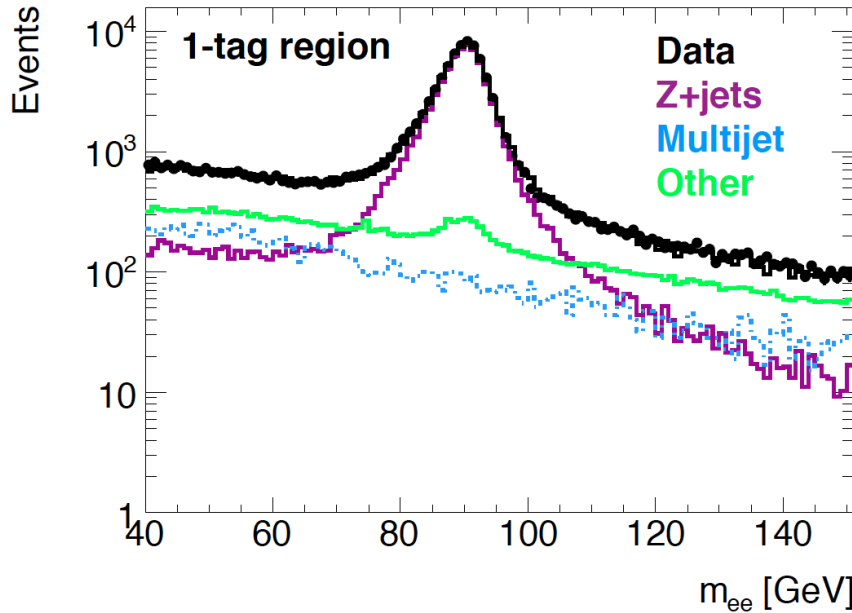


Figure 8.13: Example of the multijet template fit to the  $m_{ee}$  distribution in the 1-tag region for the estimation of the multijet background. The data are shown as black points, and the multijet template is shown in blue after being fit to the data.  $Z + \text{jets}$  is represented with the purple histogram and all other backgrounds ( $t\bar{t}$ , single-top, diboson) are in green.

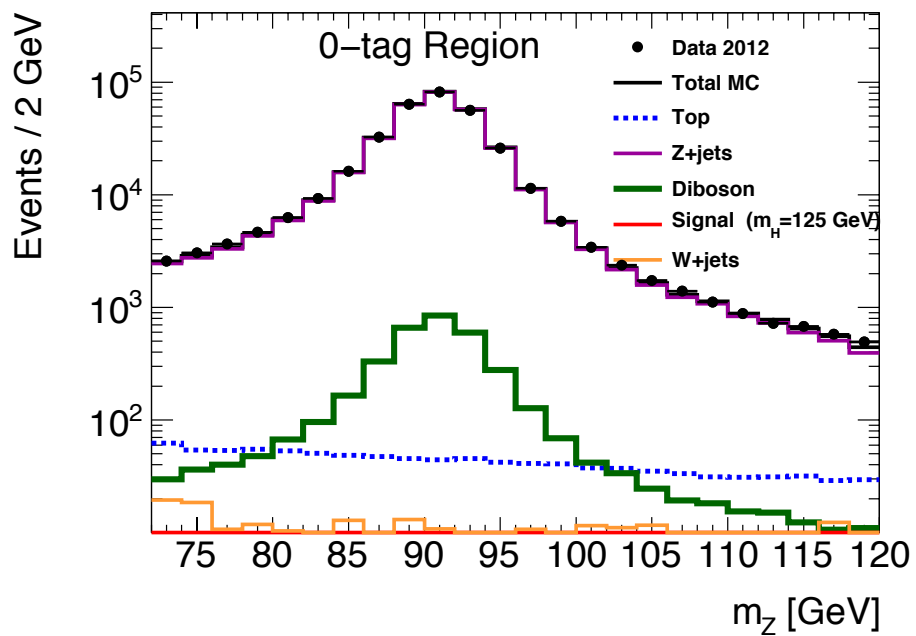


Figure 8.14: Plot of the di-lepton invariant mass for the muon channel in the 0-tag control region. For the muon channel, the contributions from both multijet and  $W+jets$  background are negligible compared to the top, diboson, and  $Z+jets$  backgrounds [109].

### 8.2.6 Modeling of the $W$ +jets Background

Because the 2-lepton analysis requires the reconstruction of two leptons passing the requirement  $83 < m_{ll} < 99$  GeV, the contribution of  $W$ +jets events to the signal regions is small. The only processes that can contribute are  $W$ +heavy flavor production in which a heavy-flavor jet decays semi-leptonically and that lepton passes the  $iso_{track}$  requirement, or a jet from  $W$ +jets production fakes a lepton. The two final leptons must then also fall into to the  $m_{ll}$  window. As shown in Figure 8.14, the contribution in the muon channel is negligible. For the electron channel, the contribution is also very small, on the order of the multijet contribution. Since the contributions from both  $W$ +jets and the multijet background require fake leptons or semi-leptonic decays of hadrons, the  $W$ +jets contribution can be estimated in the same procedure as for the multijet background alone. Rather than setting all backgrounds to their Standard Model expectation in the fit described in Section 8.2.5, no contribution is assumed from  $W$ +jets Monte Carlo. In this way, the multijet template from the electron channel will account for both the multijet and the  $W$ +jets components.

# Chapter 9

## Statistical Analysis Model

The goal of this analysis is to assess the compatibility of the data with the Standard Model predictions for the combination of the  $ZH \rightarrow \ell^+\ell^- b\bar{b}$ ,  $WH \rightarrow \ell\nu b\bar{b}$ , and  $ZH \rightarrow \nu\bar{\nu} b\bar{b}$  processes. The statistical model can fit one  $\mu$  value globally for the combination of the 0-lepton, 1-lepton, and 2-lepton channels, or alternatively fit a  $\mu$  value for each analysis channel independently. This chapter describes the fit for the 2-lepton channel, with the results following in Chapter 10. Section 9.1 introduces the concept of the profile likelihood fit, which produces the main result of this thesis. Section 9.2 follows, with a discussion of how each systematic uncertainty enters the fit as a term in the likelihood. Here, each source of uncertainty is enumerated and references are provided to the corresponding sections in Chapter 8. In Section 9.3, all distributions that are input to the profile likelihood fit are presented, and Section 9.4 describes a procedure to transform the binning of the input distributions to both increase sensitivity and decrease complexity in the fit. In the following section, Section 9.5, figures show how the power of the data, during the execution of the profile likelihood fit, al-

ters some of the modeling assumptions presented in Chapter 8. Finally, Section 9.6 contains the same distributions as Section 9.3, but after the binning transformation has been applied and the fit to data is performed.

## 9.1 Introduction to the Profile Likelihood Method

A profile likelihood is a likelihood that is maximized with respect to set of parameters whose exact values are not of interest to the measurement. This measurement is performed with the RooStats framework [95], and the parameter of interest is defined as the normalized signal strength parameter,  $\mu$ .  $\mu$  is the ratio of the cross section times branching ratio for the process measured in data to the cross section times branching ratio predicted by the Standard Model:

$$\mu = \frac{\sigma \times BR}{\sigma_{SM} \times BR_{SM}} \quad (9.1)$$

This section describes the profile likelihood method by first considering a simple cut-and-count analysis with only one bin. The likelihood of measuring  $n$  events, given expected number of background events  $B$  and number of signal events  $S$ , scaled by the signal strength parameter  $\mu$  is given by a Poisson distribution:

$$\text{Pois}(n|\mu S + B) = \frac{(\mu S + B)^n}{n!} e^{-(\mu S + B)} \quad (9.2)$$

Expanding to a measurement in  $m$  bins, with total predicted number of background events  $B$  and signal events  $S$ , the likelihood becomes:

$$\mathcal{L}(\mu) = \text{Pois}(n|\mu S + B) \left[ \prod_{i \in \text{bins}}^m \frac{\mu s_i + b_i}{\mu S + B} \right], \quad (9.3)$$

where  $s$  and  $b$  are the number of signal and background events, respectively, in bin  $i$ .

The strategy is then to extract a measurement of the parameter of interest,  $\mu = \frac{\sigma_{\text{observed}}}{\sigma_{SM}}$ , by maximizing the likelihood on the data. In reality, the signal and background contributions are dependent upon the modeling of the processes in simulation as well as various detector effects. In order to consider the impact of these effects, and to propagate their systematic uncertainties into a reliable error on the obtained value of  $\mu$ , the statistical model must incorporate these effects as parameters in the likelihood.

Parametrizing the model with these new parameters,  $\theta$ , the likelihood becomes:

$$\mathcal{L}(\mu, \theta) = \text{Pois}(n|\mu S(\theta) + B(\theta)) \left[ \prod_{i \in \text{bins}} \frac{\mu s_i(\theta) + b_i(\theta)}{\mu S(\theta) + B(\theta)} \right] \quad (9.4)$$

The content of each bin thus depends on these parameters, called nuisance parameters, which may affect the best-fit value of  $\mu$ .

The nuisance parameters parametrize the likelihood as a function of the reconstruction or identification efficiencies, and the modelling uncertainties discussed in Chapter 8.

Two general types of nuisance parameters are used, which enter as additional terms in the likelihood. The first type of nuisance parameter is called a floating normalization, which indicates that no prior distribution is assumed.

Floating parameters are used for the normalization of several background processes and also for the signal strength parameter,  $\mu$ . The floating parameters other than  $\mu$  are used for the  $Z+\text{jets}$  process with two true  $b$ -jets, for the  $Z+\text{jets}$  process with one

$c$ -jet, and for the  $t\bar{t}$  process. The data is capable of constraining these in the control regions defined in Section 7.

The second type of nuisance parameter consists of those that are implemented with a prior probability distribution function that characterizes the likelihood of obtaining a given value for that specific nuisance parameter. This type of nuisance parameter therefore adds additional terms to the likelihood function. This analysis uses Gaussian priors for all nuisance parameters with priors except for parameters for the remaining normalization uncertainties that are not floating. These use log-normal priors to avoid the possibility of obtaining a negative value. The statistical model has 76 nuisance parameters related to experimental effects, which are detailed in Section 9.2.1, and 47 additional nuisance parameters related to the modeling of the signal and background processes, which are detailed in Section 9.2.2 and Section 9.2.3.

The likelihood function is then maximized over all possible values of these parameters. Maximizing the likelihood over  $\mu$ , and the floating or constrained nuisance parameters in this unconditional manner is known as *profiling*.

When taking the natural logarithm of the likelihood, each of the Gaussian nuisance parameters contribute a term of the form:

$$-\Delta \ln(\mathcal{L}) = \frac{(\alpha' - \mu_\alpha)^2}{2\sigma^2}, \quad (9.5)$$

where  $\mu_\alpha$  is the mean of the Gaussian prior and  $\alpha'$  is the central value of the nuisance parameter as determined by maximizing the likelihood on data. For a normalization parameter, the likelihood is constructed with  $\mu_\alpha = 1$ , where 1 represents a normalization unchanged from the Monte Carlo expectation. For other parameters discussed in the next section,  $\mu_\alpha = 0$ . Therefore if the best fit to data “pulls” the central value of

the nuisance parameter away from the expected value given by the prior’s Gaussian mean, a “penalty” term is added to the negative log of the likelihood.

### Template Morphing

While the penalty terms resist pulling a nuisance parameter from its central value, the data, because it is a function of the set of nuisance parameters, may prefer the pulled value of the nuisance parameter to the central value. This indicates a possible mismodeling of that particular parameter. The nuisance parameters may either be multiplicative, such as for errors on efficiencies, luminosities, or normalizations, or not multiplicative. Non-multiplicative parameters may alter the shape of the distribution of interest. For non-multiplicative parameters, a vertical template morphing method is used. The templates consist of three binned histograms ( $m_{b\bar{b}}$  distributions, for example) for each systematic uncertainty. An example of three templates used to characterize the nuisance parameter for the  $b$ -jet energy resolution is shown in Figure 9.1. One histogram uses the nominal value of the uncertainty in question, and the other two have the uncertainty varied by  $\pm 1 \sigma$ . The nominal histogram is denoted in this section as  $H^0$ , and the up and down variations are denoted  $H^+$  and  $H^-$ , respectively. A morphing parameter,  $\alpha$ , is then introduced for each nuisance parameter and a piecewise linear interpolation is performed such that:

$$H^{int} = H^0 + \alpha(H^+ - H^0); \alpha > 0 \quad (9.6)$$

$$H^{int} = H^0 + \alpha(H^0 - H^-); \alpha < 0, \quad (9.7)$$

This means that a unit change in  $\alpha$  corresponds to a  $1\sigma$  change in the associated

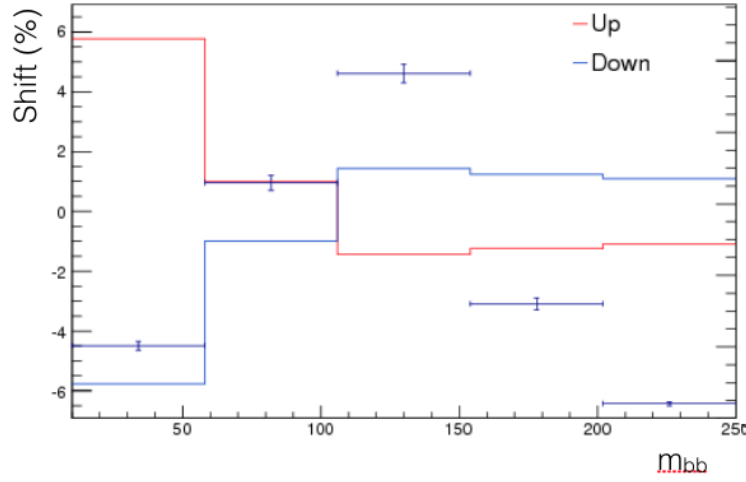


Figure 9.1: An example of a morphing template for the  $b$ -jet energy resolution. The central value of the  $m_{b\bar{b}}$  distribution is shown as the data points with arbitrary units. The  $+1\sigma$  variation is shown in red and the  $-1\sigma$  variation is the percentage shown in blue.

systematic uncertainty. The value of  $\alpha$  is obtained after maximizing the likelihood on data. Each  $H^0$  encapsulates the signal strength parameter,  $\mu$ , because the histogram's contents are  $\mu s_i + b_i$  for each bin  $i$ . The expected number of background events is thus parametrized such that for each analysis bin  $i$  and nuisance parameter  $k$ ,

$$b_i = \beta \times \left[ b_i^0 + \sum_k^{Nuis.params} (\alpha_k (b_{ik}^+ - b_{ik}^0)) \right], \quad (9.8)$$

for positive  $\alpha_k$  and similarly for negative  $\alpha_k$ ,

$$b_i = \beta \times \left[ b_i^0 + \sum_k^{Nuis.params} (\alpha_k (b_{ik}^0 - b_{ik}^-)) \right], \quad (9.9)$$

- Where  $\beta$  represents a mutiplicative normalization parameter scaling background  
 b. The same parametrization is performed for the signal expectation.

Therefore we may write the final likelihood as:

$$-\ln(\mathcal{L}(\mu, \theta(\alpha, \beta))) = \sum_i^{bins} \left[ -n_i \ln(\sum_j^{Bkgds} \beta_j H_{i,j}^{int}) + \sum_j^{Bkgds} \beta_j H_{i,j}^{int} \right] \quad (9.10)$$

$$+ \sum_j^{Bkgds} \frac{(\ln(\beta'_j) - 1)^2}{2\beta'_j \sigma_j^2} \quad (9.11)$$

$$+ \sum_k^{N_{profiled}} \frac{(\alpha_k)^2}{2\sigma_k^2} \quad (9.12)$$

where the first term represents the Poisson likelihood to observe  $n_i$  events in bin  $i$  given the interpolated value for the number of background and signal events  $H_{i,j}^{int}$ .  $\beta_j$  indicates a normalization parameter for background process  $j$ . These parameters do not apply to the signal component of  $H_{i,j}^{int}$ , and are applied in a process-specific manner. The  $\sum_j^{Bkgds}$  in the second line is a sum over the backgrounds with log-normal constraints and is a penalty term for changing these normalizations from their measured uncertainty.  $\alpha_k$  represents one of the Gaussian-constrained nuisance parameters to be profiled over, and the  $\sum_k^{N_{profiled}}$  term is a sum over the number of constrained non-multiplicative nuisance parameters in the fit. The form of  $H^{int}$  term was given in Eq. 9.6 and Eq. 9.7 and in the presence of  $k$  nuisance parameters implies taking a sum over  $k$ :

$$H^{int} = H^0 + \sum_k^{N_{profiled}} \alpha_k (H_k^+ - H^0); \alpha > 0, \quad (9.13)$$

$$H^{int} = H^0 + \sum_k^{N_{profiled}} \alpha_k (H^0 - H_k^-); \alpha < 0, \quad (9.14)$$

The best-fit value of  $\mu$ , denoted  $\hat{\mu}$ , is then extracted from the  $H^{int}$  parameter by obtaining the minimum of this log-likelihood on the data, considering all possible

values of  $\mu$  and  $\theta(\alpha, \beta)$ . In order to test the compatibility of the background-only hypothesis with the data, a test statistic  $q_\mu$  is created according to the likelihood:

$$q_\mu = -2\ln(\mathcal{L}(\mu), \hat{\theta}_\mu)/\mathcal{L}(\hat{\mu}, \hat{\theta}), \quad (9.15)$$

where  $\hat{\mu}$  and  $\hat{\theta}$  are the parameters that maximize the likelihood (with the constraint  $0 \leq \hat{\mu} \leq \mu$ ), and  $\hat{\theta}_\mu$  are the nuisance parameter values that maximize the likelihood for a given  $\mu$ . The compatibility of the background only model with the observed data and the exclusion intervals presented in Chapter 10 are derived with the  $CL_s$  method [66, 103].

### 9.1.1 Variables and Analysis Regions in the Likelihood

Two distributions enter the profile likelihood fit. The most important variable is the di-jet invariant mass,  $m_{b\bar{b}}$ . The product of the Poisson terms in the likelihood multiplies over each bin in the  $m_{b\bar{b}}$  histograms for each of the 2-tag categories (LL, MM, TT) and over each of the  $p_T^Z$  bins and jet categories (2-jet and 3-jet). Additionally, valuable information for the normalization of  $Z$ +jets flavor fractions is obtained by including the  $MV1c$  weight distribution of the tagged jet from the 1-tag regions. The  $m_{b\bar{b}}$  distribution is utilized in 5  $p_T^Z$  bins for the 2-lepton analysis. The  $MV1c$  distribution is only used in two  $p_T^Z$  bins to preserve statistical power and to avoid irregularities due to the  $p_T$  dependence of the  $b$ -tagging scale factors. This results in 34 analysis regions for the 2-lepton analysis, plus five additional region for the top control region with one electron and one muon, as discussed in Section 7.4.5. Table 9.1 summarizes the analysis regions included in the fit.

Channel		2-lepton	Number of Regions
1-tag	2-jet	$MV1c$	2
	3-jet	$MV1c$	2
Top $e - \mu$	2+3jet	$m_{b\bar{b}}$	5
2L-tag		$m_{b\bar{b}}$	5
2M-tag	2-jet	$m_{b\bar{b}}$	5
2T-tag		$m_{b\bar{b}}$	5
2L-tag		$m_{b\bar{b}}$	5
2M-tag	3-jet	$m_{b\bar{b}}$	5
2T-tag		$m_{b\bar{b}}$	5

Table 9.1: The regions entering the profile likelihood fit for the analysis, and the distributions used to create the templates. Vertically merged rows should be interpreted as regions treated with one distribution.

## 9.2 Systematic Uncertainties

The number of nuisance parameters in the analysis is high, at over 120, but splitting the modeling uncertainties and experimental uncertainties into many physically-motivated nuisance parameters provides a more conservative estimate of uncertainty in the background models. For example, consider a study comparing two Monte Carlo generators for the  $Z + \text{jets}$  background, which dominates the 2-lepton analysis. The two generators may have differing predictions for the ratios of the flavors of the jets that constitute the Higgs candidate as well as for the  $p_T^Z$  distribution. Because the analysis is performed in five bins of  $p_T^Z$ , the data can provide a strong constraint on the uncertainty of the  $p_T^Z$  distribution. If only one correlated nuisance parameter were considered to describe the differences between the two generators, the single parameter may be pulled to a value that the data prefer for the  $p_T^Z$  distribution but incorrect for the flavor fractions, and it would imply that the flavor fractions are known with the same degree of uncertainty as the  $p_T^Z$  distribution, which may be an aggressively

small uncertainty. In that case, completely unrelated nuisance parameters may be adjusted in the fit to account for the fact that the flavor fractions were pulled away from their true values. By allowing two separate nuisance parameters, the  $p_T^Z$  and flavor fractions can each be constrained by different regions of the analysis independently. For example, this is achieved in the analysis by having regions split by  $p_T^Z$  and also including the  $MV1c$  distribution in the fit. Such a splitting allows more freedom in the profile likelihood fit and is a more conservative description of the uncertainties in the analysis.

The remainder of this section covers all of the sources of systematic uncertainty in the analysis and how they are parametrized in the profile likelihood fit. Section 9.2.1 details the contribution of 76 nuisance parameters related to experimental uncertainties. Sections 9.2.2 and 9.2.3 detail the contribution of the remaining 47 nuisance parameters in the model. Not all parameters are used for all backgrounds or for all kinematic regions of the analysis. This section clarifies exactly which parameters are used in which regions. The nuisance parameters and their variations are parametrized with the following variables:

1.  $\phi$  represents an unconstrained normalization factor,
2.  $\eta(\alpha)$  represents a relative change in the overall normalization as function of the nuisance parameter,  $\alpha$ ,
3.  $\sigma(\alpha)$  parametrizes an uncertainty in the shape of the distribution of the discriminating variable as function of the nuisance parameter,  $\alpha$ .

$\alpha$  represents a particular configuration of the nuisance parameters and  $\alpha = 0$  corresponds to the nominal expectation. According to this representation,  $\phi$  may take on any value in the interval  $(0, \infty)$  and  $\eta(0) = 1$ . For a given nuisance parameter  $\alpha_i$ , the case when  $\alpha_i = 0$  implies that the data are insensitive to the nuisance parameter. If  $\sigma_i(\alpha_i = 1)$ , the data cannot give any constraint on the value of that uncertainty, while  $\sigma_i(\alpha_i) < 1$  indicates that the analysis has sufficient sensitivity to constrain the uncertainty beyond the value defined in the construction of the prior.

In the fit model, nuisance parameters with the same name are correlated. Therefore, to decorrelate them across regions or channels a short string is added to the name, thus representing where that parameter applies. These strings are as follows:

- Jet Multiplicity: JX with X=2,3
- $p_T^V$  region (bin): BX with X=0,1,2,3,4
- $b$ -tagging bin: TTypeX with X='',1l,mm,tt,XX which represent 1, 2L, 2M, 2T, and 2M+2T  $b$ -tag regions

In the following section, other parameter-specific naming conventions are described where appropriate. In the tables below, beginning with Table 9.2, the regions listed are the regions where the nuisance parameter is applied and decorrelated. For example “all regions” means the nuisance parameter is applied and correlated everywhere while “2/3 jet, 1/2 tag” means it is decorrelated between 2 and 3-jets as well as between 1 and 2-tags.

### 9.2.1 Experimental Systematic Uncertainties

The following section describes the uncertainties related to detector effects. The majority of these corrections have been provided by dedicated measurements in the ATLAS experiment, with several possible configurations for how the error can be treated. The rest have been developed as part of this analysis. An important point to keep in mind is that between low and high  $p_T^Z$  regions, light and heavy-flavor jets, and various amounts/types of  $E_T^{\text{miss}}$ , the phase space of this analysis is tremendous. In a given corner of this phase space a certain *component* of an uncertainty can be dominant while almost negligible in another where a different component is large. If these two components arise from truly different sources then one must be sure to properly decorrelate them before attempting a profile likelihood maximization such as the one described above. When such a decorrelation is performed, the components of the uncertainty are briefly described. A summary is contained in Table 9.2. Finally, Section 9.2.1 describes a smoothing procedure that is used to minimize the effects of limited statistics in the Monte Carlo simulation when creating the morphing templates.

#### Luminosity and Pile-up Uncertainty

Section 3.3 presented the technique for the measurement of the integrated luminosity in ATLAS. The uncertainty on the integrated luminosity is  $\pm 2.8\%$ , and is applied to the signal and background processes that are estimated from Monte Carlo simulation. Additionally, an uncertainty due to the modeling of the additional interactions a bunch crossing is applied following Reference [3]. This uncertainty is necessary

because additional energy in the calorimeter is accounted for during jet and electron reconstruction presented in Chapter 5.

### **Electron-specific Uncertainties**

The electron trigger [68], reconstruction, and identification [110] efficiencies are corrected according to Chapter 6 and have a relatively small associated error  $\mathcal{O}(1\%)$ . A value for the systematic uncertainty is derived by shifting a scale factor coherently to evaluate one number for the combined uncertainty of all three components. For the electron efficiency, the associated nuisance parameter is `ElecEffic`<sup>1</sup>. Uncertainties on the electron energy and resolution corrections [51] are evaluated separately by shifting the electron energies up and down and re-selecting events and named `ElecE` and `ElecEResol` respectively.

### **Muon-specific Uncertainties**

The muon trigger, reconstruction, and identification [28] efficiencies are corrected according to Chapter 6 and also have relatively small associated errors,  $\mathcal{O}(1\%)$ . As in the electron case, each efficiency scale factor is shifted coherently to evaluate one systematic variation to represent a combined uncertainty for all muon-related efficiencies. In this case, the associated nuisance parameter is `MuonEffic`. Uncertainties on the resolution smearing from the Inner Detector and Muon Spectrometer components of the muon reconstruction [28] are evaluated separately by shifting the smearing up and down by one standard deviation and reselecting events. These nuisance parameters

---

<sup>1</sup>This font is used to indicate the names of parameters in the fit model

are named `MuonEResolID` and `MuonEResolMS` respectively.

### Jet-specific Uncertainties

The experimental uncertainties related to jets are uncertainties on the jet energy scale (JES), resolution, and the jet-vertex-fraction cut efficiency (JVF) (See Chapter 6).

**The Jet Energy Scale Uncertainty** A detailed discussion of the JES and its associated uncertainty is found in Reference [6], and a discussion of the uncertainties can be found in Reference [1]. As discussed in Section 5.5.1, the Global Sequential Calibration is used to calibrate the energy scale of the reconstructed jets. The JES uncertainties have been broken down into 56 nuisance parameters:

- 47 uncertainties for the various in-situ jet energy scale calibration analyses are combined in an eigenvector decomposition into 6 parameters (`JetNP1-JetNP6_rest`).
- 2 uncertainties for  $\eta$  inter-calibration: a comparison of PYTHIA to HERWIG and the statistical component of this comparison. These uncertainties arise from potential mismodeling of the additional radiation that may affect the  $p_T$  and  $\eta$  of the dijet system. The associated nuisance parameters are `JetEtaModel` and `JetEtaStat`.
- 1 for jets with  $p_T > 1$  TeV, this uncertainty is negligible for this analysis and no nuisance parameter is assigned.
- 1 for the non-closure of Monte Carlo simulations relative to full simulation MC12a/PYTHIA8 The Global Sequential Calibration was derived in different

Monte Carlo simulation than the one used by some background processes. To account for the residual Monte Carlo to Monte Carlo differences, an error is estimated. The associated nuisance parameter is `JetNonClos`.

- 4 for pile-up uncertainties, 3 of which are dependent of the average number of interactions per bunch crossing and the number of primary vertices in the event, and the last is dependent on the energy density of the event,  $\rho$ . The associated nuisance parameters are: `JetMu`, `JetNPV`, `JetPilePt` and `JetPileRho`.

Beyond these 13 nuisance parameters, 4 additional nuisance parameters are added to account for uncertainties related to the flavor of the jet and the event topology:

- 1 for differences in the calorimeter response of  $b$ -jets is derived by studying the detector response using a variety of different Monte Carlo simulations. The associated parameter is `JetFlavB` and is only assigned to true  $b$ -jets in the simulation.
- 1 to account for  $\mu$  and  $\nu$  energy uncertainties when they originate from  $b$ -hadron decays[37]. The associated nuisance parameter is `JetBE` and is only assigned to true  $b$ -jets in the simulation.
- 1 for the uncertainty on the mixture of light-quarks and gluons. The associated nuisance parameter is `JetFlavComp_X`.
- 1 for the uncertainty on the jet energy scale for gluon jets, which is `JetFlavResp_X`.

The flavor composition and response above are decorrelated for different processes because the mixture of quarks and gluons in a given process can be different.  $X$  is

replaced with `Wjets`, `Zjets`, `Top`, or `VHVV` for the  $W+\text{jets}$ ,  $Z+\text{jets}$ ,  $t\bar{t}$ , or diboson background processes. The quark/gluon mixture is assumed to be 50% with a 50% uncertainty. After including all sources of uncertainty, the total fractional systematic uncertainty on the JES ranges from 3% at 20 GeV to 1% for a 1 TeV jet.FIXME  
(add this plot!)

**Jet Energy Resolution Uncertainty** The jet energy resolution can influence the categorization of events between the 2-jet and 3-jet analysis regions as jets near the  $p_T$  cutoff in the selection may have truly been jets above or below that threshold. To describe the uncertainty of the jet energy resolution (JER), one for all jets, and one specifically for  $b$ -jets.

- 1 for jet resolution, `JetEResol`.
- 1 for  $b$ -jet resolution[37], only applied to true  $b$ -jets to account for variations in the contributions of leptons from semileptonic decays. This nuisance parameter is `BJetReso`.

The magnitude of the relative JER ranges from  $\sim 25\%$  at 20 GeV to  $\sim 3\%$  near 1 TeV, and is found to be well described by the Monte Carlo simulation when validated by in-situ analyses using the dijet balance and bisector methods.FIXME - cite The relative uncertainty was determined from observed differences in the resolution between data and Monte Carlo simulations in those studies as well as from uncertainties on the methods themselves. This is known to be an overestimate of the error, therefore constraints in the profile likelihood fit can be expected. An estimate of the impact of the JER uncertainties is obtained in this analysis by smearing the jet  $p_T$  according

to a Gaussian distribution centered at 1, with a width equal to the true resolution plus the value of the relative uncertainty, which is a function of the jet’s  $p_T$  and  $\eta$ .

**Jet Vertex Fraction Uncertainty** The JVF efficiency uncertainty is obtained from the differences between data and Monte Carlo simulation in the JVF cut efficiency in  $Z+jets$  events [2]. A shift of  $\pm 0.03$  in the JVF value creates the same efficiency difference in Monte Carlo as the measured discrepancy between the data and Monte Carlo at the  $JVF = 0.50$  nominal value, and is thus chosen as the estimate for the JVF uncertainty’s effect on the analysis. This nuisance parameter is `JetJVF`.

### Missing Transverse Energy

As  $E_T^{\text{miss}}$  is composed of all objects in the event, all systematic variations of object energies are propagated to the  $E_T^{\text{miss}}$  calculation. Uncertainties on  $E_T^{\text{miss}}$  originate from uncertainty of the scale (`METScaleSoftTerms`) and resolution (`METResoSoftTerms`) of energy in calorimeter clusters which have not been associated with a reconstructed object.

### Flavor Tagging

As discussed in Section 6.2.3, the  $MV1c$  discriminant is used to separate *light* and *heavy*-flavor jets. In the Monte Carlo simulation, jets are labeled as either  $b$ ,  $c$  or *light*, and scale factors have been derived for each flavor as a function of jet  $p_T$  and  $MV1c$  output [50] in order to correct the tagging efficiency in Monte Carlo simulation to match the efficiency measured in data. Representative scale factors with the associated uncertainty were shown in Figure 6.9. The scale factors have

associated errors that are a mixture of experimental errors (i.e. JES), theoretical errors, and statistical errors from the data in each of the  $p_T$ ,  $MV1c$ , and  $\eta$  bins. As with the JES uncertainties, an eigenvector decomposition is performed, yielding only the leading 10 uncertainties for  $b$ -jets, 15 for  $c$ -jets and 10 for *light*-jets. As this analysis is very sensitive to possible  $p_T$  dependence of the flavor tagging scale factors, it is crucial to cautiously correlate low and high jet  $p_T$  effects.

The generator dependence observed for the  $b$  and  $c$ -jet tagging efficiencies was presented in Section 7.2.5. Because the analysis uses several Monte Carlo generators, scale factors were derived to correct each generator to the PYTHIA6 efficiency, which is the generator used to derive the flavor tagging efficiency scale factors. Examples of these scale factors were shown in Figure 7.2. A systematic uncertainty is taken to be 50% of the scale factor. Corresponding nuisance parameters to these uncertainties are: `BTagBSherpa`, `BTagBPythia8`, `BTagCSherpa`, `BTagCPythia8`.

As discussed in Section 7.2.5, truth-tagging is used for samples without a truth-matched  $b$ -jet and a bias has been measured as a function of  $\Delta R(\text{jet},\text{jet})$  for events with two  $c$ -jets only. The effect was not seen in *light-light*, nor *c-light* events and truth-tagging is not used in events with a truth-matched  $b$ -jet. A correction has been derived and (Section 7.2.5) with full details given in Reference [109]. The corresponding nuisance parameter for the uncertainty in this correction is `BTagTruthTagDR`.

## **Smoothing**

The uncertainties on physics objects such as electrons, muons, and jets are evaluated in two different ways: either shifting weights (scale factors) or re-selecting events

with the updated object kinematics. In the case of flavor tagging, where a scale factor is used to correct the simulation efficiency to match the efficiency measured in data, this weight is shifted up (down) and the change in the final distribution is noted as the  $+1$  ( $-1$ )  $\sigma$  shift. For jet energy scale (JES) uncertainties, the jet energies are shifted and therefore events may migrate in or out of the kinematic acceptance. Again the difference in the final variable is noted as the  $1\ \sigma$  error. However, if either the variations are small or the number of events in the bin is small, the  $1\ \sigma$  shift may be convoluted with the statistical uncertainty of the Monte Carlo sample. In the case of multiple JES errors, the Monte Carlo statistical error should not be counted for each individual JES error. To mitigate these effects, two algorithms are used to merge consecutive bins in the morphing templates. First, bins from one extremum to the next are merged until only one local extremum exists. If there are more than two extrema, merging is performed at each step of this iterative process where the difference between merged and unmerged templates is smallest. Second, the bins resulting from the first algorithm are sequentially merged, starting from the upper end of the  $m_{b\bar{b}}$  distribution, until the statistical uncertainty in each of the merged bins, calculated in the nominal template, is smaller than 5%.

In the 1-tag regions where the  $MV1c$  distribution is used in the fit, no merging of bins is performed since the  $MV1c$  distribution used is discrete, due to a finite number of operating points. Only a pruning is performed in this region in order to drop one-sided systematics in any  $MV1c$  bin.

### **List of Experimental Nuisance Parameters**

The nuisance parameters described above in Section 9.2.1 are summarized here in Table 9.2.

Nuisance Parameter	Description	NP Count	Section
Luminosity (2)			
Lumi	error on total lumi.	1	
MuScale	error of profile	1	9.2.1
Leptons (6)			
ElecEffic	trigger, reco., and id. efficiencies	1	
ElecE	energy scale	1	9.2.1
ElecEResol	energy resolution	1	
MuonEffic	trigger, reco., and id. efficiencies	1	
MuonEResolID	energy resolution from inner detector	1	9.2.1
MuonEResolMS	energy resolution from muon system	1	
Jet Energy Scale (23)			
JetNPX	in-situ calibration uncertainty ( $X = 1\text{-}6\text{rest}$ )	6	
JetEtaModel	$\eta$ inter-calibration model	1	
JetEtaStat	statistical error of $\eta$ inter-calibration	1	
JetNonClos	calibration non-closure	1	
JetMu	$\mu$ correction	1	
JetNPV	uncertainty due to $N_{PV}$ correction	1	
JetPilePt	pile-up in jet area correction	1	9.2.1
JetPileRho	pile-up in jet area correction	1	
JetFlavB $^\dagger$	$b$ -jet energy scale	1	
JetBE $^\dagger$	$b$ -jet scale for $\mu$ and $\nu$ energy	1	
JetFlavComp_X $^\ddagger$	light quark vs gluon fraction	4	
JetFlavResp_X $^\ddagger$	response of light quarks vs gluon jets	4	
Jet Energy Resolution (2)			
JetEResol	resolution applied to all jets	1	
BJetReso $^\dagger$	$b$ -jet specific resolution	1	9.2.1
Jet Quality (1)			
JetJVF	jet vertex fraction efficiency	1	9.2.1
$E_T^{\text{miss}}(2)$			
METResoSoftTerms	resolution of soft component	1	
METScaleSoftTerms	scale of soft component	1	9.2.1
Flavor Tagging (40)			
BTagBNEffic	$b$ -jet uncertainty in 10 eigenvectors ( $N = 0 - 9$ )	10	
BTagCNEffic	$c$ -jet unc. in 15 eigenvectors ( $N = 0 - 14$ )	15	9.2.1
BTagLNEffic	light-jet unc. in 10 eigenvectors ( $N = 0 - 9$ )	10	
BTagTruthTagDR	correction to bias from truth-tagging	1	7.2.5
BTag(B/C)Sherpa		2	
BTag(B/C)Pythia8	generator-dependent tagging efficiency	2	7.2.5
Total	76 with priors, 0 floating		

Table 9.2: A summary of the names and meaning of experimental systematic uncertainties, as well as the associated nuisance parameter names. For flavor composition and response systematics,  $X = \text{Zjets, Top, VHVV}$ .<sup>201</sup>

$\dagger$ : Applied only to truth-matched  $b$ -jets.  $\ddagger$ : Applied only to non-truth-matched  $b$ -jets.

### 9.2.2 Systematic Uncertainties for Signal Modeling

The modeling of the signal processes is discussed in detail in Section 8.1. This section lists all the nuisance parameters associated with the signal model in Table 9.3. For the signal processes  $qq \rightarrow WH$ ,  $qq \rightarrow ZH$  and  $gg \rightarrow ZH$ , the uncertainties are parametrized separately. The nuisance parameters are fully correlated in all regions of phase-space. Finally, the  $qq \rightarrow VH$  (denoted with `qqVH`) and  $gg \rightarrow ZH$  (denoted with `ggZH`) errors that are specific to those production processes are never correlated.

### 9.2.3 Systematic Uncertainties for Background Modeling

This section lists every non-experimental systematic uncertainty that enters, as a nuisance parameter, into the profile likelihood fit. Table 9.4 lists the nuisance parameters for the  $Z+jets$  background. The nuisance parameters for the  $t\bar{t}$  background are found in Table 9.5, and the parameters for the diboson backgrounds are enumerated in Table 9.6.

#### **$Z+jet$ Modeling Uncertainties**

The modeling of the  $Z+jet$  component of the background was discussed in detail in Section 8.2.1. The systematic uncertainties on the parameters of interest were determined through a mixture of data-driven and Monte Carlo approaches described in that section. Below, Table 9.4 provides a summary of these uncertainties. The total number of  $Z+jet$  background events is parametrized as a function of the nuisance

parameters according to:

$$N_Z = N_{Zl} + N_{Zcl} + N_{Zh} \quad (9.16)$$

$$N_{Zl} = \eta(\alpha_{ZlNorm}) \left( N_{Zl}^{2Jet} + \eta(\alpha_{ZlNorm\_J3}) N_{Zl}^{3Jet} \right) \quad (9.17)$$

$$N_{Zcl} = \phi_{Zcl} \left( N_{Zcl}^{2Jet} + \eta(\alpha_{ZclNorm\_J3}) N_{Zcl}^{3Jet} \right) \quad (9.18)$$

$$N_{Zh} = \phi_{Zh} \left( N_{Zh}^{2Jet} + \eta(\alpha_{ZhNorm\_J3}) N_{Zh}^{3Jet} \right) \quad (9.19)$$

where

$$N_{Zh}^{iJet} = N_{Zbb}^{iJet} + \eta(\alpha_{ZblZbbRatio}) N_{Zbl}^{iJet} + \eta(\alpha_{ZbcZbbRatio}) N_{Zbc}^{iJet} + \eta(\alpha_{ZccZbbRatio}) N_{Zcc}^{iJet} \quad (9.20)$$

with  $iJet$  being either 2 jets or 3 jets, depending on the analysis region in question.

### $t\bar{t}$ Modeling Uncertainties

Table 9.5 summarizes the nuisance parameters related to the modeling of the  $t\bar{t}$  background. The uncertainties were calculated in Section 8.2.2 and relied on comparisons of several Monte Carlo programs, because of the difficulty in creating a region in Data that can isolate the  $t\bar{t}$  background from the  $W+jets$  or single top backgrounds with sufficient statistics to yield robust estimates of the uncertainties.

The total number of  $t\bar{t}$  events is given, as a function of the nuisance parameters, by

$$N_{t\bar{t}} = \phi_{t\bar{t}} \left( N_{t\bar{t}}^{2Jet} + \eta(\alpha_{ttbarNorm\_J3}) N_{t\bar{t}}^{3Jet} \right) \quad (9.21)$$

where

$$N_{t\bar{t}}^{iJet} = \left( N_{t\bar{t}}^{lowpV} + \eta(\alpha_{ttbarHighPtV}) N_{t\bar{t}}^{highpV} \right)^{iJet} \quad (9.22)$$

with  $iJet$  equal to 2 jets or 3 jets and  $\phi$  and  $\eta$  are defined at the beginning of Section 9.2:  $\phi$  is a normalization parameter, and  $\eta$  is a relative normalization change as a function of the nuisance parameter  $\alpha$ .

### Diboson Modeling Uncertainties

Table 9.6 summarizes the nuisance parameters related to the modeling of the diboson backgrounds. The uncertainties were calculated in Section 8.2.3 and relied on comparisons of several Monte Carlo programs. It is difficult to create a high-statistics control region for the diboson process in data that can isolate the diboson processes in data, given the large cross section of the  $Z+jets$  backgrounds. Furthermore the Higgs peak in  $m_{b\bar{b}}$  is overlapping with the diboson peak, further reducing the purity of any control region.

Nuisance Parameter	Description	qqVH	qqZH	ggZH	N <sub>param</sub>	Section
$\mu$	ratio to SM cross section	float	float	float	1	–
TheoryQCDscale	Scale Uncertainty	1%	1%	50%	2	–
TheoryPDF	PDF Sets	2.4%	2.4%	17%	2	8.1.2
TheoryAcc_PS	Parton Shower, had. and UE Acceptance	7% - 13% in different $p_T^V$ and $N_{jets}$	S	–	1	8.1.1
TheoryVHPT	NLO EW Correction	S	S	–	1	–
TheoryAcc_J2	Inclusive Acceptance	3.0%	3.4%	1.5%	2	–
TheoryAcc_J3	Scale Acc. 3-jet / 2-jet	-1.1%	-0.9%	-1.9%	2	8.1.3
	Scale Acc. 3-jet / 3-jet	4.1%	3.5%	3.3%	2	–
TheoryAccPDF	PDF Acc. 2-jet	3.5%	3.0%	2.1%	2	–
	PDF Acc. 3-jet	2.8%	5.0%	3.4%	2	–
TheoryVPtQCD	QCD Scale	S	S	S	2	–
Total		14 with priors, 1 floating				–

Table 9.3: Details of the nuisance parameters used to parametrize the systematics on the modeling of the signal processes. All signal systematics are correlated throughout all phase space regions, but de-correlated between the  $q\bar{q} \rightarrow VH$  ( $qqVH$ ) and  $gg \rightarrow ZH$  ( $ggZH$ ) processesd. S = “Shape”.

Nuisance Parameter	Description	Correlation/Samples	Value	$N_{param}$	Section
Z1Norm	Z1 normalization	all regions	5%	1	
Z1Norm_J3	Z1 3/2-jet ratio	3Jet regions	5%	1	
norm_Zcl	Zcl norm	all regions	Float	1	
Zc1Norm_J3	Zcl 3/2-jet ratio	3Jet regions	26%	1	
norm_Zbb	Zhf normalization	all regions	Float	1	8.2.1
ZbbNorm_J3	Zhf 3/2-jet ratio	3Jet regions	20%	1	
Zb1ZbbRatio	Zbl/Zbb ratio	2, 3Jets	12%	2	
ZbcZbbRatio	Zbc/Zbb ratio	all regions	12%	1	
ZccZbbRatio	Zcc/Zbb ratio	all regions	12%	1	
ZDPhi	$\Delta\phi$ shape	Z+b/c, Zl × 2, 3Jets	S	4	8.2.1
ZPtV	$p_T^V$ shape	Z+b/c, Zl each in all regions	S	2	8.2.1
ZMbb	$m_{b\bar{b}}$ shape	Z+b/c, Zl each in all regions	SO	2	8.2.1
Total		16 with priors, 2 floating			

Table 9.4: The nuisance parameters used in the fit to parametrize the normalization of the  $Z+jets$  backgrounds and the correlation of these parameters between regions.  $Zhf = Zbb+Zcc+Zbl$ ,  $Z+b/c=$ all  $Z+jets$  besides  $Z+l$ ,  $S=$ “Shape”, and  $SO=$ “Shape Only” meaning explicitly the normalization of each N-jet/M-b-tag/ $p_T^Z$  region is preserved while the shape is varied. Further details are given in Section 8.2.1.

Nuisance Parameter	Description	Correlation	Value	N param	Section
norm_ttbar	$t\bar{t}$ normalization	all regions	Float	1	
ttbarHighPtZ	high/low $p_T^Z$	$p_T^Z > 120 \text{ GeV}$	7.5%	1	8.2.2
ttbarNorm_J3	3/2-jet ratio	3-jet in 2,0+1 lepton	20%	2	8.2.2
TopPt	top $p_T$ corr. variation	all regions	S	1	8.2.2
TtbarMBBCont	$m_{b\bar{b}}$ shape	all regions	SO	1	8.2.2
Total		5 with priors, 1 floating			

Table 9.5: The nuisance parameters used in the fit to parametrize the systematics on the  $t\bar{t}$  background. S=“Shape” and SO=“Shape Only” meaning explicitly the normalization of each N-jet/M- $b$ -tag/ $p_T^Z$  region is preserved while the shape is varied.

Nuisance Parameter	Description	Correlation	WW	WZ	ZZ	Section
VVJetScalePtST1	Scale		S	S	S	
VVJetScalePtST2	Scale		S	S	S	
VVJetPDFAlphaPt	PDF, $\alpha_S$ 2-jet PDF, $\alpha_S$ 3-jet	all regions	2% 3%	2% 4%	3% 3%	8.2.3
VVMbb_WW	$m_{b\bar{b}}$ shape		SO	–	–	
VVMbb_WZ	$m_{b\bar{b}}$ shape		–	SO	–	
VVMbb_ZZ	$m_{b\bar{b}}$ shape		–	–	SO	
Total	6 with priors, 0 floating					

Table 9.6: The nuisance parameters used in the fit to parametrize the systematics on the diboson backgrounds. For  $VVJetPDFAlphaPt$ , the two values represent the normalization change in 2/3Jet region respectively. S=“Shape”, and SO=“Shape Only” meaning explicitly the normalization of each N-jet/M- $b$ -tag/ $p_T^Z$  region is preserved while the shape is varied.

### 9.2.4 Pruning of the Systematic Uncertainties

When the number of events in the Monte Carlo simulation’s  $m_{b\bar{b}}$  distribution is small, an analysis region may have morphing templates with large fluctuations that can introduce noise into the profile likelihood fit. Therefore, the uncertainties are treated according to the following procedure, which is carried out for each process in each analysis region after the  $m_{b\bar{b}}$  or  $MV1c$  distribution is manipulated according to the procedures discussed in Section 9.4.

- Reduce statistical fluctuations by the smoothing procedure described in Section 9.2.1. Only to those systematic uncertainties which require a re-sampling of the events (i.e. JES and not  $b$ -tagging).
- Neglect the normalization uncertainty if, for a given sample in a given region, either is true:
  - The variation is less than 0.5%.
  - Both up ( $+1 \sigma$ ) and down ( $-1 \sigma$ ) variations have the same sign.
- Neglect the shape uncertainty if, for a given sample in a given region, either is true:
  - Not one single bin has a deviation over 0.5% after the overall normalization is removed.
  - If only up ( $+1 \sigma$ ) or the down ( $-1 \sigma$ ) variation is non-zero and passed the previous pruning steps.
- Neglect both the shape and normalization uncertainty if:

- The signal content is less than 2% of the total background in all bins and the shape and normalization error are each  $< 0.5\%$  of the total background.
- The signal content in at least one bin has a signal contribution  $> 2\%$  of the total background in that bin, and if the shape and normalization error are each  $< 2\%$  of the signal yield.

### 9.3 Input Distributions to the Fit

This section shows figures for all of the 2-jet analysis regions that enter the profile likelihood fit. The 3-jet figures are shown in Appendix A. The error band on the Monte Carlo prediction represents the sum of the statistical and systematic errors listed above, before any are constrained by the fit. All Monte Carlo predictions are at their Standard Model cross section. The normalizations may change during the fitting process. The corresponding distributions after the profile likelihood fit is performed are found in Section 9.6.

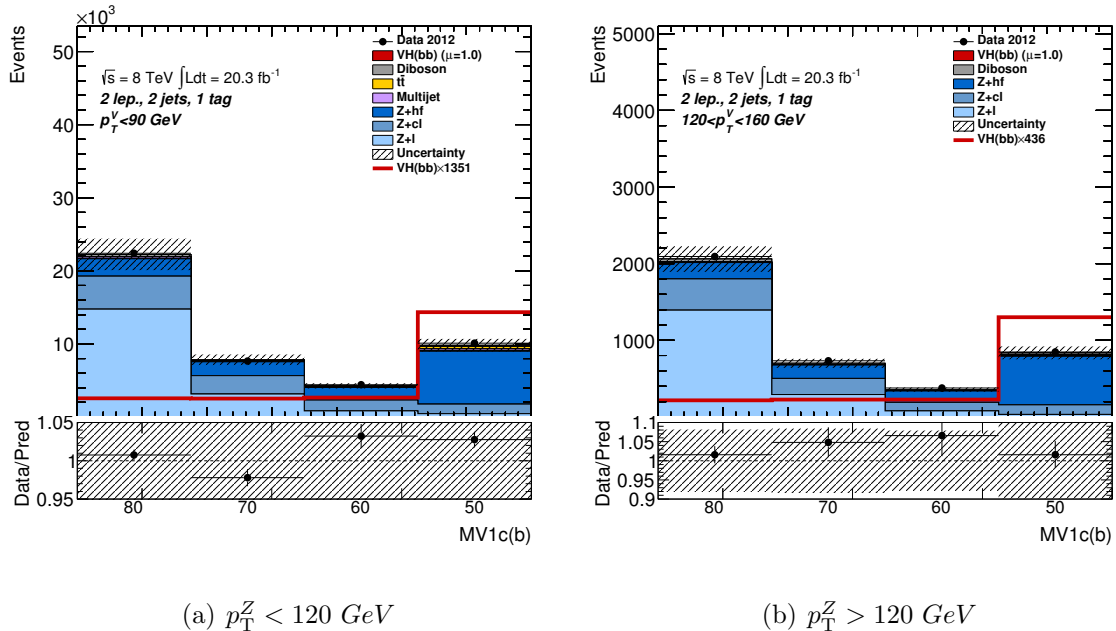


Figure 9.2: Pre-fit  $MV1c$  distributions of the tagged jet in 2-lepton events in the 1-tag, 2-jet analysis regions. The pre-fit background expectation is indicated by the dashed blue line.

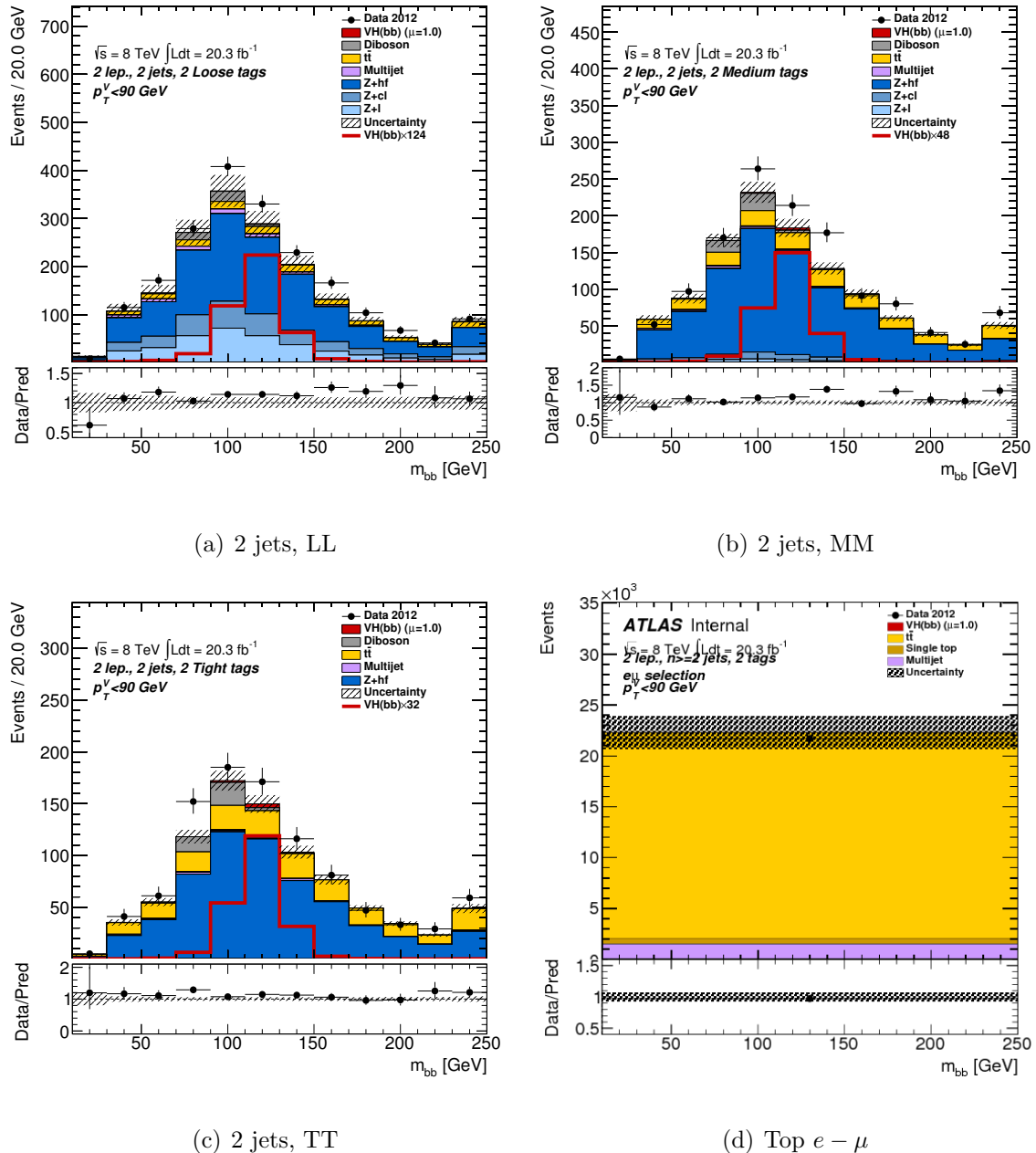


Figure 9.3: Pre-fit plots for the  $m_{b\bar{b}}$  distribution in 2-lepton events in the  $LL$ ,  $MM$  and  $TT$  tag categories for the 2-jet events.

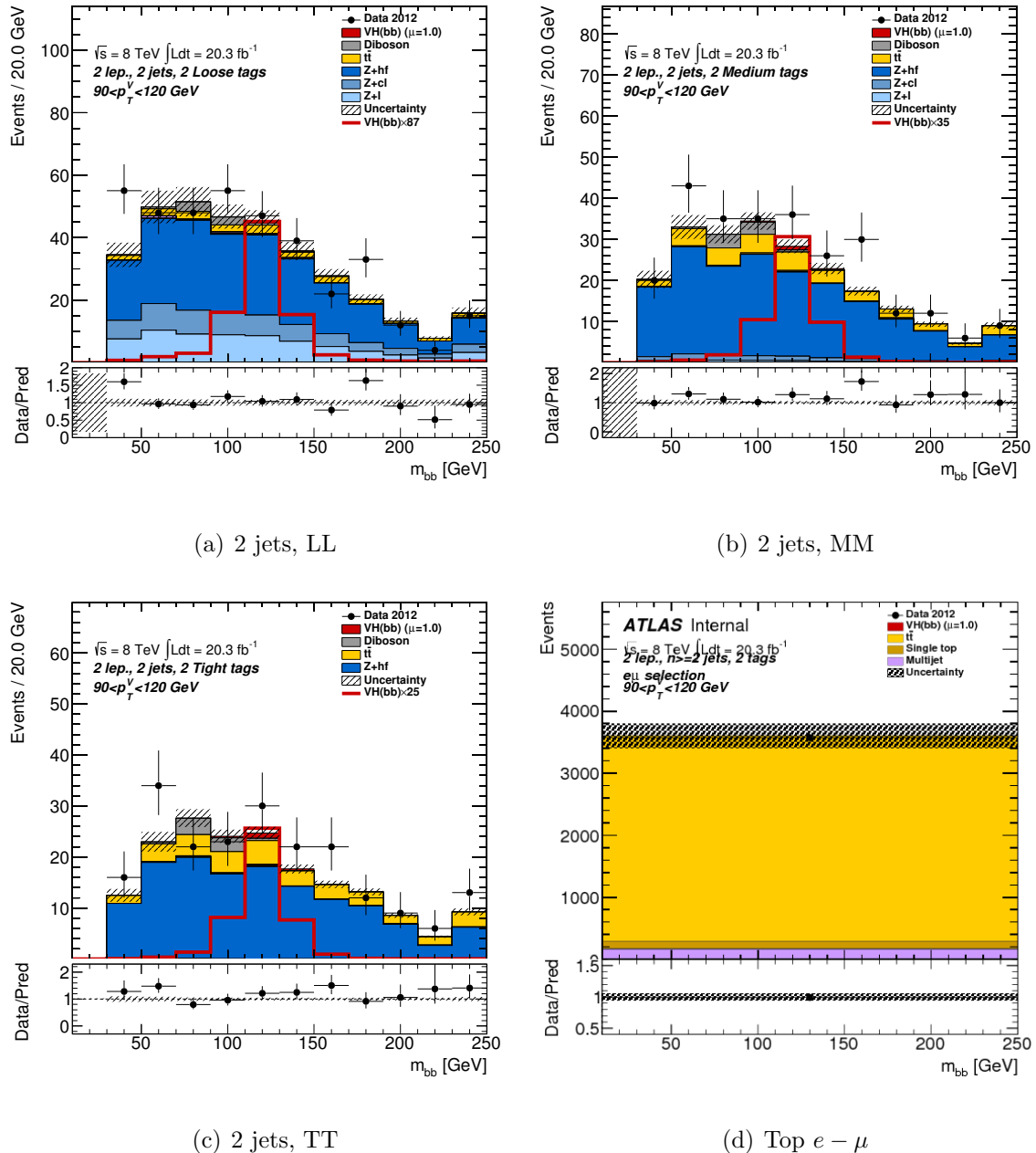


Figure 9.4: Pre-fit plots for the  $m_{b\bar{b}}$  distribution in 2-lepton events in the  $LL$ ,  $MM$  and  $TT$  tag categories for the 2-jet events.

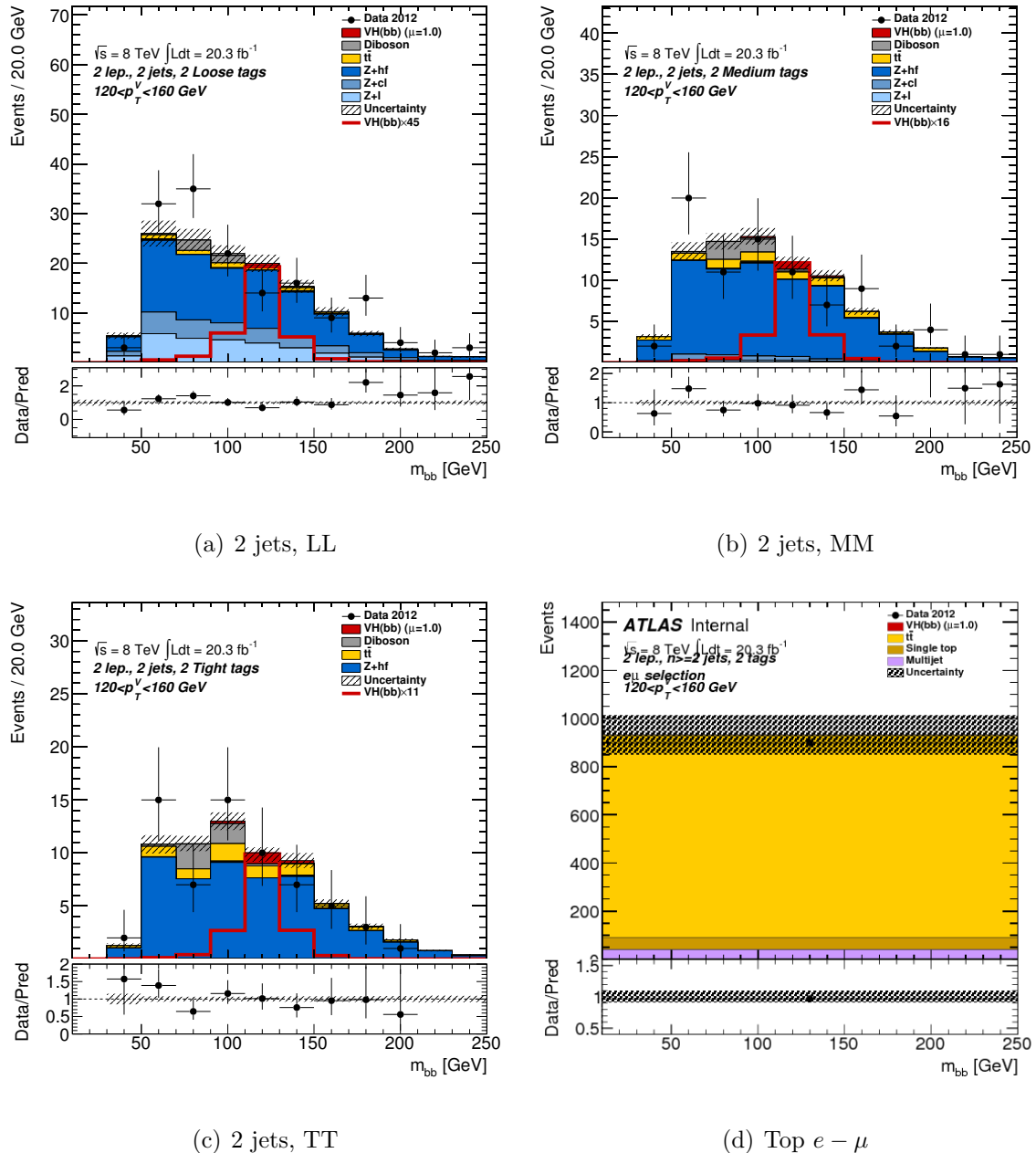


Figure 9.5: Pre-fit plots for the  $m_{b\bar{b}}$  distribution in 2-lepton events in the  $LL$ ,  $MM$  and  $TT$  tag categories for the 2-jet events.

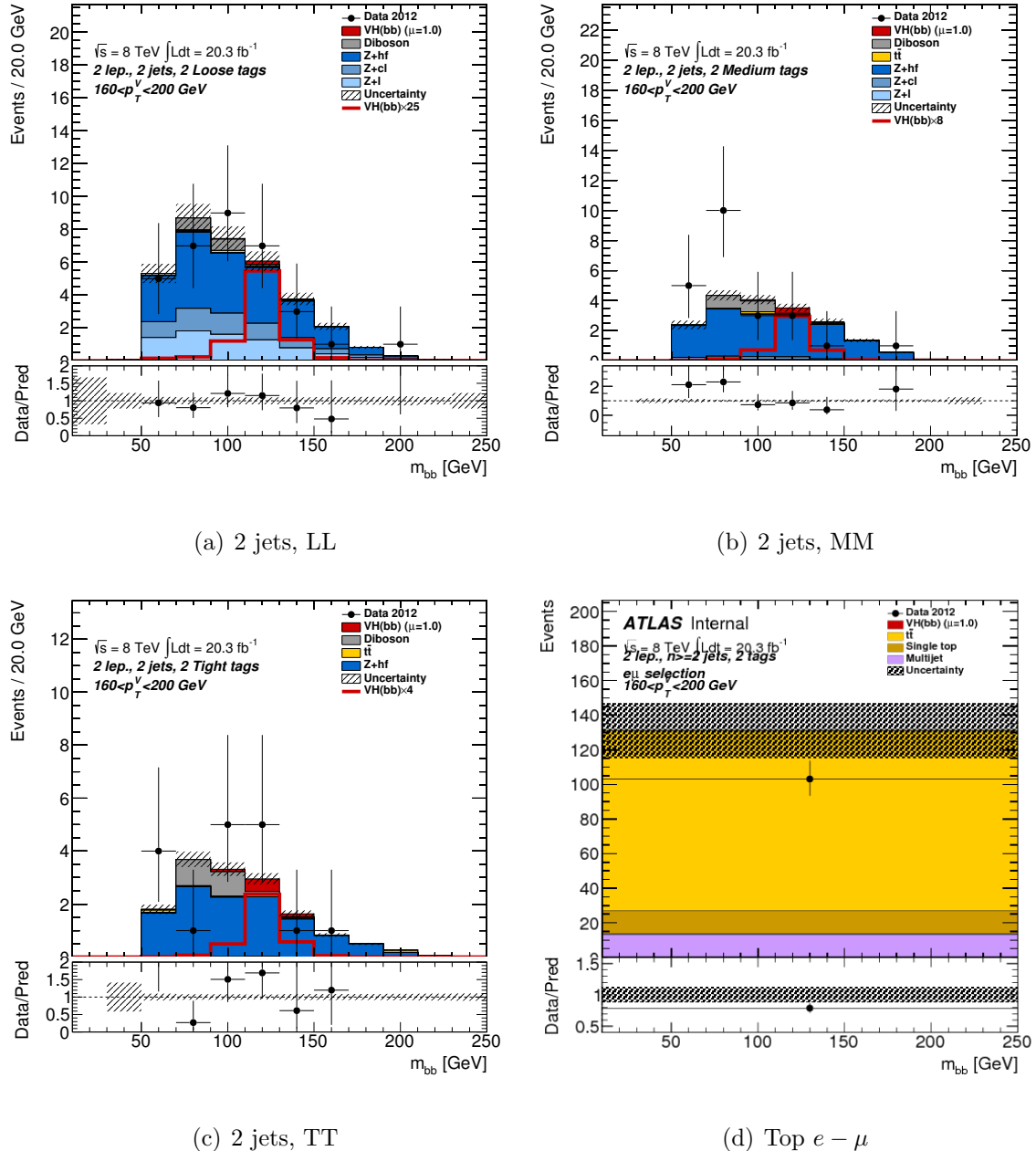


Figure 9.6: Pre-fit plots for the  $m_{b\bar{b}}$  distribution in 2-lepton events in the  $LL$ ,  $MM$  and  $TT$  tag categories for the 2-jet events.

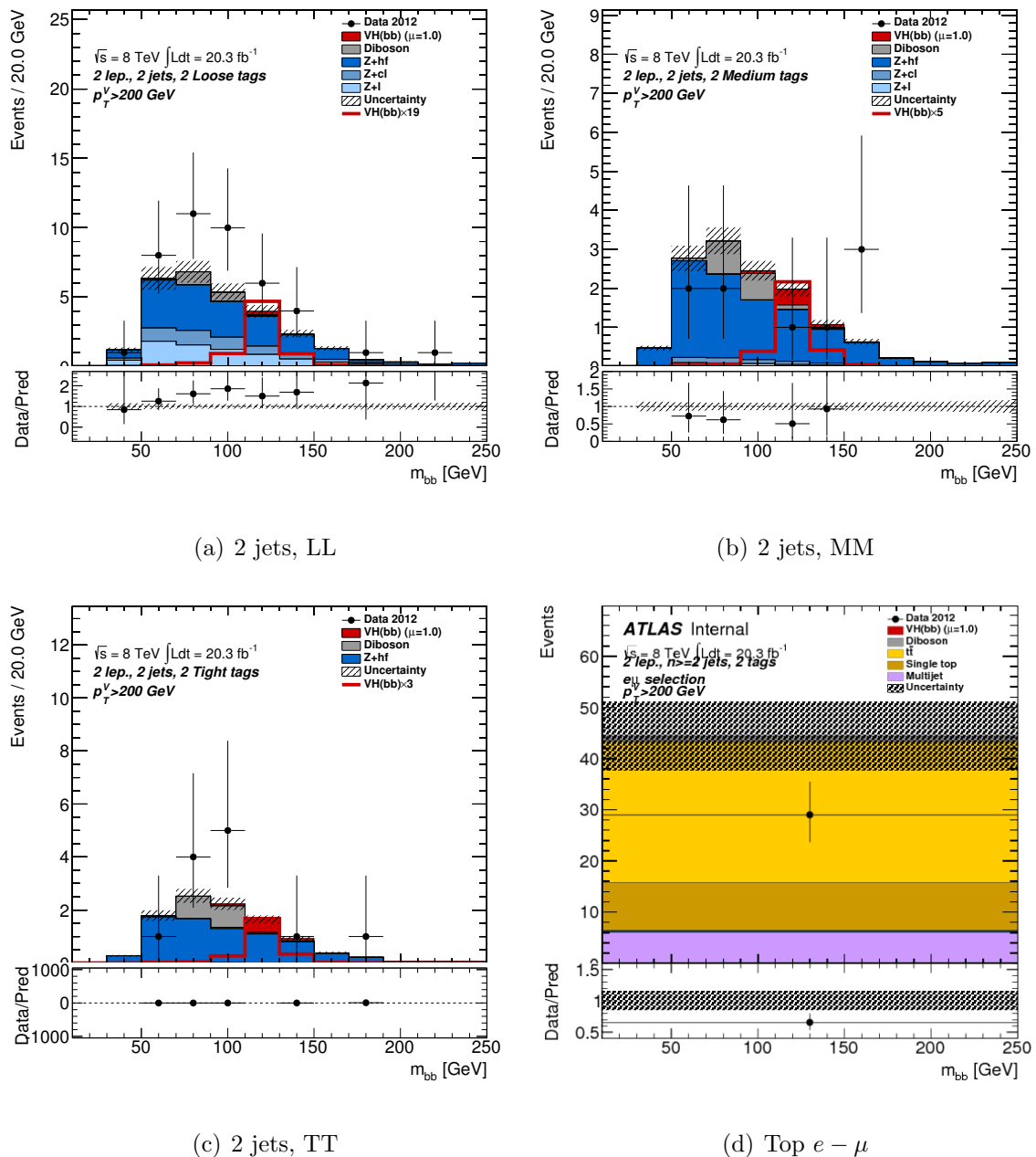


Figure 9.7: Pre-fit plots for the  $m_{b\bar{b}}$  distribution in 2-lepton events in the  $LL$ ,  $MM$  and  $TT$  tag categories for the 2-jet events.

## 9.4 Binning Transformation

A simple rebinning of the  $m_{b\bar{b}}$  distribution could be performed in order to reduce statistical uncertainties in the tails of the dijet mass. However, this also reduces the sensitivity in the signal-rich regions because the Higgs candidate's  $m_{b\bar{b}}$  peak may fall into one bin. Instead, variable-sized binning is used. To optimize the signal strength while giving stability to the profile likelihood fit, an improved variable-sized rebinning is performed on the distributions entering the fit.

The two figures of merit used to optimize the binning are the final expected sensitivity and the reduction of the number of bins. As an example, the total number of bins in the analysis, if the  $m_{b\bar{b}}$  distribution has a fixed bin width of 20 GeV (in the range  $10 \text{ GeV} < m_{b\bar{b}} < 250 \text{ GeV}$ ), is almost 400, and running the fit over so many bins is more CPU-intensive and less stable than over fewer bins.

### 9.4.1 General description

To remap the histograms entering in the profile likelihood fit, the following function is defined:

$$Z(I[k, l]) = Z(z_s, n_s(I[k, l]), N_s, z_b, n_b(I[k, l]), N_b) \quad (9.23)$$

where:

- $I[k, l]$  is an interval of the histograms containing the bins between the bin  $k$  and the bin  $i$ ,
- $N_s$  is the total number of signal events in the histogram,

- $N_b$  is the total number of background events in the histogram,
- $n_s(I[k, l])$  is the total number of signal events in the interval  $I[k, l]$ ,
- $n_b(I[k, l])$  is the total number of background events in the interval  $I[k, l]$ ,
- $z_s$  and  $z_b$  are parameters used to tune the algorithm.

Different possible  $Z$  functions have been tested and the optimized result has been called Transformation D. This transformation uses a  $Z$  function defined as:

$$Z = z_s n_s / N_s + z_b n_b / N_b \quad (9.24)$$

where  $z_s$  and  $z_b$  are parameters, which can be used to optimize the strategy. In addition to the condition on  $Z$ , the new bins must also be constructed such that the relative statistical uncertainty on the background is less than 10%.

## $m_{b\bar{b}}$ Shape Optimization and Transformation D

This optimization has the advantage of increasing the number of bins where signal is expected while avoiding the proliferation of bins in background-only regions. The optimized binning has the parameters shown in Table 9.7.

Distribution	2-jet Region	3-jet Region
2-lepton $m_{b\bar{b}}$	$z_s = 4, z_b = 4$	$z_s = 2, z_b = 2$

Table 9.7: Binning optimization for the  $m_{b\bar{b}}$  distribution with Transformation D.

Using this transformation compared with the 20 GeV bins in  $m_{b\bar{b}}$  used for Reference [7] reduces the total number of bins by almost 45% and improves the final result by 2% in the total expected sensitivity. As an example, one of the  $m_{b\bar{b}}$  distributions, before and after the transformation can be seen in Figure 9.8.

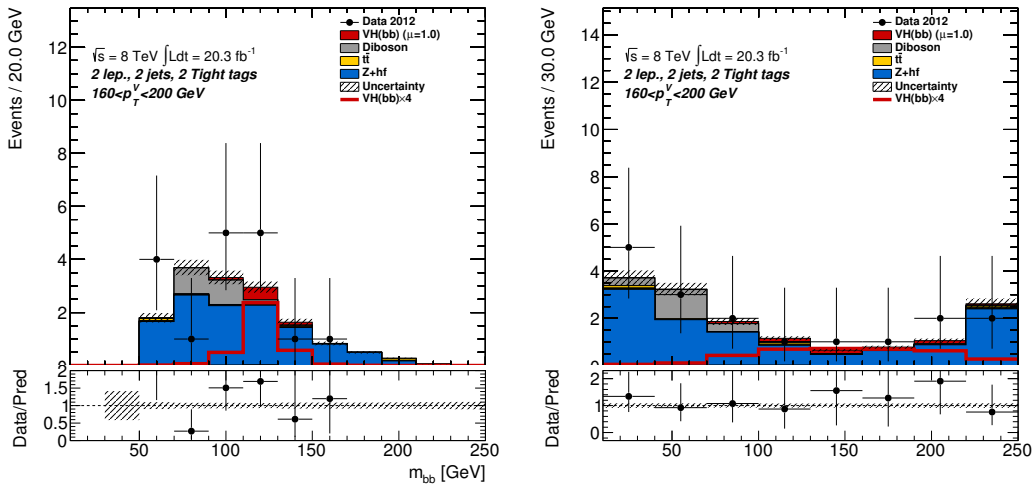


Figure 9.8: Example of the effect of the binning transform on the  $m_{b\bar{b}}$  output for one of the signal regions. Left: Before the binning transformation. Right: After the binning transformation. The units on the  $x$ -axis have become arbitrary after the transformation is performed.

## 9.5 Interpreting the Profile Likelihood Fit

When the profile likelihood fit is performed, each nuisance parameter may change from the nominal value, and its error may be constrained by the fit if the data is capable of providing a tighter constraint than the uncertainty that was assumed upon the construction of the prior. The profile likelihood fit then returns the parameter of interest,  $\mu = \frac{\sigma^{observed}}{\sigma_{SM}}$ . A value of  $\mu = 1$  implies that the data prefer the Standard Model cross section times branching ratio for the  $ZH \rightarrow \ell^+\ell^- b\bar{b}$  process. In this section the pulls and correlations of the nuisance parameters are presented and discussed. The Asimov dataset is constructed from the nominal Monte Carlo expectation according to Reference [66]. The pulls in the Asimov dataset are zero by construction. The size of the constraints on the nuisance parameters in the Asimov dataset are a statement about the power of the data to constrain the parameters. If a nuisance parameter is constrained in the Asimov dataset, it is reasonable that it will also be constrained in the fit to data.

For each set of nuisance parameters, the resulting pulls and constraints from the fit to data are compared to those of the fit to the Asimov data to study correlations among the parameters. Due to the large number of nuisance parameters in the fit (over 120), it is inevitable that some parameters will appear significantly pulled, so visual inspection of every parameter may be misleading. Instead, a few example parameters are shown, which contain a subset of the most important parameters in terms of their contribution to the total error on  $\mu$ . The expectation is that a parameter will be zero in the case of perfect Monte Carlo modeling of the signal and backgrounds, so

any pull away from zero indicates that the fitting procedure has preferred to change the background model to agree with the data. Pulls with value 1 represent a  $1\sigma$  departure from the inputted central value, where  $\sigma$  represents one standard deviation of the constraining function. Examples of the distributions of pulls and constraints of some nuisance parameters are shown in:

- Figure 9.9 for the  $b$ -tagging parameters,
- Figure 9.10 for the  $Z+jets$  modeling parameters,
- Figure 9.11 for normalization parameters.

Additional pull plots for parameters may be found in Reference [109]. The contributions of the 12 sources of systematic uncertainties that are the greatest contributors to the total systematic uncertainty on  $\mu$  are shown in Figure 9.12. The impact of each source of uncertainty is calculated by obtaining the change in the  $\mu$  value when the given uncertainty is shifted by  $\pm 1\sigma$  from its best-fit value. A validation of the statistical model presented here follows in Chapter 10.

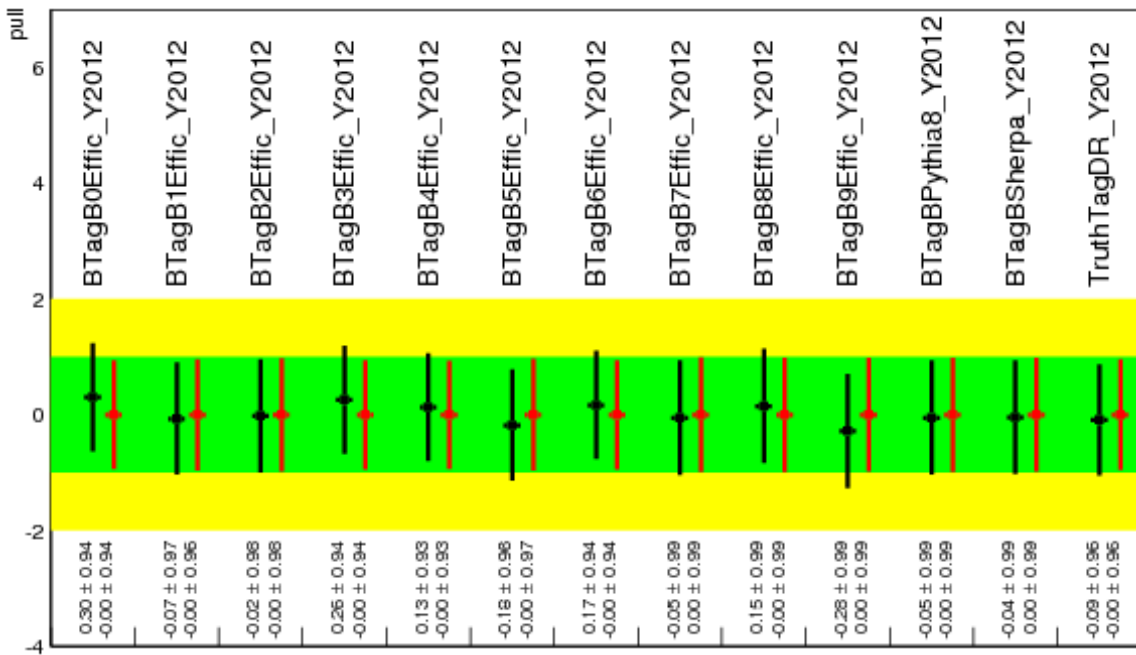


Figure 9.9: Pull plots for  $b$ -tagging nuisance parameters in the 2-lepton fit. The fit to the Asimov data set is shown in red and the fit to the data in black.

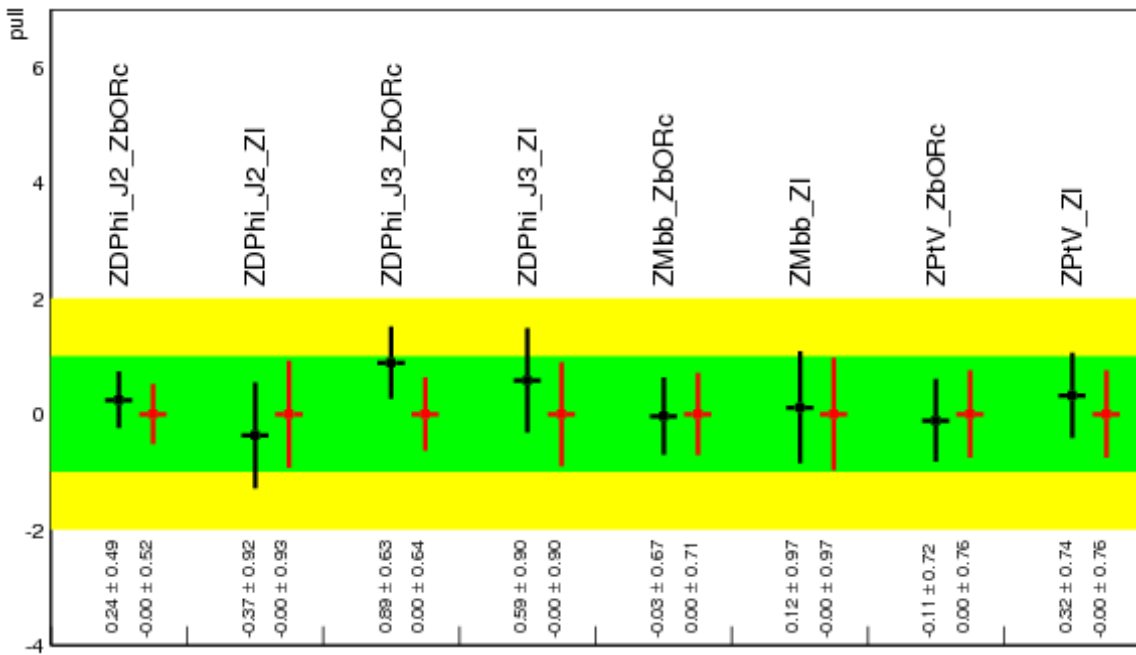


Figure 9.10: Pull plots for  $Z$ +jets modeling parameters in the 2-lepton fit. The fit to the Asimov data set is shown in red and the fit to the data in black.

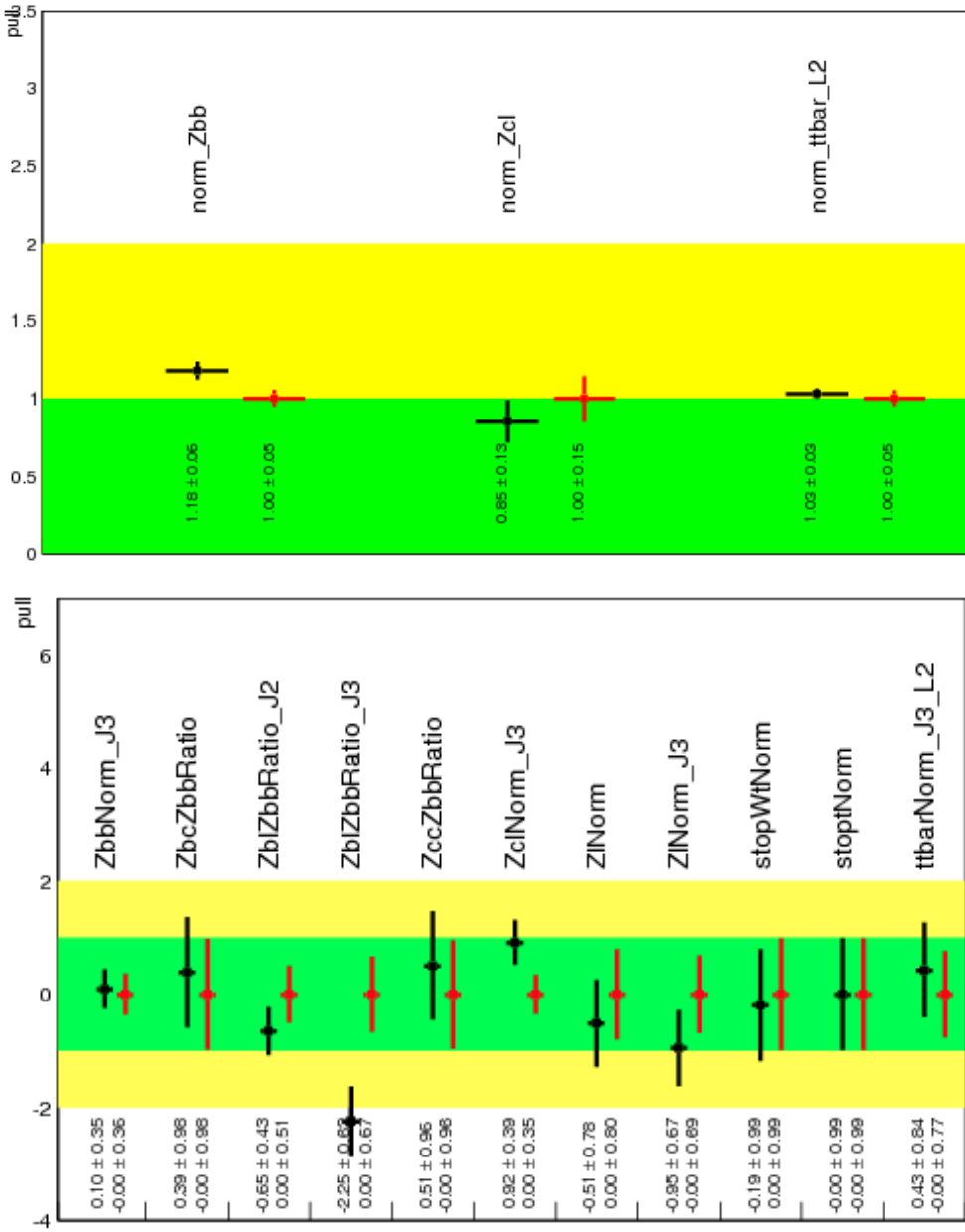


Figure 9.11: Pull plots for normalization parameters in the 2-lepton fit. The fit to the Asimov data set is shown in red and the fit to the data in black. In the top panel, the  $y$ -axis is a measure of the floating normalization factor, rather than a pull of a constrained parameter. In the bottom panel, one parameter is observed to be pulled near 2 standard deviations from its central value. For the pull in  $ZblZbbRatio\_J3$ , this indicates that in the 3-jet signal region, the ratio of  $Zbl$  to  $Zbb$  event yields is 2.25 standard deviations below expectation, or 27% below expectation. This must be considered in the context that the  $Zbb$  normalization scale factor is 1.2, so the  $Zbl$  normalization is itself in closer agreement with the Standard Model expectation. Such a pull can occur when the background in one control region fluctuates with respect to another.

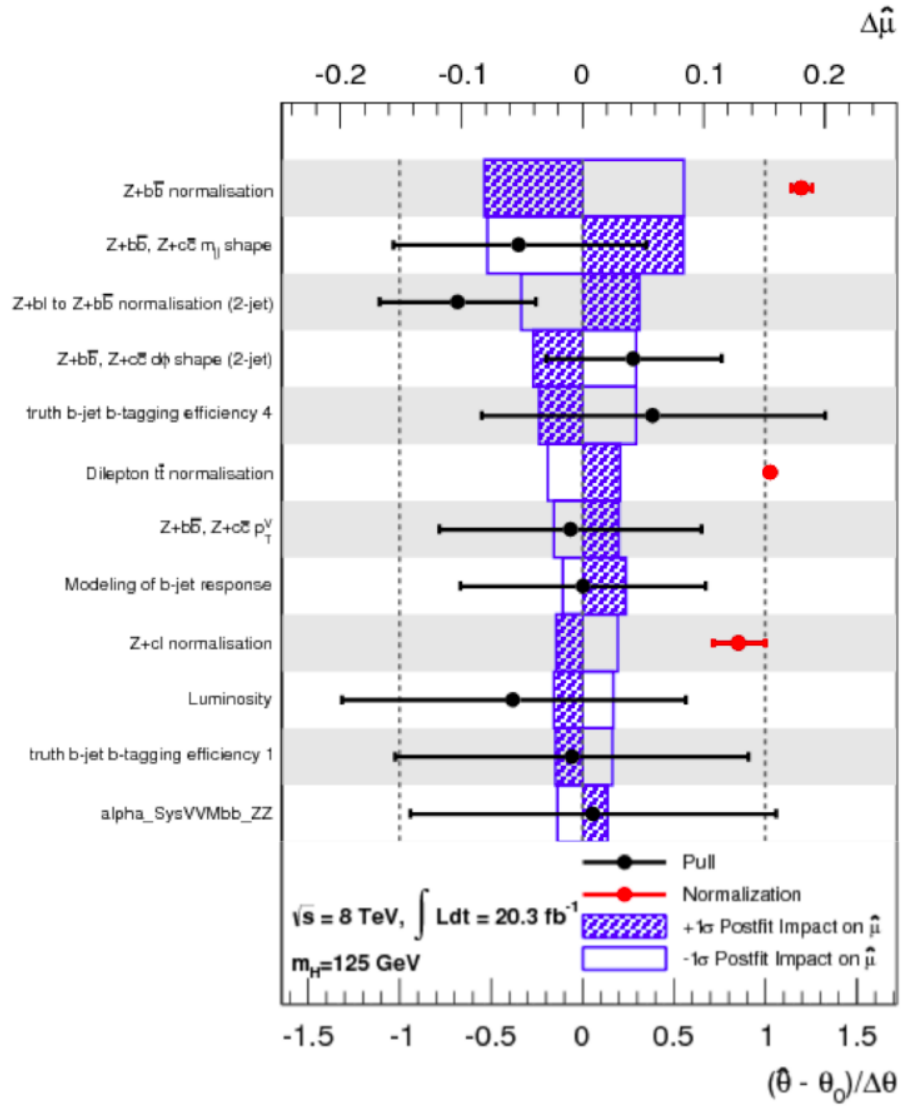


Figure 9.12: Ranking of the impact on  $\mu$  for the systematic uncertainties in the profile likelihood fit. The central value of the point for each nuisance parameter represents the pull of that parameter, and the value of the pull is given by the bottom axis. The post-fit impact of the uncertainty on the total uncertainty in  $\mu$  is given by the size of the blue boxes, with values corresponding to the upper  $x$ -axis. The  $+1\sigma$  variation is represented by the shaded blue box, while the  $-1\sigma$  variation is represented by the empty blue box.

## 9.6 Post-fit Distributions

This section contains the MV1c and  $m_{b\bar{b}}$  distributions in the 2-jet analysis regions after the fit to data. Post-fit distributions for the 3-jet region are found in Appendix B.

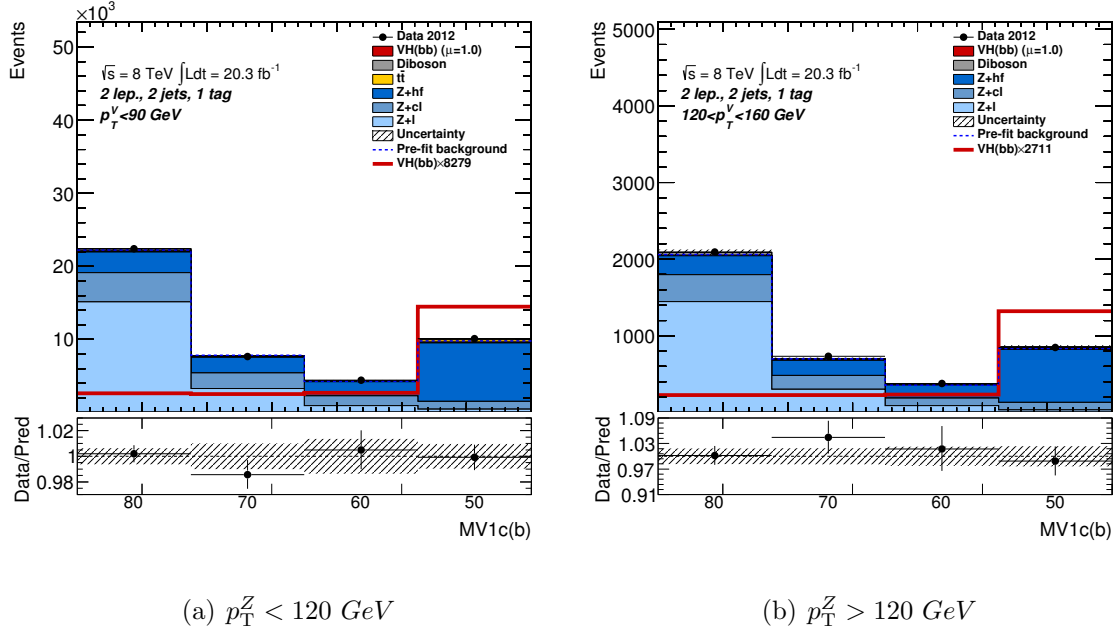


Figure 9.13: Post-fit plots for the  $MV1c$  distribution in 2-lepton events in the 1-tag, 2-jet analysis regions. The pre-fit background expectation is indicated by the dashed blue line.

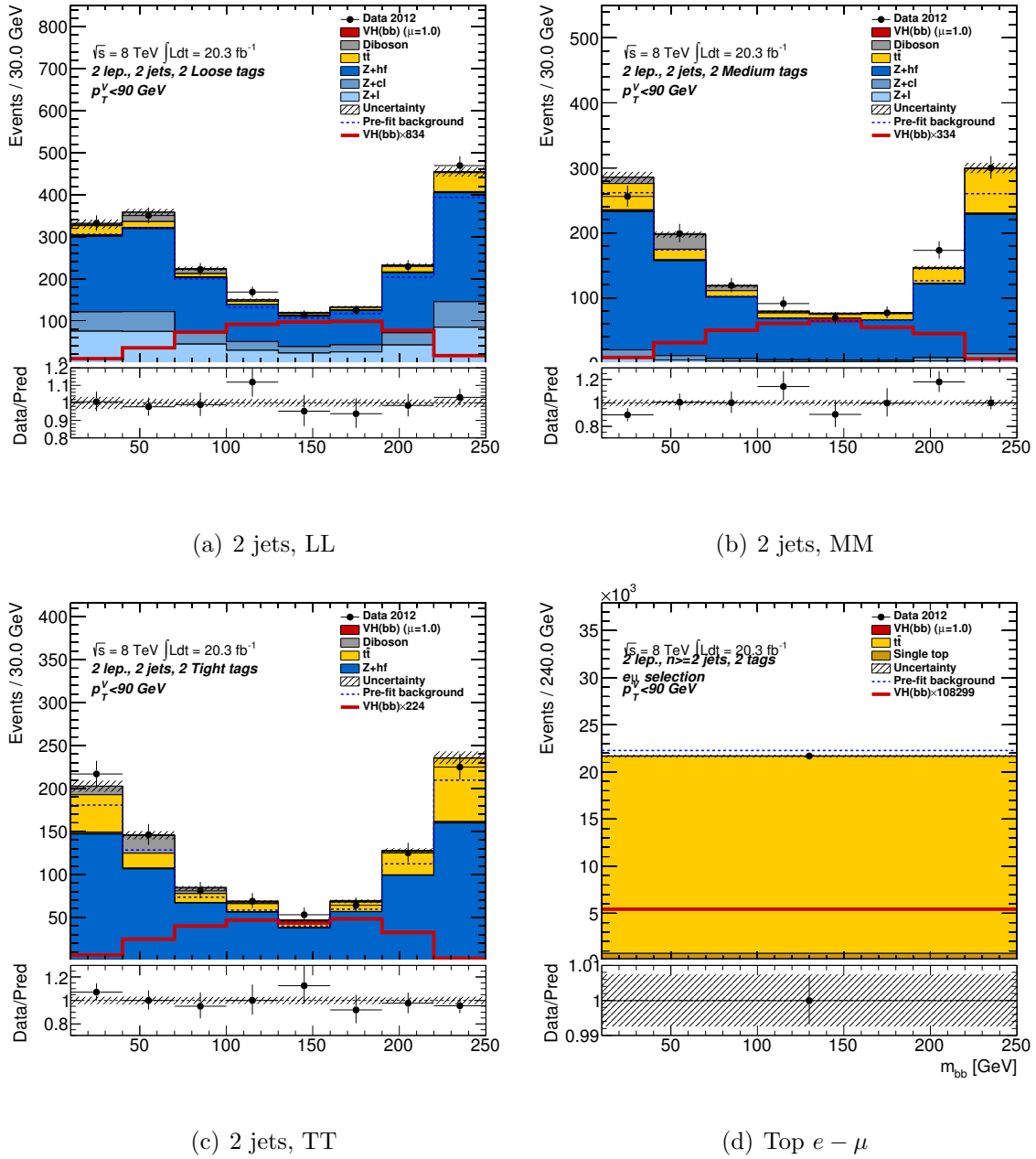


Figure 9.14: Post-fit plots for the  $m_{b\bar{b}}$  distributions in the  $LL$ ,  $MM$ ,  $TT$ , and top  $e-\mu$  categories for the 2-jets events in the 2-lepton fit. The pre-fit background expectation is indicated by the dashed blue line.

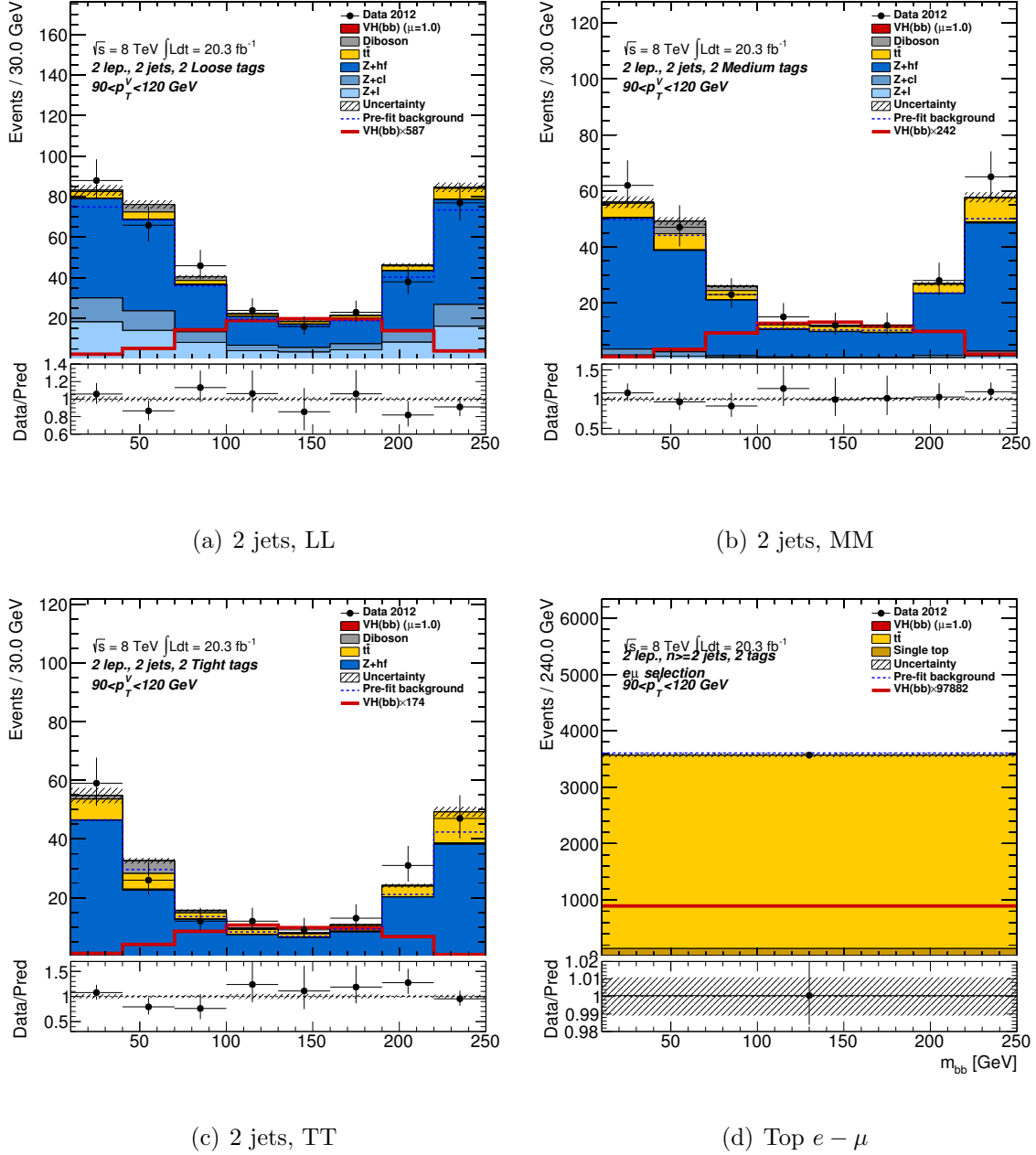


Figure 9.15: Post-fit plots for the  $m_{b\bar{b}}$  distributions in the  $LL$ ,  $MM$ ,  $TT$ , and top  $e-\mu$  categories for the 2-jets events in the 2-lepton fit. The pre-fit background expectation is indicated by the dashed blue line.

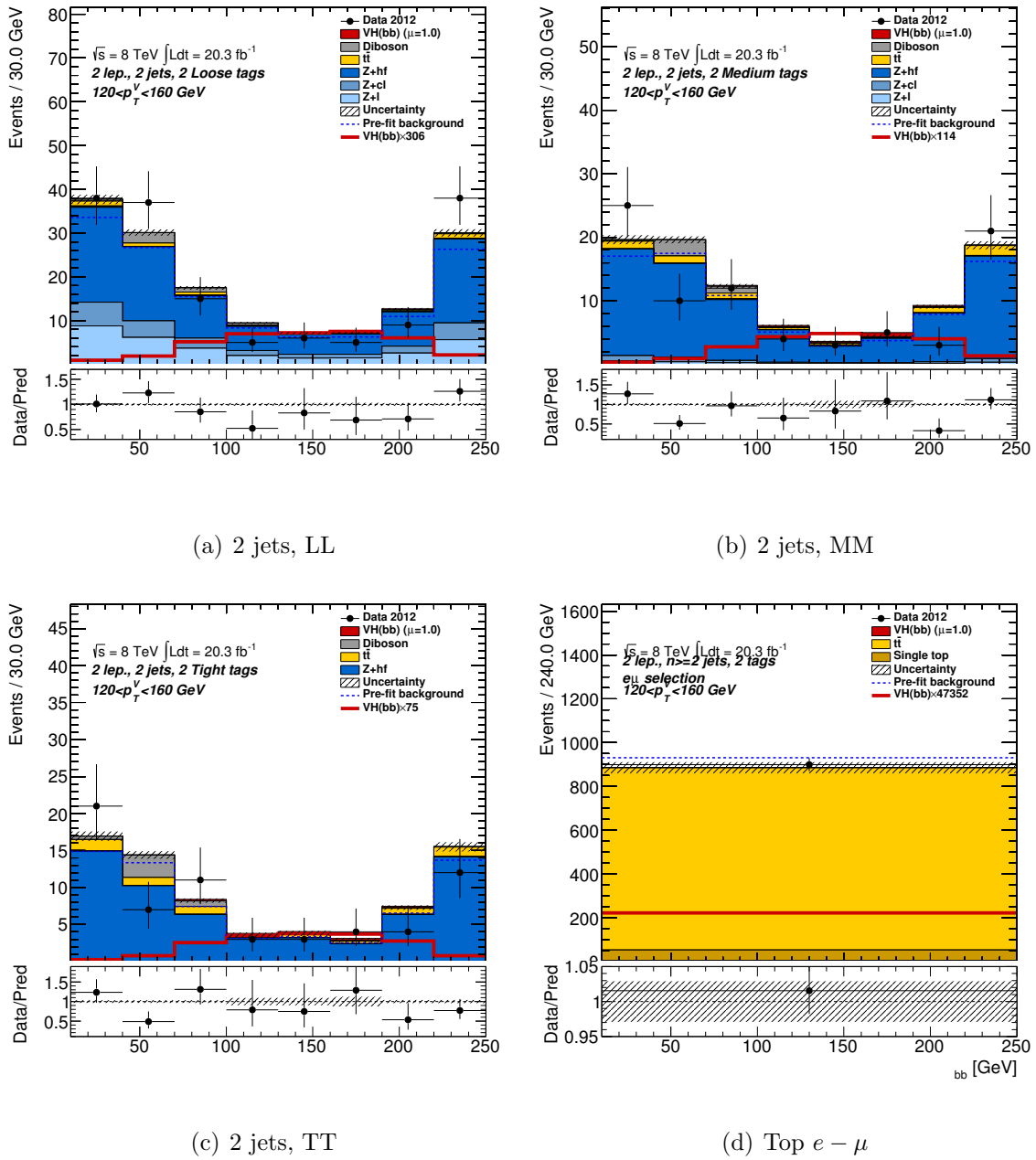


Figure 9.16: Post-fit plots for the  $m_{b\bar{b}}$  distributions in the  $LL$ ,  $MM$ ,  $TT$  and top  $e - \mu$  categories for the 2-jets events in the 2-lepton fit. The pre-fit background expectation is indicated by the dashed blue line.

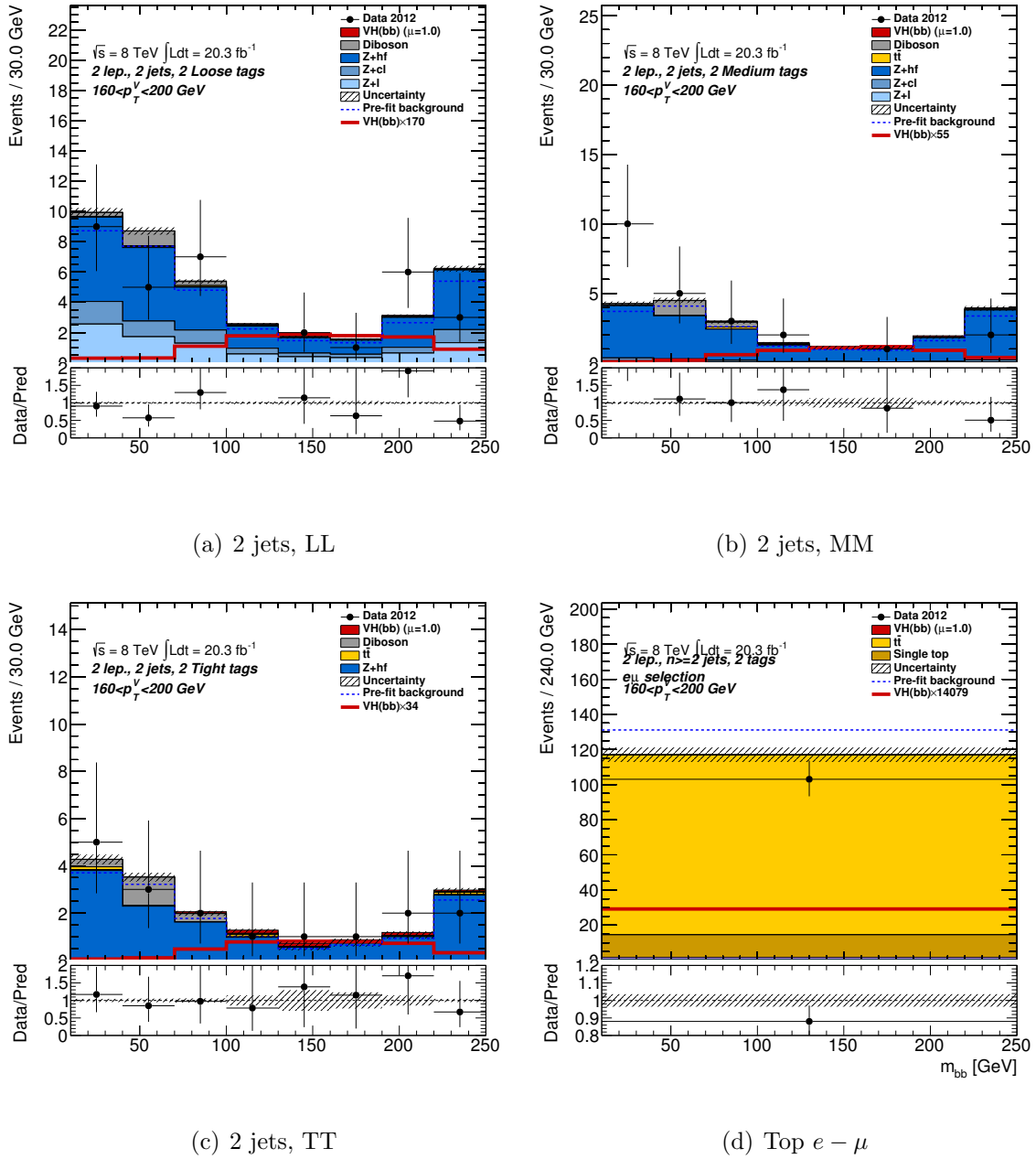


Figure 9.17: Post-fit plots for  $m_{bb}$  distributions in the  $LL$ ,  $MM$ ,  $TT$ , and top  $e - \mu$  categories for the 2-jets events in the 2-lepton fit. The pre-fit background expectation is indicated by the dashed blue line.

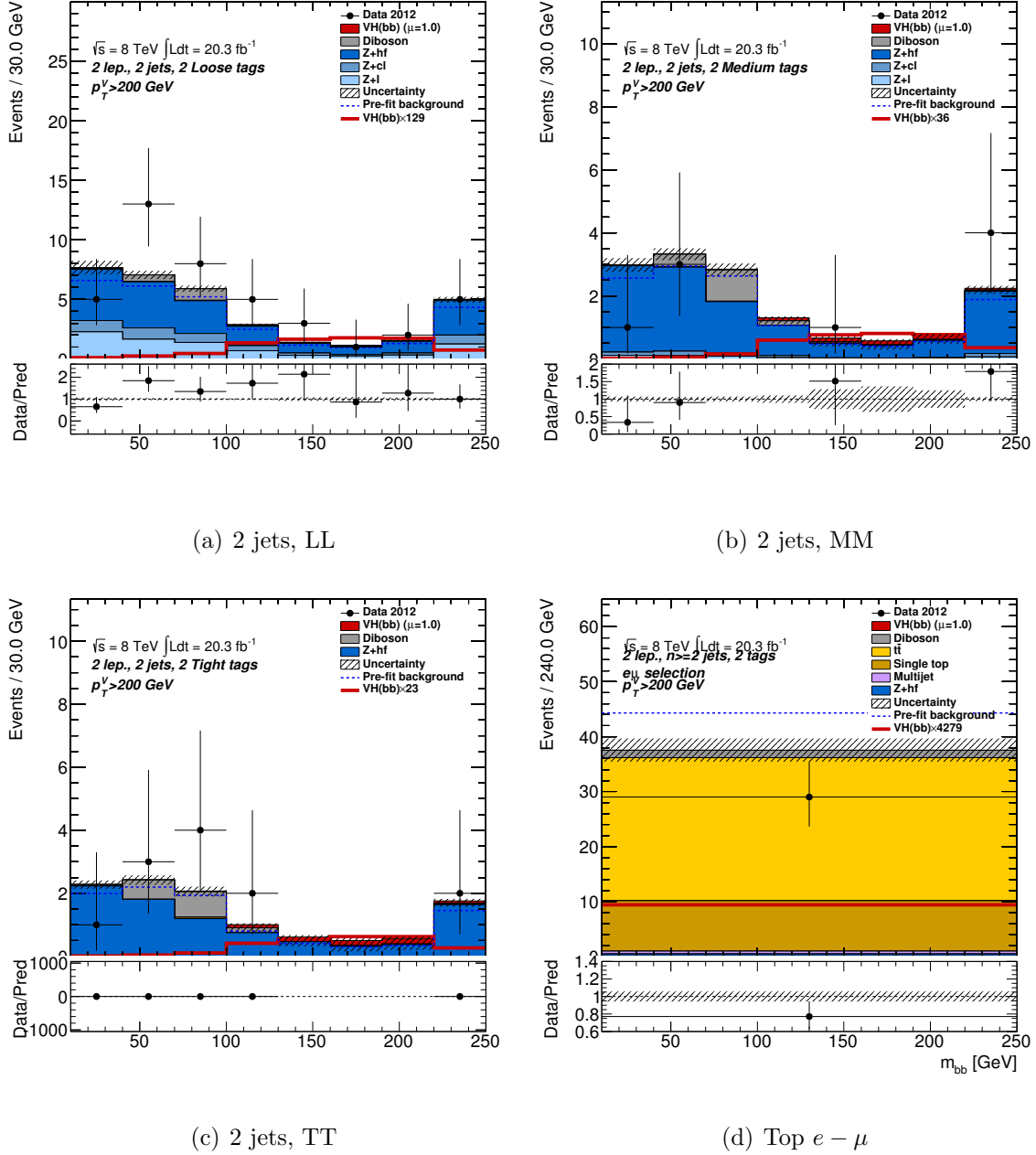


Figure 9.18: Post-fit plots for  $m_{jj}$  distribution in the  $LL$ ,  $MM$ ,  $TT$ , and top  $e - \mu$  categories for the 2-jets events in the 2-lepton fit. The pre-fit background expectation is indicated by the dashed blue line.

# Chapter 10

## Results

This chapter presents a validation of the statistical method presented in the previous chapters, as well as the results of the search for the  $ZH \rightarrow \ell^+\ell^-b\bar{b}$  process. Section 10.1 presents the validation of the statistical model through a measurement of the diboson processes  $WW$ ,  $WZ$ , and  $ZZ$ . For the 2-lepton channel, the  $ZZ$  contribution is the dominant diboson contribution because the two  $b$ -tag requirement accepts  $Z \rightarrow b\bar{b}$  events while rejecting  $WZ$  events efficiently. With this validation complete, final results on the  $ZH \rightarrow \ell^+\ell^-b\bar{b}$  search are presented in Section 10.2. A discussion of the results follows in Section 10.3

### 10.1 Validation through Diboson Process

Since the diboson processes, particularly  $ZZ$  production with  $Z \rightarrow b\bar{b}$ , have the same final state as the  $ZH \rightarrow \ell^+\ell^-b\bar{b}$  signal process and a cross section  $\sim 5$  times larger, as well as a peak in  $m_{b\bar{b}}$  near the Higgs signal region, the observation of the diboson

processes is a powerful validation of the statistical model presented in Chapter 9. The same profile likelihood fit from that chapter is performed again, but with one change. In addition to the Higgs signal strength,  $\mu$ , a multiplicative scaling of the cross section times branching ratio for the diboson processes ( $WW$ ,  $WZ$ , and  $ZZ$ ) is left freely floating in the fit. This diboson signal strength parameter is represented by  $\mu_D$ . No significant differences are observed in the pulls or constraints of any nuisance parameters between the diboson fit and the Higgs fit. As an example, modeling parameters for the  $Z$ +jets background are compared in Figure 10.1 for the two fits. The Higgs fit is shown in red and the diboson fit is shown in black. These parameters are among the largest contributors to the error on the  $\mu$  and  $\mu_D$  values, and are almost identical between the two fits.

Performing the fit for  $\mu_D$  yields the floating normalization factors given in Table 10.1 for the other backgrounds in the event. Within the stated uncertainties, these are consistent with the floating normalization factors generated in the Higgs fit, shown in Table 10.2. For comparison, the results from the 7 TeV analysis presented in Reference [7] are shown in Table 10.3 and are compatible with the 8 TeV result. The probability,  $p_0$  to obtain a result at least as diboson-like in the absence of a true diboson process as the observed result is 0.0352, corresponding to a significance of  $1.81\sigma$ .

A useful visualization is created by subtracting all backgrounds from the Monte Carlo event yield except the diboson and Higgs candidate events. An equivalent number of events is then also subtracted from the data bin-by-bin, resulting in Figure 10.2.

Process	Scale factor
$\mu_D$	$0.55 \pm 0.32$
$Z + bb$	$1.20 \pm 0.06$
$Z + cl$	$0.85 \pm 0.15$
$t\bar{t}$	$1.03 \pm 0.03$

Table 10.1: Floating normalizations for the Diboson fit.

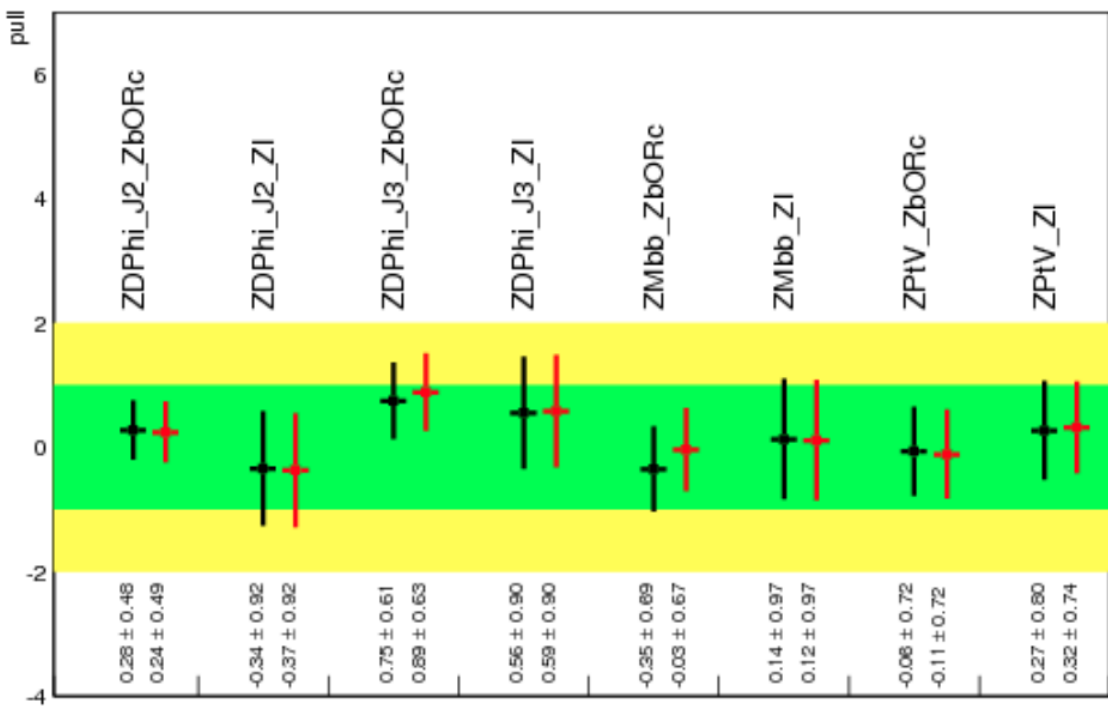


Figure 10.1: Pull plots for  $Z$ +jets modeling parameters in the 2-lepton fit. The fit for the Higgs  $\mu$  is shown in red and the fit for the diboson  $\mu_D$  is shown in black.

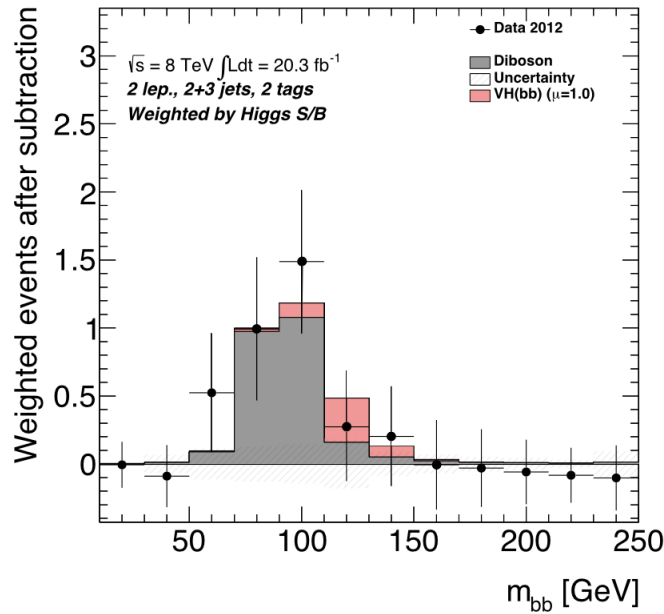


Figure 10.2: The distribution of  $m_{b\bar{b}}$  in data after subtraction of all backgrounds except for the diboson processes, as obtained with the dijet mass analysis for the  $\sqrt{s} = 8$  TeV data. The contributions from all  $p_T^V$  intervals, number-of-jets and 2-tag  $b$ -tagging categories are summed and weighted by their respective values of the ratio of expected diboson boson signal to fitted background. The contribution of the associated  $ZH$  production of a Standard Model Higgs boson with  $m_h = 125$  GeV is shown as expected for the Standard Model cross section (indicated as  $\mu = 1.0$ ). The size of the combined statistical and systematic uncertainty on the fitted background is indicated by the hatched band.

## 10.2 Higgs Search Results

With the model validated in Section 10.1, the results for the Higgs  $\mu$  are finalized. This section reports the results of the profile likelihood fit in which the normalized Higgs signal strength,  $\mu$ , is a floating parameter. Table 10.2 shows the floating normalizations as determined from the profile likelihood fit. The values for the other  $Z + \text{jets}$  backgrounds are a function of the nuisance parameters as described in Section 9.2.3. Table 10.3 shows the floating normalizations as determined in the 7 TeV analysis from Reference [7]. The two tables are not directly comparable because the 7 TeV data were not re-analyzed with the same set of nuisance parameters as for the 8 TeV analysis, so some differences are to be expected between the background normalizations.

Process	Scale factor
$\mu$	$0.17 \pm 1.4$
$Z + bb$	$1.18 \pm 0.06$
$Z + cl$	$0.85 \pm 0.13$
$t\bar{t}$	$1.03 \pm 0.03$

Table 10.2: Floating normalizations for the Higgs fit at  $\sqrt{s} = 8$  TeV.

Process	Scale factor
$\mu$	$0.6 \pm 4.0$
$Z + bb + Z + bc + Z + cc$	$1.27 \pm 0.12$
$Z + cl$	$0.95 \pm 0.52$
$t\bar{t}$	$1.12 \pm 0.07$

Table 10.3: Floating normalizations for the Higgs fit  $\sqrt{s} = 7$  TeV.

### 10.2.1 Higgs Signal Strength

The extracted signal strength parameter,  $\mu$ , for the  $ZH \rightarrow \ell^+\ell^-b\bar{b}$  analysis and its statistical and systematic uncertainties are presented in Table 10.4. Details of the contribution of the other nuisance parameters to the total uncertainty on  $\mu$  are shown in Figure 9.12. The analysis of the 7 TeV data had much less statistical power, and a result of  $\mu = 0.6 \pm 4.0$ .

Best Fit $\mu = 0.17 +1.41 -1.30$		
Type of Uncertainty	Magnitude	Percent of Total
Statistical Uncertainty	+1.17 – 1.06	63%
Total Systematic Uncertainty	+0.86 – 0.76	37%

Table 10.4: Best fit value of  $\mu$  and the corresponding statistical and systematic uncertainties.

### 10.2.2 Limits on the Cross Section for the $ZH \rightarrow \ell^+\ell^-b\bar{b}$ Process

The expected and observed upper limits on the normalized signal strength as a function of the Higgs boson mass are shown in Figure 10.3. At a Higgs mass of 125 GeV, the observed upper limit is 2.76 times the Standard Model cross section, which is to be compared with an expected value of 2.54 in the absence of signal.

Given that the observed limit on the  $ZH \rightarrow \ell^+\ell^-b\bar{b}$  process is 2.76 times the Standard Model expectation, a significant result is not expected for the  $p_0$  value. The probability,  $p_0$ , of obtaining a result at least as signal-like as the observed value  $\mu = 0.17$ , in the absence of signal, is 0.449, which corresponds to a significance of

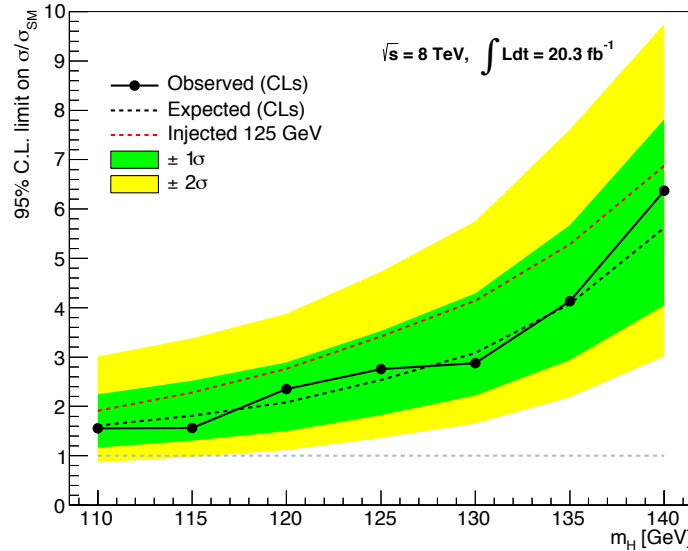


Figure 10.3: Expected 95% confidence level upper limits on the normalized signal strength parameter  $\mu$  as a function of Higgs boson mass for the  $ZH \rightarrow \ell^+ \ell^- b\bar{b}$  analysis. The expected upper limit is given for the background-only hypothesis. The green and yellow bands represent the  $1\sigma$  and  $2\sigma$  ranges of the expectation for the upper limit in the absence of a signal. The dashed line represents the observed upper limit.

0.13 $\sigma$ . Figure 10.4 shows the observed local  $p_0$  value as a function of the Higgs boson mass.

### 10.3 Discussion of Results

This  $ZH \rightarrow \ell^+ \ell^- b\bar{b}$  search is statistically limited. According to Table 10.4, 63% of the total error on the  $\mu$  measurement is statistical, and the systematic uncertainty is driven by the modeling of the  $Zbb$  process, which should also improve with more data. Given that the LHC plans to restart for Run II with increased instantaneous luminosity and a higher center of mass energy, the  $ZH \rightarrow \ell^+ \ell^- b\bar{b}$  process will remain

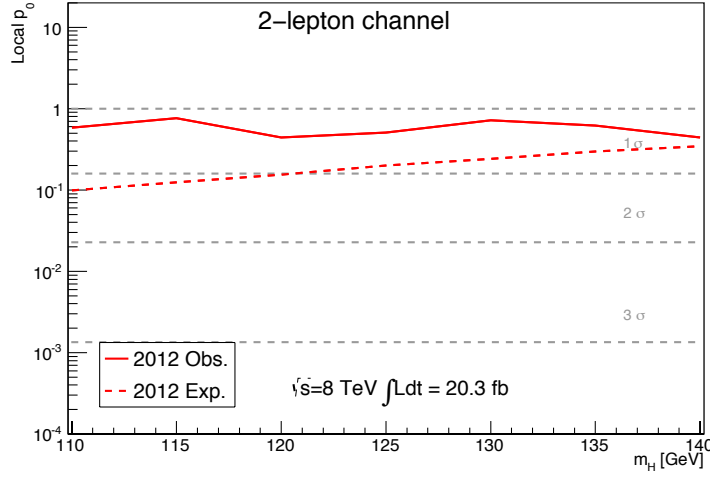


Figure 10.4: The observed local  $p_0$  as a function of the Higgs boson mass for the  $ZH \rightarrow \ell^+ \ell^- b\bar{b}$  analysis. The dashed curves shows the expected local  $p_0$  under the hypothesis of a Standard Model Higgs boson signal at that mass point.

a promising part of the Higgs measurement program. At  $\sqrt{s} = 13$  TeV the signal and leading cross sections each scale up by a factor of  $\sim 2$ , so an additional  $25 \text{ fb}^{-1}$  or data would yield a 70

As an alternative to searching exclusively for  $ZH \rightarrow \ell^+ \ell^- b\bar{b}$  production, these results can be combined with searches for  $ZH \rightarrow \nu\bar{\nu} b\bar{b}$  and  $WH \rightarrow \ell\nu b\bar{b}$  yielding a result for associated production with  $H \rightarrow b\bar{b}$  inclusively. This combination follows in Chapter 11.

# Chapter 11

## Combined Search

### 11.1 Motivation for the Combination

In order to increase the sensitivity of the search for Higgs production in association with a vector boson and decaying to a pair of  $b$ -quarks, additional search channels are added to the previously-discussed  $ZH \rightarrow \ell^+ \ell^- b\bar{b}$  dijet-mass analysis. This chapter summarizes the results of a combined  $ZH \rightarrow \ell^+ \ell^- b\bar{b}$ ,  $WH \rightarrow \ell\nu b\bar{b}$ , and  $ZH \rightarrow \nu\bar{\nu} b\bar{b}$  search, which is presented in its entirety in References [29, 109]. Adding search channels takes advantage of the greater production cross section of the  $WH \rightarrow \ell\nu b\bar{b}$  process and the comparatively greater  $Z$ -decay branching ratio to neutrinos of the  $ZH \rightarrow \nu\bar{\nu} b\bar{b}$  process to increase the statistical power of the search. In practice, this means adding analysis regions with 1 lepton and with 0 leptons to complement the 2-lepton analysis.

The summary of the combined search at  $\sqrt{s} = 8$  TeV is presented in the following sections. Section 11.2 provides information on the object and event-level topological requirements to categorize events into either the 0-lepton or 1-lepton analysis. Section 11.3 summarizes the additional studies on the modeling of the background processes that are important to the combined search but are not already discussed in Chapter 8 for the 2-lepton analysis. The extension of the statistical model from Chapter 9 to include new analysis regions and nuisance parameters for the combined analysis analysis is contained in Section 11.4. The  $\sqrt{s} = 7$  TeV analysis, previously reported in Reference [7], is summarized in Section 11.5 along with its combination with the  $\sqrt{s} = 8$  TeV analysis. The results for the search at  $\sqrt{s} = 8$  TeV analysis alone, and also the combination with  $\sqrt{s} = 7$  TeV data are discussed in Section 11.6.

## 11.2 Object and Event Selection

### 11.2.1 Event Selection

The selection of events for the combination is the same as that described in Chapter 7 for the  $ZH \rightarrow \ell^+ \ell^- b\bar{b}$  analysis, except that additional  $E_T^{\text{miss}}$ -based triggers must be used to collect data for the 0-lepton channel. The 1-lepton channel uses all the single-lepton triggers, and in events with  $p_T^W > 120$  GeV, the  $E_T^{\text{miss}}$  triggers are also used to supplement muon triggers, which have acceptance inefficiencies in certain  $\phi$  and  $\eta$  regions. These triggers are summarized in Table 11.1.

Trigger Object	Data Period	Trigger Names	$iso_{track}$	$L (fb^{-1})$
$E_T^{\text{miss}} < 160 \text{ GeV}$	A-B5	EF_xe80T_tclcw_loose	NA	1.92
	B6-L	EF_xe80_tclcw_loose		18.13
$E_T^{\text{miss}} > 160 \text{ GeV}$	A-B5	EF_xe80_tclcw	NA	2.13
	B6-L	EF_xe80_tclcw_loose		18.13
single electron	A-L	EF_e24vhi_medium1	✓	
single muon		EF_e60_medium1 EF_mu24i_tight EF_mu36_tight	✓	20.3
di-electron di-muon	A-L	EF_2e12Tvh_loose1 EF_2mu13		20.3

Table 11.1: Trigger table used in the 2012 data analysis. NA implies that the requirement is not applicable for that trigger, while a ✓ implies that the  $iso_{track}$  requirement is applied.

### 11.2.2 Lepton Selection for Event Categorization

The selection of leptons is discussed in detail Section 7.2.1. For the combination of the three different lepton channels, a variety of lepton categories are used. Table 11.2 summarizes the lepton requirements in each of the three lepton channels. Tighter lepton requirements are chosen for the 1-lepton analysis than the 2-lepton analysis in order to reject multijet background originating from jets mistakenly reconstructed as leptons.

Analysis Channel	Loose Lepton	Medium Lepton	Tight Lepton
0-lepton	0	—	—
1-lepton	0	0	1
2-lepton	1	1	—

Table 11.2: Signal lepton selection from the 3 inclusive lepton definitions.

### 11.2.3 Jet Selection for Event Categorization

For the 0-lepton and 1-lepton channels, the rejection of events from the  $t\bar{t}$  background processes is a greater concern than for the 2-lepton channel. Veto jets were defined in Section 7.2.3 as being jets with  $p_T > 20$  GeV and  $2.5 < |\eta| < 4.5$ . In the 1-lepton channel,  $t\bar{t}$  events with one hadronically decaying  $W$ -boson will often have such a jet in addition to the two  $b$ -jets. In the 0-lepton channel the same is true and also applies to fully-hadronic top decays. Therefore, additional event-level vetoes on the presence of veto jets are applied. The jet multiplicity requirements for each analysis channel are given in Table 11.3.

Jet Type	Signal	Veto
0-lepton		0
1-lepton	2 or 3	—
2-lepton		—

Table 11.3: Jet multiplicity requirements for each analysis channel. The 2-lepton channel does not veto events based on the presence of the veto jets.

### 11.2.4 Event Kinematic Selection

For the combined search, the 0-lepton and 1-lepton channels must be created through new event-level kinematic requirements. The kinematic requirements for selecting each of the analysis channels are summarized in Table 11.4. As in the case of the 2-lepton selection presented in Chapter 7, the 0-lepton and 1-lepton analyses are also split into bins of  $p_T^V$ , and each bin has a requirement on the maximum separation of the Higgs candidate jet in  $\Delta R$ . This  $p_T$ -dependent requirement is motivated by the fact that more boosted Higgs candidates will have more collimated decay products.

In the 0-lepton analysis, several angular requirements are placed on the physics objects such as  $\Delta\phi(E_T^{\text{miss}}, p_T^{\text{miss}})$ ,  $\Delta\phi(E_T^{\text{miss}}, \text{jets})$ , and  $\Delta\phi(V, H)$  in order to optimize the analysis for sensitivity and to reject fake  $E_T^{\text{miss}}$ . Additionally, some requirements are placed on the sum of the transverse momentum of the signal jets in the event. In the 1-lepton selection, a cut on the scalar sum of the  $p_T$  of all objects in the event,  $M_{eff}$ , is made at 180 GeV in the lowest two  $p_T^W$  bins, while cuts on the  $E_T^{\text{miss}}$  are made in the highest three  $p_T^W$  bins to optimize the sensitivity of the analysis. A requirement of  $m_T^W < 120$  is made for all bins of  $p_T^W$ , where  $m_T^W = \sqrt{2p_T^\ell E_T^{\text{miss}}(1 - \cos \Delta\phi(\ell, E_T^{\text{miss}}))}$  is the transverse mass of the  $W$ -boson. The kinematic requirements of the 2-lepton channel are the same as those presented in Chapter 7.

### 11.3 Background Modeling

The modeling of the  $Z + \text{jets}$ ,  $t\bar{t}$ , and diboson backgrounds and the systematic uncertainties associated with the models is discussed in detail in Chapter 8. For the combined search, the  $W + \text{jets}$  and single-top background models become important sources of uncertainty. Additionally, the modeling of the multijet background in the 0-lepton and 1-lepton channels contributes significantly to some signal regions, which is not the case for the 2-lepton channel. Section 11.3.1 summarizes the  $W + \text{jets}$  modeling and Section 11.3.2 summarizes the single-top modeling. The estimation of the multijet background for the 0-lepton and 1-lepton channels is made with templates created in data and is summarized in Section 11.3.3. The full details of these modeling studies are left to Reference [109].

Variable	Dijet Mass Analysis									
	Common Selection									
$p_T^V$ (GeV)	0-90	90-120	120-160	160-200	> 200					
$\Delta R(jet_1, jet_2)$	0.7-3.4	0.7-3.0	0.7-2.3	0.7-1.8	< 1.4					
	0-Lepton Selection									
$p_T^{\text{miss}}$ (GeV)	NU	Ref. [109]	> 30							
$\Delta\phi(E_T^{\text{miss}}, p_T^{\text{miss}})$			< $\pi/2$							
$\Delta\phi(E_T^{\text{miss}}, jets)$			> 1.5							
$\Delta\phi(V, H)$			> 2.8							
$\sum p_T^{jet_i} N_{jet} = 2$			> 120							
$\sum p_T^{jet_i} N_{jet} = 3$			> 150							
	1-Lepton Selection									
$M_{eff}$ (GeV)	-	> 180	-							
$E_T^{\text{miss}}$ (GeV)			> 20		> 50					
$m_T^W$ (GeV)		< 120								
	2-Lepton Selection									
$m_{\ell\ell}$ (GeV)	83-99									
$E_T^{\text{miss}}$ (GeV)	< 60									

Table 11.4: Event kinematic selection. NU stands for ‘Not Used’. The 90-120 GeV bin of the 0-lepton analysis utilizes a special trigger parametrization, described in Reference [109].

### 11.3.1 $W+\text{jets}$ Modeling

The  $W+\text{jets}$  background is the background process that contributes the second highest yield to the 1-lepton channel, after the  $t\bar{t}$  process. Six possible flavor combinations are considered for  $W+\text{jet}$  events, and they are categorized according to the flavor of the two leading jets in  $p_T$ .  $Wl$  represents processes with only light jets among the leading two in  $p_T$ .  $Wcl$  and  $Wcc$  represent processes with one or two  $c$ -jets and no  $b$ -jets.  $Wbl$ ,  $Wbc$ , and  $Wbb$  represent processes with a true  $b$ -jet, a true  $b$ -jet and a true  $c$ -jet, and two true  $b$ -jets, respectively, while the sum of the three is called  $W+\text{hf}$  (hf to represent heavy-flavor). The  $W+\text{jets}$  processes are modeled with the SHERPA generator [80] and interfaced with CT10 PDFs. As in the case for the  $Z+\text{jets}$  background discussed in Chapter 8, mismodeling of the angular separation of the two leading jets in  $\Delta\phi$  as well as in the  $p_T^W$  distribution is observed.

A reweighting is applied to  $Wl$  and  $Wcl$  events as a function of  $\Delta\phi$ , separately for  $p_T^W < 120$  GeV,  $p_T^W > 120$  GeV, and the 2-jet and 3-jet regions, following Reference [109]. An example of the mismodeled  $\Delta\phi$  distribution before correction and after correction is shown in Figure 11.1. Systematic uncertainties are set to be half the correction value on these samples. Additionally, the full value of this correction value is taken as an estimate for the systematic uncertainty on the shape of the  $\Delta\phi$  distribution for  $W+\text{jets}$  events of any other flavor combination. No correction is applied to those  $W+\text{jets}$  samples because the number of events in the control regions do not permit the observation of a significant mismodeling. After the application of the correction to the  $\Delta\phi$  distribution, many variables in the  $W+\text{jets}$  background samples

are more well-modeled, including the  $p_T^W$  spectrum. The  $p_T^W$  distribution before and after the application of the  $\Delta\phi$  correction is shown in Figure 11.2.

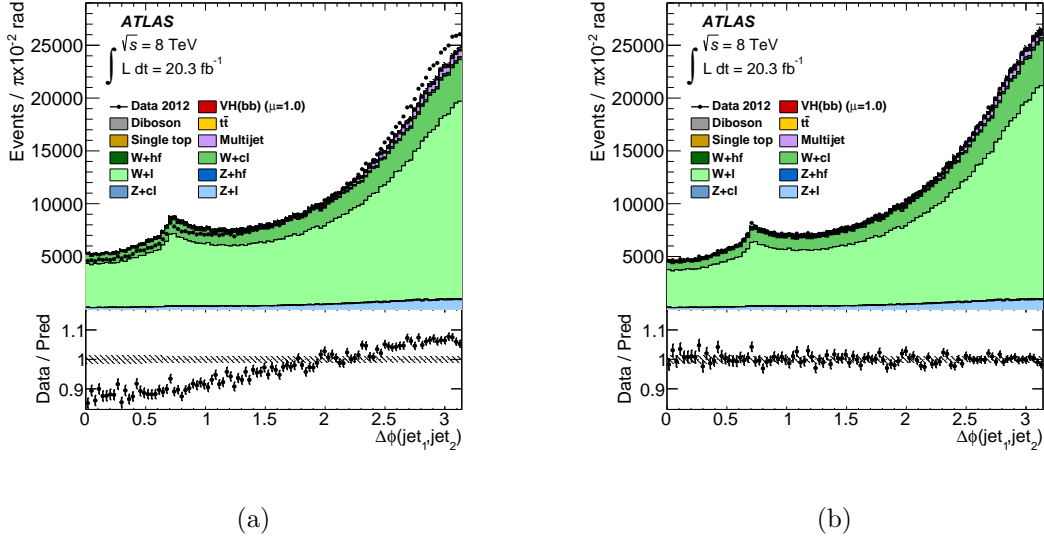


Figure 11.1: The  $\Delta\phi$  distribution observed in data (points with error bars) and expected (histograms) for the 2-jet 0-tag control region of the 1-muon sub-channel, (a) before and (b) after reweighting. All  $p_T^W$  intervals are combined. The multijet and simulated-background normalizations are provided by the multijet fits. The size of the statistical uncertainty is indicated by the shaded band. The data-to-background ratio is shown in the lower panel [29].

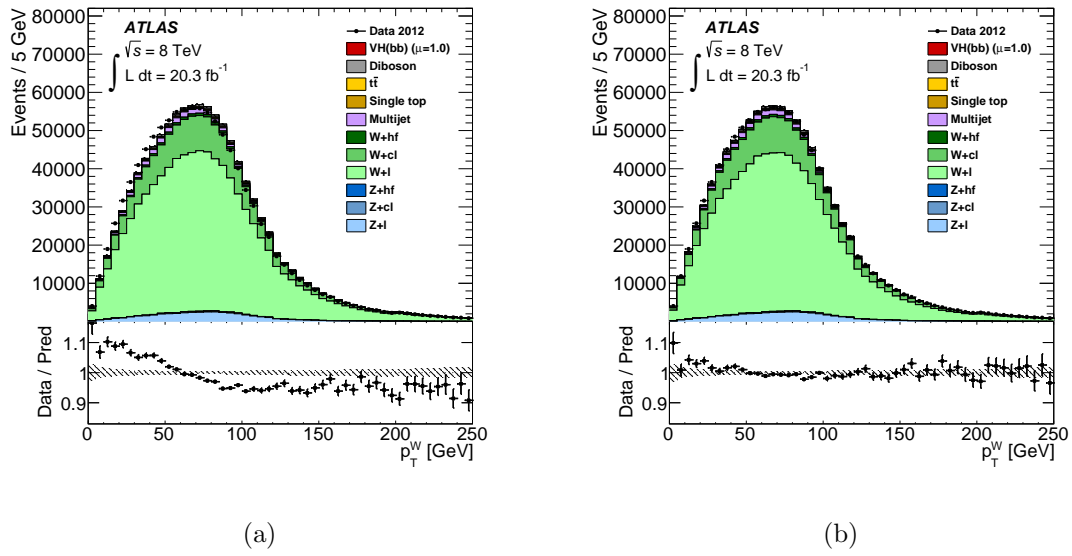


Figure 11.2: The  $p_T^W$  distribution observed in data (points with error bars) and expected (histograms) for the 2-jet 0-tag control region of the 1-muon sub-channel, (a) before and (b) after  $\Delta\phi$  reweighting. The multijet and simulated-background normalizations are provided by the multijet fits. The size of the statistical uncertainty is indicated by the shaded band. The data-to-background ratio is shown in the lower panel [29].

The normalization of the  $Wl$  background is taken directly from the Standard Model expectation in the Monte Carlo simulation, and an uncertainty of 10% is estimated using the observed agreement between data and Monte Carlo simulation in the control region with zero  $b$ -tags. For the  $Wcl$  and  $Wbb$  backgrounds, the normalizations are left floating in the profile likelihood fit. The relative ratio of the 3-jet to 2-jet production cross sections for the  $Wl$  and  $Wc$  background processes are taken from Monte Carlo simulation with an estimated uncertainty of 10% calculated by comparison between the nominal SHERPA sample and an ACERMC sample.

Since the final state for the signal process and the  $Wbb$  process is the same, it is difficult to obtain a control region in data, and additional systematic uncertainties on the  $Wbb$  process are estimated from event-generator-level Monte Carlo comparisons. The predictions of the nominal SHERPA generator are compared to those of POWHEG+PYTHIA8 [90, 107], of aMC@NLO+HERWIG++ [11] and of ALPGEN+HERWIG [64]. Further comparisons are made between samples generated using aMC@NLO with varied renormalization ( $\mu_R$ ) and factorization ( $\mu_F$ ) scales<sup>1</sup>, independently modified by factors of 2 or 0.5, and also with a variety of PDF sets (CT10, MSTW2008NLO and NNPDF2.3 [46]). These studies result in an estimated uncertainty of 10% for the 3-jet to 2-jet ratio, correlated between all  $W$ +jets processes with two true  $c$ -jets or at least one true  $b$ -jet [29].

Additionally, uncertainties on the shape of the  $m_{b\bar{b}}$  and  $p_T^W$  distributions are assessed. When the  $m_{b\bar{b}}$  shape uncertainty increases the dijet-mass distribution by 23%

---

<sup>1</sup>The nominal scales are taken as  $\mu_R = \mu_F = [m_W^2 + p_T(W)^2 + m_b^2 + (p_T(b)^2 + p_T(\bar{b})^2)/2]^{1/2}$ .

at 50 GeV, it decreases it by 28% at 200 GeV. It is treated as uncorrelated for the  $Wl$ ,  $Wcl$ ,  $Wbb + Wcc$  and  $Wbl + Wbc$  processes. For the  $Wbb + Wcc$  processes, the uncertainty is further decorrelated among  $p_T^W$  intervals. When the  $p_T^W$  shape uncertainty increases the  $p_T^W$  distribution by 9% for  $p_T^W = 50$  GeV, it decreases it by 23% at 200 GeV [29]. It is treated as correlated for the  $W+hf$  processes, but uncorrelated between the 2-jet and 3-jet analysis regions.

Predictions using the inclusive production of all flavors by SHERPA and ALPGEN<sup>2</sup> are compared after full reconstruction and event selection to assign uncertainties on the flavor fractions, properly taking into account heavy-flavor production at both the matrix-element and parton-shower levels. The following uncertainties are assigned in the  $W+hf$  samples: 35% for the ratio  $Wbl/Wbb$  and 12% for each of the ratios  $Wbc/Wbb$  and  $Wcc/Wbb$  [29]. The uncertainty on the  $Wbl/Wbb$  ratio is uncorrelated among  $p_T^W$  intervals. Further details on all  $W+jets$  modeling studies are found in Reference [109], and Table 11.6 summarizes the uncertainties entering the profile likelihood fit.

### 11.3.2 Single-top Modeling

The Monte Carlo simulation used for the modeling of the single-top processes was discussed in Section 8.2.4 and full details are contained in Reference [109]. This section only discusses the associated systematic uncertainties as contained in Reference [29]. The theoretical uncertainties on the cross sections of the three processes contributing

---

<sup>2</sup>For ALPGEN, the production of light flavors and heavy flavors are performed separately at the matrix-element level. A dedicated procedure, based on the  $\Delta R$  between  $b$ -partons, is used to remove the overlap between  $b\bar{b}$  pairs produced at the matrix-element and parton-shower levels.

to single-top production are 4%, 4%, and 7% for the  $s$ -channel,  $t$ -channel, and  $Wt$  production, respectively [84].

After applying the kinematic selection for the 1-lepton channel, predictions of the nominal generators are compared with those obtained using a variety of other generators:

- ACERMC and MC@NLO for the  $s$ -channel process,
- POWHEG+HERWIG, and MC@NLO for  $Wt$  production with ACERMC,
- aMC@NLO for  $Wt$  production with ACERMC+HERWIG, [74, 82],
- for all three processes, the impact of ISR/FSR is evaluated using ACERMC.

Systematic uncertainties on the acceptance for each of the three processes are estimated as the largest deviations observed between the nominal and varied Monte Carlo generator, separately for  $p_T^V < 120$  GeV and  $p_T^V > 120$  GeV, and for 2- and 3-jet events. These uncertainties are be as large as 52% for 2-jet events in the  $t$ -channel at low  $p_T^V$ , of the order of 5% for  $Wt$  production (except for 3-jet events at high  $p_T^V$ : 15%), and  $\sim 20\%$  for the  $s$ -channel [29].

In addition to acceptance uncertainties, the effects of the modeling variations described above on the kinematic variables entering the analysis are evaluated, and three shape systematic uncertainties are applied for  $Wt$ -channel single-top production. An uncertainty on the shape of the  $m_{b\bar{b}}$  distribution in the high  $p_T^V$  interval for 2-jet events is applied such that when a shift from the nominal model increases the rate by 20% for  $m_{b\bar{b}} = 50$  GeV, it decreases it by 40% at 200 GeV. A second uncertainty on the  $m_{b\bar{b}}$  shape for 3-jet events is applied, with corresponding shifts of 25%

and 20%. Finally, a third uncertainty is on the  $p_T$  distribution of the second-leading jet in the low  $p_T^V$  interval for 2-jet events [29]. These uncertainties are summarized in Table 11.7.

### 11.3.3 Multijet Background Estimate from Data

The estimate of the multijet background in the 2-lepton channel is given in Section 8.2.5. Detailed descriptions of the estimates of the multijet background in the 0-lepton and 1-lepton channels are contained in Reference [109], and only summarized here for completeness of the discussion of the background processes. Multijet processes have very large cross sections and may contribute to the analysis regions if jets are mistakenly reconstructed as leptons (for the 1-lepton and 2-lepton channel), or if a jet’s energy is mismeasured (for the 0-lepton channel).

#### 0-lepton Multijet Estimate

In the 0-lepton channel, the multijet background is estimated from data using an “ABCD method”. In this method, the data are divided into four regions based two variables:

- $\min[\Delta\phi(\vec{E}_T^{\text{miss}}, \text{jet})]$ ,
- $\Delta\phi(\vec{E}_T^{\text{miss}}, \vec{p}_T^{\text{miss}})$ ,

such that three of the regions are dominated by background (B,C, and D). For events with real  $E_T^{\text{miss}}$  from neutrinos, it is expected that the directions of  $\vec{E}_T^{\text{miss}}$  and  $\vec{p}_T^{\text{miss}}$  are similar. In events with fake  $E_T^{\text{miss}}$  arising from a jet energy measurement fluctuation,

it is expected that the direction of  $\vec{E_T^{\text{miss}}}$  is close to the direction of the mismeasured jet. The signal region (A) is therefore selected with  $\min[\Delta\phi(\vec{E_T^{\text{miss}}}, \text{jet})] > 1.5$  and  $\Delta\phi(\vec{E_T^{\text{miss}}}, \vec{p_T^{\text{miss}}}) < \pi/2$ . In region C, the requirement on  $\Delta\phi(\vec{E_T^{\text{miss}}}, \vec{p_T^{\text{miss}}})$  is reversed. In regions B and D,  $\min[\Delta\phi(\vec{E_T^{\text{miss}}}, \text{jet})] < 0.4$  is required, with requirements on  $\Delta\phi(\vec{E_T^{\text{miss}}}, \vec{p_T^{\text{miss}}})$  as in regions A and C, respectively. A comparison of the  $\min[\Delta\phi(\vec{E_T^{\text{miss}}}, \text{jet})]$  distributions for  $\Delta\phi(\vec{E_T^{\text{miss}}}, \vec{p_T^{\text{miss}}})$  above and below  $\pi/2$  shows that these two variables are only weakly correlated, and this observation is confirmed in a multijet event sample simulated with PYTHIA8. The prediction of the multijet events in the signal region (A) is thus given by

$$N_{QCD}(A) = \frac{N(B)}{N(D)} \times N(C), \quad (11.1)$$

where  $N(B)$ ,  $N(C)$ , and  $N(D)$  represent the data yield minus the contributions from electroweak backgrounds in regions B, C, and D respectively after all selection cuts except those mentioned in this section.

The robustness of this background estimation is assessed by varying the values of  $\min[\Delta\phi(\vec{E_T^{\text{miss}}}, \text{jet})]$  chosen to define the B and D regions of the method, and additionally, by replacing the  $b$ -tagging fractions measured in region D by those measured in region B. A systematic uncertainty of 100% is assessed for this small ( $\sim 1\%$ ) background, and it is treated as uncorrelated between 2-jet and 3-jet, 1-tag and 2-tag categories.

## 1-lepton Multijet Estimate

In the 1-lepton channel, the multijet background is determined separately for the electron and muon processes. For each signal or control region, a multijet-background template is obtained in a multijet-enriched region after subtracting the small contribution from other background processes. The other backgrounds are taken from Monte Carlo simulation and with normalizations improved by scale factors obtained from a preliminary global fit. The multijet-enriched region is obtained by modifying the nominal lepton selection requirements to use medium, instead of tight, leptons and loosening both the track and calorimeter-based isolation criteria in the following way [109]:

- The track-based isolation is changed to the intervals 5%–12% and 7%–50% for electrons and muons respectively, instead of < 4%,
- The calorimeter-based isolation is loosened to < 7% from < 4%.

The sample sizes of the multijet-templates are however rather small in the 2-tag regions, due to the effectiveness of the *MV1c* algorithm. Since it is observed that the kinematic properties of the 1-tag and 2-tag events in the multijet-dominated regions are similar, 1-tag events are used to enrich the 2-tag multijet templates. Events in the 1-tag category are promoted to the 2-tag category by assigning to the untagged jet an emulated *MV1c* value that is drawn from the appropriate *MV1c* distribution observed in the corresponding 2-tag multijet template. This distribution depends on the rank (leading or sub-leading) of the untagged jet and on the *MV1c* value of the tagged jet. To cope with residual differences observed in some distributions between

these pseudo-2-tag multijet events and the actual 2-tag multijet events, a reweighting is applied according to the *MV1c* of the tagged jet and, for the electron sub-channel, according to  $\Delta R(\text{jet}_1, \text{jet}_2)$  and  $p_T^W$ . This procedure is applied in each of the 2- and 3-jet, LL, MM and TT categories.

The normalizations of the multijet templates are then obtained by fits to the  $E_T^{\text{miss}}$  distributions in the 2- and 3-jet, 1- and 2-tag (LL, MM and TT combined) categories, with floating normalizations for the templates of the other background processes. The templates for these other background processes are taken from the improved Monte Carlo simulation mentioned above.

The multijet background in the 1-lepton channel is concentrated at low  $p_T^W$ . In the 2-jet, 2-tag sample with  $p_T^W < 120$  GeV the multijet contribution ranges from 11% of the total background in the LL category to 6% in the TT category. The main purpose of including the  $p_T^W < 120$  GeV intervals is to provide constraints on the largest backgrounds ( $V+\text{jets}$  and  $t\bar{t}$ ) in the profile likelihood fit. Since the multijet background is twice as large for  $p_T^W < 120$  GeV in the 1-electron sub-channel than in the 1-muon sub-channel, only the 1-muon sub-channel is kept in the profile likelihood fit for  $p_T^W < 120$  GeV so as to provide the most reliable constraints on the non-multijet backgrounds. The resulting loss in sensitivity is 0.6%. For  $p_T^W > 120$  GeV, the multijet background is much smaller: 4% and 2% in the LL and TT categories, respectively, for 2-jet events [29]. Further details are found in Reference [109].

Multijet normalization uncertainties arise in the 1-lepton channel from the statistical uncertainties of the multijet fits and from uncertainties on the non-multijet

background subtractions performed to construct the templates. Normalization uncertainties are also assessed in the LL, MM and TT categories to cover differences between multijet fits performed inclusively in the 2-tag regions and in the individual categories. In the 2-jet 2-tag region of the electron sub-channel, the overall normalization uncertainties amount to 11%, 14% and 22% in the LL, MM and TT categories, respectively. In the muon sub-channel, the corresponding uncertainties are about three times larger because of the smaller size of the multijet-enriched samples [109].

Shape uncertainties for the templates are assessed in the various regions by comparison of evaluations obtained using multijet-enriched samples defined by isolation requirements different from those applied in the nominal template construction. In the electron sub-channel, an alternative template is constructed with a track-based isolation in the 12% to 50% interval, and another alternative template with a calorimeter-based isolation in the 0% to 4% interval [29]. In the muon sub-channel, the results obtained with the nominal multijet template are compared with those obtained with tighter or looser isolation requirements, defined by track-based isolation intervals of 7%–9.5% and 9.5%–50%, respectively. Furthermore, half of the  $\Delta R(\text{jet}_1, \text{jet}_2)$  and  $p_T^W$  reweightings for the electron sub-channel are taken as systematic uncertainties. These uncertainties are summarized in Table 11.8.

## 11.4 Extension of the Profile Likelihood Fit

The statistical method for the profile likelihood fit with the combined analysis is identical to the method presented in Chapter 9. Table 11.5 summarizes the analysis regions that enter into the combined 0+1+2-lepton analysis for the  $\sqrt{s} = 8$  TeV data.

The calculation of the  $p_0$  for search sensitivity and upper limits on the Higgs cross section follow identical procedures as before. In particular, the test statistic  $q_\mu$  is constructed from the profile likelihood ratio  $q_\mu = -2 \ln \Lambda_\mu$  with  $\Lambda_\mu = \mathcal{L}(\mu, \hat{\vec{\theta}}_\mu) / \mathcal{L}(\hat{\mu}, \hat{\vec{\theta}})$ , where  $\hat{\mu}$  and  $\hat{\vec{\theta}}$  are the parameters that maximize the likelihood with the constraint  $0 \leq \hat{\mu} \leq \mu$ , and  $\hat{\vec{\theta}}_\mu$  are the nuisance parameter values that maximize the likelihood for a given value of  $\mu$ . This test statistic is used for exclusion intervals derived with the  $CL_s$  method [66, 103]. To measure the compatibility of the background-only hypothesis with the observed data,  $p_0$ , the test statistic used is  $q_0 = -2 \ln \Lambda_0$ .

		Combined Analysis		
Channel		0 lepton	1 lepton	2 lepton
1-tag	2-jet	$MV1c$		
	3-jet	$MV1c$		
2L-tag		$m_{b\bar{b}}$		
2M-tag	2-jet	$m_{b\bar{b}}$		
2T-tag		$m_{b\bar{b}}$		
2L-tag		$m_{b\bar{b}}$		
2M-tag	3-jet	$m_{b\bar{b}}$		
2T-tag		$m_{b\bar{b}}$		

Table 11.5: The regions entering the likelihood fit for the combined analysis and the distributions used.

Aside from the additional fit regions described in Table 11.5, the combined analysis has additional nuisance parameters for the modeling of the  $W+jets$ , single-top, and 0-lepton and 1-lepton multijet estimations. The  $W+jet$  nuisance parameters are summarized in Table 11.6 and the single-top nuisance parameters are summarized in Table 11.7. Table 11.8 summarizes the nuisance parameters for the multijet backgrounds. Over 180 nuisance parameters are part of the profile likelihood fit. The

behavior of the fit is studied, as in Chapter 9, by comparing the pulls and constraints of the nuisance parameters to those expected from the Asimov dataset. Full details of these comparisons are contained in Reference [109]. The ranking of the top 15 sources of uncertainty in terms of their impact on the  $\mu$  measurement is given in Figure 11.4.

After the execution of the profile likelihood fit, the uncertainties that have the greatest impact on the measurement of the signal strength,  $\mu$ , are the uncertainties on:

- the shape of the  $m_{b\bar{b}}$  distribution in the  $Wbb$  and  $Wcc$  processes
- the  $t\bar{t}$  background normalization in the 2-lepton channel,
- the  $Zbb$  background normalization,
- the relative ratio of the  $Zbl$  to  $Zbb$  normalization,
- the leading component of the  $b$ -tagging efficiency measurement.

Nuisance Parameter	Description	Correlation/Samples	Value	Count	Section
W1Norm	W1 normalization	all regions	10%	1	
W1Norm_J3	W1 3/2-jet ratio	3Jet regions	10%	1	
norm_Wc1	Wcl normalization	all regions	Float	1	
Wc1Norm_J3	Wcl 3/2-jet ratio	3Jet regions	10%	1	
norm_Wbb	Whf normalization	all regions	Float	1	
WbbNorm_J3	Whf 3/2-jet ratio	3Jet regions	10%	1	11.3.1
Wbb/WbbRatio	Wbl/Wbb ratio	$p_T^V = [0-90], [90-120], 120+$ GeV <sup>†</sup>	35%	3	
Wbc/WbbRatio	Wbc/Wbb ratio	all regions	12%	1	
Wcc/WbbRatio	Wcc/Wbb ratio	all regions	12%	1	
WDPPhi	$\Delta\phi$ shape	Wlf, Wcl, W1 $\times$ 2, 3Jets	S	6	
m <sub>b̄b̄</sub>	shape	$Wbb/Wcc (p_T^V = [0-90], [90-120], 120+$ GeV) <sup>†</sup>	SO	6	
WpT	$p_T^V$ shape	Wbc/Wbl, Wcl, Wl each in all regions	S	2	
Total		23 with priors, 2 floating			

Table 11.6: The nuisance parameters used in the fit to parametrize the normalization of the  $W+jets$  backgrounds and the correlation of these parameters between regions. <sup>†</sup> Regions separated by a ““ indicate a decorrelation of the parameter between those regions. 3/2-jet ratio refers to the ratio of the number of events in the 3-jet region to the number in the 2-jet region, and  $Wxx/Wyy$  refers to the ratio of the number of events with leading two jets of flavor  $xx$  to the number of events with jets of flavor  $yy$ .  $Whf = Wbb + Wcc + Wbl$ , S=“Shape”, and SO=“Shape Only” meaning explicitly that the normalization of each N-jet/M-b-tag/ $p_T^V$  region is preserved while the shape is varied. Further details are given in Reference [109].

Nuisance Parameter	Description	2-jet		3-jet		Section
		low $p_T^V$	high $p_T^V$	low $p_T^V$	high $p_T^V$	
stopsNorm SChanAcerMC SChanAcerMCPS	cross section AcerMC vs Powheg+Pythia	13% 6%	22% 8%	4% 4%	18% 4%	11.3.2
	shower uncertainty					
	t-channel					
stopNorm TChamPtB2	cross section aMCatNLO vs. AcerMC	52%	25%	4%	12%	11.3.2
	Wt channel					
stopWtNorm WtChanAcerMC WtChanPythiaHerwig	cross section AcerMC vs Powheg+Pythia	1% S/5%	S/-2% 3%	7% S/4%	S/-15% 5%	11.3.2
	Shower uncertainty					
	Total	8 with priors, 0 floating				

Table 11.7: The nuisance parameters used in the fit to parametrize the systematics on the single top background. All nuisance parameters are correlated across the full phase-space. The value represents the normalization change in the given region for the given NP while S=“Shape” is used to note regions where a shape variation exists. Low  $p_T^V$  is below 120 GeV and high is above this value.

Nuisance Parameter	Description	Region	Value	NP Count	Section
MJ_L0	normalization	0-lepton 2,3-jet 1/2-tag >,< 120 GeV	100%	6	11.3.3
		1-lepton			
SysJJMuNorm	normalization	2-jet 1/2L/2M/2T-tag 3-jet 1/2-tag	12/28/42/60% 11/14%	4 2	
SysMJE1Norm	normalization	2-jet 1/2L/2M/2T-tag 3-jet 1/2-tag	3/11/14/22% 4/6%	4 2	
SysJJMuTrkIso	template <i>isotrack</i> cut	2/3-jet 1/2-tag	S	4	11.3.3
SysMJE1TrkIso	template <i>isotrack</i> cut	2/3-jet 1/2-tag	S	4	
SysMJE1CaloIso	template <i>isocalo</i> cut	2-jet 1/2-tag	S	2	
SysMJDRe	reweight for spoofed events	(ele) 2-jet 2-tag	S	1	
SysJJvpt	reweight for spoofed events	(ele) 2-jet 2-tag	S	1	
		2-lepton			
MJ_L2	normalization	top e- $\mu$ decorrelated <sup>†</sup>	100%	1	8.2.5
Total		31 with priors, 0 floating			

Table 11.8: Normalization nuisance parameters for multijet entering the fit. The 0-lepton uncertainties are correlated between regions. <sup>†</sup> Regions separated by a “ indicate a decorrelation of the parameter between those regions. For example for SysMJE1CaloIso, the parameter is decorrelated among the 2-jet 1-tag and 2-jet 2-tag regions, resulting in 2 total nuisance parameters. All 2-lepton uncertainties are correlated except for when the top  $e - \mu$  control region is included in the 2-lepton standalone fit [109].

## 11.5 Inclusion of the $\sqrt{s} = 7$ TeV Analysis

The analysis of the  $\sqrt{s} = 7$  TeV data is discussed in its entirety in Reference [7] and details of the physics object and event selection are not discussed here. The major differences between the  $\sqrt{s} = 7$  TeV analysis and the  $\sqrt{s} = 8$  TeV analysis are:

- The 2-tag category in the  $\sqrt{s} = 7$  TeV is inclusive, but in the  $\sqrt{s} = 8$  TeV analysis it is subdivided into three levels of tagging criteria, increasing the sensitivity,
- The  $\sqrt{s} = 7$  TeV analysis does not perform a kinematic likelihood fit to improve the resolution of  $m_{b\bar{b}}$ ,
- The calibration of physics objects and the associated experimental systematic uncertainties are evaluated using different datasets.

Given the last bullet point, the systematic uncertainties in the  $\sqrt{s} = 7$  TeV analysis are assumed to be uncorrelated with those in the  $\sqrt{s} = 8$  TeV analysis. Furthermore, the  $\sqrt{s} = 8$  TeV analysis has a different phase space both because of the center-of-mass energy and because the kinematic definitions of the analysis regions are not the same in the two analyses. Because of the phase space differences, the background modeling uncertainties are also not assumed to be correlated. Thus the  $\sqrt{s} = 7$  TeV analysis results are treated independently from  $\sqrt{s} = 8$  TeV results except for correlations on the theoretical uncertainties on the signal processes. To obtain a measurement of the Higgs signal strength that combines the data from the two analyses, a single parameter of interest can be used to represent the signal strength in each year, rather than two separate parameters.

## 11.6 Results of the Combined Analysis

### 11.6.1 Validation through Diboson Processes

**Diboson Observation** The diboson production process with a  $Z$ -boson decaying to a pair of  $b$ -quarks and produced in association with either a  $W$  or a  $Z$ -boson has a similar signature to the  $VH$  processes, but with  $m_{b\bar{b}}$  peaking at lower values. However, it has a cross section  $\sim 5$  times larger than the signal. Therefore, as a validation of this analysis procedure, a separate fit to the diboson process is performed for the combination of the  $\sqrt{s} = 7$  TeV and 8 TeV analyses and the  $\sqrt{s} = 8$  TeV analysis alone. As the main purpose of this is validation, no attempt was made to optimize the event-level kinematic requirements towards diboson production. In the profile likelihood fit, the normalizations of the diboson contributions are allowed to vary with a single multiplicative scale,  $\mu_D$ , with respect to the Standard Model expectation. A Standard Model Higgs boson with  $m_H = 125$  GeV is included in the fit with signal strength  $\mu$ . The Higgs signal strength extracted from this fit is identical to the result from the nominal Higgs-only fit.

The fitted signal strength for the diboson process in the combination of the 0-, 1- and 2-lepton channels in the  $\sqrt{s} = 8$  TeV analysis is found to be  $\mu_D = 0.79 \pm 0.11(\text{stat.}) \pm 0.16(\text{syst.})$ . For the  $\sqrt{s} = 7$  TeV analysis, the best-fit is  $\mu_D = 0.50 \pm 0.30(\text{stat.}) \pm 0.38(\text{syst.})$ . The combination of the two yields  $\mu_D = 0.75 \pm 0.10(\text{stat.}) \pm 0.15(\text{syst.})$ . The diboson signal is observed with a significance of  $4.7\sigma$ , compared to an expected significance of  $5.6\sigma$ . Figure 11.3 shows the dijet mass distribution for the combination of all lepton channels in the  $\sqrt{s} = 8$  TeV analysis. The contribution of

all background processes except the diboson and Higgs processes is subtracted from both the data and the total background expectation.

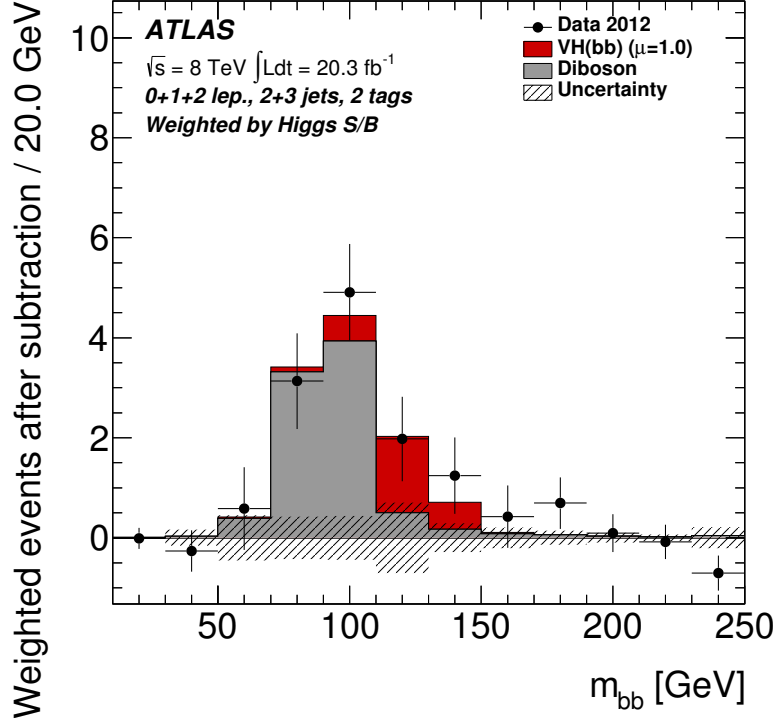


Figure 11.3: The distribution of  $m_{b\bar{b}}$  in data after subtraction of all backgrounds except for the diboson processes, as obtained with the dijet mass analysis for the  $\sqrt{s} = 8$  TeV data. The contributions from all lepton channels,  $p_T^V$  intervals, number-of-jets and 2-tag  $b$ -tagging categories are summed and weighted by their respective values of the ratio of expected Higgs boson signal to fitted background. The contribution of the associated  $WH$  and  $ZH$  production of a Standard Model Higgs boson with  $m_h = 125$  GeV is shown as expected for the Standard Model cross section (indicated as  $\mu = 1.0$ ). The size of the combined statistical and systematic uncertainty on the fitted background is indicated by the hatched band.

### 11.6.2 Higgs Analysis Results

The profile likelihood fit with the Higgs boson signal strength,  $\mu$ , floating is performed with the diboson contributions constrained to their Standard Model values

within their uncertainties described in Section 8.2.3. Results are extracted independently for the dijet-mass analysis at  $\sqrt{s} = 7$  TeV and at  $\sqrt{s} = 8$  TeV. Unless otherwise specified, all results refer to a Higgs boson mass of 125 GeV. The data have sufficient power to constrain the largest background-normalization nuisance parameters, which are left free to float in the fit. This applies to the  $t\bar{t}$ ,  $Wbb$ ,  $Wcl$ ,  $Zbb$  and  $Zcl$  processes. The corresponding “rescaling factors”, the factors applied to the background normalizations as resulting from the global fit to the  $\sqrt{s} = 8$  TeV data, are shown in Table 11.9. Most importantly, the  $Zbb$  background normalization factor is 1.10 in the combination, compared to 1.2 for the 2-lepton fit in Chapter 10. Because this parameter is so closely tied to the Higgs signal strength, one expects a higher signal strength to be observed for the 2-lepton channel in the combined analysis than for the stand-alone 2-lepton analysis. The  $t\bar{t}$  normalization parameter is decorrelated across the three lepton channels because the phase space of the  $t\bar{t}$  process probed by the 0, 1, and 2-lepton channels is much different. Each channel takes its  $t\bar{t}$  normalization from the 2-jet region. In the 2-lepton channel, this region probes phase space almost entirely consisting of events with two leptonically-decaying top quarks. In the 1-lepton channel, the 2-jet region is a mixture of fully leptonic top decays and decays in which a  $W$ -boson from one of the top quarks decays hadronically and one of those jets does not pass the kinematic selection. Finally, the phase space probed by the 0-lepton channel consists of some events in which a fully leptonic decay has no detected leptons, and events in which semileptonic top decays have a jet that does not pass the kinematic selection.

Process	Scale factor
$t\bar{t}_{L0}$	$1.37 \pm 0.13$
$t\bar{t}_{L1}$	$1.12 \pm 0.06$
$t\bar{t}_{L2}$	$1.05 \pm 0.18$
$Wbb$	$0.87 \pm 0.15$
$Wcl$	$1.03 \pm 0.09$
$Zbb$	$1.10 \pm 0.06$
$Zcl$	$0.83 \pm 0.11$

Table 11.9: Rescaling factors obtained from the global fit to the  $\sqrt{s} = 8$  TeV data for the normalization of the  $t\bar{t}$ ,  $Wbb$ ,  $Wcl$ ,  $Zbb$ , and  $Zcl$  backgrounds for the 2-jet events. The errors include the statistical and systematic uncertainties. The  $t\bar{t}$  factors are decorrelated across each lepton channel, and  $L0$ ,  $L1$ , and  $L2$  represent the 0, 1, and 2-lepton channels, respectively.

In the same way as is performed in Chapter 9, the post-fit impact of each nuisance parameter on the final  $\mu$  result is calculated for the analysis and shown in Figure 11.4. In the combined analysis, the modeling uncertainties related to the  $W$ +heavy-flavor backgrounds have among the largest impact on the signal strength result, in addition to the uncertainties for the  $Z$ +heavy-flavor modeling uncertainties.

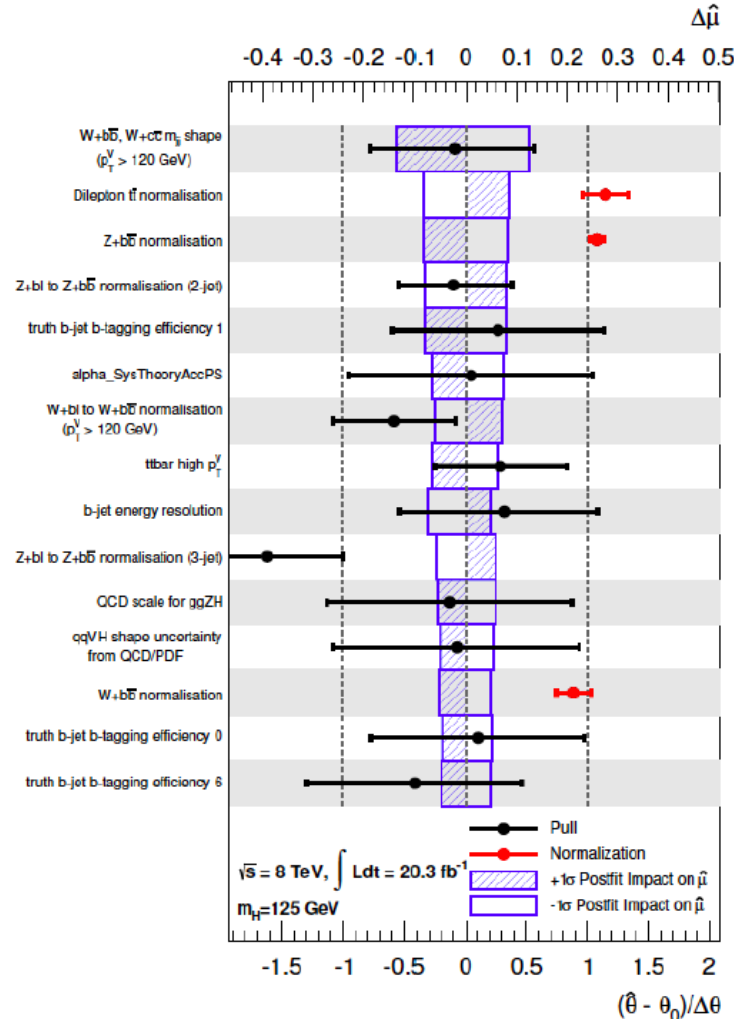


Figure 11.4: Impact of systematic uncertainties on the fitted signal-strength parameter  $\hat{\mu}$  for the  $\sqrt{s} = 8$  TeV data. The systematic uncertainties are listed in decreasing order of their impact on  $\hat{\mu}$  on the  $y$ -axis. The boxes show the variations of  $\hat{\mu}$ , referring to the top  $x$ -axis, when fixing the corresponding individual nuisance parameter  $\theta$  to its post-fit value  $\hat{\theta}$  modified upwards or downwards by its post-fit uncertainty, and repeating the fit as explained in the text. The hatched and open areas correspond to the upwards and downwards variations, respectively. The filled circles, referring to the bottom  $x$ -axis, show the deviations of the fitted nuisance parameters  $\hat{\theta}$  from their nominal values  $\theta_0$ , in terms of standard deviations with respect to their nominal uncertainties  $\Delta\theta$ . The associated error bars show the post-fit uncertainties of the nuisance parameters, relative to their nominal uncertainties. The red circles with their error bars show the fitted values and uncertainties of the normalization parameters that are floating in the fit and have a pre-fit value of one.

## Higgs Signal Strength

The normalized Higgs signal strength is shown Figure 11.5 for the  $\sqrt{s} = 7$  TeV and  $\sqrt{s} = 8$  TeV analyses, as well as the combination of the two at a Higgs mass of 125 GeV. For the combination of the  $\sqrt{s} = 7$  TeV and  $\sqrt{s} = 8$  TeV analyses, the best-fit value is  $\mu = 0.90 \pm 0.41(\text{stat.}) \pm 0.36(\text{syst.})$  for a Higgs with a mass of 125 GeV. For the  $\sqrt{s} = 8$  TeV analysis the best-fit is  $\mu = 1.09 \pm 0.43(\text{stat.}) \pm 0.43(\text{syst.})$ . The  $\sqrt{s} = 7$  TeV analysis best fit value is  $\mu = -1.6 \pm 1.2(\text{stat.}) \pm 0.9(\text{syst.})$ . A negative signal strength such as this indicates that an upward fluctuation from the expected number of background events was observed, and the fit thus prefers a negative Higgs signal strength to maximize the likelihood. These values are consistent with the Standard Model expectation of  $\mu = 1$ . Comparing the 2-lepton channel results from Chapter 10 to those obtained here in the combination reveals that the signal strength is higher in the combination. This is due to the fact that the  $Z + \text{jets}$  background constraint is more powerful because of the larger statistics available through the 0-lepton channel.

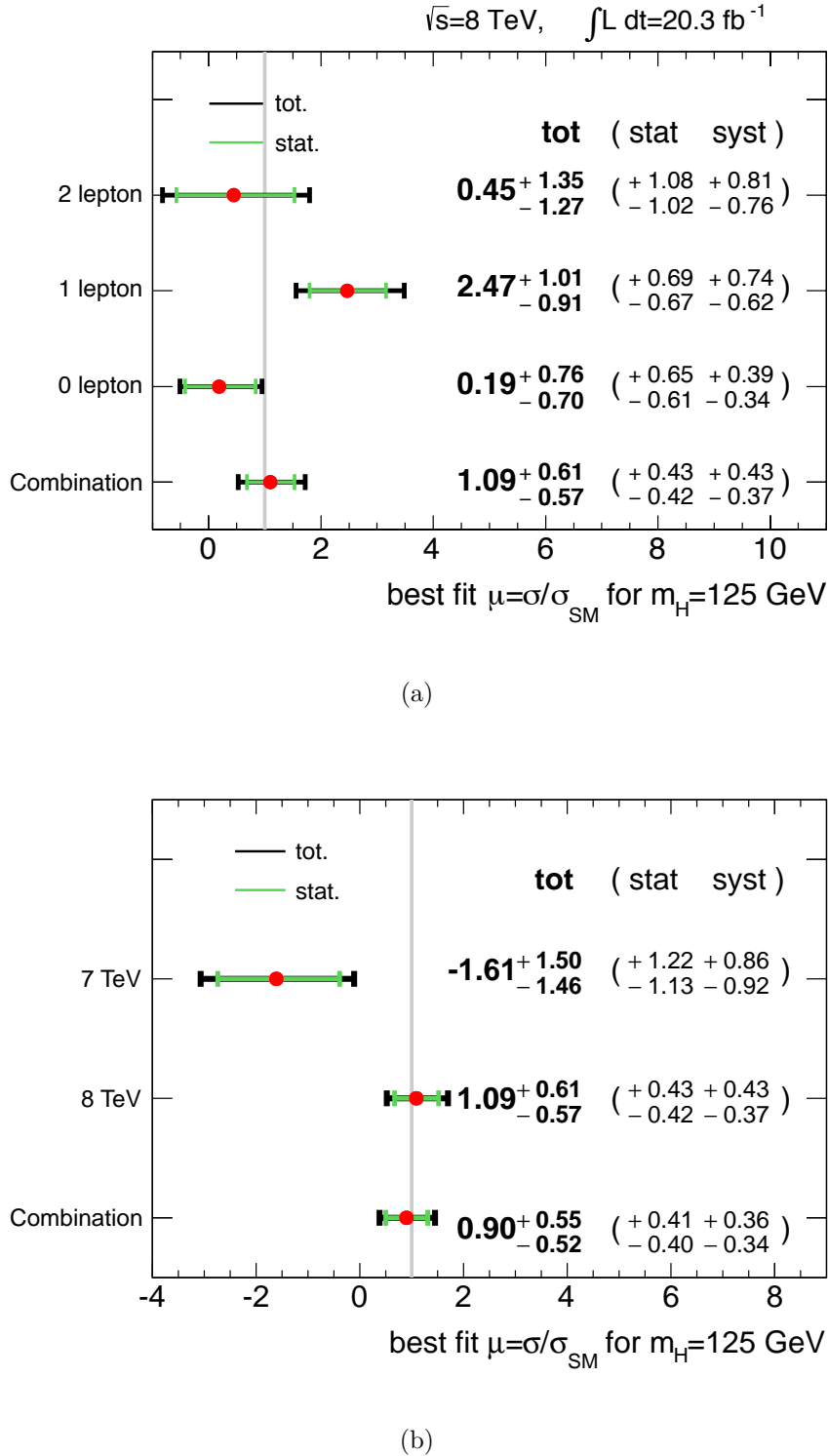


Figure 11.5: The fitted values of the Higgs-boson signal strength parameter  $\mu$ . The top graph is the result of fitting a  $\mu$  parameter for each lepton selection in the  $\sqrt{s} = 8 \text{ TeV}$  analysis only, while the bottom graph shows a comparison of the  $\sqrt{s} = 7 \text{ TeV}$  analysis and the  $\sqrt{s} = 8 \text{ TeV}$  analysis. Additional 7 TeV results are contained in Reference [7].

### **Excess Relative to Background Expectation**

A slight excess of events is observed relative to the background-only hypothesis for the  $\sqrt{s} = 8$  TeV analysis. The reported values of  $p_0$  correspond to the values at a Higgs mass of 125 GeV, the observed ATLAS value. For the  $\sqrt{s} = 8$  TeV dataset and all channels combined, the probability,  $p_0$ , of obtaining a result at least as signal-like as the observed result, if no signal is present, corresponds to a  $2.0\sigma$  excess, to be compared to an expectation of  $1.9\sigma$  in the background-only hypothesis.

For the  $\sqrt{s} = 7$  TeV dataset, the expected significance is  $0.7\sigma$ , but a deficit in the data is observed. After combining the  $\sqrt{s} = 7$  TeV and  $\sqrt{s} = 8$  TeV analyses, the observed and expected significances are 1.8 and 2.0, respectively.

### **Upper Limit on the Cross Section**

The 95% confidence-level upper limits on the Higgs boson production cross section are shown in Figure 11.6 for the combination of the  $\sqrt{s} = 7$  TeV and  $\sqrt{s} = 8$  TeV datasets.

The observed limit for  $m_h = 125$  GeV when combining the  $\sqrt{s} = 7$  TeV and  $\sqrt{s} = 8$  TeV datasets is 2.3 times the Standard Model value, to be compared to an expected limit of 1.01 in the absence of signal. If the analysis is restricted to the  $\sqrt{s} = 7$  TeV dataset, the observed limit is 2.3 times the Standard Model value and the expected limit is 3.2. Restricting to the  $\sqrt{s} = 8$  TeV dataset, the observed limit is 2.14 times the Standard Model value, with an expected limit of 1.06 in the absence of signal.

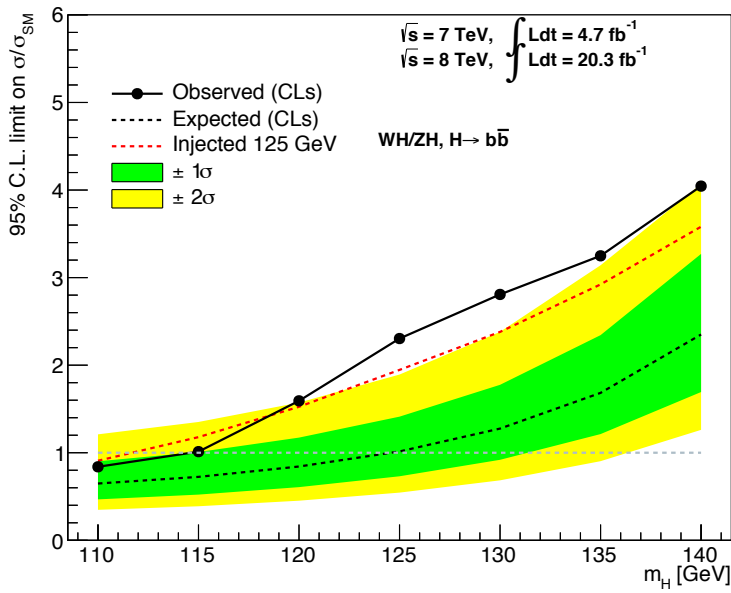


Figure 11.6: Expected 95% C.L. upper limits on the normalised signal strength as a function of Higgs boson mass for all channels after the combination of the  $\sqrt{s} = 7 \text{ TeV}$  and  $\sqrt{s} = 8 \text{ TeV}$  analyses. The expected upper limit is given for the background-only hypothesis in blue, and the black dashed line corresponds to the expected upper limit after the injection of the Higgs signal process at  $m_H = 125 \text{ GeV}$ .

# Chapter 12

## Conclusion and Future Prospects

The ATLAS and CMS experiments at the CERN laboratory discovered a new boson with  $m = 125$  GeV using the data collected from the LHC collisions of 2011 and 2012. This boson has so far proved to be consistent with the Higgs boson of the Standard Model. Two important and as of yet unobserved properties are the production of the Higgs boson in association with a vector boson, and the decay of the Higgs boson to a pair of  $b$ -quarks. This thesis presented a search for that process and decay. The strategy of this search is to use the dijet invariant mass distribution to identify a statistically significant difference between the observed data and null hypothesis of a background-only model. Chapter 10 presented a search for the  $ZH \rightarrow \ell^+ \ell^- b\bar{b}$  process using a profile likelihood fit to allow data to constrain the major backgrounds. Three parameters were presented. First, the parameter  $\mu$  is measured, which is a ratio of the observed to expected cross section times branching ratio for the  $ZH \rightarrow \ell^+ \ell^- b\bar{b}$  process. The result is  $\mu = 0.17 \pm 1.4$ . Additionally, an upper limit at the 95% confidence level has been observed to be 2.76 times the

Standard Model cross section, to be compared with an expectation of 2.54 in the absence of signal. Finally, a  $p_0$  value is calculated to determine the significance of the deviation from the background-only hypothesis, but the level of rejection not significant, only corresponding to a significance of  $0.13\sigma$ .

To improve the sensitivity of this search, Chapter 11 combines the  $ZH \rightarrow \ell^+\ell^- b\bar{b}$  search from Chapter 10 with two other search channels to probe the  $WH \rightarrow \ell\nu b\bar{b}$  and  $ZH \rightarrow \nu\bar{\nu} b\bar{b}$  processes, and also to combine the data from  $\sqrt{s} = 7$  TeV collisions from 2011 data-taking. The results from this search yield a more sensitive expected upper limit on the process of 1.01 times the Standard Model expectation in the absence of signal, with an observed upper limit of 2.3 times the Standard Model value. The observed value of the Higgs signal strength,  $\mu$ , is found to be  $\mu = 0.90 \pm 0.41(\text{stat.}) \pm 0.36(\text{syst.})$  for a Higgs with a mass of 125 GeV. The statistical significance of the deviation from the background-only hypothesis is  $2.0\sigma$  for the  $\sqrt{s} = 8$  TeV analysis alone, which is reduced to  $1.8\sigma$  when combined with the  $\sqrt{s} = 7$  TeV data because of the deficit observed in that dataset.

These measurements are currently statistically limited, particularly for the case of the  $ZH \rightarrow \ell^+\ell^- b\bar{b}$ -only search. Already, an updated measurement has been published by the ATLAS experiment that utilizes a multivariate technique to improve the sensitivity of the search [29]. This search also does not have the sensitivity to claim a discovery of the associated production processes. Therefore the search for these processes will be an interesting path of research as the LHC resumes collisions at a higher center of mass energy in 2015. Due to the large contribution of the un-

certainties associated with the modeling of the  $Z +$  heavy-flavor jets processes to the total error on the  $\mu$  measurements presented in this thesis, it is clear that a better understanding of these backgrounds will be crucial to future searches. Furthermore, as the single-top background will rise more rapidly with center of mass energy than the  $Z$ -jets processes, the  $ZH \rightarrow \nu\bar{\nu}b\bar{b}$  and  $ZH \rightarrow \ell^+\ell^-b\bar{b}$  processes could each provide greater sensitivity than the  $WH \rightarrow \ell\nu b\bar{b}$  search, placing greater importance on the understanding of the  $Z$ -jets modeling. Early estimates indicate that with  $25\text{fb}^{-1}$  of data at  $\sqrt{s} = 13$  TeV combined with the Run I data, a significance level of  $5\sigma$  can be obtained for the combined 0+1+2 lepton analysis.

# Bibliography

- [1] Jes uncertainty twiki.  
<https://twiki.cern.ch/twiki/bin/viewauth/AtlasProtected/JetUncertainties2012>.
- [2] Jvf uncertainty twiki.  
<https://twiki.cern.ch/twiki/bin/viewauth/AtlasProtected/JVFUncertaintyTool>.
- [3] Pile up rescaling.  
<https://twiki.cern.ch/twiki/bin/view/AtlasProtected/InDetTrackingPerformanceGuidelines>.
- [4] The ATLAS Simulation Infrastructure. *Eur. Phys. J.*, C70:823, 2010.
- [5] Summary of ATLAS Pythia 8 tunes. Technical Report ATL-PHYS-PUB-2012-003, CERN, Geneva, Aug 2012.
- [6] Jet energy scale and its systematic uncertainty in proton-proton collisions at  $\sqrt{s} = 7$  tev with atlas 2011 data. *ATLAS-CONF-2014-004*, 2013.
- [7] Search for the standard model higgs boson in associated production with a vector boson and decaying to bottom quarks with the atlas detector. Technical Report ATL-COM-PHYS-2013-465, CERN, Geneva, Aug 2013.
- [8] D. Adams et al. Track reconstruction in the ATLAS Muon Spectrometer with MOORE 007. ATLAS Technical Report ATL-SOFT-2003-007, 2003.
- [9] S. Agostinelli et al. GEANT4: A simulation toolkit. *Nucl. Instrum. Meth.*, A506:250–303, 2003.
- [10] ALICE Collaboration. The ALICE Experiment at the CERN Large Hadron Collider. *JINST*, 3:S08002, 2008.
- [11] K. Arnold et al. Herwig++ 2.6 Release Note. 2012.
- [12] ATLAS Collaboration. A measurement of the ATLAS muon reconstruction and trigger efficiency using J/psi decays. ATLAS Conference Note: ATLAS-CONF-2011-021, <https://cdsweb.cern.ch/record/1336750?ln=en>.

## Bibliography

---

- [13] ATLAS Collaboration. Athena Computing Framework ATLAS Internal Web-page.  
<https://twiki.cern.ch/twiki/bin/viewauth/Atlas/AthenaFramework>.
- [14] ATLAS Collaboration. ATLAS Detector and Physics Performance Technical Design Report.  
<http://atlas.web.cern.ch/Atlas/GROUPS/PHYSICS/TDR/access.html>.
- [15] ATLAS Collaboration. Atlas flavour tagging twiki.  
<https://twiki.cern.ch/twiki/bin/view/AtlasProtected/BTagCalib2014>.
- [16] ATLAS Collaboration. ATLAS Public Luminosity Plots.  
<https://twiki.cern.ch/twiki/bin/view/AtlasPublic/LuminosityPublicResults>.
- [17] ATLAS Collaboration. Calibration of  $b$ -tagging using dileptonic top pair events in a combinatorial likelihood approach with the ATLAS experiment. ATLAS Conference Note: ATLAS-CONF-2014-004, <https://cdsweb.cern.ch/record/1664335?ln=en>.
- [18] ATLAS Collaboration. Commissioning of the atlas high-performance b-tagging algorithms in the 7tev collision data. ATLAS Conference Note: ATLAS-CONF-2011-102, <https://cdsweb.cern.ch/record/1369219?ln=en>.
- [19] ATLAS Collaboration. Electron Efficiencies for 2012 Analyses. ATLAS web page  
<https://twiki.cern.ch/twiki/bin/viewauth/AtlasProtected/EfficiencyMeasurements2012>.
- [20] ATLAS Collaboration. Electron efficiency measurements with the ATLAS detector using the 2012 LHC proton-proton collision data. ATLAS Conference Note: ATLAS-CONF-2014-032, <https://cds.cern.ch/record/1706245?ln=en>.
- [21] ATLAS Collaboration. Expected Performance of the ATLAS Experiment - Detector, Trigger and Physics.  
<http://arxiv.org/abs/0901.0512>.
- [22] ATLAS Collaboration. Improved Luminosity Determination in  $pp$  Collisions at  $\sqrt{s} = 7$  TeV using the ATLAS Detector at the LHC. ATLAS Conference Note: ATLAS-CONF-2012-080, <https://cdsweb.cern.ch/record/1460392?ln=en>.
- [23] ATLAS Collaboration. Inputs to Jet Reconstruction and Calibration with the ATLAS Detector Using Proton-Proton Collisions at  $\sqrt(s) = 900$  GeV. ATLAS Conference Note: ATLAS-CONF-2010-016, <https://cdsweb.cern.ch/record/1276555?ln=en>.
- [24] ATLAS Collaboration. Jet-area-based pile-up subtraction.  
<https://twiki.cern.ch/twiki/bin/viewauth/AtlasProtected/JetAreas>.

## Bibliography

---

- [25] ATLAS Collaboration. Liquid argon calorimeter technical design report. CERN-LHCC-96-041, <http://cdsweb.cern.ch/record/331061>.
- [26] ATLAS Collaboration. Measurement of the  $b$ -tag Efficiency in a Sample of Jets Containing Muons with  $5 \text{ fb}^{-1}$  of Data From the ATLAS Detector . ATLAS Conference Note: ATLAS-CONF-2012-043, <https://cdsweb.cern.ch/record/1435197?ln=en>.
- [27] ATLAS Collaboration. Performance of primary vertex reconstruction in proton-proton collisions at  $\sqrt{s} = 7 \text{ tev}$  in the atlas experiment. ATLAS Conference Note: ATLAS-CONF-2010-069, <https://cdsweb.cern.ch/record/1281344?ln=en>.
- [28] ATLAS Collaboration. Preliminary results on the muon reconstruction efficiency, momentum resolution, and momentum scale in ATLAS 2012 pp collision data. ATLAS Conference Note: ATLAS-CONF-2013-088, <https://cdsweb.cern.ch/record/1580207?ln=en>.
- [29] ATLAS Collaboration. Search for the  $bb$  decay of the Standard Model Higgs boson in associated ( $W/Z$ ) $H$  production with the ATLAS detector. <http://arxiv.org/pdf/1409.6212v1.pdf>.
- [30] ATLAS Collaboration. Tile calorimeter technical design report. CERN-LHCC-96-042, <http://cdsweb.cern.ch/record/331062>.
- [31] ATLAS Collaboration. *ATLAS Muon Spectrometer Technical Design Report*. CERN, Geneva, 1997.
- [32] ATLAS Collaboration. The ATLAS Experiment at the CERN Large Hadron Collider. *JINST*, 3:S08003, 2008.
- [33] ATLAS Collaboration. Jet energy measurement with the ATLAS detector in proton-proton collisions at  $\sqrt{s} = 7 \text{ TeV}$ . <http://arxiv.org/abs/1112.6426>, 2011.
- [34] ATLAS Collaboration. Luminosity Determination in  $pp$  Collisions at  $\sqrt{s} = 7 \text{ TeV}$  using the ATLAS Detector at the LHC. *European Physics Journal C*, 71:1630, 2011.
- [35] ATLAS Collaboration.  $b$ -jet tagging calibration on c-jets containing  $d^{*+}$  mesons. *ATLAS-CONF-2012-039*, 2012.
- [36] ATLAS Collaboration. Electron performance measurements with the ATLAS detector using the 2010 LHC proton-proton collision data. *Eur. Phys. J. C*, 72:1909, 2012.

## Bibliography

---

- [37] ATLAS Collaboration. Invariant mass studies for the  $h \rightarrow b\bar{b}$  measurements for lhc. Technical Report ATL-COM-PHYS-2012-1451, CERN, Geneva, Nov 2012.
- [38] ATLAS Collaboration. Measurement of the mistag rate with  $5 \text{ fb}^{-1}$  of data collected by the atlas detector. *ATLAS-CONF-2012-040*, 2012.
- [39] ATLAS Collaboration. Observation of a new particle in the search for the Standard Model Higgs boson with the ATLAS detector at the LHC.  
<http://arxiv.org/abs/1207.7214>, 2012.
- [40] ATLAS Collaboration. Performance of Missing Transverse Momentum Reconstruction in Proton-Proton Collisions at  $\sqrt{s} = 7 \text{ TeV}$  with ATLAS. *Eur.Phys.J.C*, 72:1844, 2012.
- [41] ATLAS Collaboration. Invariant mass studies for the  $h \rightarrow b\bar{b}$  measurements for lhcp. Technical Report ATL-COM-PHYS-2013-449, CERN, Geneva, Aug 2013.
- [42] ATLAS Collaboration. Electron reconstruction and identification efficiency measurements with the ATLAS detector using the 2011 LHC proton-proton collision data.  
<http://arxiv.org/abs/1404.2240>, 2014.
- [43] ATLAS Collaboration. Measurements of Higgs boson mass from the  $H \rightarrow \gamma\gamma$  and  $H \rightarrow ZZ^* \rightarrow 4l$  channels with the ATLAS detector using  $25 \text{ fb}^{-1}$  of pp collision data.  
<http://arxiv.org/abs/1406.3827>, 2014.
- [44] ATLAS Collaboration. Measurements of Higgs boson production and couplings in the four-lepton channel in pp collisions at center-of-mass energies of 7 and 8 TeV with the ATLAS detector.  
<http://arxiv.org/abs/1408.5191>, 2014.
- [45] ATLAS Experiment @ 2011 CERN. ATLAS Photos.  
<http://www.atlas.ch/photos/index.html>.
- [46] Richard D. Ball, Valerio Bertone, Stefano Carrazza, Christopher S. Deans, Luigi Del Debbio, et al. Parton distributions with LHC data. *Nucl. Phys.*, B 867:244–289, 2013.
- [47] W. et al Bell. Measurement of top quark pair differential cross section with ATLAS in pp collisions at  $\text{sqrt}(s)=7 \text{ TeV}$ : Measurement of top quark pair differential cross section with ATLAS using  $5/\text{fb}$  of data collected in 2011 and the rel.17 version of the Atlas software . Technical Report ATL-COM-PHYS-2012-1137, CERN, Geneva, Jul 2012.

## Bibliography

---

- [48] D. Belohrad, J.-J. Gras, L.K. Jensen, O.R. Jones, M. Lud-wig, P. Odier, J.J. Savioz, and S. Thoulet. Commissioning and first performance of the LHC beam current measurement systems. <http://accelconf.web.cern.ch/AccelConf/IPAC10/papers/mope059.pdf>.
- [49] M. Benedikt and others (eds.). The LHC design report v.3 : the LHC Injector Chain. **CERN-2004-003-V-3**, <http://cdsweb.cern.ch/record/823808>.
- [50] P Berta, F Filthaut, V Dao, E Le Menedeu, F Parodi, G Piacquadio, T Scanlon, M Ughetto, and L Zhang. Continuous  $b$ -tagging for the ATLAS experiment. Technical Report ATL-COM-PHYS-2014-035, CERN, Geneva, Jan 2014.
- [51] J-B Blanchard, J-B de Vivie, and P Mastrandrea. In situ scales and smearings from Z and  $J/\Psi$  events. Technical Report ATL-COM-PHYS-2013-1653, CERN, Geneva, Dec 2013.
- [52] J.P. Blewett. 200 gev intersecting storage accelerators. Proceedings of the 8th International Conference on High-Energy Accelerators, CERN, Geneva Switzerland (1971).
- [53] Michiel Botje, Jon Butterworth, Amanda Cooper-Sarkar, Albert de Roeck, Joel Feltesse, et al. The PDF4LHC Working Group Interim Recommendations. 2011.
- [54] Oliver Brein, Abdelhak Djouadi, and Robert Harlander. NNLO QCD corrections to the Higgs-strahlung processes at hadron colliders. *Phys.Lett.*, B579:149–156, 2004.
- [55] O.S. Bruning and others (eds.). The LHC design report v.1 : the LHC Main Ring. **CERN-2004-003-V-1**, <http://cdsweb.cern.ch/record/782076>.
- [56] O.S. Bruning and others (eds.). The LHC design report v.2 : the LHC Infrastructure and General Services. **CERN-2004-003-V-2**, <http://cdsweb.cern.ch/record/815187>.
- [57] M. Cacciari, G. P. Salam, and G. Soyez. The anti- $kt$  jet clustering algorithm. *JHEP*, 04:063, 2008.
- [58] M. Ciccolini, Ansgar Denner, and S. Dittmaier. Strong and electroweak corrections to the production of Higgs + 2 jets via weak interactions at the LHC. *Phys. Rev. Lett.*, 99:161803, 2007.
- [59] M.L. Ciccolini, S. Dittmaier, and M. Kramer. Electroweak radiative corrections to associated WH and ZH production at hadron colliders. *Phys.Rev.*, D68:073003, 2003.

## Bibliography

---

- [60] CMS Collaboration. Precise determination of the mass of the Higgs boson and studies of the compatibility of its couplings with the standard model.  
<http://cds.cern.ch/record/1728249/>.
- [61] CMS Collaboration. The CMS Experiment at the CERN Large Hadron Collider. *JINST*, 3:S08004, 2008.
- [62] CMS Collaboration. Observation of a new boson at a mass of 125 GeV with the CMS experiment at the LHC.  
<http://arxiv.org/abs/1207.7235>, 2012.
- [63] The NNPDF Collaboration. A determination of parton distributions with faithful uncertainty estimation. arXiv:0808.1231 [hep-ph].
- [64] G. Corcella et al. HERWIG 6: an event generator for Hadron Emission Reactions With Interfering Gluons. *JHEP*, 010:0101, 2001.
- [65] T Cornelissen et al. Concepts, design and implementation of the atlas new tracking (newt). ATLAS Technical Report ATL-SOFT-PUB-2007-007, <https://cdsweb.cern.ch/record/1020106>, 2007.
- [66] Glen Cowan et al. Asymptotic formulae for likelihood-based tests of new physics. *Eur. Phys. J.*, C71:1554, 2011.
- [67] D. Lopez Mateos, E.W.Hughes, A. Schwartzman. A Sequential Multi-Variate Jet Calibration Based On Global Properties of the Jet Structure. ATLAS internal note: ATL-COM-PHYS-2010-058.
- [68] D Damazio, T Kono, F Monticelli, and G Pasztor. Performance of the ATLAS Electron and Photon Triggers in  $p\text{-}p$  Collisions at  $\sqrt{s} = 8$  TeV in 2012. Technical Report ATL-COM-DAQ-2013-121, CERN, Geneva, Oct 2013.
- [69] Ansgar Denner, Stefan Dittmaier, Stefan Kallweit, and Alexander Muck. EW corrections to Higgs strahlung at the Tevatron and the LHC with HAWK. *PoS*, EPS-HEP2011:235, 2011.
- [70] A. Djouadi, J. Kalinowski, and M. Spira. HDECAY: A program for Higgs boson decays in the Standard Model and its supersymmetric extension. *Comput. Phys. Commun.*, 108:56–74, 1998.
- [71] R. Duda and P. Hart. Use of the Hough Transformation to Detect Lines and Curves in Pictures. *Comm. ACM*, 15, 1972.
- [72] V. Cindro et al. The ATLAS beam conditions monitor. *Journal of Instrumentation*, 3(02):P02004, 2008.

## Bibliography

---

- [73] L. Evans and P. Bryant. LHC Machine. *JINST*, 3:S08001, 2008.
- [74] Rikkert Frederix, Stefano Frixione, Valentin Hirschi, Fabio Maltoni, Roberto Pittau, et al. W and  $Z/\gamma^*$  boson production in association with a bottom-antibottom pair. *JHEP*, 09:061, 2011.
- [75] R. Frühwirth et al. Application of Kalman Filtering to Track and Vertex Fitting. *Nucl. Inst. Meth. A*, 262, 1987.
- [76] R. Frühwirth, W. Waltenberger, and P. Vanlaer. Adaptive vertex fitting. *J. Phys. G*, 34, 2007.
- [77] C. Weiser G. Piaquadio. A new inclusive secondary vertex algorithm for b-jet tagging in ATLAS. *Journal of Physics: Conference Series*, 119(3):032032, 2008.
- [78] Shireen Gangal and Frank J. Tackmann. Next-to-leading-order uncertainties in higgs + jets from gluon fusion. *Phys. Rev. D*, 87:093008, May 2013.
- [79] Sheldon L. Glashow. Partial-symmetries of weak interactions. *Nuclear Physics*, 22(4):579–588, 1961.
- [80] T. Gleisberg et al. Event generation with SHERPA 1.1. *JHEP*, 02:007, 2009.
- [81] Piotr Gononka and Zbigniew Was. PHOTOS Monte Carlo: A Precision tool for QED corrections in  $Z$  and  $W$  decays. *Eur.Phys.J.*, C45:97–107, 2006.
- [82] V. Herschi et al. Automation of one-loop QCD corrections. *JHEP*, 05:044, 2011.
- [83] J. Alison, K. Brendlinger, S. Heim, J. Kroll, C.M. Lester. Description and Performance of the Electron Likelihood Tool at ATLAS using 2012 LHC Data. ATLAS Internal Communication **ATL-COM-PHYS-2013-378** (2013).
- [84] Nikolaos Kidonakis. Differential and total cross sections for top pair and single top production. pages 831–834, 2012.
- [85] Hung-Liang Lai, Marco Guzzi, Joey Huston, Zhao Li, Pavel M. Nadolsky, et al. New parton distributions for collider physics. *Phys.Rev.*, D82:074024, 2010.
- [86] D. Levin. Muonrecpedia.  
<https://twiki.cern.ch/twiki/bin/view/AtlasProtected/MuonRecoPedia>.
- [87] LHC Higgs Cross Section Working Group, S. Dittmaier, C. Mariotti, G. Passarino, and R. Tanaka (Eds.). Handbook of LHC Higgs Cross Sections: 2. Differential Distributions. *CERN-2012-002*, CERN, Geneva, 2012.

## Bibliography

---

- [88] LHC Higgs Cross Section Working Group, S. Heinemeyer, C. Mariotti, G. Passarino, and R. Tanaka (Eds.). Handbook of LHC Higgs Cross Sections: 3. Higgs Properties. *CERN-2013-004*, CERN, Geneva, 2013.
- [89] LHCb Collaboration. The LHCb Detector at the LHC. *JINST*, 3:S08005, 2008.
- [90] Gionata Luisoni, Paolo Nason, Carlo Oleari, and Francesco Tramontano.  $HW^\pm/HZ + 0$  and 1 jet at NLO with the POWHEG BOX interfaced to GoSam and their merging within MiNLO. *JHEP*, 1310:083, 2013.
- [91] G.P. Salam M. Cacciari. Pileup subtraction using jet areas. *Phys. Lett. B*, 119, 2008.
- [92] S. Maettig. *Luminosity Measurements with the ATLAS Detector*. PhD thesis, University of Hamburg, 2012.
- [93] A.D. Martin, W.J. Stirling, R.S. Thorne, and G. Watt. Parton distributions for the LHC. *Eur.Phys.J.*, C63:189–285, 2009.
- [94] Mike Lamont. The First Years of LHC Operation for Luminsity Production. IPAC13 Presentation  
<https://accelconf.web.cern.ch/accelconf/IPAC2013/talks/moyab101talk.pdf>.
- [95] L. Moneta et al. The RooStats Project. In *Proceedings of the 13th International Workshop on Advanced Computing and Analysis Techniques in Physics Research, ACAT2010*, Proceedings of Science, 2010.
- [96] K. et al. Nakamura. *Review of particle physics*. *J. Phys. G*.
- [97] P. Nason and C. Oleari. NLO Higgs boson production via vector-boson fusion matched with shower in POWHEG. *JHEP*, 1002:037, 2010.
- [98] R. Nicolaidou, L. Chevalier, S. Hassani, J. F. Laporte, E. Le Menedeu, and A. Ouraou. Muon identification procedure for the ATLAS detector at the LHC using Muonboy reconstruction package and tests of its performance using cosmic rays and single beam data. *Journal of Physics: Conference Series*, 219(3):032052, 2010.
- [99] Carlo Oleari and Laura Reina.  $W^\pm b\bar{b}$  production in POWHEG. *JHEP*, 1108:061, 2011.
- [100] E.A. Paschos. *Electroweak theory*. Cambridge University Press, 2007.
- [101] M.E. Peskin and D. V. Schroeder. *An Introduction to Quantum Field Theory*. Westview Press, 1995.

## Bibliography

---

- [102] J. Pumplin, D.R. Stump, J. Huston, H.L. Lai, Pavel M. Nadolsky, et al. New generation of parton distributions with uncertainties from global QCD analysis. *JHEP*, 0207:012, 2002.
- [103] Alexander L. Read. Presentation of search results: The CL(s) technique. *J.Phys.*, G28:2693–2704, 2002.
- [104] Elzbieta Richter-Was, D Froidevaux, and Luc Poggioli. Atlfast 2.0 a fast simulation package for atlas. Technical Report ATL-PHYS-98-131, CERN, Geneva, Nov 1998.
- [105] S. Alioli et al. NLO Higgs boson production via gluon fusion matched with shower in POWHEG. *JHEP*, 0904:002, 2009.
- [106] A. Salam. Elementary particle theory: Relativistic groups and analyticity (Nobel Symposium No. 8), 1968.
- [107] T. Sjostrand, S. Mrenna, and P. Skands. Brief Introduction to PYTHIA 8.1. *Comput. Phys. Comm.*, 178:85, 2008.
- [108] Iain W. Stewart and Frank J. Tackmann. Theory uncertainties for higgs mass and other searches using jet bins. *Phys. Rev. D*, 85:034011, Feb 2012.
- [109] The ATLAS Collaboration. Supporting document for “Search for the Production of a Standard Model Higgs Boson produced in association with a Vector Boson and decaying to a pair of b-quarks. ATLAS Internal Communication **ATL-COM-PHYS-2014-051** (2014).
- [110] The ATLAS Collaboration. Supporting document on electron efficiency measurements using the 2012 LHC proton-proton collision data. ATLAS Internal Communication **ATL-COM-PHYS-2013-1295** (2014).
- [111] The ATLAS Collaboration. Updated coupling measurements of the Higgs boson with the ATLAS detector using up to  $25 \text{ fb}^{-1}$  of proton-proton collision data. ATLAS Internal Communication **ATLAS-CONF-2014-09** (2014).
- [112] S. van der Meer. Calibration of the effective beam height in the ISR. CERN note: CERN-ISR-PO-68-31, <https://cdsweb.cern.ch/record/296752>, 1968.
- [113] M. Villa. The luminosity monitor of the ATLAS experiment. In *Nuclear Science Symposium Conference Record (NSS/MIC)*, pages 1028–1033, IEEE, 2009.
- [114] W. Lampl et al. Calorimeter clustering algorithms: description and performance. ATLAS Note**ATL-LARG-PUB-2008-002**(2008).

## *Bibliography*

---

- [115] Z. Was. TAUOLA the library for tau lepton decay, and KKMC / KORALB / KORALZ /... status report. *Nucl.Phys.Proc.Suppl.*, 98:96–102, 2001.
- [116] Steven Weinberg. A model of leptons. *Phys. Rev. Lett.*, 19(21):12641266, 1967.
- [117] Wikimedia Commons. Standard Model of Elementary Particles.  
[http://commons.wikimedia.org/wiki/File:Standard\\_Model\\_of\\_Elementary\\_Particles.svg](http://commons.wikimedia.org/wiki/File:Standard_Model_of_Elementary_Particles.svg).
- [118] A. Yamamoto et al. Progress in ATLAS central solenoid magnet. *IEEE T. Appl. Supercond.*, 10:353, 2000.

# Appendix A

## Prefit distributions for the 3-jet region

This appendix contains the 3-jet analysis regions present in the 2-lepton profile likelihood fit. The distributions shown are those before the binning transformation discussed in Section 9.4 is applied, and before the fit is performed. The red histogram in each figure represents the signal shape, where the signal cross section has been scaled up to ease viewing of the shape.

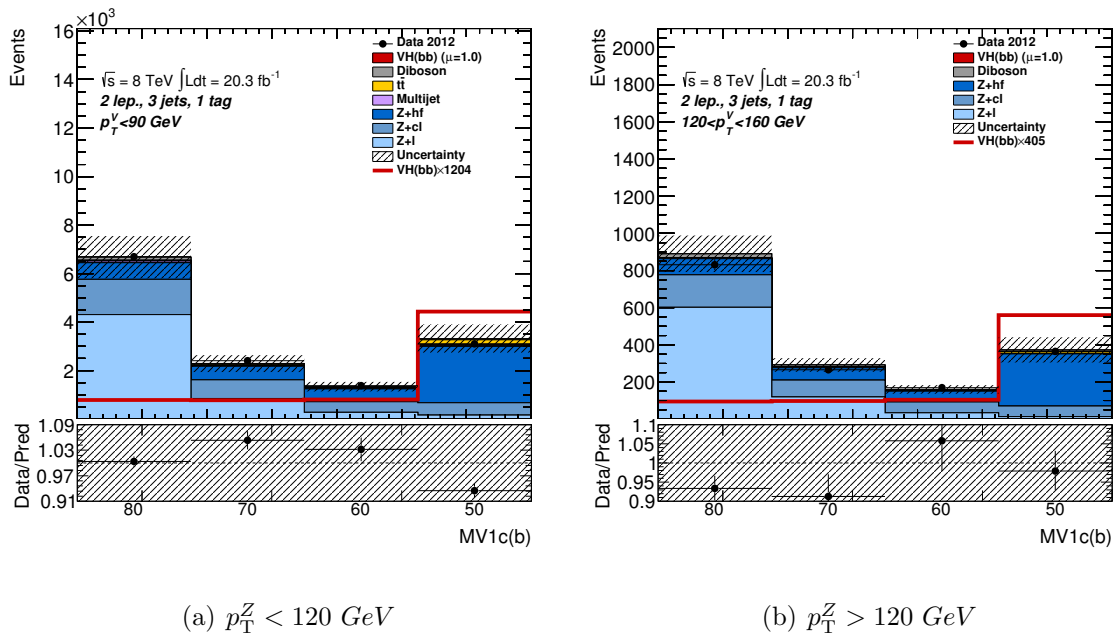


Figure A.1: Pre-fit MV1c distributions in 2-lepton events in the 1-tag, 3-jet analysis regions. The pre-fit background expectation is indicated by the dashed blue line.

*Appendix A: Prefit distributions for the 3-jet region*

---

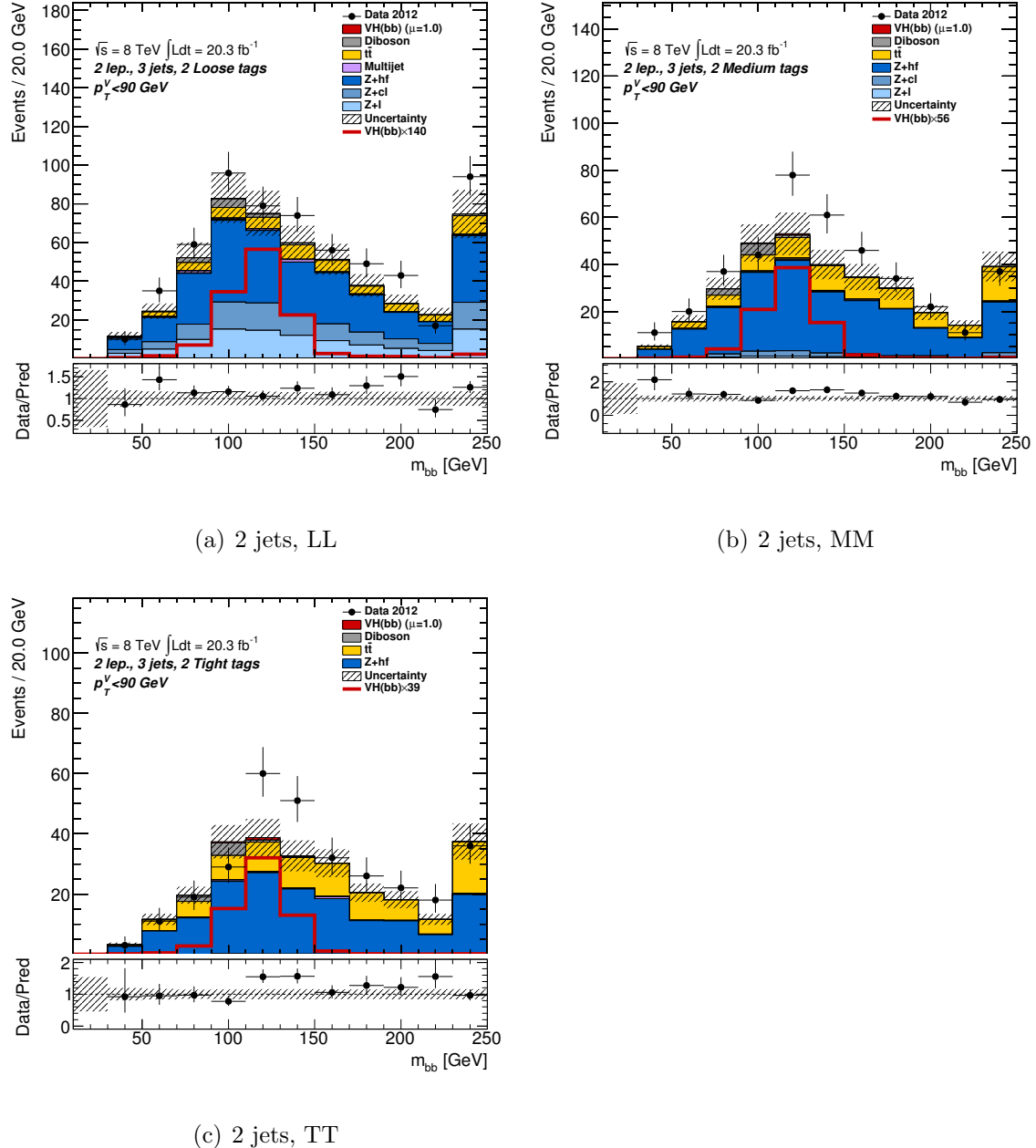


Figure A.2: Pre-fit plots for the  $m_{b\bar{b}}$  distribution in 2-lepton events in the *LL*, *MM* and *TT* tag categories for the 3-jet events.

*Appendix A: Prefit distributions for the 3-jet region*

---

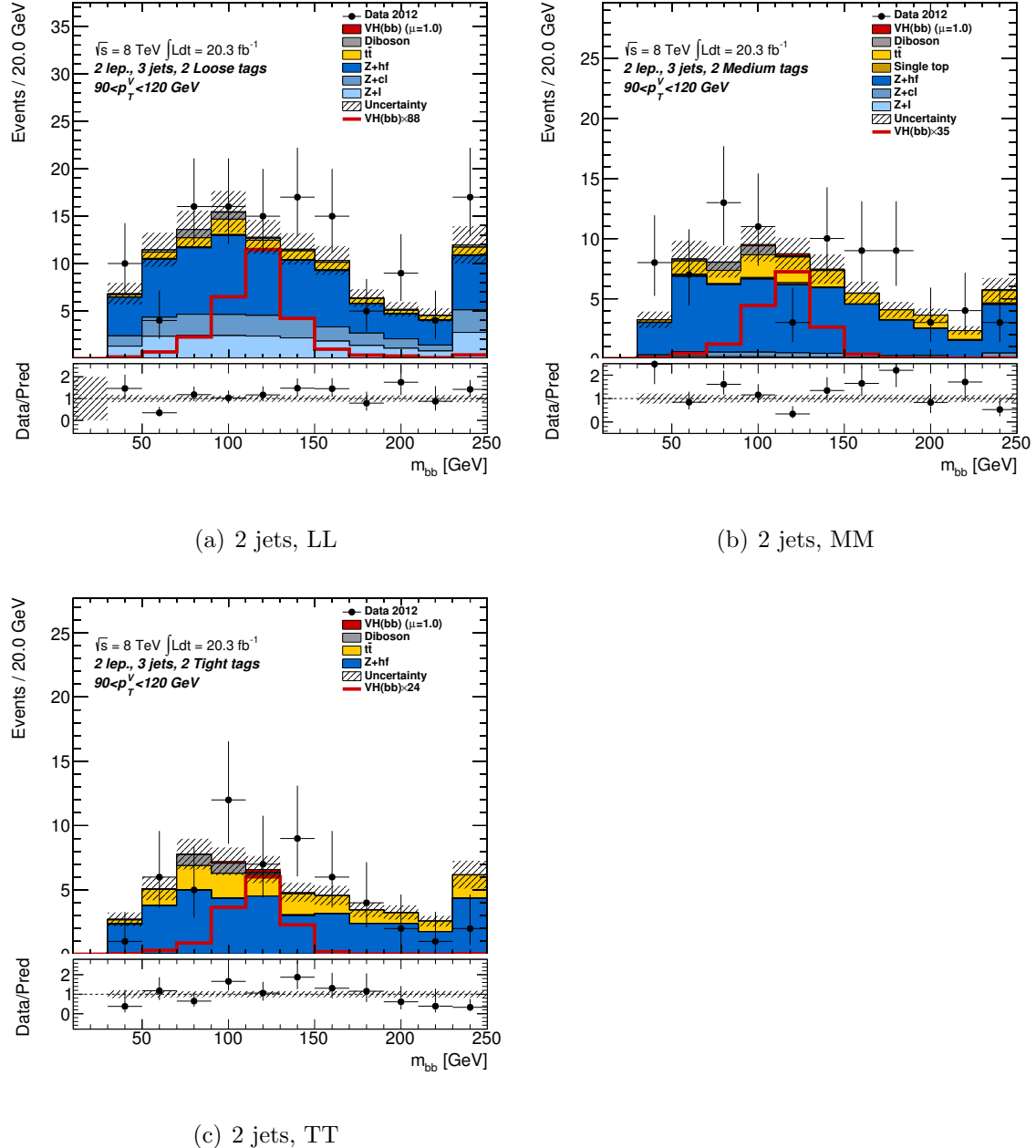


Figure A.3: Pre-fit plots for the  $m_{bb}$  distribution in 2-lepton events in the *LL*, *MM* and *TT* tag categories for the 3-jet events.

Appendix A: Prefit distributions for the 3-jet region

---

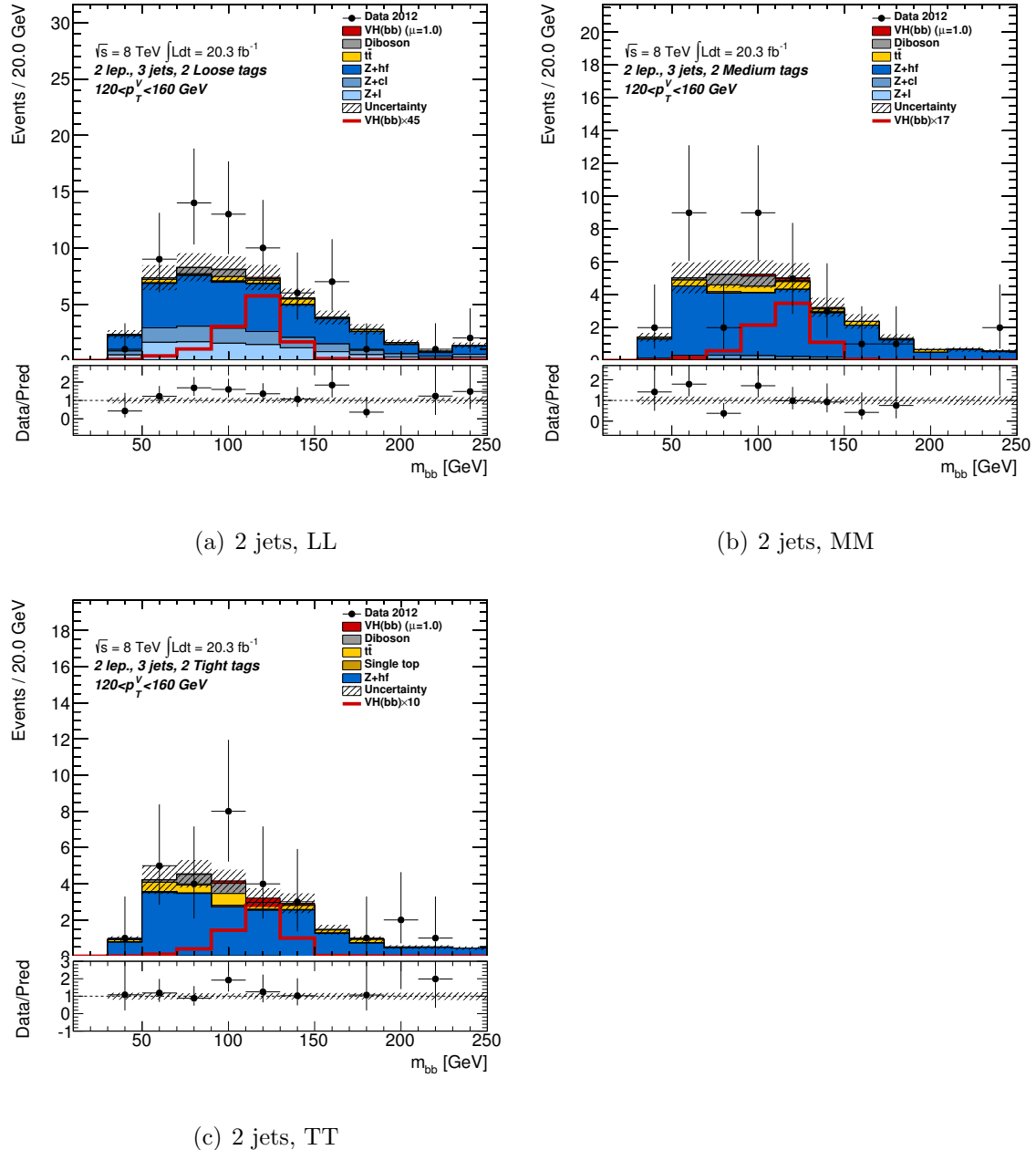


Figure A.4: Pre-fit plots for the  $m_{b\bar{b}}$  distribution in 2-lepton events in the *LL*, *MM* and *TT* tag categories for the 3-jet events.

*Appendix A: Prefit distributions for the 3-jet region*

---

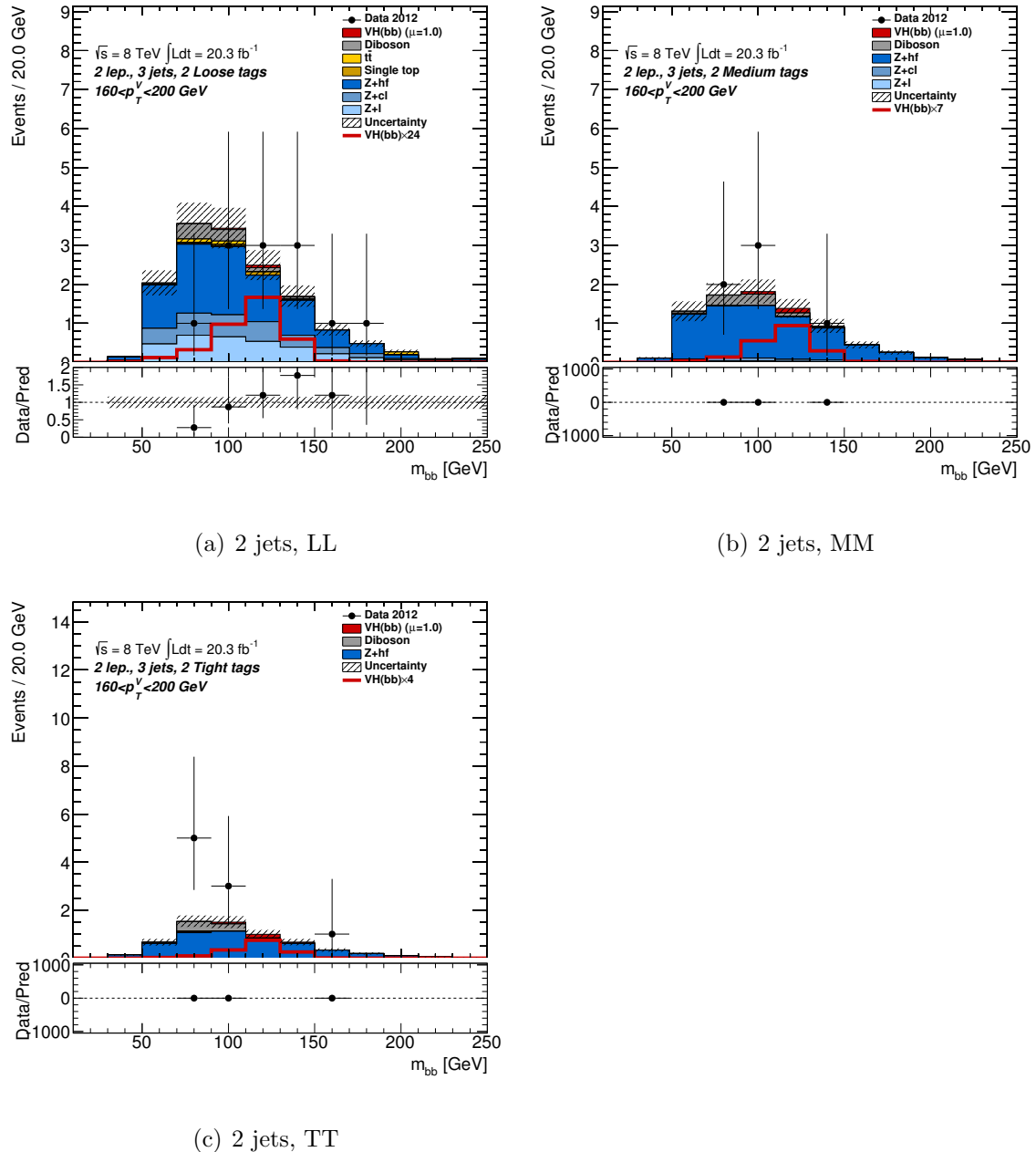


Figure A.5: Pre-fit plots for the  $m_{b\bar{b}}$  distribution in 2-lepton events in the *LL*, *MM* and *TT* tag categories for the 3-jet events.

*Appendix A: Prefit distributions for the 3-jet region*

---

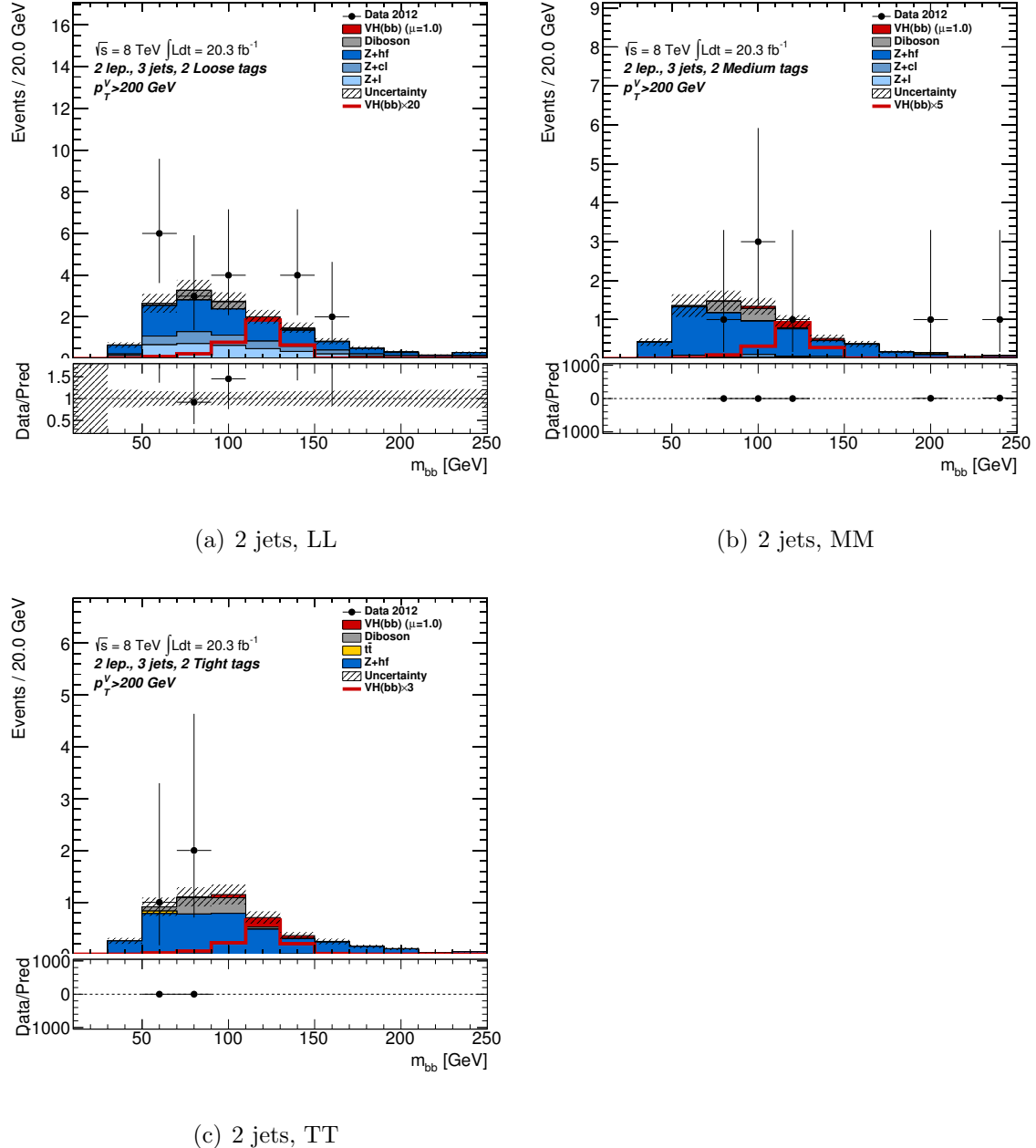


Figure A.6: Pre-fit plots for the  $m_{b\bar{b}}$  distribution in 2-lepton events in the *LL*, *MM* and *TT* tag categories for the 3-jet events.

## Appendix B

# Postfit distributions for the 3-jet region

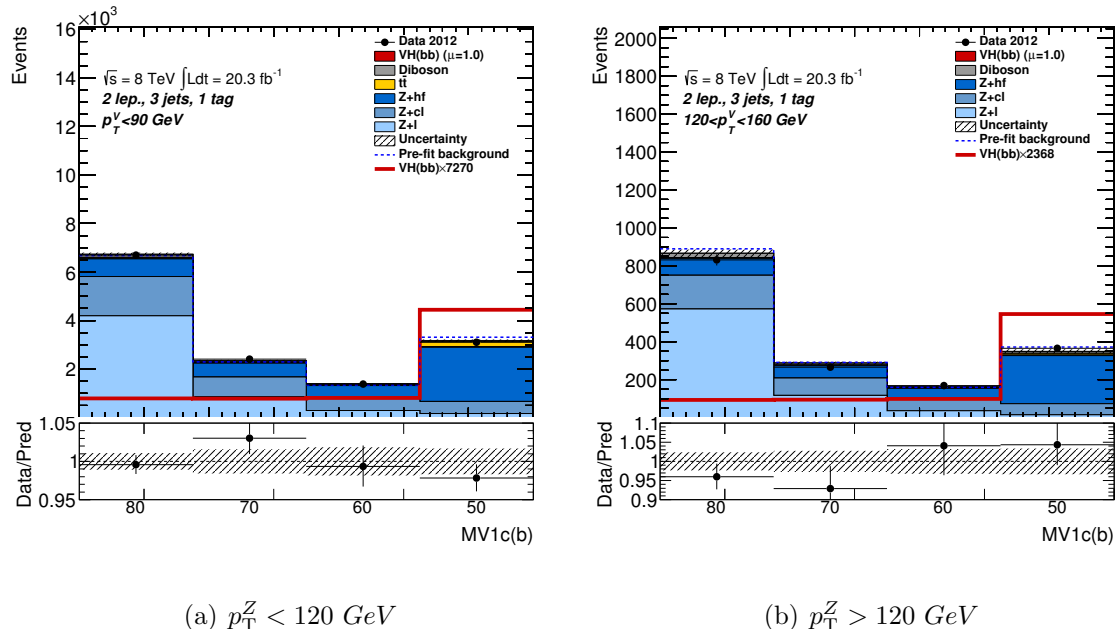


Figure B.1: Post-fit plots for the MV1c distribution in 2-lepton events in the 1-tag, 3-jet analysis regions. The pre-fit background expectation is indicated by the dashed blue line.

*Appendix B: Postfit distributions for the 3-jet region*

---

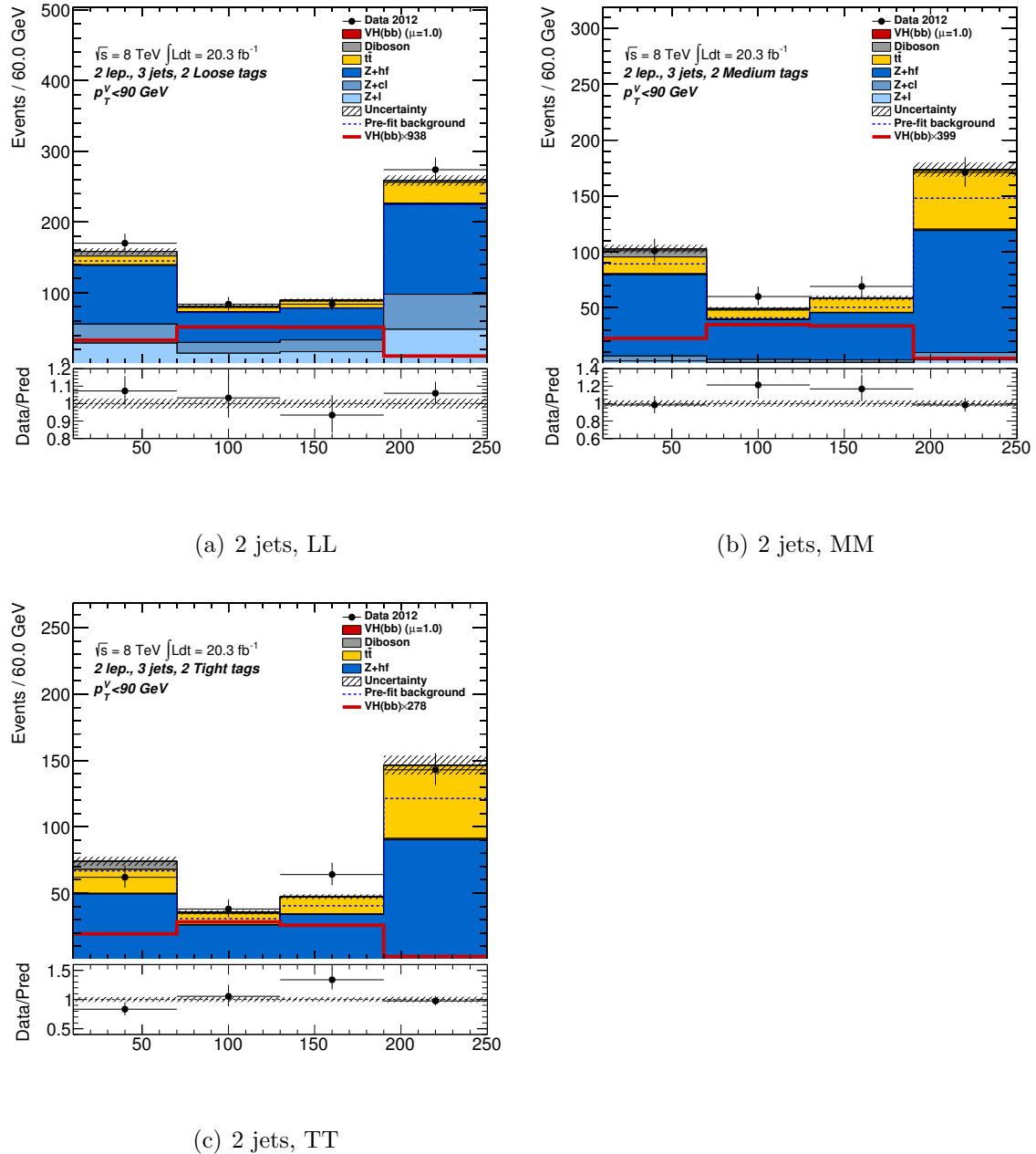


Figure B.2: Post-fit plots for  $m_{b\bar{b}}$  distribution in 2-lepton events in the  $LL$ ,  $MM$  and  $TT$  tag categories for the 3-jets events in the 2-lepton fit. The pre-fit background expectation is indicated by the dashed blue line.

*Appendix B: Postfit distributions for the 3-jet region*

---

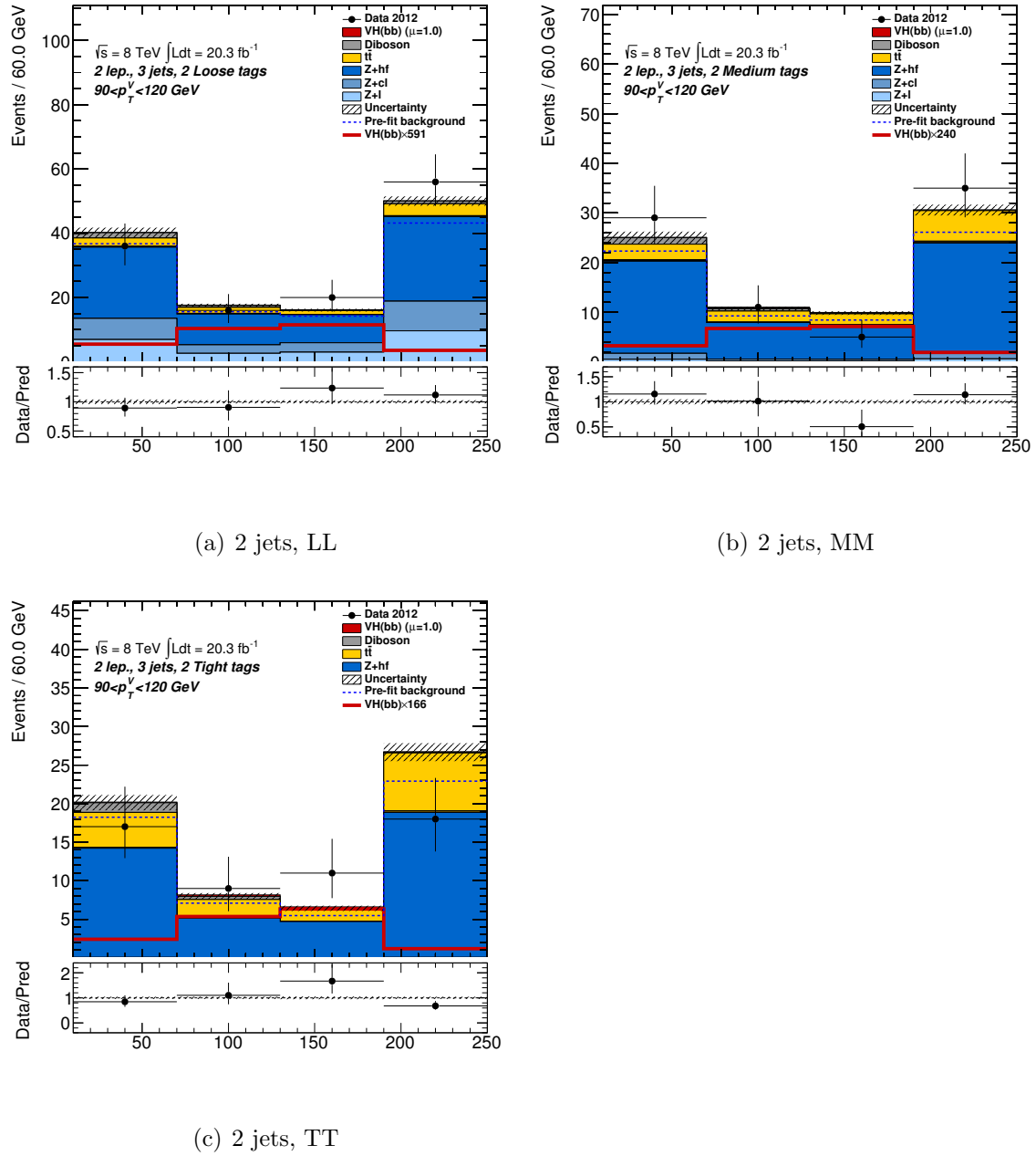


Figure B.3: Post-fit plots for  $m_{b\bar{b}}$  distribution in 2-lepton events in the  $LL$ ,  $MM$  and  $TT$  tag categories for the 3-jets events in the 2-lepton fit. The pre-fit background expectation is indicated by the dashed blue line.

*Appendix B: Postfit distributions for the 3-jet region*

---

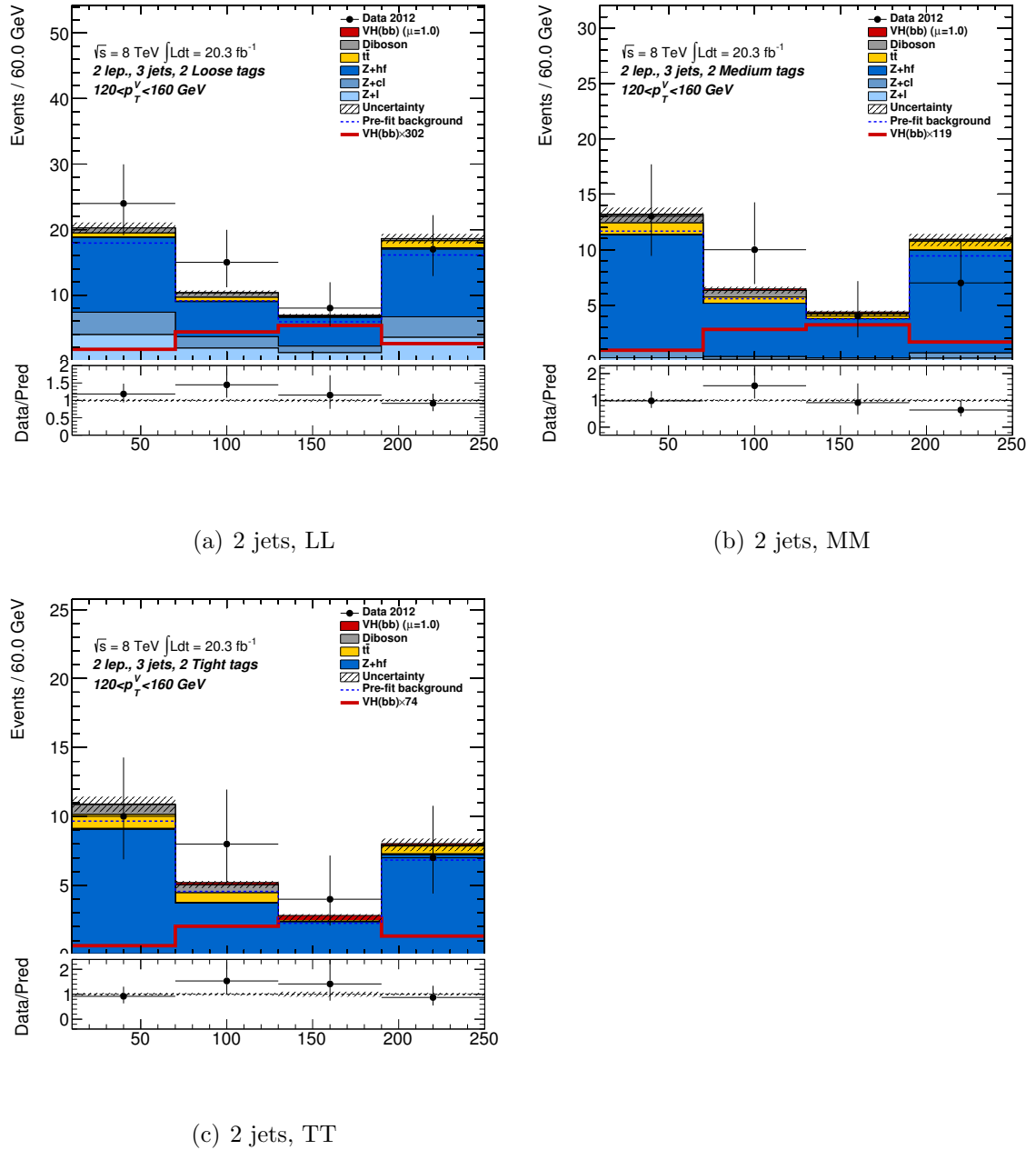


Figure B.4: Post-fit plots for  $m_{b\bar{b}}$  distribution in 2-lepton events in the  $LL$ ,  $MM$  and  $TT$  tag categories for the 3-jets events in the 2-lepton fit. The pre-fit background expectation is indicated by the dashed blue line.

*Appendix B: Postfit distributions for the 3-jet region*

---

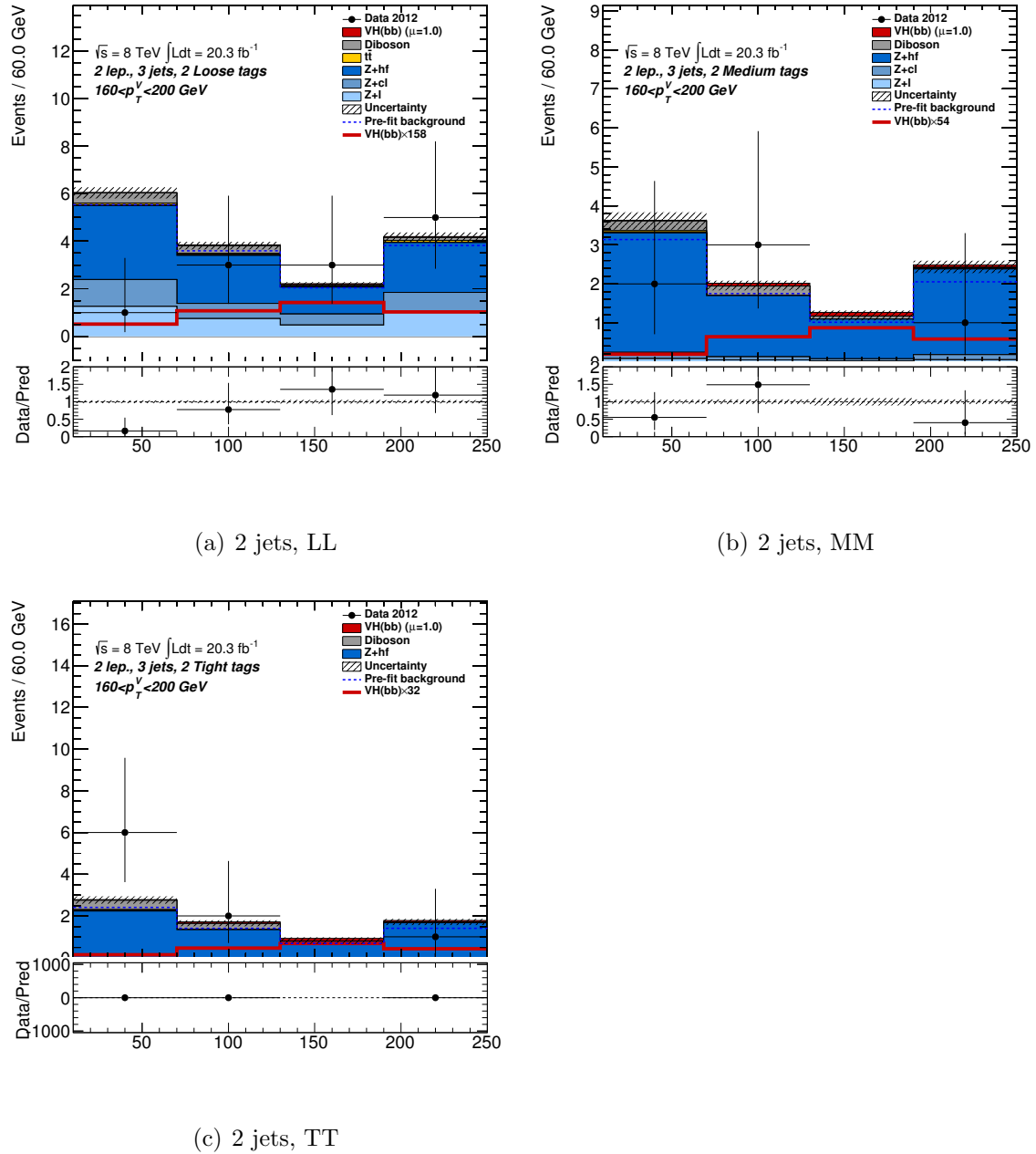


Figure B.5: Post-fit plots for  $m_{b\bar{b}}$  distribution in 2-lepton events in the  $LL$ ,  $MM$  and  $TT$  tag categories for the 3-jets events in the 2-lepton fit. The pre-fit background expectation is indicated by the dashed blue line.

*Appendix B: Postfit distributions for the 3-jet region*

---

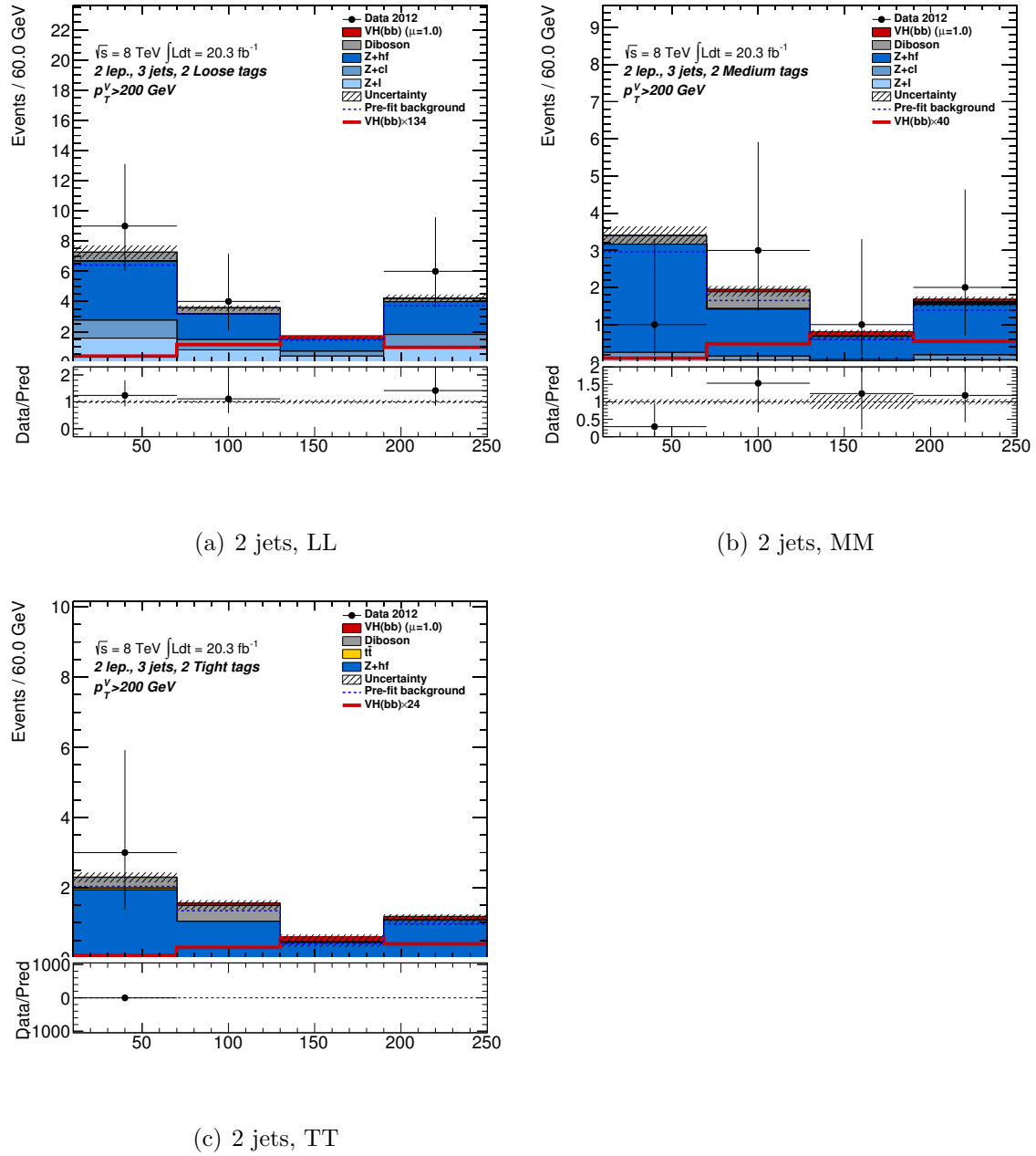


Figure B.6: Post-fit plots for  $m_{b\bar{b}}$  distribution in 2-lepton events in the  $LL$ ,  $MM$  and  $TT$  tag categories for the 3-jets events in the 2-lepton fit. The pre-fit background expectation is indicated by the dashed blue line.